

**Turbulent dispersion
in the
Atmospheric Convective Boundary Layer**

Promotoren:

Prof. Dr. A. A. M. Holtslag
Hoogleraar Meteorologie en Luchtkwaliteit
Wageningen Universiteit

Prof. Dr. Ir. P. J. H. Builtjes
Senior Onderzoeker
Nederlandse Organisatie voor
Toegepast-natuurwetenschappelijk Onderzoek TNO, Apeldoorn
Gast-docent Atmosferische Chemie
Meteorologisch Instituut, Vrije Universiteit Berlijn

Co-promotor:

Dr. J. Vilà-Guerau de Arellano
Universitair Docent, leerstoelgroep Meteorologie en Luchtkwaliteit
Wageningen Universiteit

Samenstelling promotiecommissie:

Prof. Dr. E. Fedorovich
University of Oklahoma (USA)

Prof. Dr. F.T.M.Nieuwstadt
Technische Universiteit Delft

Dr. H. van Dop
Univeriteit Utrecht

Prof. J. Grasman
Wageningen Universiteit

Turbulent dispersion in the Atmospheric Convective Boundary Layer

Turbulente dispersie in de atmosferische convectieve grenslaag

Alessandro Dosio

Proefschrift
ter verkrijging van de graad van doctor
op gezag van de rector magnificus
van Wageningen Universiteit,
Prof. Dr. Ir. L. Speelman,
in het openbaar te verdedigen
op woensdag 25 mei 2005
des namiddags te vier uur in de Aula.

ISBN 90-8504-171-6

Foreword

I would have never been able to complete this work without the help and support of many people. I am therefore very glad to have the opportunity to express my gratitude to all the people who have helped, encouraged, and supported me, in this experience.

Firstly, I would like to thank Prof. Peter Builtjes, who has believed in me since we worked together at TNO-Apeldoorn, and who has provided excellent scientific support. Through the Centre of Expertise Emissions and Assessment he has also provided an essential link in the collaboration between Wageningen University-WIMEK (Wageningen Institute for Environment and Climate Research) and TNO-MEP (Netherlands Organisation for Applied Scientific Research-Institute for Environment, Energy and Process Innovation) which has enabled this project to come about.

Many thanks also go to Prof. Bert Holtslag, who welcomed me at the Meteorology and Air Quality Section of Wageningen University. The years I have spent in the department have been greatly rewarding, both from the scientific and personal point of view, and I am really grateful to have been part of this group.

I am sincerely grateful to my daily supervisor, Dr. Jordi Vilá-Guerau de Arellano, for his constant guidance, support and inspiration, and for letting the door of his office always open for discussions and brainstorming. He certainly deserves most of the credit for teaching me how scientific research can be carried out with dedication and rigor, but especially with passion and great enthusiasm.

I would also like to thank Dr. Stefano Galmarini for encouraging me to go to the Netherlands and for his constant help and support over many years.

I have deeply appreciated the numerous fruitful discussions and meetings with many colleagues from other Dutch Universities, in particular Dr. Harm Jonker, Dr. Margreet van Zanten, and Dr. Stephan de Roode, who have all helped me on several occasions with the set up and testing of the model.

All the numerical simulations carried out in this study have been performed on the TERAS supercomputer of the National Computing Center SARA, under financial support by the National Computer Facilities (NCF-NWO, The Netherlands) (project number SG-132).

Special thanks to Prof. F. Nieuwstadt (Delft University), Prof. E. Fedorovich (University of Oklahoma), Dr. Han van Dop (IMAU - Utrecht University) and Prof. J. Grasman (Wageningen University) for carefully and critically reading this work, and for agreeing to be part of my Doctoral Committee.

Many thanks to all the people of the Meteorology and Air Quality Section for the open and friendly atmosphere that has made this department a very special place to work in. I am especially grateful

to Bas, who, among many other things, kindly provided the Dutch translation of the summary at the end of this thesis. Two other people who also deserve special credit are Gerrie and Kees, who were always available and ready to help me to solve my countless technical (logistic, hardware, software, ...) and bureaucratic problems.

I would also like to take this opportunity to thank Dr. Marc Sutton from the Centre for Ecology and Hydrology of Edinburgh (UK) for the trust he has placed in me in offering me an exciting new position within his research team.

Thanks to all the people who have shared with me the experience of living and working abroad, and for the many enjoyable times we spent together, in particular Francesco and Francesca, Jeff and Christelle, Manuel, Axel, Gabriella and Cisco.

Sono profondamente grato a tutta la mia famiglia che ha sempre creduto in me. Grazie per avermi permesso, con il vostro aiuto e costante supporto, di vivere questa esperienza nel modo piu' proficuo e sereno possibile.

Finally, thanks to a very special person, my wife Elizabeth, whose strength, courage, and the patience has inspired me throughout, and without whom I would be a much poorer man.

Contents

1	Introduction	1
1.1	Background	1
1.2	Turbulent motion in the Atmospheric Boundary Layer	3
1.3	Motivation of the work and research questions	5
1.3.1	Turbulent dispersion in the CBL	5
1.3.2	Research questions	7
1.4	Different approaches to studying atmospheric dispersion	7
1.4.1	Theoretical analysis	7
1.4.2	Experimental observations	8
1.4.3	Physical and mathematical models	9
1.5	Outline of the thesis	13
2	Large-Eddy Simulation model: description, improvements and testing	17
2.1	Simulation of turbulent flow in the Atmospheric Boundary Layer	17
2.1.1	DNS, LES and RANS	17
2.1.2	LES studies of turbulent dispersion in the Atmospheric Boundary Layer . .	19
2.2	Brief history of the Dutch Atmospheric LES	21
2.3	Description of the LES	23
2.3.1	The governing equations	23
2.3.2	The filtered equations	24
2.3.3	Sub-grid Scale model	25
2.3.4	Surface model	27
2.4	Improvements to the code	29
2.4.1	Non-equidistant grid	29
2.4.2	Lagrangian Particle Module	31
2.5	APPENDIX A: The Kappa scheme	34
2.6	APPENDIX B: The Poisson Solver	37
3	Relating Eulerian and Lagrangian Statistics for the Turbulent Dispersion in the Atmospheric CBL	41
3.1	Introduction	41
3.2	Theoretical background	43
3.3	Description of the numerical experiment	44
3.3.1	Lagrangian particle model	45

3.3.2	Definition of statistical variables	46
3.4	Eulerian statistics	48
3.4.1	Spatial analysis	49
3.4.2	Temporal analysis	54
3.4.3	Validation of Taylor's hypothesis of frozen turbulence in atmospheric flows	55
3.5	Lagrangian statistics	56
3.6	Horizontal and vertical dispersion	60
3.6.1	Horizontal dispersion	61
3.6.2	Vertical dispersion	61
3.7	Relationship between Eulerian and Lagrangian frameworks	65
3.7.1	Integral Lagrangian time scale	65
3.7.2	Value of the ratio β_j	67
3.8	Conclusions	68
3.9	APPENDIX A: Definition of statistics	70
3.9.1	Eulerian statistics	70
3.9.2	Lagrangian statistics	70

4 Statistics of absolute and relative dispersion in the Atmospheric Convective Boundary

Layer		71
4.1	Introduction	71
4.2	Theoretical background	73
4.3	Numerical Setup	74
4.3.1	Model description	74
4.3.2	Flow characteristics	75
4.3.3	Plume concentration calculation	75
4.3.4	Definition of statistical parameters	75
4.4	Results and discussion	77
4.4.1	Dispersion in absolute coordinate system	77
4.4.2	Meandering component	80
4.4.3	Dispersion in relative coordinate system	85
4.4.4	Validation of Gifford formula	92
4.5	Conclusions	97

5 Dispersion of a passive tracer in buoyancy- and shear-driven boundary layers

5.1	Introduction	99
5.2	Description of the numerical experiment	100
5.3	Dispersion in a pure-convective boundary layer	103
5.3.1	Velocity variances	104
5.3.2	Mean plume height and dispersion parameters	104
5.3.3	Non dimensional crosswind-integrated ground concentrations	110
5.4	Dispersion in a buoyancy- and shear-driven boundary layer	111
5.4.1	Velocity variances	111
5.4.2	Mean plume height and dispersion parameters	113
5.4.3	Crosswind-integrated and ground concentrations	116

5.4.4	Meandering and relative dispersion in a buoyancy- and shear-driven boundary layers	120
5.4.5	Concentration fluctuations	121
5.5	Parameterization for the dispersion in a buoyancy- and shear-driven boundary layers	122
5.5.1	Horizontal dispersion parameter	122
5.5.2	Vertical dispersion parameter	124
5.6	Conclusions	125
5.7	APPENDIX A: List of symbols	127
6	The dispersion of chemically reactive species in the atmospheric boundary layer	129
6.1	Introduction	129
6.2	Governing equations and dimensionless numbers	131
6.3	The presence of the chemical terms in the averaged equations	134
6.3.1	Non-linear flux of the reactive species	136
6.3.2	Segregation of species	139
6.4	Chemically reactive plumes	140
6.4.1	The effect of chemistry: simple decay	140
6.4.2	The effect of turbulence on chemistry: non-linear reaction	143
6.5	Conclusions and future perspectives	145
7	Summary and Perspectives	147
7.1	General conclusions	147
7.2	Future perspective	151

Chapter 1

Introduction

1.1 Background

Atmospheric dispersion is concerned with the physical and chemical processes that airborne materials undergo from their emission into the atmosphere to their removal by deposition or rainfall. These processes include the transport and mixing of contaminants, their chemical/radioactive transformation, and their dilution and deposition.

Atmospheric dispersion is a very common phenomenon, which can be observed at different spatial and temporal scales, from the local meandering of a smoke plume from a stack, to the global transport of ashes from a volcanic eruption. Other examples of dispersion related problems include toxic, chemical or nuclear releases, tropospheric ozone formation and transport, as well as urban or industrial releases. The study of atmospheric dispersion, therefore, has significant implications on a broad range of atmospheric pollution problems, from forecasting urban air quality to quantifying sources and sinks of greenhouse gases.

However, predicting with accuracy the transport of pollutants emitted from a source is a very challenging and complex problem. In fact, atmospheric dispersion is influenced by many factors such as source characteristics, meteorological conditions and topographic characteristics of the terrain. Additionally, during transport and mixing, the airborne material may undergo different physical processes such as dilution, deposition and chemical transformations. Understanding the complexity of these various processes is therefore essential in order to predict the impact on human health and on the environment, and to determine the most efficient strategies to control and reduce its most harmful consequences. A schematic representation of the various issues involved in the multi-disciplinary study of atmospheric dispersion, from the emission of pollutants to air-quality regulatory procedures is shown in Figure 1.1.

In this doctoral thesis the focus is mainly on the physical processes involved in the dispersion of pollutants, namely transport, mixing and chemical transformations.

The large-scale transport of pollutants in the atmosphere is mainly governed by the mean flow field, such as synoptic-scale circulation, or mesoscale phenomena (for instance sea-breezes and mountain-valley flows). This mean flow causes the axis of the plume to be aligned with the mean wind direction. However, the spread of the material is heavily influenced by the local properties of the atmospheric flow, namely the instantaneous and chaotic fluctuations of the wind velocity

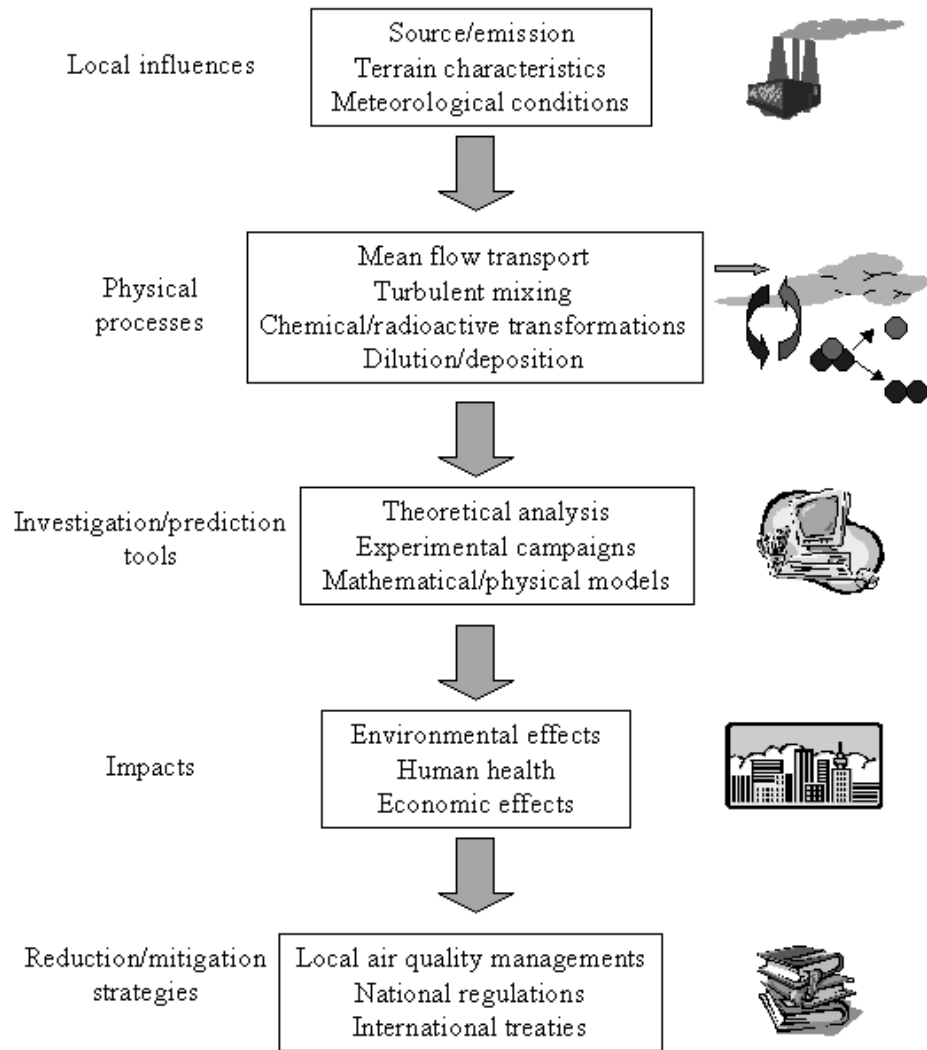


Figure 1.1: Atmospheric dispersion is a multi-disciplinary issue. Transport of pollutants is influenced by local physical properties such as meteorological conditions and characteristics of the terrain. During the transport, the airborne material undergoes different processes, from turbulent mixing to chemical transformations and deposition. Atmospheric dispersion has significant implications from a human perspective, which require local, national and international strategies to prevent and mitigate possible negative effects on human health and the environment (adapted from Jones, 2004).

1.2. Turbulent motion in the Atmospheric Boundary Layer



Figure 1.2: Atmospheric dispersion is a common phenomenon. However, the interaction between the airborne material and the atmospheric flow is a very complex process (photograph from www.freefoto.com) .

known as turbulence.

Turbulence is a peculiar characteristic of the Atmospheric Boundary Layer (ABL), the lower layer of the atmosphere just above the Earth's surface. Its chaotic nature implies that the transport of material is a stochastic (i.e. random) process, hence the final status of the system is strongly influenced by small perturbations in the initial conditions. For instance, particles of contaminant that are released simultaneously can be rapidly separate by the small turbulent motions and subsequently follow completely diverging trajectories. This phenomenon is commonly experienced by observing balloons simultaneously released into the air: balloons that are released from the same point can be ultimately found hundreds of kilometers apart (*Jones, 2004*).

Atmospheric turbulence is also the main factor governing the distribution and concentration of pollutants emitted in the ABL. For example, in the case of strong winds and energetic turbulent mixing, pollutants are rapidly dispersed and diluted into the atmosphere. On the contrary, in light wind conditions and weak turbulence, pollutants tend to accumulate near to their source, causing air-pollution episodes commonly experienced in urban and industrialized areas. A typical example of an industrial plume dispersing in the atmosphere is shown in Figure 1.2.

To understand and predict atmospheric dispersion it is therefore essential to study and analyze the characteristics and the properties of the turbulent motion in the ABL.

1.2 Turbulent motion in the Atmospheric Boundary Layer

Turbulent motion in the ABL is generated by the interaction between the atmospheric flow and the Earth's surface. In particular, there are two distinct mechanisms for turbulence production in the ABL: the difference in temperature between the ground and the overlying air (quantified by a positive/negative surface heat flux) and the friction between air and the surface, which causes the

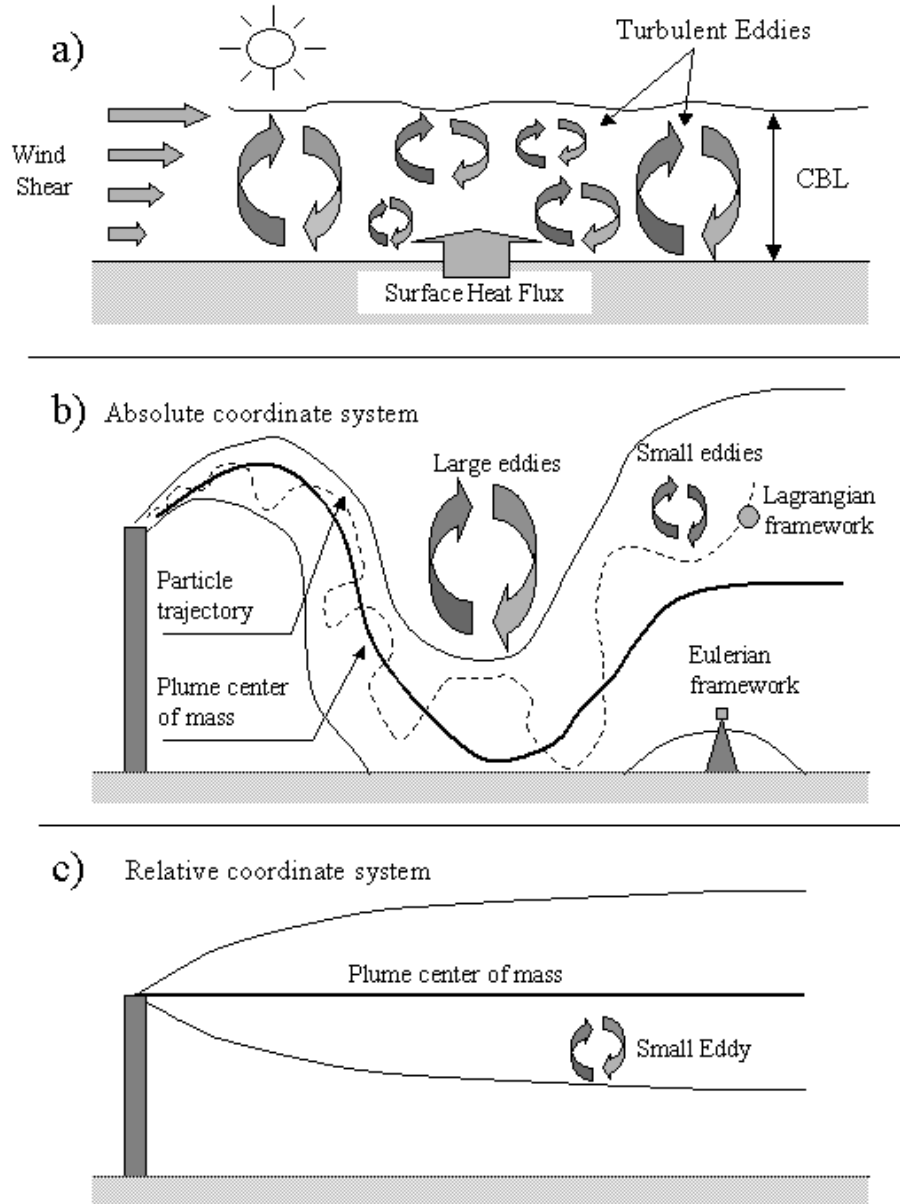


Figure 1.3: a) Schematic illustration of the two main driving mechanisms for turbulence production in the ABL. During sunny days and low wind speed conditions, large-scale motion known as thermal convection is generated and the ABL is referred to as the Convective Boundary Layer (CBL). b) Idealized representation of a plume dispersing in the CBL in the absolute (fixed) coordinates system. The different effect of large- and small-scale turbulent eddies on the plume evolution are illustrated. In the picture, an example of particle trajectory is also shown: in the Lagrangian framework, dispersion is studied in a reference frame that moves with the particles. c) Idealized representation of the same plume in the relative coordinate system, which is the coordinate system of the plume's center of mass: in this framework the large-scale motion is removed and only the small-scale eddies contribute to the dispersion.

1.3. Motivation of the work and research questions

wind speed to change with height (wind shear). The combination of these two driving mechanisms, called *thermal* and *mechanical* forcing respectively, generates irregular movements of air that are usually referred to as turbulent eddies. These eddies range in size from a few millimeters to the entire depth of the ABL (1-2 Km) (Figure 1.3a).

The ABL is usually classified by the relative importance of the thermal and mechanical forcing. In conditions of strong winds and weak solar insolation, wind shear is the main responsible for the production of turbulence, and the ABL is said to be in *neutral* conditions. During nighttime, the ABL is in *stable* conditions, because turbulence produced by the friction with the surface is suppressed by the stratification of the air due to the cooling of the surface.

Finally, during sunny days with low wind speed, the heating of the surface generates a large-scale, organized motion of warm air (updrafts) and cold air (downdrafts) known as thermal convection. This motion is typically inhomogeneous and non-isotropic (i.e. it is dependent on the direction). In particular, the area occupied by the updrafts is smaller (30-40 %) than that occupied by the downdrafts (60-70 %). As a consequence, the vertical upward motion is stronger than the downward one. Typical vertical velocities measured in the middle of the CBL are of the order of 2 m/s for the positive vertical motion and less than 1 m/s for the subsidence motion. During convective (or *unstable*) conditions the ABL is referred to as the Convective Boundary Layer (CBL).

Our research focuses mainly on the influence of turbulent motion on plume dispersion in the CBL.

1.3 Motivation of the work and research questions

1.3.1 Turbulent dispersion in the CBL

When a plume is emitted in the CBL, its shape, structure, and evolution are determined by the interaction between the plume and the turbulent eddies. In particular, eddies that are much larger than the plume size cause the plume to *meander*, which is the large-scale movement of the plume as a whole and the sweeping of the plume's center of mass. Turbulent eddies that are much smaller than the plume size, on the contrary, are mainly responsible for the growth of the instantaneous plume width, by causing an increasing entrainment of air into the body of the plume. The different effect of large and small-scale turbulent eddies on the motion and spread of a dispersing plume is illustrated in Figure 1.3b.

The non-homogeneity of the turbulent motions in the vertical direction has a great effect on the behavior of a plume with respect to its release height. As mentioned earlier, the area occupied by the updrafts is smaller than that occupied by the downdrafts. As a consequence, a plume that is emitted from an elevated source, is more likely to be caught by a downdraft, and, consequently, rapidly transported towards the surface. As a result, very high ground-concentrations are measured near the emitting source. On the contrary, a plume emitted near the ground will be rapidly transported upwards by the thermals. This plume behavior was first experimentally observed in the early 1970's by Willis and Deardorff (see Section 1.4.3) by simulating the CBL with a water-tank experiment, and has been more recently confirmed by numerous field campaigns and numerical experiments.

Dispersion in absolute and relative coordinate system

Large-scale turbulent eddies are the main responsible for the motion of the plume's center of mass, whereas small-scale eddies tend to mix the contaminant inside the plume and consequently increase the plume size. Therefore the dispersion of a plume as seen from a fixed point of view, or *absolute* coordinate system, is driven by the combined effect of large- and small-scale turbulent motions (Figure 1.3b).

However, if we observed the plume from the point of view of its center of mass (or, equivalently, if we had a measurement device placed on the plume's center of mass), we would perceive the effect of the small-scale eddies only. In other words, by studying dispersion in the coordinate system of the plume's center of mass, the so-called *relative* coordinate system, it is possible to separate the different contributions of small- and large-scale motions on the plume evolution.

In the relative coordinate system, the (vertically) inhomogeneous meandering motion is removed, and only the small homogeneous turbulent eddies contributes to the dispersion process. As a result, the shape and structure of the plume becomes simpler (Figure 1.3c), and its evolution can be described by means of well-known analytical tools (Gaussian models, see Section 1.4.3).

Dispersion in Eulerian and Lagrangian frameworks

A plume dispersing in the atmosphere can be conveniently described as an ensemble of particles (for instance the molecules of pollutants) that move in the flow. Each particle follows a trajectory that is influenced by the combination of the mean wind and the local turbulent properties of the flow.

Usually, dispersion properties, such as the concentration of the pollutant, are calculated or measured at fixed points in space (that is in a fixed reference frame). For instance, the concentration of a pollutant at a certain distance from the emitting source is calculated by measuring the number of particles that have reached the measurement point at the same time. This approach, known as *Eulerian* approach, is most commonly used in field experiments, as well as in laboratory experiments or Eulerian numerical models (see Section 1.4.3).

Alternatively, it is possible to calculate the dispersion properties of the plume in a reference frame that moves with the particles themselves. In other words, each particle is considered separately, and each trajectory is followed singularly. This method, known as *Lagrangian* (or particle) approach, is the most natural approach for theoretical investigation of turbulent dispersion (see Section 1.4.1) because it allows us to relate the displacement of the particles to the properties of their turbulent velocities. Additionally, the particle approach constitutes the basis for a class of mathematical models known as Lagrangian models (see Section 1.4.3).

These two approaches (Eulerian and Lagrangian) are schematically shown in Figure 1.3b.

The main novelty of this doctoral research is the simultaneous investigation of dispersion in different frameworks. Consequently, new insight is gained on the physical process of dispersion in turbulent flow such as the CBL. More precisely, plume dispersion is analyzed in both absolute (fixed) and relative (to the plume center of mass) coordinate systems. Higher-order statistics are calculated in order to investigate the plume variability (concentration fluctuations) and the symmetry (skewness) of the concentration distribution. These properties are related to the turbulence

1.4. *Different approaches to studying atmospheric dispersion*

characteristics of the atmospheric CBL, such as the non-homogeneity of the (vertical) turbulent motion and the effect of the boundary conditions (reflection at the surface and the top of the CBL). Turbulent dispersion is also studied in both the Eulerian and the Lagrangian frameworks within the same (numerical) experiment, in order to relate theoretical analysis to experimental (and numerical) studies. By so doing, the validity of the relationship between dispersion characteristics and turbulent velocity fluctuations (the so called Taylor's theorem, see below) can be tested as well as the relationship between their spatial correlation along-wind and the temporal correlation at a fixed point (frozen-turbulence hypothesis).

1.3.2 Research questions

The main scientific objectives of this research are summarized as follows:

- 1) To analyze the dispersion properties from the point of view of a particle carried by the flow (Lagrangian framework) and to relate these to the turbulent characteristics in the fixed (Eulerian) framework.
- 2) To separate the different contributions of large- and small-scale turbulent motions by studying dispersion in absolute and relative coordinate systems.
- 3) To study the variability and the structure of the plume concentration (such as the symmetry of the scalar distribution along the plume center of mass) by calculating higher-order statistics (such as the variance of the concentration and the skewness of the plume position) in absolute and relative coordinate systems.
- 4) To investigate turbulent dispersion in a CBL driven by the combined effect of thermal and mechanical forcing, in order to study the effect of wind shear on the plume spread.
- 5) To analyze the effect of turbulent motion on chemical transformations in a dispersing plume and to study the dependence of the concentration fluctuations on the ratio between the time scale of the turbulent motion to the time scale of chemical reaction.

1.4 Different approaches to studying atmospheric dispersion

The study of atmospheric dispersion is strictly related to the understanding of the turbulent motion. A systematic investigation of the effect of atmospheric properties on gas diffusion began at the beginning of the 20-th century, mainly through theoretical studies and experimental field campaigns. Nowadays, a broad range of tools and methodologies are available for investigating turbulent dispersion. The most significant ones are described below.

1.4.1 Theoretical analysis

The most significant contribution to the theoretical investigation of turbulent dispersion is the seminal work by *Taylor* (1921) who established the relationship between dispersion parameters (particles' spread) and the turbulent characteristics of the flow (correlation of velocity fluctuations) in the Lagrangian framework (Taylor's theorem). The correlation coefficients were further related to the turbulent spectra through Fourier analysis. This relationship was used to identify the eddies

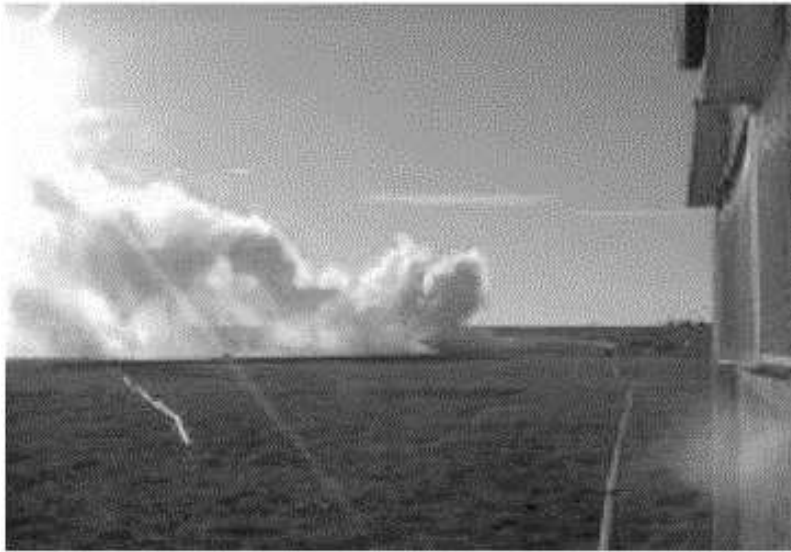


Figure 1.4: An example of a experimental measurement of plume dispersion (*Ott and Jørgensen, 2001.*)

that have the greatest influence on the dispersion process. Taylor's works have been widely applied in studies of atmospheric dispersion in the ABL and they provided the basis for many later developments.

Taylor's theorem of turbulent dispersion will be investigated in Chapter 3.

1.4.2 Experimental observations

Field experiments are of extreme importance in atmospheric studies because they are a direct measure of the physical reality. An example of experimental measurement of plume dispersion is shown in Figure 1.4. The most significant experimental campaigns for the study of atmospheric dispersion are listed below.

The experimental campaign named "Project Prairie Grass" (*Barad, 1958*), was carried out in Nebraska in the summer of 1956 in a virtually flat terrain covered with natural prairie grass. Small amounts of SO_2 were released from near ground level in both unstable and stable conditions. Extensive meteorological measurements were taken on-site during the trials. From the analysis of the Prairie Grass experimental data, *Pasquill* (1961) defined different horizontal and vertical dispersion rates as a function of wind speed and atmospheric stability classes. This method (extended by *Gifford, 1960*) became the established technique for estimating plume growth.

In the "CONvective Diffusion Observed with Remote Sensors (CONDORS) experiment (*Eberhard et al., 1988; Briggs, 1993*) extensive analysis was performed on the behavior of a plume emitted by a continuous point source in the highly convective ABL. In particular remote-sensing measurement devices such as radar and lidar were used to measure dispersion properties in three-dimensions. Plumes from both surface and elevated releases were analyzed, confirming the different behaviors of a plume with respect to the emission height, as shown earlier by the laboratory results by *Dear-dorff and Willis* (see below).

1.4. Different approaches to studying atmospheric dispersion

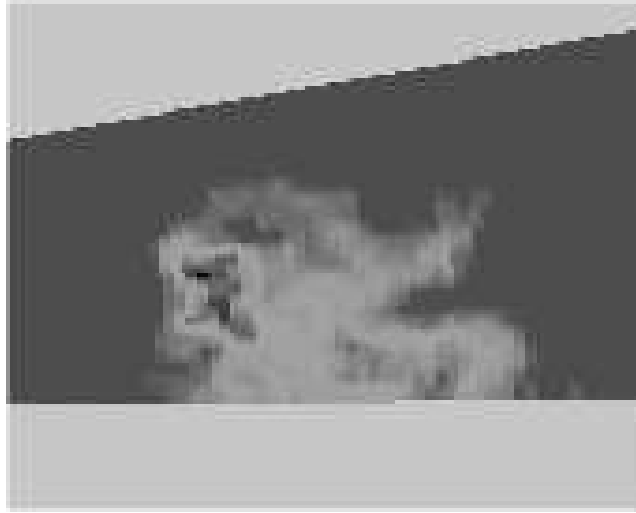


Figure 1.5: A vertical crosswind section of a plume dispersing the atmospheric CBL as measured by a Lidar (*Ott and Jørgensen, 2001.*).

Remote-sensing detectors have been widely used in atmospheric experimental research, because they allow the detailed visualization and measurements of variables such as atmospheric composition, temperature and wind. When a lidar (acronym for LIght Detection And Ranging) is used to analyze atmospheric dispersion, it transmits electromagnetic radiation through the plume, and receives the portion of light scattered back from the plume particles. Recently (*Ott and Jørgensen, 2001*), a lidar was used to visualize two-dimensional vertical crosswind sections of a plume at a certain distance from the emitting source. An example of these measurements is shown in Figure 1.5, where the complex and inhomogeneous structure of the plume is visible.

Experimental measurements of turbulent dispersion are usually carried out with respect to a fixed reference system (Eulerian framework). However, it is also possible to measure dispersion properties in the Lagrangian framework, by following the trajectories of neutrally-buoyant balloons released in the atmosphere (*Gifford, 1955; Angell, 1964; Hanna, 1981*). However, Lagrangian measurements are extremely complex, due to the complicated experimental setting required in order to trace the balloon trajectory, the small number of balloons used, and the short sampling time (which rarely exceeds 30 minutes). As a consequence, experimental estimates of Lagrangian dispersion characteristics only have an accuracy of about 50% (*Hanna, 1981*).

Experimental observations, both in Eulerian and Lagrangian frameworks, have been used in this doctoral research to thoroughly validate the results.

1.4.3 Physical and mathematical models

A model is an idealized representation of reality. It does not provide information on all the features of the real physical system, but is used to study the issues of interest related to the problem we wish to solve. Models are widely used either as a prediction tool for real-case scenario (such as weather forecasts or air pollution assessment and control) or as an academic tool to validate

scientific theories or investigate physical processes that are too complex to be observed in a field experiment. In contrast to field measurements, in fact, these models represent a very controlled experiment, because the flow characteristics are prescribed through initial and boundary conditions and their results do not depend on local features like terrain characteristics or local meteorological conditions.

Generally, we can define two broad classes of models:

- a) physical models - a scaled-down representation of reality,
- b) mathematical models - a description of the system using mathematical relationships and equations.

a) Physical Models

Physical models are a scaled-down representation of the reality in a controlled laboratory environment. Two main experimental devices are used to simulate dispersion in a turbulent flow in either a pure convective or neutral situation, namely water-tanks and wind tunnels.

Water-tanks

Water-tanks are devices in which water is used to simulate the atmospheric turbulent motion of the CBL. Two kinds of water-tanks exist: convective water-tanks heated from below, and saline water-tanks in which the flow motion is driven by the different density of salted water.

Water-tanks have been extensively used in the past to study dispersion. In a series of seminal experiments in the 1970's and 1980's, Deardorff and Willis collected a thorough and extensive dataset of measurements that provided the basis for understanding the behavior of a plume in the CBL (Willis and Deardorff, 1976; Willis and Deardorff, 1978; Willis and Deardorff, 1981; Deardorff and Willis, 1982; Deardorff and Willis, 1984; Deardorff and Willis, 1985). In particular, by studying plumes emitted at different heights, the influence of the source height on the ground concentration was investigated. It was shown that a plume emitted from an elevated release is quickly transported downwards by the subsidence motion, due to the inhomogeneous structure of the turbulent motion in the CBL.

Recently Hibberd (2000) and Weil *et al.* (2002) improved the measurement technique, calculated higher-order plume statistics like concentration fluctuations, and extended the study of dispersion to buoyant plumes.

Wind tunnels

Wind tunnels are a small-scale reproduction of the ABL in which a trace gas is emitted in a wind field generated by a turbine. Wind tunnels are particularly suited to studying dispersion in nearly neutral conditions, although thermal stratified facilities also exist. Wind tunnels are also particularly used to study the distribution of pollutants on urban areas by modelling buildings and local topography (for a general review see Fedorovich, 2004).

In the seminal work by Fackrell and Robins (1982) concentration fluctuations of a dispersing plume in the neutral ABL were studied and it was found that they depend critically on the emitting source size. Builtjes and Talmon (1987) have since studied the effect of turbulent fluctuations on chemical

1.4. Different approaches to studying atmospheric dispersion

reactions by distinguish between large- and-small scale motions (called macro- and micro-mixing).

Results from both water-tanks experiments and wind tunnels have been extensively used in this doctoral research as a validation of the results.

b) Mathematical Models

Mathematical models solve the mathematical equations that describe the physics and chemistry governing the transport, mixing and transformations of pollutants in the atmosphere.

Dispersion models calculate the concentration of pollutant downwind of a source given detailed information on the source characteristics, the meteorological conditions, the topography of the area, etcetera.

The quality of the model prediction is largely dependent on the accuracy of the description of the physical and chemical processes that govern atmospheric dispersion. In particular, since pollutant transport is driven by the combination of the mean flow and the turbulent mixing, a correct description of these physical processes is essential for an accurate prediction of atmospheric dispersion.

Mathematical models are classified according to their complexity and the grade of accuracy by which they represent the physical reality. Broadly speaking, we can distinguish between steady-state (Gaussian) models and complex models.

Steady-state models (Gaussian models)

Steady-state Gaussian-plume models are currently the most commonly used dispersion models to estimate the impact of emission sources for air-quality regulatory purposes (Turner, 1994).

The term "Gaussian" comes from the well-known Gaussian (or normal) distribution, which is used to calculate the crosswind and vertical distribution of the pollutant at a certain distance downwind the emitting source. This bell-shaped distribution is described by the following formula (in one dimension):

$$c(z) = \frac{Q}{\sqrt{2\pi}\sigma U} \exp \left[-\frac{(z - z_0)^2}{2\sigma^2} \right] \quad (1.1)$$

where Q is the rate of emission, U is the main wind speed, z_0 is the vertical position of the plume center of mass, and σ is the standard deviation of the concentration. The Gaussian formula is an analytical solution of the equation for the diffusion of a pollutant (under some assumptions on the flow characteristics). An illustration of a plume as simulated by a (two-dimensional) Gaussian formulation is shown in Figure 1.6.

Gaussian models are based on several assumptions, the most relevant being (Ministry for the Environment New Zealand, 2004):

1) During the transport from the source to the receptor point, the mass of pollutant is assumed to remain constant, i.e. none of the material is removed through chemical reactions, gravitational fall, or turbulent impact (although chemical transformations can be taken into account by a separate module).

2) Gaussian models assume that the pollutant is transported in a straight line instantly. They do not account for turning or rising wind caused by the topography or inhomogeneity of the terrain.

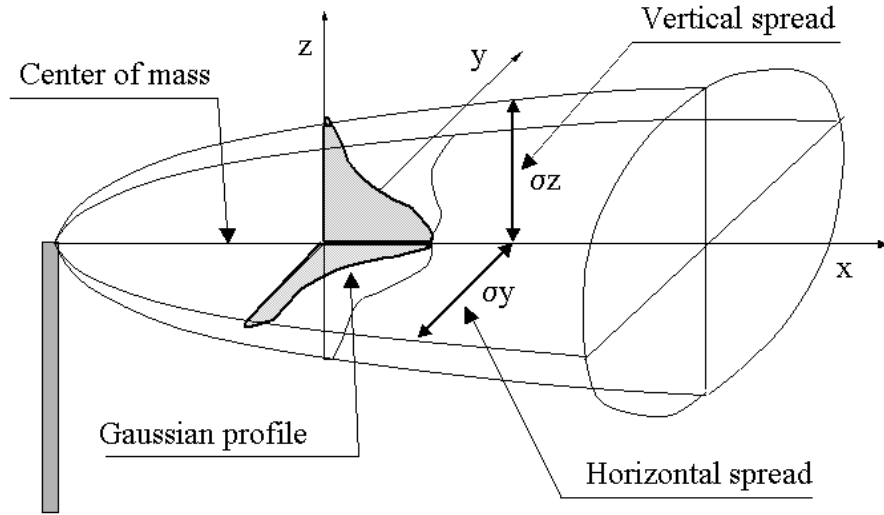


Figure 1.6: An illustration of a plume as simulated by a two-dimensional Gaussian dispersion model.

3) The meteorological conditions are assumed to persist unchanged over the time of transport from source to receptor (steady-state condition). In other words, Gaussian models assume that the atmosphere is uniform across the entire modelling domain, and that transport and dispersion conditions exist unchanged long enough for the material to reach the receptor.

4) Gaussian-plume models 'break down' during low wind speed or calm conditions due to the inverse wind speed dependence of the steady-state plume equation.

It is evident that these assumptions (particularly numbers 3 and 4) are significantly limiting if Gaussian models are to be used to simulate dispersion in convective situations. As explained earlier, in fact, in the CBL, the area occupied by the updraft is smaller than that occupied by the downdrafts. This results in an inhomogeneous and non-Gaussian distribution of the vertical velocity, which requires a more detailed description of the turbulent structure of the CBL. Moreover, due to the change in wind speed with height near the surface, it is not possible to select a single wind speed to be used in a Gaussian model for ground-level releases.

However, even with these limitations, this type of models can provide reasonable results when used appropriately, and their errors and uncertainties are generally well understood. Moreover, their use is relatively simple and computationally very inexpensive, and they can be run with very simple input data developed from standard meteorological recordings (*van Ulden and Holtslag, 1985*).

Complex dispersion models

Nowadays, models have been developed that are able to simulate the spatial and temporal variability of meteorological conditions (mean flow and turbulent mixing), which is one of the most critical factors in the prediction of atmospheric dispersion. In general, we can distinguish between two main classes of complex models: Eulerian (or grid-point) models and Lagrangian (or particle) models. Pollutant concentration in an Eulerian model is represented by the spatial distribution on a three-dimensional grid of points, whereas Lagrangian models simulate the trajectories of numerous particles driven by the flow.

The three-dimensional meteorological field necessary to calculate either pollutant concentration or particles' trajectories is usually calculated by solving a system of mathematical equations describing the dynamics of the most relevant atmospheric variables, such as wind, temperature and humidity. These models are usually referred to as prognostic models, because they provide a forecast (or a prognosis) of the meteorological conditions given the initial status of the system (available for instance from experimental measurements).

Another class of meteorological models includes the so-called diagnostic models, in which the three-dimensional meteorological field is retrieved by interpolating the available experimental measurements, without calculating its temporal evolution. Obviously, these models rely heavily on the availability of data.

Finally, the so-called Lagrangian stochastic models directly formulate the particle position and velocity in terms of stochastic differential equations that describe the turbulent motion of the ABL. In this doctoral research, the meteorological field is simulated by a Large-Eddy Simulation (LES) model, which is the best tool available at the current time to describe the turbulent motion in the CBL (for a detailed description of the LES see Chapter 2). The dispersion of tracers emitted in the simulated flow is calculated either by solving an equation for its concentration (the Eulerian approach, used in Chapters 3, 5, and 6), or by calculating the trajectories of fictitious particles (the Lagrangian approach adopted in Chapter 4). An example of a plume simulated by the LES is shown in Figure 1.7.

1.5 Outline of the thesis

In close connection with the research questions addressed in Section 1.3.2, the structure and contents of each Chapter of the thesis are briefly described below.

Chapter 2: Large-Eddy Simulation model: description, improvements and testing

Chapter 2 describes the way in which turbulent dispersion in the Atmospheric Boundary Layer can be studied by means of numerical simulation. The model used in this research is described, with the focus being on the modifications introduced into the code in order to compute the particles' trajectories.

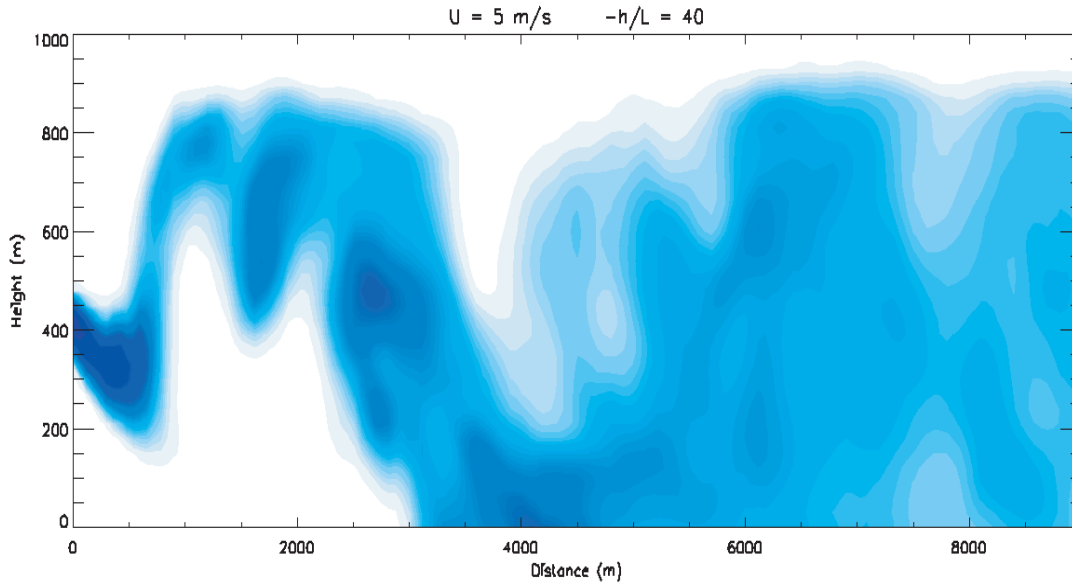


Figure 1.7: Example of a plume dispersing in the CBL as simulated by a LES.

Chapter 3: Relating Eulerian and Lagrangian Statistics for the Turbulent Dispersion in the Atmospheric Convective Boundary Layer

Atmospheric dispersion is studied by analyzing the behavior of a plume in two different frameworks, the Eulerian one and the Lagrangian one. In the Eulerian framework, statistical properties (such as mean concentration, variance etc.) are calculated at fixed positions. This approach is most commonly used in field measurements and in laboratory experiments. In the Lagrangian framework, the dispersion characteristics are calculated by tracking the trajectories of all the particles and computing their relative distances. This is the most natural approach for theoretical investigation of turbulent dispersion. In Chapter 3, we discuss turbulent dispersion in both the Eulerian and Lagrangian frameworks and we study the relationship between dispersion characteristics in the two frameworks. This relationship is important in relating the theoretical analysis to the experimental studies.

Chapter 4: Statistics of absolute and relative dispersion in the Atmospheric Convective Boundary Layer

In Chapter 4 turbulent dispersion is analyzed in absolute and in relative coordinate system, which is the reference system of the plume's center of mass. By so doing, we are able to separate the effect of the large-scale motion, which is inhomogeneous and non-Gaussian, from the small-scale motion, which is homogeneous and isotropic. By calculating the relative concentration and the position (more precisely the probability distribution function) of the plume center of mass, one is able to retrieve the statistics of the absolute concentration. The study of higher-order statistics such as the skewness of the position in absolute and relative coordinate systems, allows the structure and variability of the plume concentration (such as the symmetry of the concentration distribution along

1.5. Outline of the thesis

the plume centerline) to be investigated.

Chapter 5: Dispersion of a passive tracer in buoyancy- and shear-driven boundary layers

In Chapter 5, the effects of different combinations of thermal and mechanical forcing on plume dispersion are investigated. When the flow is forced by the combined effect of buoyancy and shear, the characteristics of the turbulent field are different from either the pure convective or pure shear flow. Although dispersion in either pure convective or neutral conditions has been widely investigated in the past, less is known on the behavior of a plume dispersing in a CBL driven by both buoyancy and shear. In this Chapter we show that wind shear reduces vertical dispersion and enhances the horizontal plume spread. A parameterization for the shear contribution to the horizontal and vertical dispersion is also proposed.

Chapter 6: The dispersion of chemically reactive species in the Atmospheric Boundary Layer

In this Chapter a review of different studies on the interaction between turbulent transport and chemical reactions is included. Model results and experimental studies of turbulent reacting flows in the atmospheric boundary layer are presented to show the modifications and control exerted by turbulence on the reactivity as a function of the ratio of the time scale of turbulence to the time scale of the chemical reaction (the Damköhler number). By studying the plume dispersion of a reactant the dependence of concentration fluctuations on the Damköhler number has also been analyzed.

Chapters 3 to 6 inclusive have been also published, or submitted for publication, as independent journal papers.

Chapter 2

Large-Eddy Simulation model: description, improvements and testing

This Chapter briefly describes the different numerical techniques currently used to simulate the Atmospheric Boundary Layer. The model used in this work is then thoroughly described, with focus being on the governing equations, the subgrid parameterization and the surface layer model. Finally, the main modifications added to the code used in this research are described.

2.1 Simulation of turbulent flow in the Atmospheric Boundary Layer

2.1.1 DNS, LES and RANS

As discussed in Chapter 1, the ABL is defined as the layer of air just above the Earth's surface. Within this layer, turbulent motion of air is generated by the combined effect of the friction against the surface and the cooling/heating of the ground. Although no unique definition of turbulence exists, *Lumley and Panofsky* (1964) pointed out the turbulence's most significant characteristics:

- 1) Turbulence is stochastic: turbulent processes are described by non-linear equations, which are highly sensitive to small differences in the initial conditions.
- 2) Turbulence is three dimensional and rotational.
- 3) Turbulence is dissipative: the turbulent energy is produced at large scales and is transported towards the smallest scales of motion (a process called energy cascade), where it is finally dissipated into heat.
- 4) Turbulence is characterized by large Reynolds number (i.e. large spatial dimension and small viscosity).

The turbulent motions for an incompressible flow in a rotating reference system, can be described by a system of non-linear equations for the conservation of mass and momentum: the continuity equation and the Navier-Stokes equations, respectively.

The discretized version of these equations can, in principle, be solved numerically by computing each equation on a defined number of points, the so-called numerical grid. As discussed by *Stevens and Lenschow* (2001), problems associated with the cloud-free ABL involve scales spanning at

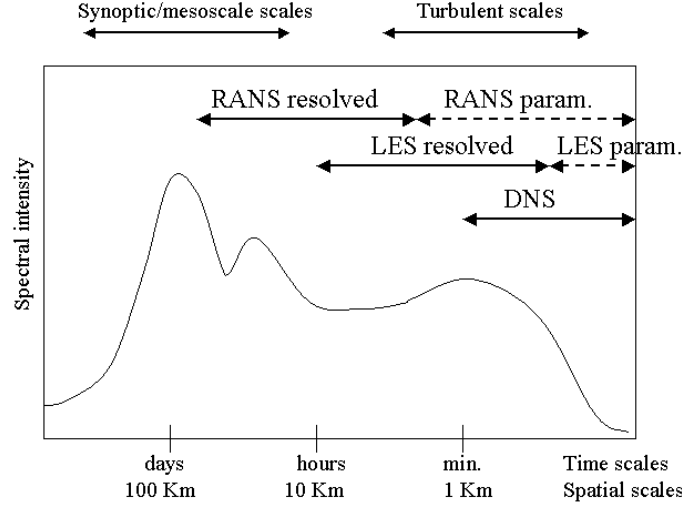


Figure 2.1: Schematic representation of the temporal/spatial scales resolved by the three numerical techniques (RANS, LES and DNS). The line represents a schematic example of energy spectrum of the wind velocity; peaks in the spectrum show which scale contributes most to the turbulent kinetic energy.

least 7 orders of magnitude; this implies that the system of equations describing the dynamics of the entire ABL on all the scales of motion, involves so many degrees of freedom that it is impossible to be solved for any computer nowadays.

Three different approaches for the numerical simulation of turbulent flows can be distinguished, depending on the spatial and time scales of the physical process being investigated: Direct Numerical Simulation (DNS), Large-Eddy Simulation (LES) and Reynolds-Averaged Navier-Stokes (RANS) models. A schematic representation of the different techniques in terms of the temporal and spatial scales solved by the models, is shown in Figure 2.1.

A DNS explicitly solves the Navier-Stokes equations. Therefore, in a DNS, all eddies down to the dissipation scale are simulated with accuracy but, as previously mentioned, due to the large span of temporal and spatial scales, only turbulent flows with a low Reynolds number (typically around 10^3) can be simulated.

For higher Reynolds numbers (or larger spatial and temporal scales), a direct numerical solution of the Navier-Stokes equations is not feasible; therefore both RANS and LES solve a system of equations in which only scales of motion within a lower limit (as given by the grid size) and a upper limit (given by the size of the computational domain) are explicitly solved, whereas the small scales motions are expressed as a function of the resolved variables.

RANS models are commonly used in the study of mesoscale phenomena, which have spatial scales of the order of tenths/hundreds *Km* and temporal scales of hours/days. In these models, the separation between resolved and parameterized scales is based on the presence of the so-called *spectral gap*, which divides the mesoscale/synoptic scales from the turbulence scale. This means that in a RANS there is no dynamical information about the turbulent scales, because all the degrees

2.1. Simulation of turbulent flow in the Atmospheric Boundary Layer

of freedom smaller than the size of the largest (energy-containing) turbulent eddies are averaged over. It must be noted that the evidence of the gap is still a matter of discussion (*Courtney and Troen*, 1990; *Galmarini and Thunis*, 1999; *Jonker et al.*, 1999), and a net separation of scales is well defined only for the vertical component of the wind.

The term Large Eddy Simulation (LES) was introduced by *Leonard* (1974). This technique is nowadays regarded as one of the most powerful computational tools available for the study of the ABL (*Stevens and Lenschow*, 2001).

By solving the governing equation with a LES, most of the energy (70 – 80%) of the turbulent motion is solved explicitly. The so-called “large eddies” are those motion elements that carry most of the kinetic energy, and are the largest contribution to the turbulent fluxes. These motions are simulated using a three-dimensional time-dependent numerical integration scheme, which resolves only the scales larger than the size of the numerical grid (Δ). In other words, a system of equations is solved in which eddies of size less than $O(\Delta)$ are removed (or *filtered*) from the dynamics. Thus, in LES, eddies significantly larger than Δ are solved explicitly, and their statistical and spectral properties can be calculated in great detail.

When the system of equations is filtered, the resulting equations for the large-scale component of the motion contain non-linear terms representing the effect of the small scales on the large ones; these so-called sub-grid scale (SGS) components are not solved explicitly, but are represented as a function of the resolved variables (see Section 2.3.3).

Although the LES has been showed to be the most advanced tool for the study of the ABL, it has three principal weaknesses:

- 1) It is numerically expensive: a typical domain covers an area of 5 Km in each horizontal direction and 2 Km in the vertical one. In order to solve accurately the flow in the domain, a grid with typically 10^6 points is required.
- 2) Most of the LES are applied only to idealized, horizontally homogeneous and flat domains. In contrast to field measurements, the numerical simulation represents a very controlled experiment, because the flow characteristics are prescribed through initial and boundary conditions. On the other hand, the comparison with the observational data, which can be affected by the inhomogeneity of the ground or large-scale forcing, can be problematic.
- 3) Since the Navier-Stokes equations are solved numerically on a discrete grid, numerical and truncation errors are introduced. Moreover, near the ground, where strong mean gradients are present and the eddies are smaller than the numerical grid, the flow field is strongly affected by the SGS model. However, *Nieuwstadt et al.* (1991) showed that even with a relatively coarse grid, when the SGS Reynolds stress is a relatively small part of the total turbulence produced Reynolds stress (like in the CBL), the results produced by LES are not dependent on the quality of the model. In other words the statistics of the large-scales motions explicitly solved are not sensitive to errors in the SGS effects (*Stevens and Lenschow*, 2001).

2.1.2 LES studies of turbulent dispersion in the Atmospheric Boundary Layer

LES studies of the ABL began in the 1970s with the seminal studies of *Deardorff* (*Deardorff*, 1970b; *Deardorff*, 1974). For the first time, the structure of the turbulent flow was analyzed in unprecedented detail. In particular, the structure of the inhomogeneous turbulent motions of the CBL,

characterized by large weak downdrafts surrounded by strong and narrow updrafts, was studied. New scaling quantities, the convective velocity (w_*) and the CBL height (z_i), were also introduced and successfully applied to scale observational data and numerical results. A high-resolution LES performed by *Schmidt and Schumann* (1989) showed that the strongest updrafts, which have the size of the CBL, can penetrate into the capping inversion and transport warm air from the free troposphere into the CBL. This phenomenon, known as entrainment, is an important process for the growth of the CBL.

The ability of the LES to reproduce fully the three-dimensional turbulent motion was applied successfully to investigate many different atmospheric processes, from turbulence production and decay to cloud formation. One of the most important applications of LES was the analysis of the behavior of a plume of contaminants dispersing in the CBL. A brief list of the seminal works investigating different aspects of turbulent dispersion is reported below.

The first numerical simulation of a plume dispersing in the CBL was performed by *Lamb* (1978), who showed that if the plume was released above the surface layer, it would be quickly caught by the downdrafts and transported to the surface, due to the non-Gaussian characteristics of the convective turbulent motion. As a result, the ground concentration would reach a maximum close to the release point. This result, later confirmed by the experimental work by *Willis and Deardorff* (1978), has been an important breakthrough in the study of air pollution, because it has shown the inability of steady-state models to correctly predict dispersion in the CBL. Lately, *Nieuwstadt and de Valk* (1987) extended the LES study of plume dispersion in the CBL to buoyant plumes.

Other LES studies of turbulent diffusion include the work by *Moeng and Wyngaard* (1984), who showed that the transport of scalar in the CBL is asymmetric: a tracer released at the top of the CBL (the so called top-down diffusion) is characterized by a different eddy diffusivity than a scalar released at the surface (bottom-up diffusion). Consequently, the bottom-up scalar can be transported by large thermals directly from the source to the top of the CBL, without diffusion into the middle of the CBL. As a result of this so called counter-gradient transport, the bottom-up diffusion is more effective than the top-down diffusion.

The study of turbulent dispersion was extended to chemically reactive species by investigating the influence of turbulence on chemical reactions. The first LES of an atmospheric boundary layer with reactive species was carried out by *Schumann* (1989). He focused mainly on the segregation of species caused by the coherent structures generated in the CBL, and showed that chemical transformation proceeds at a slower rate in the CBL because of insufficient mixing. A complete review of the studies of dispersion of chemically reactive species in the CBL can be found in Chapter 6.

The first LES study of the effect of wind shear on turbulent dispersion was carried out by *Mason* (1992). In fact, when the flow is forced by the combined effect of buoyancy and wind shear, the turbulent structure of the CBL is different than in either pure-convective or neutral conditions (*Sykes and Henn*, 1989; *Moeng and Sullivan*, 1994). A systematic study of the effect of different combinations of thermal and mechanical forcing on turbulent dispersion is presented in Chapter 5.

2.2 Brief history of the Dutch Atmospheric LES

The Large-Eddy Simulation code used in this research (Dutch Atmospheric LES) was first used to study the decay of turbulence in the CBL by *Nieuwstadt and Brost* (1986). Major improvements to the code were added by *Cuijpers and Duynkerke* (1993), who adapted the LES for the study of the specific characteristics of the atmospheric boundary layer. Their addition of a conservation equation for the total humidity, and the replacement of the potential temperature θ with the liquid-water potential temperature θ_l , allowed clouds formation and evolution to be investigated.

The Dutch Atmospheric LES was first compared to other codes in the work by *Nieuwstadt et al.* (1991). The results of a simulated dry CBL were compared and validated, and showed a very good agreement with experimental measurements. This study proved that the turbulence statistics (up to the third-order moments) calculated by the LES do not depend significantly on the SGS model or numerics. Other LES intercomparisons were performed later, in particular for studies of cloudy boundary layers. Later on, the code was used in the study of different atmospheric flows. A list of the main results and studies carried out with the Dutch LES is reported below.

1) Turbulent dispersion.

The dispersion of a plume in the CBL has been extensively studied by *Nieuwstadt and de Valk* (1987), *van Haren and Nieuwstadt* (1989) and *Nieuwstadt* (1992). In these works, a line source of passive tracer was emitted in the simulated CBL and the dispersion parameters were calculated and analyzed. The influence of large- and small-scale motions on dispersion was also analyzed by decomposing the total dispersion in the meandering and relative diffusion components. In *Meeder* (1998) and *Meeder and Nieuwstadt* (2000) turbulent dispersion of chemically reactive plumes in the neutral ABL was investigated. The effect of turbulent mixing on chemistry was studied by using a SGS model for the chemical reactions inside the numerical grid cell. The study showed that the SGS mixing played an important role close to the source.

2) Cloudy Boundary Layers.

The investigation of cloudy boundary layers (in particular strato- and shallow-cumulus) was carried out in many studies (*Cuijpers and Duynkerke*, 1993; *Cuijpers*, 1994; *Siebesma and Cuijpers*, 1995; *Siebesma and Holtslag*, 1996; *van Zanten*, 2000; *Neggers*, 2002; *Siebesma et al.*, 2003; *Neggers et al.*, 2003). In these works, the convective turbulent motion induced by the clouds, entrainment process, and cloud size statistics, were thoroughly discussed, in order to understand the main mechanisms of cloud formation and evolution, and to develop parameterizations to be used in large scale models like the operational weather forecast models.

The Dutch LES was compared to several other codes in studies related to stratocumulus (*Moeng et al.*, 1996; *Duynkerke et al.*, 1999; *Stevens and Co-authors*, 2004) or shallow cumulus (*Brown et al.*, 2002; *Stevens et al.*, 2001; *Siebesma et al.*, 2003). The effect of longwave radiative cooling at the top of a smoke cloud on turbulence has been reported in a LES intercomparison study by *Bretherton et al.* (1999).

In the study by *Siebesma and J.Jonker* (2000) it was shown that cloud geometric and morphological properties (fractal boundaries) were nicely simulated by the Dutch LES, when compared to observations (*Lovejoy*, 1982).

The combined effect of ultraviolet radiation and turbulent mixing on chemistry in a cloud-topped boundary layer, was investigated by *Vilà-Guerau de Arellano and Cuijpers* (2000). The study showed that the chemical sources and sinks in the cloud influence the vertical concentration profiles of the reactants.

3) Interaction between boundary layer and mesoscale.

From the study of the energy spectra *Jonker et al.* (1999) showed that the dominant contribution to the variance of potential temperature and turbulent velocities originates from a scale of the order of the boundary layer height. The energy spectra of passive scalars in the CBL behaves differently from that of velocity or temperature. Depending on the boundary conditions of the scalar (the surface flux and the entrainment flux), the spectrum is dominated by the largest scales of motion (tenths of kilometers, i.e. mesoscale). Mesoscale fluctuations were also investigated by *de Roode et al.* (2004), who used a LES to simulate a CBL in a very large domain ($25.6 \times 25.6 \text{ Km}^2$). Their results showed the need for a large domain size to allow the development of mesoscale fluctuations, especially in the study of stratocumulus clouds.

4) Turbulent reacting flows.

The influence of turbulent transport on chemical reactions in a point source release was investigated by *Meeder* (1998), who studied chemical reactions in point source releases. In the study by *Petersen et al.* (1999), an irreversible binary reaction involving the bottom-up and top-down diffusing scalars was investigated. Later, *Vinuesa and Vilà-Guerau de Arellano* (2003) studied the importance of the chemical terms for the fluxes and (co)-variances of reactants in a CBL by explicitly calculating these terms in the flux budget equation. In this study, it was shown that the vertical profile of the turbulent flux of the reactant species departed from the linear profile, which was characteristic for the flux of inert species emitted at the surface. Based on this result, *Vinuesa and Vilà-Guerau de Arellano* (2004) proposed a parameterization for the limitation of the chemical reactivity in the CBL.

In the study by *Jonker et al.* (2004), the spectra of the variance of the concentration of chemically reactive species in a CBL were studied. For a simple first-order reaction, it was found that the characteristic length scale (defined by the position of spectral peak) demonstrated a clear dependence on the reaction rate: an increase in the reaction rate lead to a significant decrease in the length scale of the species.

5) CBL with wind shear.

The role of the wind shear in the development, growth and maintenance of the CBL was studied by *Pino et al.* (2003), who showed that the CBL growth is affected by both surface-flux and entrainment-flux of heat and moisture. The analysis of the turbulent kinetic energy (TKE) budget showed the important contribution of wind shear at the surface and in the entrainment zone. As a consequence, the entrainment flux was enhanced, resulting in an increased growth of the boundary layer.

6) Stable Boundary Layer.

In the study by *Galmarini et al.* (1998) the LES results for the turbulent structure of a weakly

2.3. Description of the LES

stable ABL were compared to a one-dimensional model. The results were shown to be in good agreement with local-similarity theory and experimental data.

Recently (*Beare et al.*, 2005), a bench-mark case was selected to evaluate and compare the performances of 10 different LES models for the Stable Boundary Layer, as part of the GABLS (Global energy and water cycle experiment Atmospheric Boundary Layer Study) initiative. Although the results depended on the grid resolution and the subgrid models, they were generally in good agreement with local-similarity theory and experimental data, providing an improved understanding of the turbulent structure in the stable ABL.

The recent parallelization of the code allows a large number of grid points (up to 512x512x128) to be used, in order to either simulate a very large domain or to study the turbulent motion with a very fine resolution. The former is the approach used in Chapter 3, where a large domain is used to calculate energy spectra and integral time- and length-scales. A very fine grid (10x10x10 m) is used instead in Chapter 4 to analyze the effect of the internal mixing on concentration statistics for a dispersing plume.

2.3 Description of the LES

2.3.1 The governing equations

The system of equations governing the thermodynamics of the atmospheric flow in the ABL can be written in incompressible form (e.g. *Moeng*, 1998) as:

$$\frac{\partial u_i}{\partial x_i} = 0 \quad (2.1)$$

$$\frac{\partial u_i}{\partial t} = -u_j \frac{\partial u_i}{\partial x_j} + \frac{\theta_l}{\theta_0} \delta_{i3} g - 2\varepsilon_{ijk} \Omega_j u_k - \frac{1}{\rho} \frac{\partial p}{\partial x_i} + \nu \frac{\partial^2 u_i}{\partial x_j^2} \quad (2.2)$$

$$\frac{\partial \theta_l}{\partial t} = -u_j \frac{\partial \theta_l}{\partial x_j} + S_{\theta_l} \quad (2.3)$$

$$\frac{\partial q}{\partial t} = -u_j \frac{\partial q}{\partial x_j} + S_q \quad (2.4)$$

where the Boussinesq approximation has been applied.

Equation (2.1) (also known as continuity equation), expresses the mass conservation, equations (2.2) (known as Navier-Stokes equations, where $u_i = (u, v, w)$ is the wind speed), refer to the momentum conservation, and equations (2.3) and (2.4) are the conservation equations for the liquid water potential temperature θ_l and the total humidity q . Note that in all the simulations performed in this research, a dry CBL was simulated, therefore $\theta_l = \theta$. In (2.2) ρ is the density of the flow and p is the pressure, δ_{ij} is the Kronecker delta, ε_{ijk} is the alternating unit tensor, Ω_j the earth's

angular velocity in the j direction.

Finally, the terms S_{θ_l} and S_q in equations (2.3-2.4) represent the source and the sinks of the variable, like the (divergence of the) radiative flux for the potential temperature equation or the phase changes for water.

An equation for the conservation of a scalar c can be added to the system in the form

$$\frac{\partial c}{\partial t} = -u_j \frac{\partial c}{\partial x_j} + S_c, \quad (2.5)$$

where S_c is a source/sink term representing, for example, chemical reactions.

2.3.2 The filtered equations

An exact numerical solution (DNS) of the system (2.1-2.5) is possible only for low Reynolds numbers, because solving all the scales of motion in a three-dimensional grid would require a number of grid points that would be far beyond the capability of any computer currently available. In a LES, only the scales of motion larger than a filter size are explicitly resolved, whereas the smaller ones need to be parameterized.

The filtering procedure is summarized by the following expression:

$$\psi = \langle \psi \rangle + \psi'', \quad (2.6)$$

which describes how each variable ψ is decomposed into a resolved part $\langle \psi \rangle$ and a *subgrid* (or, more precisely, *subfiltered*) part ψ'' . Different types of filters can be applied. In our particular case, the numerical grid itself is used as a filter, so that the filter operator $\langle \rangle$ is coincident with the volume average over the grid cell.

The filter operator is usually supposed to possess the following properties:

$$\langle \langle \psi \rangle \rangle = \langle \psi \rangle \quad (2.7)$$

$$\langle \frac{\partial \psi}{\partial x_i} \rangle = \frac{\partial \langle \psi \rangle}{\partial x_i} \quad (2.8)$$

It must be noticed that not all the forms of the filter fulfill conditions (2.7)-(2.8). However, *Ghosal and Moin* (1995) showed that the error associated with the non fulfillment of condition (2.8) is of the same order as the discretization error.

By applying the filter decomposition (2.6) to the equations (2.1)-(2.5), the system of governing equations becomes:

$$\frac{\partial \langle u_i \rangle}{\partial x_i} = 0 \quad (2.9)$$

$$\frac{\partial \langle u_i \rangle}{\partial t} = -\frac{\partial \langle u_j \rangle \langle u_i \rangle}{\partial x_j} + \frac{\langle \theta_l \rangle}{\theta_0} \delta_{i3} g - 2\varepsilon_{ijk} \Omega_j \langle u_k \rangle - \frac{\partial \langle \pi \rangle}{\partial x_i} - \frac{\partial \tau_{ij}}{\partial x_j} \quad (2.10)$$

2.3. Description of the LES

$$\frac{\partial \langle \theta_l \rangle}{\partial t} = -\frac{\partial \langle u_j \rangle \langle \theta_l \rangle}{\partial x_j} - \frac{\partial \langle u_j'' \theta_l'' \rangle}{\partial x_j} + \langle S_{\theta_l} \rangle \quad (2.11)$$

$$\frac{\partial \langle q \rangle}{\partial t} = -\frac{\partial \langle u_j \rangle \langle q \rangle}{\partial x_j} - \frac{\partial \langle u_j'' q'' \rangle}{\partial x_j} + \langle S_q \rangle \quad (2.12)$$

$$\frac{\partial \langle c \rangle}{\partial t} = -\frac{\partial \langle u_j \rangle \langle c \rangle}{\partial x_j} - \frac{\partial \langle u_j'' c'' \rangle}{\partial x_j} + \langle S_c \rangle, \quad (2.13)$$

where θ_0 is the reference state potential temperature and the viscous dissipation term $\nu \frac{\partial^2 u_i}{\partial x_j^2}$ in the Navier-Stokes equation is neglected after scale analysis (e.g. *Stull*, 1988).

The new system of equations (2.9)-(2.13) appears similar to the original one (2.1)-(2.5), but new terms of the form $\frac{\partial \langle u_j'' \psi'' \rangle}{\partial x_j}$ appear due to the filtering process. These terms are referred to as *subgrid fluxes* and they are new unknown variables in the system. As a consequence, they need to be expressed as a function of known (resolved) quantities.

The term τ_{ij} is the *subgrid stress tensor* defined as:

$$\tau_{ij} \equiv \langle u_i u_j \rangle - \langle u_i \rangle \langle u_j \rangle - 2/3 \delta_{ij} \langle e \rangle, \quad (2.14)$$

where $\langle e \rangle = 1/2(\langle u_i u_i \rangle - \langle u_i \rangle \langle u_i \rangle)$ is the subgrid Turbulent Kinetic Energy (TKE). This form of the subgrid stress tensor is chosen in order to distinguish between isotropic and anisotropic parts (*Deardorff*, 1974). The $2/3 \langle e \rangle$ term is then added back into the pressure term $\langle \pi \rangle$, which now reads:

$$\langle \pi \rangle = \frac{\langle p \rangle}{\rho_0} + 2/3 \langle e \rangle. \quad (2.15)$$

The pressure term $\langle p \rangle$ is determined by solving a Poisson equation (see Appendix B).

2.3.3 Sub-grid Scale model

A common way to calculate the SGS terms is by means of the so-called K-diffusion method, in which the subgrid stress tensor and the subgrid fluxes are expressed as the product of an eddy viscosity K (or eddy diffusivity) and the local gradient of the resolved variable:

$$\begin{cases} \tau_{ij} = -K_m \left(\frac{\partial \langle u_j \rangle}{\partial x_i} + \frac{\partial \langle u_i \rangle}{\partial x_j} \right) \\ \langle u_i'' \psi'' \rangle = -K_\psi \left(\frac{\partial \langle \psi \rangle}{\partial x_i} \right), \end{cases} \quad (2.16)$$

where ψ represents a generic scalar variable like temperature, moisture or chemical reactant. For these quantities, the same eddy diffusivity is used.

The eddy diffusivity coefficient K can be written as function of the subgrid turbulent kinetic energy $\langle e \rangle = 1/2 \langle u_i'' u_i'' \rangle$, and a length-scale λ .

An additional prognostic equation for $\langle e \rangle$ has then to be added to the system of equations:

$$\begin{aligned} & \frac{\partial \sqrt{\langle e \rangle}}{\partial t} + \langle u_j \rangle \frac{\partial \sqrt{\langle e \rangle}}{\partial x_j} = \\ & = \frac{1}{2\sqrt{\langle e \rangle}} \left[-K_\psi \frac{g}{\theta_0} \frac{\partial \langle \theta_l \rangle}{\partial z} + K_m \left(\frac{\partial \langle u_j \rangle}{\partial x_i} + \frac{\partial \langle u_i \rangle}{\partial x_j} \right) \frac{\partial \langle u_i \rangle}{\partial x_j} \right] + \\ & + \frac{\partial}{\partial u_j} \left(2K_m \frac{\partial \sqrt{\langle e \rangle}}{\partial x_i} \right) - \frac{c_\epsilon \langle e \rangle}{2\lambda}, \end{aligned} \quad (2.17)$$

where the form of the dissipation term is found by integrating the three dimensional energy spectrum $E(k) = \alpha \epsilon^{2/3} k^{-5/3}$, from a filter wavenumber k_f to infinity (van Zanten, 2000). The value of the Kolmogorov constant α is 1.5, k is the wavenumber and ϵ is the viscous dissipation.

The filter wavenumber is defined as

$$k_f = \frac{2\pi}{c_f \lambda}, \quad (2.18)$$

where $c_f = 2.5$ (Cuijpers, 1990) and the length scale λ is related to the grid size Δ defined as

$$\Delta = \frac{1}{1/\Delta x + 1/z(k)}, \quad (2.19)$$

where Δx is the grid size in the horizontal direction ($\Delta x = \Delta y$) and $z(k)$ is the height of the k -th level.

Finally, the dissipation constant is defined as

$$c_\epsilon = \frac{2\pi}{c_f} \left(\frac{3}{2} \alpha \right)^{-3/2} = 0.7. \quad (2.20)$$

From Equation (2.17), an expression for the eddy diffusivity coefficient is found by assuming that the production (shear) term balances the dissipation (Deardorff, 1974), in the case of isotropic turbulence. This leads to

$$K_m = c_m \lambda \sqrt{\langle e \rangle}, \quad (2.21)$$

where the constant c_m is expressed as

$$c_m = \frac{c_f}{2\pi} \left(\frac{3}{2} \alpha \right)^{-3/2} = 0.12. \quad (2.22)$$

Similarly, the exchange coefficient for the scalar variables K_ψ is derived by calculating the dissipation rate of the potential temperature variance in the inertial subrange in the case of isotropic turbulence, which leads to

$$K_\psi = c_h \lambda \sqrt{\langle e \rangle}, \quad (2.23)$$

2.3. Description of the LES

with

$$c_h = \frac{c_f}{2\pi} \left(\frac{3}{4}\beta \right)^{-1} \left(\frac{3}{2}\alpha \right)^{-\frac{1}{2}} = 3c_m. \quad (2.24)$$

Recently, the length-scale λ used in equations (2.21) and (2.23) was adjusted to take into account the stable stratification at the top of the CBL (entrainment zone), where λ becomes very small (see *van Zanten, 2000* for details).

2.3.4 Surface model

In order to calculate the subgrid fluxes (equation 2.16), the vertical gradients of the variables have to be determined. In the mixed layer, the profiles of the variables are assumed to be linear, so that they can be simply approximated by finite differences, for instance $\frac{\partial \langle u \rangle}{\partial z} = \frac{\Delta \langle u \rangle}{\Delta z}$. In the surface layer, in which the profiles are characterized by large gradients, the finite differences approximation may lead to large errors, especially if the numerical grid is coarse. Moreover, the flow near the ground must satisfy the boundary conditions given by the surface fluxes $\langle w''\psi'' \rangle > 0$.

In the surface layer, the Monin-Obukhov similarity theory is then used. This assumes that the gradient of the variable is scaled by the dimensionless height

$$\zeta \equiv z/L, \quad (2.25)$$

where $L = \frac{-\theta_0 u_*^3}{g w' \theta'}$ is the Monin-Obukhov length. The dimensional stability functions are defined as:

$$\Phi_m(\zeta) = \frac{kz}{u_*} \frac{\partial V}{\partial z} \quad (2.26)$$

$$\Phi_h = \frac{kz}{\psi_*} \frac{\partial \langle \psi \rangle}{\partial z}. \quad (2.27)$$

In equations (2.26)-(2.27) $V = \sqrt{\langle u \rangle^2 + \langle v \rangle^2}$ is the horizontal wind speed, and ψ is a scalar quantity like the potential temperature (θ), total humidity (q) or a chemical specie. The friction velocity u_* and ψ_* are defined as:

$$u_*^2 = \sqrt{\langle u''w'' \rangle^2 + \langle v''w'' \rangle^2} \quad (2.28)$$

$$\psi_* = -\frac{\langle w''\psi'' \rangle}{u_*}. \quad (2.29)$$

Integrating equation (2.26) between z_0 (height at which $V(z_0) = 0$) and a generic height z , leads to

$$V(z) = \frac{u_*}{k} \left\{ \ln \frac{z}{z_0} - \Psi_m\left(\frac{z}{L}\right) \right\}, \quad (2.30)$$

where

$$\Psi_m\left(\frac{z}{L}\right) = \int_0^{z/L} \frac{1 - \Phi_m(\zeta)}{\zeta} d\zeta \quad (2.31)$$

represents the correction to the logarithmic profile due to non-neutral conditions ($\Psi_m = 0$ in neutral conditions).

Similarly from Equation (2.27):

$$\langle \psi(z) \rangle = \langle \psi(z_0) \rangle + \frac{\Psi_*}{k} \left\{ \ln \frac{z}{z_0} - \Psi_h\left(\frac{z}{L}\right) + \Psi_h\left(\frac{z_0}{L}\right) \right\}. \quad (2.32)$$

In the LES, the stability functions are parameterized using the following relationships (*Businger et al.*, 1971; *Dyer*, 1974; *Hogstrom*, 1988):

$$\begin{aligned} \Phi_m &= \begin{cases} (1 - 16\zeta)^{-1/4} & \text{if } \zeta < 0 \\ 1 + 5\zeta & \text{if } \zeta > 0 \end{cases} \\ \Phi_h &= \begin{cases} (1 - 16\zeta)^{-1/2} & \text{if } \zeta < 0 \\ 1 + 5\zeta & \text{if } \zeta > 0 \end{cases} \\ \Psi_m\left(\frac{z}{L}\right) &= \begin{cases} 2 \ln \left(\frac{1 + \Phi_m^{-1}}{2} \right) + \ln \left(\frac{1 + \Phi_m^{-2}}{2} \right) - 2 \tan^{-1}(\Phi_m^{-1}) + \frac{\pi}{2} & \text{if } \zeta < 0 \\ -5\zeta & \text{if } \zeta > 0 \end{cases} \\ \Psi_h\left(\frac{z}{L}\right) &= \begin{cases} 2 \ln \left(\frac{1 + \Phi_h^{-1}}{2} \right) & \text{if } \zeta < 0 \\ -5\zeta & \text{if } \zeta > 0 \end{cases} \end{aligned}$$

The friction velocity is calculated from equation (2.30):

$$u_* = kV \left(\ln \frac{z}{z_0} - \Psi_m\left(\frac{z}{L}\right) \right), \quad (2.33)$$

whereas Ψ_* is calculated from the prescribed values of the surface fluxes (bottom boundary condition):

$$\Psi_* = - \frac{\langle w''\psi'' \rangle_0}{u_*}. \quad (2.34)$$

Surface values of the variables are calculated according to equations (2.30)-(2.32) using the value of the variable at the first computational level ($z = 1$).

Finally, the vertical gradients are calculated from equations (2.26) and (2.27).

In the limit of free convection ($u_* = 0$) the following relationships are used to calculate the temperature and moisture profiles (*Garratt*, 1992):

$$\frac{\partial \langle \psi \rangle}{\partial z} = -0.7 \langle w''\psi'' \rangle_0^{2/3} \left(\frac{g}{c_0} \right) z^{-4/3}. \quad (2.35)$$

2.4 Improvements to the code

For this research, two main improvements to the LES were implemented. The first was the modification of some of the routines in the parallel version of the code, in order to use a non-equidistant numerical grid. The second consisted in the introduction of a Lagrangian particle module to calculate the trajectories of the particles released in the turbulent flow. These modifications are discussed in detail in the following Sections.

2.4.1 Non-equidistant grid

As discussed in Section 2.1, the LES only solves scales of motion larger than the numerical grid. Many studies (e.g. *Nieuwstadt et al.*, 1991) showed that the statistical results (mean profiles of variables, second and third-order moments), do not depend on the resolution of the numerical grid for a well-mixed boundary layer. However, in regions where strong gradients are present, like near the surface or in the entrainment zone, it is important to solve these gradients in the most accurate way. Moreover, as pointed out by *Schmidt and Schumann* (1989), in the analysis of the energy spectra, good agreement between theoretical analysis and numerical results is found only if the numerical grid is fine enough to truly resolve at least a significant portion of the large-scale end of the inertia range.

This means that the numerical grid must be fine enough to resolve the most relevant scales of motion, and, at the same time, the numerical domain should be large enough to take into account the largest scale of motion.

A compromise between these two limiting situations can be found if a non-equidistant grid is used, with finer resolution in the regions where the eddies have a smaller length scale and the gradients are sharper, typically near the surface and in the entrainment zone. On the other hand, in regions like the middle of the CBL (where the characteristic eddy size is larger than the grid) and in the free troposphere (which is usually a zone of little interest) a coarse grid is sufficient to solve the most relevant scales of motion with sufficient detail.

A test to compare the performances of the model in the Surface Layer using a equidistant and a non-equidistant grid was performed. The results are shown and discussed in the following Section. The modifications introduced in the Poisson solver and in the advection numerical scheme are described in Appendixes A and B.

Equidistant grid versus non-equidistant grid: sensitivity test

In order to find the best compromise between numerical accuracy and time/CPU consumption, two simulations were performed: the first one (case EQUI) used a vertical grid of 128 points with a very fine constant resolution of 10 m; the second one (case NON-EQUI) used a non-equidistant, stretched grid whose first layer was 5 m deep and the successive ones, within the surface layer, increased exponentially. Above the surface layer, a constant grid of 15 m was used. A schematic plot of the numerical grids is shown in Figure 2.2.

The advantage of using a non-equidistant grid was twofold: it allowed us to use a finer grid in the regions where the gradients are sharper, and, additionally, a vertical grid of 96 points was used instead of 128 points (case EQUI)). This resulted in the equations being solved on a numerical grid

Case	EQUI	NON-EQUI
Horizontal domain size (m)	10240	10240
$N_x=N_y$	256	256
$\Delta x=\Delta y$ (m)	40	40
Vertical domain size (m)	1275	1400
N_z	128	96
$\Delta z(1)$	10	5
$\Delta z(z > 100 \text{ m})$	10	15
$\overline{w'\theta'}_0$ (K m/s)	0.1	0.1
u_g (m/s)	2	2

Table 2.1: Initialization parameters and boundary conditions used in the simulations.

that was 25% smaller, with obvious advantages in computational time. Details of the initialization parameters used in the simulations can be found in Table 2.1.

The numerical simulations were run for three hours, and the results were time and spatially (horizontally) averaged over the third hour.

Mean profiles of the variables (wind, temperature and scalar), and the relative vertical fluxes were compared. Moreover, second-order moments and the skewness of the vertical velocity were analyzed as well. No significant difference between the two simulations were found above the surface layer, because in the region where the length scale of the turbulent eddies is larger than the numerical grid, the results should not depend on the vertical resolution.

Attention was therefore turned to the performance of the model in the surface layer, where the use of a non-equidistant grid may have a larger influence on the results. In order to compare the two simulations, the profiles of the stability functions Φ_m and Φ_h were analyzed as a function of the dimensionless height z/L . In particular, the values of Φ_m and Φ_h were calculated by using equations (2.26) and (2.27), where the mean profiles calculated by the model were first interpolated using a second order logarithmic function, and the vertical gradients were subsequently calculated analytically.

Figures 2.3a) and 2.3c) show the stability functions for the momentum (Φ_m) and potential temperature (Φ_h) as a function of the dimensionless height z/L , calculated for the two simulations. In the Figure, the empirical functions for unstable conditions (*Businger et al.*, 1971; *Dyer*, 1974; *Hogstrom*, 1988), are also shown:

$$\Phi_m = (1 - 16\zeta)^{-1/4} \quad (2.36)$$

$$\Phi_h = (1 - 16\zeta)^{-1/2}. \quad (2.37)$$

Clearly, the use of the non-equidistant grid gives a profile of Φ_m more similar to the theoretical value than the equidistant grid, which, in the surface layer, has a coarser resolution. The difference in the value of Φ_m affects the profile of mean wind, as shown in Figure 2.3b). The value of the wind speed at the first numerical grid cell reads 1.26 m/s for the non-equidistant grid (at 2.5 m, that

2.4. Improvements to the code

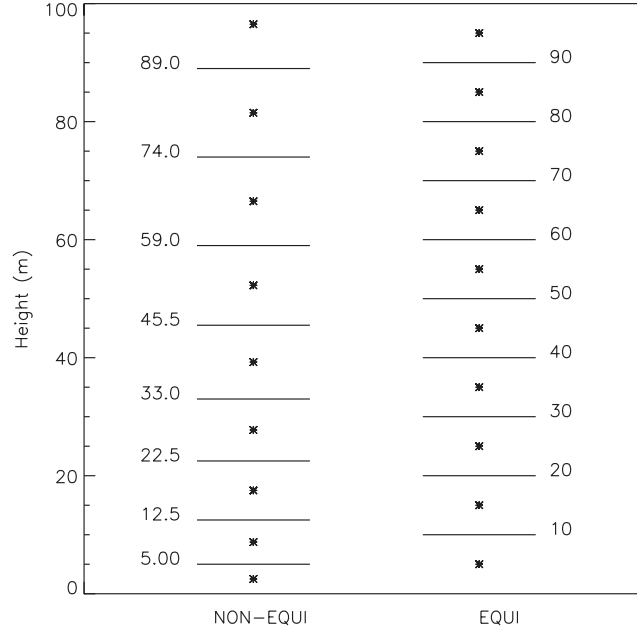


Figure 2.2: Schematic representation of the non-equidistant (left) and equidistant (right) grids. The lines represent the cell's edges, and the stars the cell's centers.

is half of the first numerical grid cell height) and 1.44 m/s for the equidistant grid (at 5 m). Since the wind at the surface ($z = z_0 = 0.15 \text{ m}$) is constrained to 0, the finer numerical grid reproduces the theoretical logarithmic wind profile more satisfactorily.

The profiles for the stability functions for the potential temperature (Figure 2.3c) do not show the same differences as for the wind, although a little improvement is found for $z/L < 2$ using the non-equidistant grid. However, the mean profiles calculated using the different grids are in very good agreement (Figure 2.3d). This is explained by the fact that the value of the temperature at the surface ($z = z_0$) is calculated by equation (2.32) rather than being constrained to a fixed value as for the wind. In this case, therefore, the resolution of the numerical grid does not have such a big impact as for the wind profile.

2.4.2 Lagrangian Particle Module

As discussed in Chapter 1, the dispersion process can be equivalently studied in two different frameworks: the Eulerian and the Lagrangian.

In the Eulerian framework, statistical properties are calculated in a fixed reference frame. This approach is most commonly used in field experiments, as well as in laboratory experiments or Eulerian numerical models.

In the Lagrangian framework, the statistical properties are calculated in a reference frame which moves with the flow. This is the most natural approach for theoretical investigation of turbulent dispersion (*Taylor, 1921; Batchelor, 1949*). In the Lagrangian framework, a plume dispersing in the atmosphere is regarded as an ensemble of particles that move in the turbulent flow. Instead of calculating the scalar concentration by means of equation (2.13), a large number of particles are

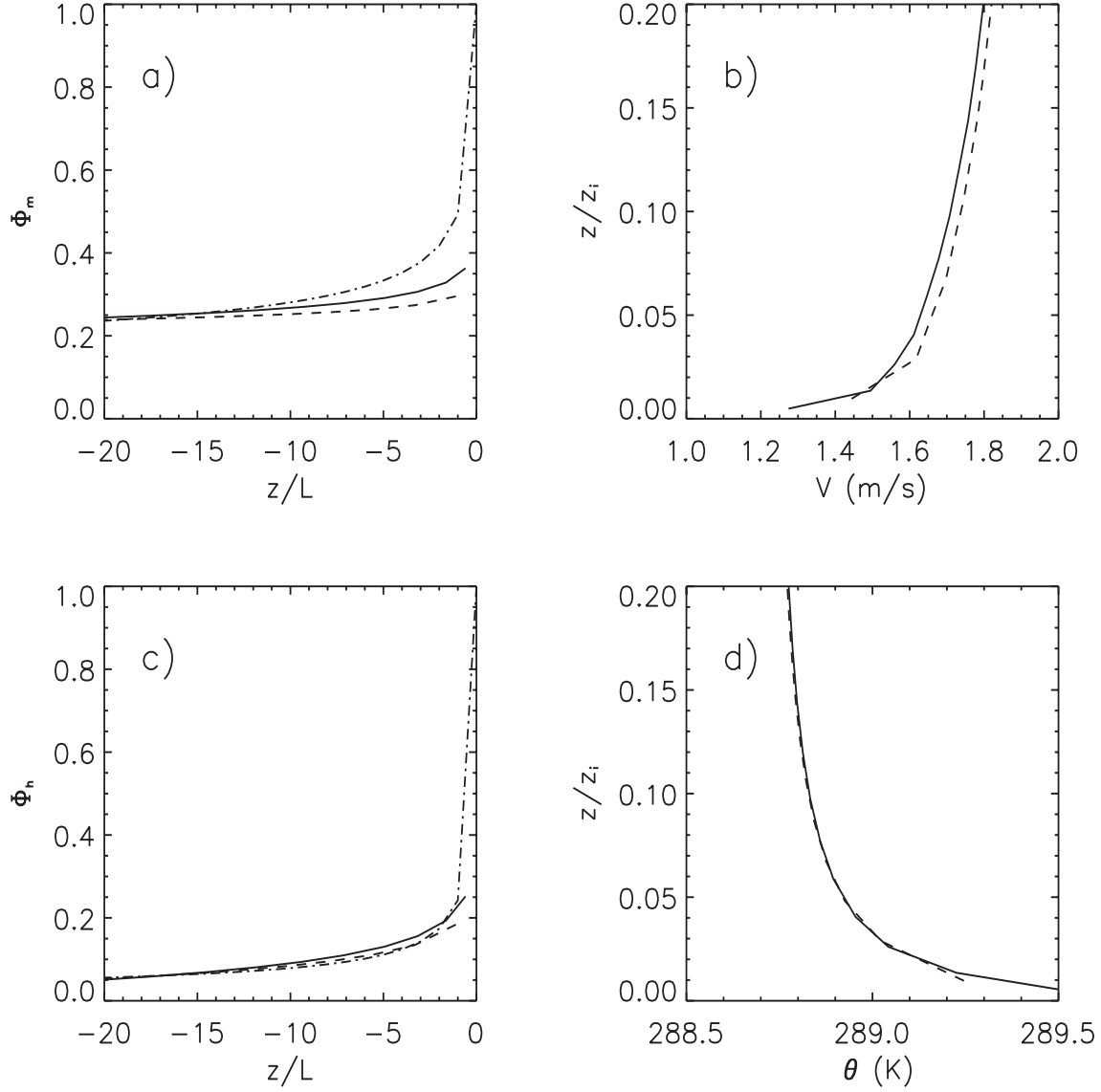


Figure 2.3: a) Comparison of the stability function Φ_m in the surface layer calculated with an equidistant (dashed line) and non-equidistant (continuous line) vertical grid. The dashed-dotted line represents the parameterized formulas by *Dyer* (1974). b) Comparison of the vertical profile of the mean horizontal wind V calculated with an equidistant (dashed line) and non-equidistant (continuous line) vertical grid. c) Same as a), but for the stability function Φ_h . d) Same as b), but for the potential temperature θ .

2.4. Improvements to the code

released in the simulated flow, and their trajectories are tracked. The concentration at any point is derived then by simply counting the number of particles in a given volume.

In addition, by investigating the dispersion in the Lagrangian framework, one is able to study and derive quantities like the Lagrangian time-scale, which is a critical parameter for both theoretical and practical applications (see Chapter 3).

The LES provides at each time t the three-dimensional velocity field $u_j(t)$, ($j = x, y, z$). The position in the direction j of the i^{th} particle at time $t + \Delta t$ is then calculated according to

$$x_j^i(t + \Delta t) = x_j^i(t) + u_j^i(t)\Delta t, \quad (2.38)$$

where Δt is the time step, and $u_j^i(t)$ is the velocity in the position of the particle, calculated by linearly interpolating the values of the resolved (Eulerian) velocity at the eight closest grid points. As pointed out by *Weil et al.* (2004), a more realistic calculation of the particles' positions should include in (2.38) the subgrid component of the velocity $u_j^{i'}$, which is not directly available from the LES. The value of $u_j^{i'}$ could be computed by solving the Langevin equation using a Markov chain process, as suggested by *Gopalakrishnan and Avissar* (2000), or by a simple random walk scheme (*Uliasz and Sorbjan*, 1999). A different approach was used by *Mason* (1992), who added a random vertical displacement to the motion of the particles close to the surface. Finally, *Weil et al.* (2004) used an adaptation of *Thomson's* (1987) Lagrangian Stochastic Model in which $u_j^{i'}$ was specified by a Gaussian PDF based on the subgrid stress tensor.

The subgrid velocity is particularly relevant in regions characterized by strong gradients, for example near the surface, and may lead to errors in the calculation of ground concentration (*Weil et al.*, 2004). In our study, particles were released between $z/z_i = 0.12$ and $z/z_i = 0.9$, where the flow was characterized by constant profiles of wind and potential temperature.

Quantities such as the Lagrangian time scale are only dependent on the velocity contributions of the largest scales of motion (*Degrazia et al.*, 1998), which are explicitly solved by the LES. This is corroborated by previous studies by *Wang et al.* (1995) and by *Gopalakrishnan and Avissar* (2000), who found no significant difference in the results if the velocity subgrid component was taken into account. The subgrid velocity $u_j^{i'}$ was therefore not included in our calculations.

A similar argument was used with respect to the choice of the interpolation method used to calculate the Lagrangian velocities $u_j^i(t)$ from the Eulerian (resolved) ones (Equation 2.38). Although linear interpolation is used by many authors (*Uliasz and Sorbjan*, 1999; *Mason*, 1992), it can be considered inadequate in some cases, because it may introduce numerical noise when a particle crosses the grid-line boundaries (*Yeung*, 2002). Nevertheless, the error (imprecision) associated with this process is only relevant at the smallest scales (i.e. scales equal or smaller than the numerical grid). Since the Lagrangian statistics (both autocorrelations and integral scales) are associated with the largest scale of motion, which are explicitly solved by the LES, we are confident that for the atmospheric flow the results are rather independent of the interpolation scheme used.

2.5 APPENDIX A: The Kappa scheme

As mentioned in Section 2.4 some routines in the parallel version of the LES needed to be modified to use a non-equidistant grid. The modification to the advection numerical scheme is now discussed.

Referring to Figure 2.4 the one-dimensional advection term can be discretized (in the center of the k -th cell) as follows:

$$\frac{\partial wc}{\partial z}|_k = \frac{f_{k+1/2} - f_{k-1/2}}{\Delta z}, \quad (2.39)$$

where c is a generic scalar variable (temperature, moisture, passive scalar). The variables $f_{k+1/2}$ and $f_{k-1/2}$ refer to the fluxes at the edge of the numerical cell. Since a staggered numerical grid is used by the model, the velocity are calculated at the edges of the cell, whereas the scalar variables are calculated in the centers (see Figure 2.4). Therefore, we can write:

$$\frac{\partial wc}{\partial z}|_k = \frac{f_{k+1/2} - f_{k-1/2}}{\Delta z} = \frac{w_{k+1}c_{k+1/2} - w_k c_{k-1/2}}{\Delta z}. \quad (2.40)$$

The problem raises now how to compute the value of $c_{k+1/2}$ and $c_{k-1/2}$ with sufficient accuracy. Following *Hirsch* (1990) we can use a Taylor expansion formula to write:

$$c_{k-1/2} = c_{k-1} + \left(\frac{\Delta z_f(k)}{2} \right) \frac{\partial c}{\partial z}|_{k-1} + K \left(\frac{\Delta z_f(k)}{2} \right)^2 \frac{\partial^2 c}{\partial z^2}|_{k-1}, \quad (2.41)$$

where K is a parameter depending on the accuracy (see below). The first- and second-order derivatives can be calculated according to (see Figure 2.4):

$$\frac{\partial c}{\partial z}|_{k-1} = \frac{c_k - c_{k-1}}{\Delta z_h(k) + \Delta z_h(k-1)} \quad (2.42)$$

$$\frac{\partial^2 c}{\partial z^2}|_{k-1} = \frac{1}{\Delta z_f(k-1)} \left(\frac{c_k - c_{k-1}}{\Delta z_h(k)} - \frac{c_{k-1} - c_{k-2}}{\Delta z_h(k-1)} \right). \quad (2.43)$$

By substituting equations (2.42) and (2.43) in (2.41) and after some manipulations, we obtain:

$$c_{k-1/2} = c_{k-1} + \frac{\Delta z_f(k-1)}{\Delta z_h(k) + \Delta z_h(k-1)} \cdot \left[(c_k - c_{k-1}) \frac{1 + K \frac{\Delta z_h(k) + \Delta z_h(k-1)}{2\Delta z_h(k)}}{2} + (c_{k-1} - c_{k-2}) \frac{1 - K \frac{\Delta z_h(k) + \Delta z_h(k-1)}{2\Delta z_h(k-1)}}{2} \right], \quad (2.44)$$

which can be rewritten as

$$c_{k-1/2} = c_{k-1} + \frac{\Delta z_f(k-1)}{\Delta z_h(k) + \Delta z_h(k-1)} \Phi(c_{k-1} - c_{k-2}), \quad (2.45)$$

2.5. APPENDIX A: The Kappa scheme

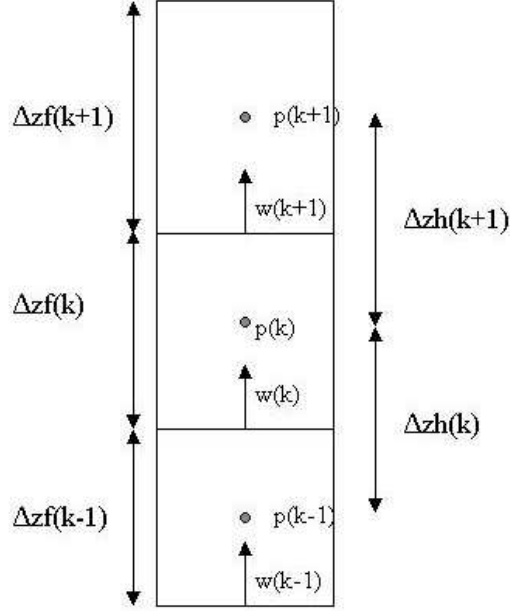


Figure 2.4: Scheme of the non-equidistant grid (in the vertical direction) used by the model.

where

$$\Phi = \frac{1 - K \frac{\Delta z_h(k) + \Delta z_h(k-1)}{2\Delta z_h(k-1)}}{2} + \frac{1 + K \frac{\Delta z_h(k) + \Delta z_h(k-1)}{2\Delta z_h(k)}}{2} \left(\frac{c_k - c_{k-1}}{c_{k-1} - c_{k-2}} \right) \quad (2.46)$$

is the *flux limiter function*. In case of equidistant grid ($\Delta z_f = \Delta z_h$) equations (2.44) and (2.46) become simply

$$\begin{aligned} c_{k-1/2} &= c_{k-1} + \frac{1+K}{4}(c_k - c_{k-1}) + \frac{1-K}{4}(c_{k-1} - c_{k-2}) = \\ &= c_{k-1} + \frac{1}{2}\Phi(c_{k-1} - c_{k-2}) \end{aligned} \quad (2.47)$$

$$\Phi = \frac{1-K}{2} + \frac{1+K}{2} \left(\frac{c_k - c_{k-1}}{c_{k-1} - c_{k-2}} \right). \quad (2.48)$$

Similar expressions can be found for $c_{k+1/2}$.

Equations (2.47)-(2.48) are at the basis of the numerical scheme known as *higher-order upwind scheme*, or, simply *Kappa scheme*. As said previously, the order of accuracy depends on the value

of the parameter K . For $K = 1, -1$ and $\frac{1}{3}$ the scheme corresponds to a 2nd order central, 2nd order upwind, and the 3rd order upwind biased discretization, respectively (*Hundsdorfer et al.*, 1996). In the present model, the value $K = 1/3$ is used.

One of the most important concern regarding a numerical scheme, especially when used for solving the transport of tracers whose concentrations can be very small, is the positiveness. A scheme is called positive if, for any non-negative initial solution $c(t_0)$, the evolving solution $c(t)$ remains non-negative for all $t \geq t_0$.

It can be shown (*Hundsdorfer et al.*, 1996), that the Kappa scheme guarantees positiveness if the flux limiter function Φ satisfies the following conditions:

$$\Phi = 0 \text{ if } r \leq 0, \quad 0 \leq \Phi \leq \delta, \quad \Phi \leq 2r, \quad (2.49)$$

where $\delta = 2$ and the *slope ratio* r is defined as:

$$r = \frac{\frac{\partial c}{\partial z}|_{k-1/2}}{\frac{\partial c}{\partial z}|_{k-3/2}} = \frac{\frac{c_k - c_{k-1}}{\Delta z_h(k)}}{\frac{c_{k-1} - c_{k-2}}{\Delta z_h(k-1)}}. \quad (2.50)$$

There are many ways to define a limiter function satisfying conditions (2.49) (see for instance *Suratanakavikul and Marquis*, 1999). The model utilizes the following flux limiter function by *Koren* (1993):

$$\Phi = \max \left[0, \min \left(2r, \frac{2}{3}r + \frac{1}{3}, 2 \right) \right], \quad (2.51)$$

which is shown to produce accurate results without losing convergence (*Suratanakavikul and Marquis*, 1999).

2.6 APPENDIX B: The Poisson Solver

In this appendix the Poisson solver is described. As explained in Section 2.4.1, this subroutine needed to be modified in order to use a non-equidistant numerical grid.

Introduction

The filtered Navier-Stokes equations can be written in the general form as (equation 2.10):

$$\frac{\partial u_i}{\partial t} = -\frac{\partial u_i u_j}{\partial x_j} + g \frac{\theta_l}{\theta_0} \delta_{i3} - 2\varepsilon_{ijk} \Omega_j u_k - \frac{\partial \tau_{ij}}{\partial x_j} - \frac{\partial \pi}{\partial x_j}, \quad (2.52)$$

where the angular brackets $\langle \rangle$ (representing the filter operator) are omitted for sake of clarity. As explained before, the modified pressure reads

$$\pi = \frac{p}{\rho_0} + 2/3e. \quad (2.53)$$

Equations (2.52) can be split in two contributions according to :

$$\frac{\partial u_i}{\partial t} = -\frac{\partial p}{\partial x_i} + Rem. \quad (2.54)$$

where Rem accounts for all the remaining terms in the r.h.s. of Equation (2.52) (advection, buoyancy, rotation and subgrid stress) except for the pressure gradient.

By introducing a fictitious velocity u^* , Equation (2.54) is decomposed as follows:

$$\begin{cases} \frac{\partial u^*}{\partial t} = Rem \\ \frac{\partial u}{\partial t} - \frac{\partial u^*}{\partial t} = -\frac{\partial p}{\partial x_i} \end{cases} \quad (2.55)$$

Applying the divergence operator to the second equation of the system (2.55) we obtain:

$$\nabla \left(\frac{\partial u}{\partial t} - \frac{\partial u^*}{\partial t} \right) = -\nabla^2 p, \quad (2.56)$$

which becomes, using the continuity equation (2.9),

$$\nabla \left(\frac{\partial u^*}{\partial t} \right) = f(u, x, y, z, t) = \nabla^2 p, \quad (2.57)$$

that is a form of the Poisson's equation. Note that $\nabla u^* \neq 0$ because the fictitious velocity represents all the remaining terms of the Navier-Stokes equation, whose divergence is not necessarily zero.

Assuming that the Rem term is known (Equation 2.55), we first calculate the pressure by solving the Poisson's equation (2.57). Once the pressure is known, we can finally solve for $\frac{\partial u}{\partial t}$ in equation (2.55).

Time discretization

The discretized form of the l.h.s. of equation (2.54) reads (leap-frog method):

$$\frac{u_i^{n+1} - u_i^{n-1}}{2\Delta t} = -\frac{\partial p}{\partial x_i} + Rem, \quad (2.58)$$

Similarly as above, a fictitious velocity u^* can be introduced and the equation (2.58) can be split into:

$$\begin{cases} \frac{u_i^* - u_i^{n-1}}{2\Delta t} = Rem \\ \frac{u_i^{n+1} - u_i^*}{2\Delta t} = -\frac{\partial p}{\partial x_i}, \end{cases} \quad (2.59)$$

which is the equivalent of the system (2.55).

By applying the divergence operator to (2.59) and making use of the continuity equation, we obtain

$$\nabla \left(\frac{u_i^*}{2\Delta t} \right) = \nabla^2 p, \quad (2.60)$$

which is the equation we need to solve, namely the discretized form of the Poisson's equation (2.57).

Spatial discretization

By defining the quantity

$$u_i^{**} \equiv \frac{u_i^*}{2\Delta t}, \quad (2.61)$$

the discretized form of the Poisson's equation (2.60) reads

$$\nabla (u_i^{**}) = \nabla^2 p. \quad (2.62)$$

Figure 2.4 shows the numerical grid used in the code, in the vertical direction. The scalar quantities (temperature, humidity, scalar and pressure) are defined in the center of the cell, whereas the wind velocities are defined at the edges, so that $p(k)$ is not at the same level then $w(k)$.

Moreover, referring to Figure 2.4, it can be noticed that, if a non-equidistant grid is used in the vertical direction, the distance between two adjacent centers (Δz_h) does not coincide with the distance between two edges (Δz_f).

In discretizing equation (2.62), we have to compute the velocity gradient (l.h.s.) and the pressure Laplacian (r.h.s) at the same level, namely at the center of the cell. Therefore, the l.h.s. can be written in the discrete (centered) form as

$$\nabla u_i^{**} = \frac{u_{i+1}^{**} - u_i^{**}}{\Delta x} + \frac{v_{j+1}^{**} - v_j^{**}}{\Delta y} + \frac{w_{k+1}^{**} - w_k^{**}}{\Delta z_f(k)}, \quad (2.63)$$

2.6. APPENDIX B: The Poisson Solver

whereas the pressure Laplacian (at the same level) is

$$\begin{aligned}\nabla^2 p = \frac{\partial}{\partial x_j} \left(\frac{\partial p}{\partial x_i} \right) &= \frac{1}{\Delta x} \left[\left(\frac{\partial p}{\partial x} \right)_{i+\frac{1}{2}} - \left(\frac{\partial p}{\partial x} \right)_{i-\frac{1}{2}} \right] + \\ &+ \frac{1}{\Delta y} \left[\left(\frac{\partial p}{\partial y} \right)_{j+\frac{1}{2}} - \left(\frac{\partial p}{\partial y} \right)_{j-\frac{1}{2}} \right] + \\ &+ \frac{1}{\Delta z_f(k)} \left[\left(\frac{\partial p}{\partial z} \right)_{k+\frac{1}{2}} - \left(\frac{\partial p}{\partial z} \right)_{k-\frac{1}{2}} \right].\end{aligned}\quad (2.64)$$

and pressure gradients at the cell's edge (point $i \pm 1/2$) are defined as

$$\begin{cases} \frac{\partial p}{\partial x} \big|_{i+\frac{1}{2}} = \frac{p_{i+1} - p_i}{\Delta x} \\ \frac{\partial p}{\partial x} \big|_{i-\frac{1}{2}} = \frac{p_i - p_{i-1}}{\Delta x}. \end{cases}\quad (2.65)$$

A similar formula holds for the y component.

The vertical pressure gradient reads:

$$\begin{cases} \frac{\partial p}{\partial z} \big|_{k+\frac{1}{2}} = \frac{p_{k+1} - p_k}{\Delta z_h(k+1)} \\ \frac{\partial p}{\partial z} \big|_{k-\frac{1}{2}} = \frac{p_k - p_{k-1}}{\Delta z_h(k)}. \end{cases}\quad (2.66)$$

As a result, the discretized form of the Laplacian of the pressure reads

$$\begin{aligned}\nabla^2 p &= \frac{p_{i+1} - 2p_i + p_{i-1}}{(\Delta x)^2} + \frac{p_{j+1} - 2p_j + p_{j-1}}{(\Delta y)^2} + \\ &+ \frac{1}{\Delta z_f(k)} \left(\frac{p_{k+1} - p_k}{\Delta z_h(k+1)} - \frac{p_k - p_{k-1}}{\Delta z_h(k)} \right),\end{aligned}\quad (2.67)$$

and the Poisson equation (2.62) becomes

$$\begin{aligned}&\frac{u_{i+1}^{**} - u_i^{**}}{\Delta x} + \frac{v_{j+1}^{**} - v_j^{**}}{\Delta y} + \frac{w_{k+1}^{**} - w_k^{**}}{\Delta z_f(k)} = \\ &= \frac{p_{i-1} - 2p_i + p_{i+1}}{(\Delta x)^2} + \frac{p_{j-1} - 2p_j + p_{j+1}}{(\Delta y)^2} + ap_{k-1} + bp_k + cp_{k+1},\end{aligned}\quad (2.68)$$

where

$$a = \frac{1}{\Delta z_f(k) \Delta z_h(k)} \quad (2.69)$$

$$c = \frac{1}{\Delta z_f(k) \Delta z_h(k+1)} \quad (2.70)$$

$$b = -(a + c). \quad (2.71)$$

Poisson Solver in the LES code

In the code used in this study, the routine FILLPS.F first computes, from Equation (2.59), the sum

$$u_i^{**} = \frac{u_i^*}{2\Delta t} = \frac{u_i^{n-1}}{2\Delta t} + Rem, \quad (2.72)$$

and then solves for the divergence ∇u_i^{**} (equation 2.63).

This is followed by the routine SOLMPJ.F that extracts the pressure p solving the Poisson's equation (2.68), given the value of ∇u_i^{**} calculated by FILLPS.F, applying a FFT in the two periodic directions (x and y), and solving a tridiagonal matrix in the vertical direction. The routine TDERIVE.F computes the velocity tendency $\frac{\partial u_i}{\partial t} \equiv u_p$, from Equation (2.54), namely

$$\frac{\partial u_i}{\partial t} \equiv u_p = Rem - \frac{\partial p}{\partial x_i} = u_i^{**} - \frac{u_i^{n-1}}{2\Delta t} - \frac{p_i - p_{i-1}}{\Delta x} - \frac{p_j - p_{j-1}}{\Delta y} - \frac{p_k - p_{k-1}}{\Delta z_h(k)}, \quad (2.73)$$

where equation (2.72) has been used, and the pressure gradient has been discretized at the same level of the velocity field.

Since by definition

$$\frac{\partial u_i}{\partial t} = \frac{u_i^{n+1} - u_i^{n-1}}{2\Delta t}, \quad (2.74)$$

the routine TSTEP.F can finally calculate the velocity at the time step $n + 1$

$$u_i^{n+1} = u_p 2\Delta t + u_i^{n-1}. \quad (2.75)$$

Chapter 3

Relating Eulerian and Lagrangian Statistics for the Turbulent Dispersion in the Atmospheric CBL

3.1 Introduction

Atmospheric dispersion is a topic of great importance especially in relation to pollutant transport. Two different approaches, known as the *Eulerian* and the *Lagrangian* frameworks, are used to describe this process.

In the Eulerian framework, statistical properties are calculated in a fixed reference frame. This approach is most commonly used in field experiments, with surface or aircraft platforms, (*Briggs*, 1993; *Lenschow and Stankov*, 1986), as well as in laboratory experiments (*Willis and Deardorff*, 1976; *Willis and Deardorff*, 1981; *Weil et al.*, 2002) or Eulerian numerical models (*Lamb*, 1978; *Henn and Sykes*, 1992; *Mason*, 1992).

In the Lagrangian framework, the statistical properties are calculated in a reference frame which moves with the flow. This is the most natural approach for theoretical investigation of turbulent dispersion, as in the works by *Taylor* (1921) and *Batchelor* (1949), who established seminal theoretical relationships between dispersion parameters and turbulent characteristics in flows characterized by homogeneous turbulence. These relationships have been widely applied in studies of atmospheric dispersion in the atmospheric boundary layer (ABL). Turbulence in the atmospheric Convective Boundary Layer (CBL), however, is vertically inhomogeneous and the flow is generally characterized by large downdrafts of cold air surrounded by narrow strong updrafts of warm air. As a result, the vertical velocity is positively skewed, and the turbulent transport is asymmetric (*Wyngaard and Weil*, 1991). Another relevant aspect in atmospheric dispersion is that the vertical transport is confined between the surface and the inversion at the top of the CBL.

Previous theoretical analysis have been applied to inhomogeneous flows, in particular in the works by *de Baas et al.* (1986), *Georgopoulos and Seinfeld* (1988) and *Degrazia et al.* (1998), who related dispersion parameters and Lagrangian properties (like the integral time scale) to spectral

The content of this Chapter has been published on *Journal of the Atmospheric Sciences* (**62**, 2005) with J. Vilà-Guerau de Arellano, A.A.M. Holtslag and P.J.H. Builtjes as co-authors.

characteristics of the atmospheric CBL.

Experimental measures of Lagrangian statistics in the CBL are very difficult to obtain. Experiments with grid-generated isotropic turbulence (e.g. *Sato and Yamamoto*, 1987; *Voth et al.*, 1998; *Ott and Mann*, 2000) are only partly representative of the turbulent transport in the atmosphere. Measurements of Lagrangian statistics in the atmosphere require the use of neutrally-buoyant balloons (*Gifford*, 1955; *Angell*, 1964; *Hanna*, 1981). As pointed out by *Hanna* (1981), due to the complicated experimental setting required in order to trace the balloon trajectory, the small number of balloons used, and the short sampling time (which rarely exceeds 30 minutes), experimental estimates of the Lagrangian time scale have solely an accuracy of about 50%.

Another alternative method to calculate Lagrangian statistics is by means of numerical simulations, that is, the trajectories of particles released in a numerically generated turbulent flow are tracked in space and time. The most accurate approach is Direct Numerical Simulation (DNS) by which the governing equations of the turbulent motion are directly solved numerically. Due to the high number of degrees of freedom needed to solve all the scales of motion of turbulence, *Yeung and Pope* (1989) and *Squires and Eaton* (1991) investigated Lagrangian properties of isotropic turbulence only at low Reynolds numbers therefore making it difficult to extrapolate the results to atmospheric applications.

Since Lagrangian statistics are strongly influenced by the large scales of motion (*Wang et al.*, 1995), a more suitable approach for studying Lagrangian statistics in the ABL is by Large Eddy Simulation (LES). By simulating the atmospheric flow with LES, the largest energy-containing scales of motion are solved directly and only the effect of the smallest (subgrid) scales are parameterized (e.g. *Nieuwstadt et al.*, 1991). To our knowledge, only very few studies have investigated Lagrangian statistics using LES: *Wang et al.* (1995) studied the ratio of the Lagrangian to the Eulerian time scales and the particle mean-square dispersion in a simulated turbulent channel flow, a highly idealized approximation of the neutral ABL. The Lagrangian statistics were only calculated for two different values of the Reynolds number ($Re = 3200$ and $Re = 21900$) and only at a few selected levels within the Boundary Layer (BL). *Uliasz and Sorbjan* (1999) calculated vertical profiles of Lagrangian time scales in the CBL but neither further investigation on other turbulence properties (such as the energy spectra) nor direct application to dispersion characteristics were made.

In our study, a LES is used to calculate Eulerian and Lagrangian statistics in the atmospheric CBL. In contrast to field measurements, the numerical simulation represents a very controlled experiment, because the flow characteristics are prescribed through initial and boundary conditions. In addition, the use of a large numerical domain and a long integration time allow us to obtain reliable statistics in both space and time.

Three main research issues are addressed in this study:

First, the turbulent characteristics of the flow are studied in the Eulerian framework by analyzing the energy spectra and velocity autocorrelations. Spatial and temporal analysis are carried out in order to derive length and time scales. These integral scales are usually related by Taylor's hypothesis of frozen turbulence. The LES results allow us to investigate the validity of Taylor's hypothesis in our numerically simulated CBL.

Second, Lagrangian statistics are calculated and the relationship between flow properties (autocorrelations) and dispersion characteristics (particles' displacements) is discussed through Taylor's

3.2. Theoretical background

analysis of turbulent dispersion (*Taylor*, 1921).

Finally, the relationship between Eulerian and Lagrangian frameworks is studied by calculating the ratio β between the Lagrangian and Eulerian time scales. This is relevant for improving the description of turbulent dispersion in the CBL and for relating theoretical approaches to experimental studies. Currently used parameterizations derived either in previous field atmospheric experiments (*Hanna*, 1981) or through theoretical analysis based on analytical spectra (*Degrazia et al.*, 1998) are validated against the LES results.

The outline of the Chapter is as follows. The theoretical background of the research is provided in Section 3.2; in Section 3.3 the numerical experimental setup is described and definitions of the calculated variables are given. The LES results for the Eulerian and Lagrangian statistics are then presented and discussed in Sections 3.4 and 3.5 respectively. In Section 3.6 the application of these statistics to atmospheric dispersion is examined. Finally in Section 3.7 the relationship between the two frameworks is studied. The range of validity of existing parameterizations for the value of the Lagrangian time and the ratio between Lagrangian and Eulerian time scales are also compared with the LES results.

3.2 Theoretical background

Dispersion in the atmosphere is related to the displacement of particles from one other. Assuming an ensemble of particles moving in the turbulent flow, the displacement in the j^{th} direction, at a time t after the release, is defined as:

$$\overline{x_j'^2(t)} = \overline{\left(x_j^i(t) - \overline{x_j^i(t)}\right)^2}, \quad (3.1)$$

where $x_j^i(t)$ is the position of the i^{th} particle and the overbar represents the average over all the particles.

Following the classical analysis of *Taylor* (1921), this displacement is expressed as a function of the properties of the turbulent flow according to

$$\overline{x_j'^2(t)} = 2\sigma_j^2 \int_0^t \int_0^{t'} R_j^L(\tau) d\tau dt', \quad (3.2)$$

where σ_j is the (square root of the) velocity variance, and $R_j^L(\tau)$ is the Lagrangian autocorrelation function, defined as

$$R_j^L(\tau) = \frac{\overline{u_j'(t)u_j'(t+\tau)}}{\sigma_j^2}. \quad (3.3)$$

Here, $u_j'(t) = u_j^i(t) - \overline{u_j^i(t)}$ is the velocity fluctuation of the i^{th} particle at time t and τ is the time lag.

Relationship (3.2) has two analytical limits for short and large times, respectively:

$$\overline{x_j'^2(t)} = \sigma_j^2 t^2 \quad t \ll T_j^L \quad (3.4)$$

$$\overline{x_j'^2}(t) = 2\sigma_j^2 T_j^L t \quad t \gg T_j^L \quad (3.5)$$

where the *Lagrangian (integral) time scale* T_j^L is defined as (e.g. *Hinze*, 1975)

$$T_j^L \equiv \int_0^\infty R_j^L(\tau) d\tau. \quad (3.6)$$

There is a large uncertainty in the value of the Lagrangian time scale and its dependance to other variables of the ABL. For instance, values reported in literature vary from $T_{v,w}^L \sim 80$ s (*Hanna*, 1981) to $T_v^L \sim 10000$ s (*Gifford*, 1987). Theoretical analysis of by *Degrazia et al.* (1998) relates the Lagrangian time scale to flow characteristics (for details see Section 7):

$$T_j^L \sim C \frac{z_i}{\sigma_j}, \quad (3.7)$$

where the value of the constant ($C \sim 0.17$) is in agreement with the experimental results by *Hanna* (1981) in the middle of the CBL.

Lagrangian statistics are seldom measured experimentally in the CBL, and T_j^L is normally inferred from Eulerian statistics using the following relationship:

$$T_j^L = \beta_j T_j^E, \quad (3.8)$$

where T_j^E is the Eulerian integral time scale, and β_j is the ratio of the Lagrangian to Eulerian time scales. Atmospheric measurements of β_j usually range between 3~4 (*Gifford*, 1955; *Angell*, 1964), whereas *Hanna* (1981) found a value of $\beta_j = 1.6$.

The value of β_j is dependent on the turbulence intensity $i = \sigma_j/U$ (where $U = U(z)$ is the mean wind speed) by the relationship

$$\beta_j = \frac{C}{i} = C \frac{U}{\sigma_j}, \quad (3.9)$$

where the value of the constant C ranges in literature from 0.35 to 0.8 (see, e.g., *Wang et al.*, 1995), with a theoretical value of 0.44 (*Wandel and Kofoed-Hansen*, 1962) and an experimentally measured value of 0.7 (*Hanna*, 1981). Numerical simulations by *Wang et al.* (1995) lead to $C = 0.6$.

LES allows us to calculate Eulerian and Lagrangian statistics for an atmospheric CBL within the same numerical experiment. From the LES results, the autocorrelation function (3.3) is calculated in both Eulerian and Lagrangian frameworks, and the integral scale (3.6) is derived. From the computed particle trajectories, dispersion statistics (3.1) are calculated and related to the turbulent characteristics of the flow through equation (3.2). By so doing, we investigate the influence of the inhomogeneity of the flow and the presence of the CBL boundaries on atmospheric dispersion.

Finally, the values of the Lagrangian time scale and the ratio β_j (3.8) are compared with experimental measurements and previous proposed parameterizations (equations 3.7 and (3.9).

3.3 Description of the numerical experiment

The LES code used here was the parallelized version of the one described by *Cuijpers and Duynkerke* (1993) and *Siebesma and Cuijpers* (1995), in which a set of filtered prognostic equations for the

3.3. Description of the numerical experiment

dynamic variables (wind velocity, potential temperature, and turbulent kinetic energy) was solved on a staggered numerical grid. The space and time integrations were computed with a Kappa (Vreugdenhil and Koren, 1993) and leap-frog numerical schemes, respectively.

The numerical domain covered an area of $10.240 \times 10.240 \text{ km}^2$. A horizontal grid length of 40 m was used (256 grid points in each horizontal direction). A non-uniform grid of 96 points was used in the vertical direction, with the vertical grid resolution varying from 5 m near to the surface to 15 m above the surface layer.

The subgrid fluxes were closed by relating them to the gradient of the solved variable by means of an exchange coefficient, which depended on the subgrid turbulent kinetic energy, and a length scale, which was related to the grid size. By so doing the grid anisotropy was to a certain extent implicitly taken into account by the subgrid closure.

The aspect ratio, that is, the ratio between the horizontal domain dimension to the CBL height z_i , was around 10 (with $z_i \sim 940 \text{ m}$). Lateral periodic boundary conditions were imposed for all the variables. A time step of 0.25 s was used.

At the top of the CBL, an inversion strength of $\Delta\theta = 5 \text{ K}$ was imposed, which strongly limited the vertical motion of the flow in the entrainment zone. As shown by Moeng and Rotunno (1990), the turbulent flow near the top of the CBL is strongly influenced by the capping inversion; the updrafts convert their kinetic energy into that of horizontal motion. Moreover, in this region, there are fewer updrafts than in the middle of the CBL. As a result, the skewness of the vertical velocity increases. The change of the turbulence structure due to the strong inversion has a large impact on the particles' vertical motion, as will be discussed later.

A geostrophic wind of 5 m/s aligned in the x direction and a heat flux of 0.156 K.m/s were imposed as constant forcing and the simulation was run for an initialization period of 2 hours (i.e. the period of CBL development needed to ensure that a (quasi-)stationary state is reached). After this period, the gradients of the mean variables were independent on time, and the turbulent kinetic energy had become constant. The average values of the convective velocity scale w_* was 1.7 m/s and the shear/buoyancy ratio u_*/w_* was equal to 0.21 (where u_* is the friction velocity). The value of the stability parameter $-z_i/L$ was ~ 40 . According to the classification used in Holtslag and Nieuwstadt (1986) this simulated flow is mainly driven by convective turbulence.

3.3.1 Lagrangian particle model

After the initialization period, 1024 particles were released on a regular horizontal grid at 50 different levels (from $z = 100 \text{ m}$ to $z = 850 \text{ m}$), that is, a total of 51200 particles. The horizontal distance (x and y direction) between the initial position of each particle was 320 m , in order to assure statistical independence. The position and velocity of each particle was recorded every 5 seconds for the following 5120 s. Here, it is important to point out that the Lagrangian statistics (autocorrelations and integral scales) are mainly dependent on the contribution of the largest scale of motion. For example, the integral scale is directly related to the peak of the energy spectra (Hanna, 1981); therefore a long sampling time is required to completely solve the most relevant scales of motion. Besides, tracking the particle using shorter time steps does not improve the results at smaller scales. In fact, since the horizontal grid size is 40 m and the mean wind speed is 5 m/s , each particle remains in the same numerical grid cell for an average time of 8 s . Scales

of motion smaller than the grid size are therefore filtered out by the LES. A test performed by tracking the particle every second did not show significant differences in the particle trajectories and velocities.

The position in direction j of the i^{th} particle was calculated according to:

$$x_j^i(t + \Delta t) = x_j^i(t) + u_j^i(t)\Delta t, \quad (3.10)$$

where Δt is the time step, and $u_j^i(t)$ is the velocity of the particle calculated by interpolating linearly the values of the resolved (Eulerian) velocity at the eight closest grid points. As pointed out by *Weil et al.* (2004), for a more realistic calculation of the particles' position, the subgrid component of the velocity $u_j^{i'}$ should be included in (3.10). The value of $u_j^{i'}$, which is not directly available from the LES, could be computed by solving the Langevin equation using a Markov chain process, as suggested by *Gopalakrishnan and Avissar* (2000) or by a simple random walk scheme (*Uliasz and Sorbjan*, 1999). A different approach was used by *Mason* (1992), who added a random vertical displacement to the motion of the particles close to the surface. Finally, *Weil et al.* (2004) used an adaptation of *Thomson's* (1987) Lagrangian Stochastic Model in which $u_j^{i'}$ is specified by a Gaussian PDF based on the subgrid stress tensor.

The subgrid velocity is particularly relevant in regions characterized by strong gradients, like near the surface, and may lead to errors in the calculation of ground concentration (*Weil et al.*, 2004). In our study, particles are released between $z/z_i = 0.12$ and $z/z_i = 0.9$, where the flow is characterized by constant profiles of wind and potential temperature.

Moreover, as discussed earlier, a quantity such as the Lagrangian time scale is dependent on the velocity contributions of the lower frequencies only, and therefore the velocity subgrid scales are not very relevant. This is corroborated by previous studies by *Wang et al.* (1995) and by *Gopalakrishnan and Avissar* (2000), who found no significative difference in the results if the velocity subgrid component was taken into account. Also, a simulation run with a finer grid (10 x 10 x 10 m) did not show differences in the results at large scales, as discussed below. The subgrid velocity $u_j^{i'}$ was therefore not included in our calculations.

A similar argument is used with respect to the choice of the interpolation method to calculate the Lagrangian velocities $u_j^i(t)$ from the Eulerian (resolved) ones (equation 3.10). Although the linear interpolation is used by many authors (*Uliasz and Sorbjan*, 1999; *Mason*, 1992), it is inadequate as it may introduce numerical noise when the particle cross the grid-line boundaries (*Yeung*, 2002). Nevertheless, the error (imprecision) associated with this process is only relevant at the smallest scales (i.e., scales equal or smaller than the numerical grid). Since the Lagrangian statistics (both autocorrelations and integral scales) are associated with the largest scale of motion, which are explicitly solved by the LES, we are confident that for the atmospheric flow the results are rather independent of the interpolation scheme used.

3.3.2 Definition of statistical variables

Autocorrelation functions and integral scales are calculated from the LES results in both the Eulerian and Lagrangian frameworks.

In the Eulerian framework, both temporal (E_t) and spatial (E_s) analysis are performed. Temporal analysis is the calculation of statistics from time series collected at fixed positions. Spatial analysis

3.3. Description of the numerical experiment

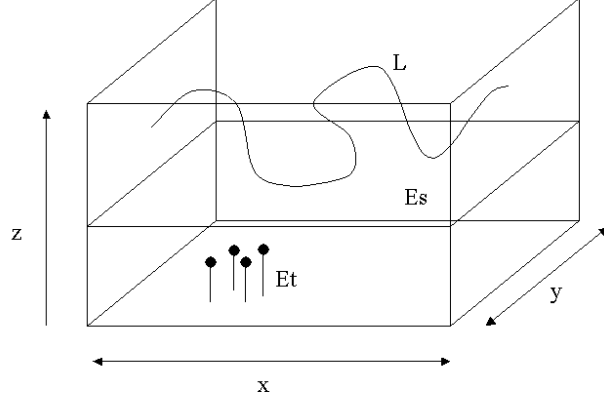


Figure 3.1: Sketch of the different methods used in this study to calculate statistics. Eulerian statistics are calculated both in space (Es) and in time (Et). Lagrangian statistics (L) are calculated by following the particles' trajectories.

is the calculation of statistics from data collected at different locations at fixed time (or averaged over a certain time).

In the Lagrangian framework (*L*), statistics are calculated from the particles velocities calculated by the LES according to (3.10). These different approaches are illustrated schematically in Figure 3.1. The theoretical definitions of the autocorrelation functions in the different frameworks is reported in the appendix. From the autocorrelation, the integral length scales (λ) and time scales (T) are derived in both Eulerian and Lagrangian frameworks. There are two drawbacks in the determination of the integral scales according to (3.6). First, if the sampling time is limited, the autocorrelation may not approach to zero, a problem encountered by *Hanna* (1981) in his Lagrangian field experiment. Second, if the autocorrelation shows oscillations around zero (e.g. *Deardorff and Willis*, 1985) the value of the integral scale calculated by (3.6) is zero. This is the case for wave-like signals, as shown by *Csanady* (1973).

The autocorrelation function for a pure stochastic motion has an exponential shape, that is, $R(\tau) = \exp(-\tau/T)$, where T is the integral scale (*Csanady*, 1973). In this case, the integral scale calculated by (3.6) is equal to the time T_e required for the autocorrelation to drop to $1/e$. Therefore, the measurement of T_e is the method commonly used in the majority of the studies related to atmospheric flows (*Hanna*, 1981; *Wang et al.*, 1995; *Deardorff and Willis*, 1985; *Mason*, 1989). As will be discussed later, in the atmospheric CBL the shape of the autocorrelation for the vertical velocity may differ from that of a simple exponential, and therefore the use of T_e as definition of integral scale is not appropriate.

In our study the integral scales are defined according to (*Lenschow and Stankov*, 1986):

$$\begin{cases} T = \max \left(\int_0^t R(\tau) d\tau \right) \\ \lambda = \max \left(\int_0^r R(r') dr' \right) \end{cases} \quad (3.11)$$

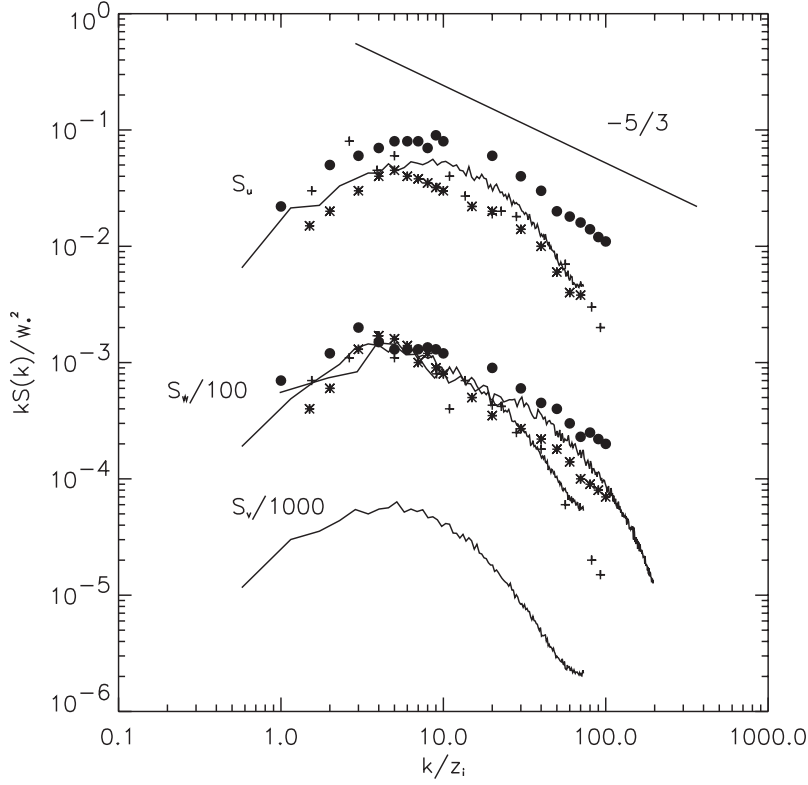


Figure 3.2: Normalized energy spectra of the wind velocity components in the middle of the boundary layer ($z/z_i = 0.5$) calculated by spatial analysis (Es). For clarity, the spectra have been divided by the factors shown near the curves. The following experimental data are also shown: * represents *Deardorff and Willis* (1985), + represents *Schmidt and Schumann* (1989), and • represents *Kaiser and Fedorovich* (1999) the thin line represents the vertical velocity spectra for a simulation with a very fine uniform numerical grid (10 x 10 x 10 m).

This definition gives the same result as (3.6) for an exponential autocorrelation, but it allows us to calculate more adequately the results for wave-like motion, like the vertical motion of a particle in the atmospheric CBL.

3.4 Eulerian statistics

Eulerian statistics are calculated in a fixed framework. Eulerian length and time scales have already been investigated in a large number of studies, both experimentally and numerically (e.g *Caughey and Palmer*, 1979; *Hanna*, 1981; *Lamb*, 1982; *Deardorff and Willis*, 1985; *Lenschow and Stankov*, 1986; *Mason*, 1989). However, there is an essential difference between field experiments and numerical studies. Field experiments (e.g *Hanna*, 1981) usually provide temporal analysis (i.e. statistics derived by the analysis of time series collected at fixed positions), whereas in numerical (e.g *Mason*, 1989) or laboratory experiments (e.g *Deardorff and Willis*, 1985) data is collected at different locations at a fixed time (or averaged over a certain time); that is, spatial analysis is used.

3.4. Eulerian statistics

These two analysis are usually related by Taylor's hypothesis of frozen turbulence (*Tennekes and Lumley, 1972*), which is always assumed but seldom validated. Here we analyze both time and spatial statistics in the Eulerian framework and evaluate the relationship between them.

3.4.1 Spatial analysis

One-dimensional spectra of the wind velocity components were obtained by Fourier transforming the LES results along the mean wind direction and then averaging these over all parallel lines. Each of these spectra was obtained from the model output every 10 minutes and then time averaged.

Figure 3.2 shows the normalized energy spectra for the wind velocity components calculated in the middle of the BL ($z/z_i = 0.50$). The LES results agree with the tank experiments by *Deardorff and Willis (1985)*, the numerical results by *Schmidt and Schumann (1989)*, and the wind tunnel data by *Kaiser and Fedorovich (1999)*. As the Figure shows, the numerical domain is sufficiently large to solve all the relevant scales of motion. In fact, the vertical profile of the velocity variances calculated as integral of the spectra (not shown) are in agreement with previous experimental and numerical studies (*Willis and Deardorff, 1974; Lenschow et al., 1980; Dosio et al., 2003*).

At short scales ($k/z_i > 20$), the slope of the spectra departs from the theoretical slope $k^{-5/3}$. This is a consequence of the finite numerical grid, as explained by *Pasquill (1974)*. However, as mentioned earlier, the autocorrelation (and therefore the length scale), depends mainly on the larger scales, which are solved by the model. To investigate the dependence of the results on the smaller scale of motion, we performed a simulation using a very fine uniform numerical grid (10m x 10m x 10 m); the result (shown only for the vertical velocity) shows that, as expected, the shape (slope) of the spectrum at short scales is improved, but at large scales ($k/z_i < 20$) the shape of the spectrum and the magnitude and position of the spectral peak (which is proportional to the integral scale) are not modified. As was also pointed out by *Schmidt and Schumann (1989)*, simulations with a different set of coefficients in the subgrid parameterization of their model showed a slight improvement in the spectra, but both the results at large scales and the agreement with measurements were not altered significantly.

Due to the scatter, it is not easy to estimate the wavelength Λ_j of the spectral peak. For the horizontal velocity, both Λ_u and Λ_v are generally in agreement with the relationship by *Caughey (1982)*:

$$\Lambda_{u,v} = 0.15z_i, \quad (3.12)$$

However, at heights $z/z_i > 0.8$, we found larger values for the wavelength, $\Lambda_{u,v} = 1.8z_i$ at $z/z_i = 0.9$ and $\Lambda_{u,v} = 1.9z_i$ at $z/z_i = 1$, respectively. For the vertical velocity, the vertical profile of Λ_w follows the curve,

$$\Lambda_w/z_i = 1.8 [1 - \exp(-8z/z_i) - 0.0003 \exp(8.5z/z_i)], \quad (3.13)$$

which is similar to the expression suggested by *Caughey and Palmer (1979)*, as shown by Figure 3.4a where the vertical profile of Λ_w/z_i is also compared with the atmospheric data by *Caughey and Palmer (1979)* and *Graf and Schumann (1992)*, and the wind tunnel data by *Kaiser and Fedorovich (1999)*.

Figure 3.3 shows the autocorrelation function for the three wind components calculated at three

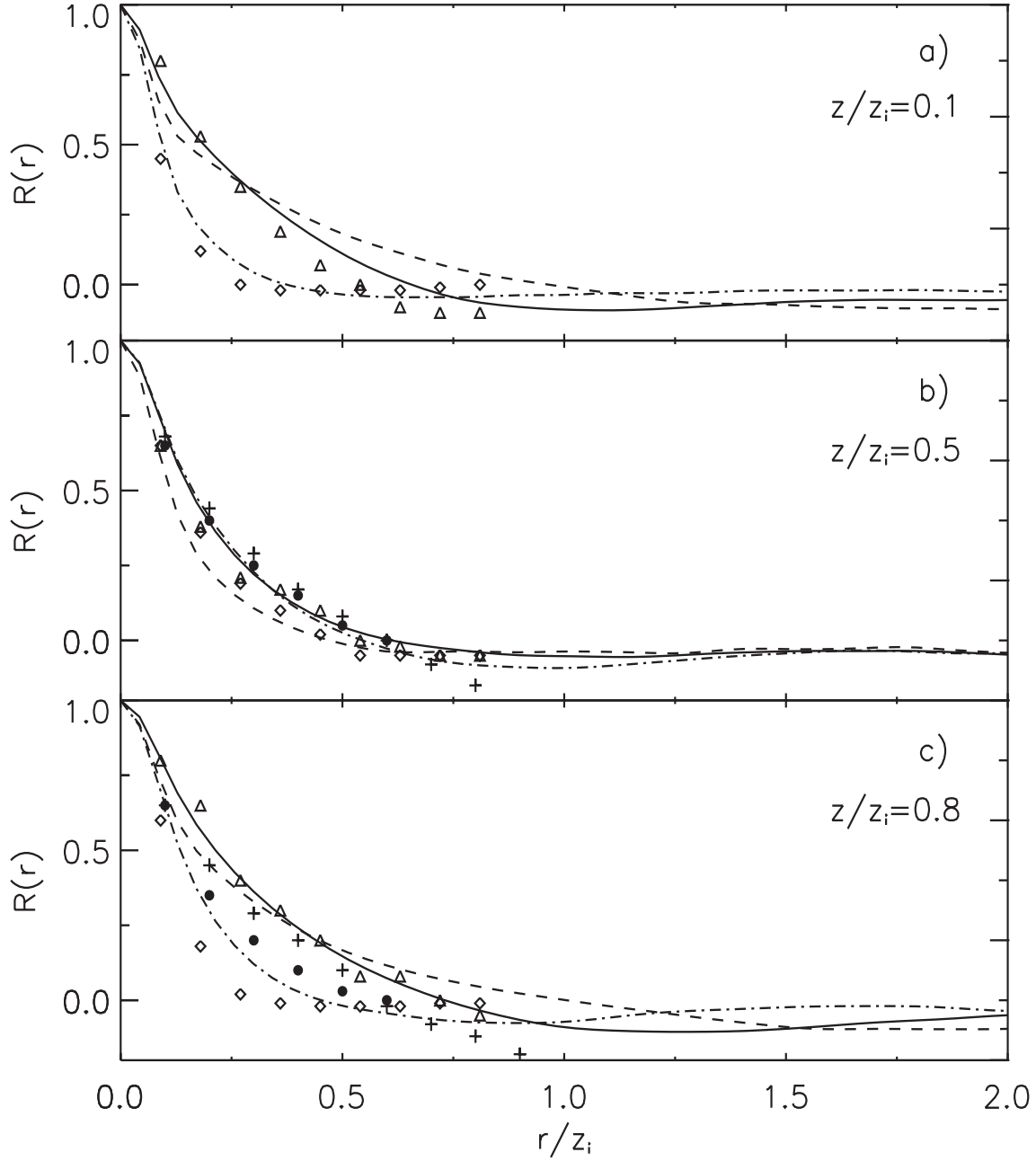


Figure 3.3: Eulerian autocorrelation function $R^E(r)$ calculated according to (3.29) at different heights as a function of the normalized space lag r/z_i . The continuous line is the u component, the dashed line is the v component, and the dashed-dotted line is the w component. The following experimental data are also shown: \triangle and \diamond represent *Mason* (1989) (u component and w component, respectively) and $+$ and \bullet represent *Deardorff and Willis* (1985) (u component and w component, respectively).

3.4. Eulerian statistics

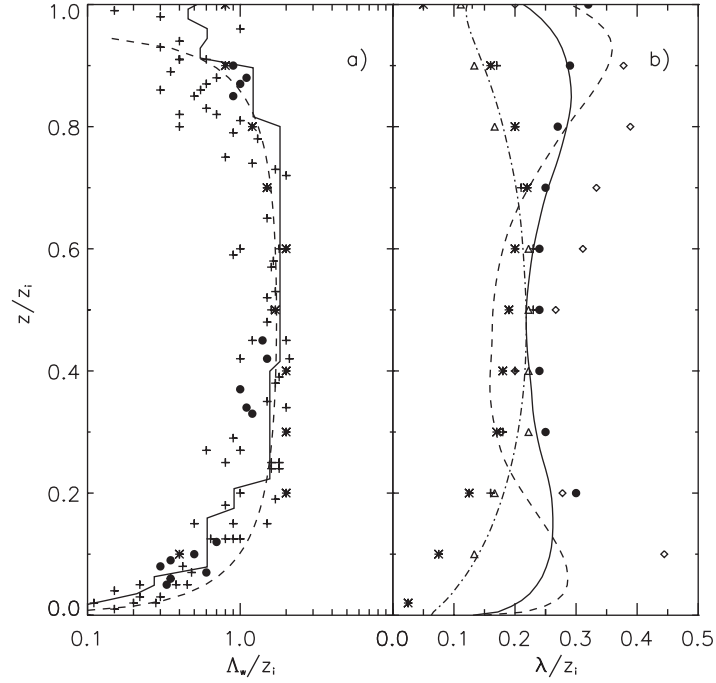


Figure 3.4: a) The continuous line is the vertical profile of the normalized length scale Λ_w (wave-length of the spectral peak) for the vertical velocity. The following experimental data are also shown: + represents *Caughey and Palmer* (1979), * represents *Kaiser and Fedorovich* (1999), and • represents *Graf and Schumann* (1992). The dashed line is the parameterized curve (3.13). b) Vertical profiles of the Eulerian length scale λ_j (normalized by the CBL height) calculated according to (3.11). The continuous line is the u component, the dashed line is the v component, and the dashed-dotted line is the w component. The following experimental data are also shown: * represents *Khanna and Brasseur* (1998), • represents *Mason* (1989), and ◇ represents *Deardorff and Willis* (1985).

different heights ($z/z_i = 0.1$, $z/z_i = 0.5$, $z/z_i = 0.8$). The results are in agreement with the experimental data by *Deardorff and Willis* (1985) and numerical experiment by *Mason* (1989). In the middle of the boundary layer, the autocorrelation function for w does not differ significantly from the autocorrelation functions for u and v . Near the surface layer and near the inversion, on the contrary, the autocorrelation function for the vertical velocity decays more rapidly than for the horizontal components.

This is corroborated by the vertical profiles of length scales λ_j (3.11), shown in Figure 3.4b. Although a direct comparison is not possible due to the different definition of the length scale, our LES results agree with previous numerical studies (*Mason*, 1989; *Khanna and Brasseur*, 1998) and laboratory experiments (*Deardorff and Willis*, 1985). The length scales remain approximately constant (with a variation of about 10% from the mean value) between $z/z_i = 0.2$ and $z/z_i = 0.7$. *Lenschow and Stankov* (1986) also showed that the profiles of the horizontal length scales remain constant with height.

In the region below $z/z_i < 0.2$ and in the entrainment zone, the length scales differ significantly from their mean value in the bulk of the CBL. In particular the vertical length scales decrease with

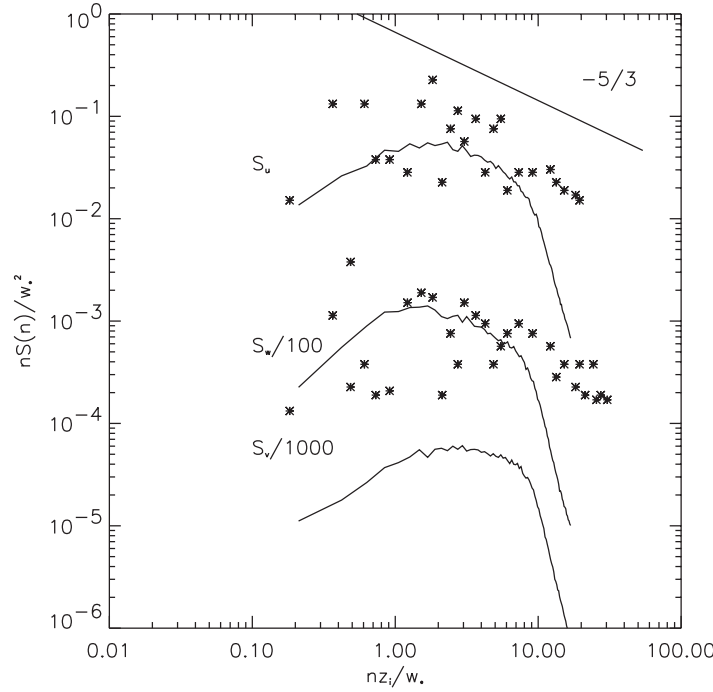


Figure 3.5: Normalized energy spectra of the wind velocity components in the middle of the boundary layer ($z/z_i = 0.5$) calculated by temporal analysis (Et). For clarity, the spectra have been divided by the factors shown near the curves. The atmospheric data by *Caughey and Palmer* (1979) are also shown (*).

height whereas the horizontal ones increase. As shown by previous studies (*Mason*, 1989; *Moeng and Rotunno*, 1990; *Khanna and Brasseur*, 1998), the flow near the inversion zone is characterized by more isolated and discrete eddies, rather than large downdrafts surrounded by narrow updrafts as in the middle of the CBL. Although the size of the eddies (updrafts) remains mostly constant with height, near the top of the CBL there are fewer updrafts than at lower levels. This leads to a increase in the skewness of the vertical velocity in the inversion zone, as shown by *Moeng and Rotunno* (1990). They also showed that in a CBL characterized by a strong inversion the updrafts convert part of their kinetic energy into that of horizontal velocity field; as a result, vertical motion is converted into horizontal.

The results of *Lenschow and Stankov* (1986) show that the horizontal length scale maintains a more constant profile near the top of the CBL, and the vertical length scale continues growing with height. Their results were obtained as average of measurements for different boundary layers, with values of the shear/buoyancy ratio u_*/w_* varying from 0.18 to 0.46 and the stability parameter $-z_i/L$ varying from 7.5 to 54. It is therefore possible that wind shear influenced the results in some cases. As shown by *Carruthers and Hunt* (1986), the values of the length scales depend on the atmospheric stability of the upper layer. *Mason* (1989) also observed that the results by *Lenschow and Stankov* (1986) near the top of the CBL could have been influenced by the presence of large scale motion in the stable layer above the inversion.

3.4. Eulerian statistics

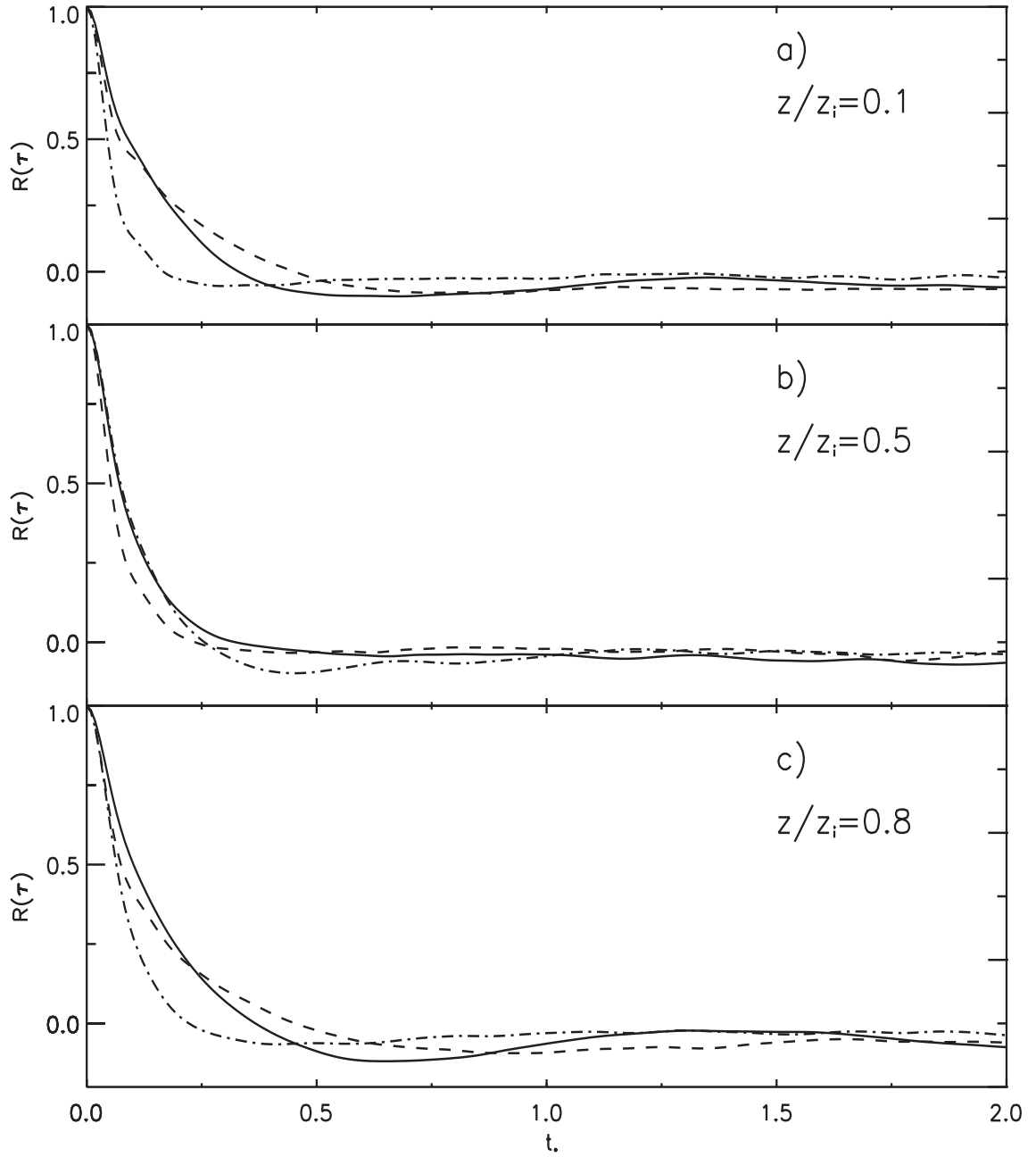


Figure 3.6: Eulerian autocorrelation function $R^E(\tau)$ calculated according to (3.26) at different heights as a function of the non dimensional time lag t_* . The continuous line is the u component, the dashed line is the v component, and the dashed-dotted line is the w component.

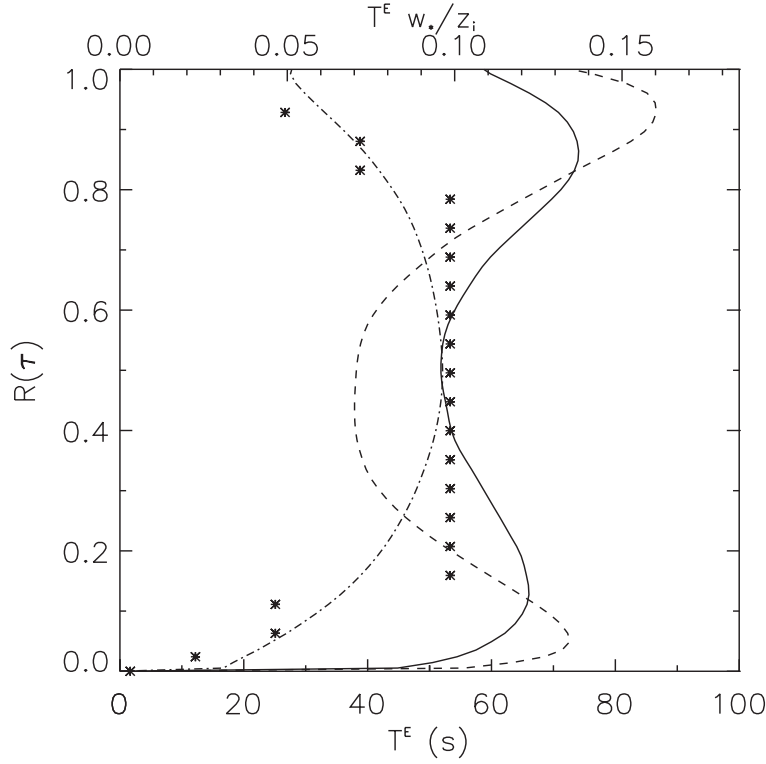


Figure 3.7: Vertical profiles of the Eulerian time scale T_j^E calculated according to (3.11). The continuous line is the u component, the dashed line is the v component, and the dashed-dotted line is the w component. In the Figure, the Eulerian time scale for the vertical wind component calculated according to (??) is also shown (*).

3.4.2 Temporal analysis

Time series for the three velocity components were collected at 1024 points uniformly distributed in the horizontal domain for each vertical level. Spectra were subsequently calculated and averaged over the points (horizontal space average over the whole domain).

Figure 3.5 shows the energy spectra for the wind velocity components calculated in the middle of the CBL ($z/z_i = 0.5$). In spite of the large scatter in the observations, our results agree qualitatively with the atmospheric data by *Caughey and Palmer* (1979) (although they show spectra only at $z/z_i = 0.9$). As explained earlier, also in this case the fall of the spectra from the theoretical slope at small scales (large frequencies) is a consequence of the time step used, but it does not influence the values of the autocorrelations and time scales.

The autocorrelations for the three wind components at different heights are shown in Figure 3.6 and the vertical profiles of time scales T_j^E calculated according to (3.11) are shown in Figure 3.7. Both the autocorrelation and the integral-scale profiles have similar values and vertical shape to the ones calculated through spatial analysis (Figures 3.3 and 3.4). Atmospheric measurement of Eulerian integral time scales for convective conditions ($-z_i/L$ ranging from -20 to -375) are reported by *Hanna* (1981), although no vertical profiles are shown. In his work, averaged values of $T_u^E \sim 44$ s

3.4. Eulerian statistics

and $T_w^E \sim 55$ s are reported, and they agree with the LES results.

Here, it is worth mentioning that the integral scales can be also calculated directly from the spectra. In fact, assuming an autocorrelation with an exponential shape *Hanna* (1981) showed that

$$T^E \sim \frac{1}{6} T_m, \quad (3.14)$$

where T_m is the period at which spectral peak occurs. Although a precise determination of the spectral peak is difficult, relationship (3.14) is generally well satisfied for all the wind components. For instance, values of the integral scales calculated at $z/z_i = 0.5$ according to (3.14) are $T_u^E = 56$ s, $T_v^E = 34$ s and $T_w^E = 53$ s. In Figure 3.7 the vertical profile of T_w^E calculated according to (3.14) is plotted, showing that the agreement is very satisfactory. However, as pointed out by *Hanna* (1981), the determination of the integral scale from the autocorrelation function is preferable, as it leads to more accurate results.

3.4.3 Validation of Taylor's hypothesis of frozen turbulence in atmospheric flows

As mentioned earlier, field experiments usually measure variables that evolve with time. In laboratory experiments and numerical simulations, on the other hand, spatial analysis is often used. The two frameworks are related by Taylor's hypothesis of frozen turbulence. Following *Pasquill* (1974), Taylor's hypothesis is applied to autocorrelations and spectra as follows:

$$R(t) = R(x) \quad \text{if } x = Ut \quad (3.15)$$

$$US(n) = S(k) \quad \text{if } n = Uk \quad (3.16)$$

This in turn leads to the relationship between Eulerian length and time scales,

$$UT^E = \lambda^E \quad (3.17)$$

where U is the (height dependent) mean wind in the x direction (along which data is collected). As explained earlier, in the simulated strongly convective CBL the wind profile is mostly constant between $z/z_i = 0.1$ and $z/z_i = 0.9$. The length scales λ^E and time scales T^E are calculated from both autocorrelation functions and spectra through equations (3.11) and (3.14) respectively. To our knowledge, this is the first time that length and time scales are calculated with two independent methods within the same experiment, allowing a direct validation of relation (3.17). The vertical profile of the ratio $\frac{1}{U} \frac{\lambda^E}{T^E}$, calculated by combining the results shown in Figure 3.4 and Figure 3.7, is close to one for all the wind components, which shows that Taylor's hypothesis (relationships 3.15 and 3.16) holds in the simulated CBL. Only in the regions very close to the surface ($z/z_i < 0.05$) and at the top of the CBL ($z/z_i > 0.95$), where a strong wind shear is present, the ratio $\frac{1}{U} \frac{\lambda^E}{T^E}$ is slightly different than 1, being 1.2 and 0.8 respectively.

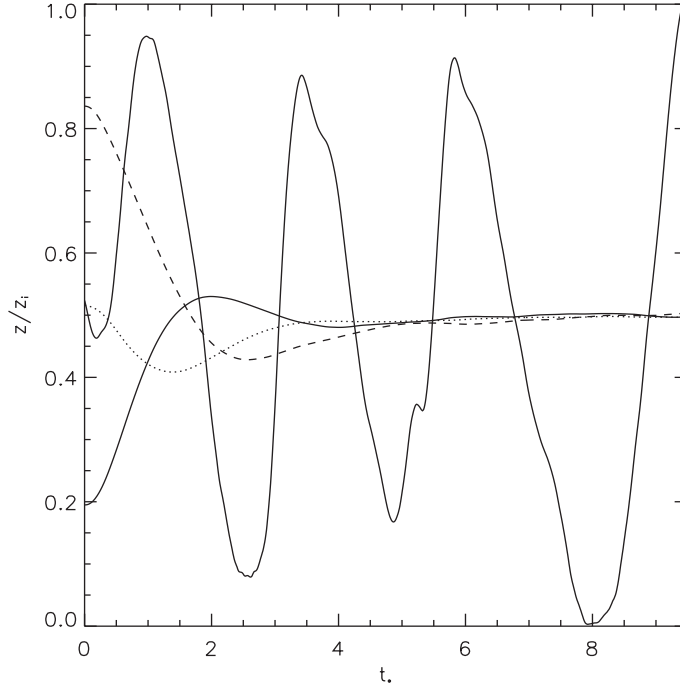


Figure 3.8: Mean plume height (plume centerline) of particles released at three different heights ($z/z_i = 0.2, 0.5, 0.85$ respectively) and example of an individual trajectory (vertical position as function of time) of a particle released at $z/z_i = 0.5$.

3.5 Lagrangian statistics

Lagrangian statistics were calculated by following, both in space and in time, the particles released at different positions in the simulated CBL. In Figure 3.8, an example of particle trajectory (i.e. vertical position as function of the non dimensional time $t_* = (z_i/w_*)t$) is shown. The particle is released in the middle of the boundary layer ($z/z_i = 0.5$) and is rapidly caught by the thermals which transport it in a wave-like motion between the boundaries of the CBL. This motion is typical of meandering plumes in a strongly convective boundary layer.

In the same picture, the mean plume height (plume centerline) of particles released at three different heights ($z/z_i = 0.2, 0.5, 0.85$ respectively) is also shown. The vertical motion at short times after the release ($t_* < 1$) is largely dependent on the release height. As shown, particles released at $z/z_i = 0.2$ are caught by the updrafts and rise very quickly, whereas particles released at $z/z_i = 0.8$ descend more slowly and remain in the upper part of the CBL for a long time. The difference in the particles' motions at short times is related to the different vertical structure of the turbulent flow at different heights of the CBL and to the conversion of vertical motion into horizontal due to the strong inversion at the top of the CBL, as explained earlier.

At longer times ($t_* > 2$), all particles are (on average) in the middle of the CBL and therefore they have a similar behavior, moving in a periodic motion between the boundaries of the CBL.

In short, the vertical inhomogeneity of the flow influences the particle motion at short times,

3.5. Lagrangian statistics

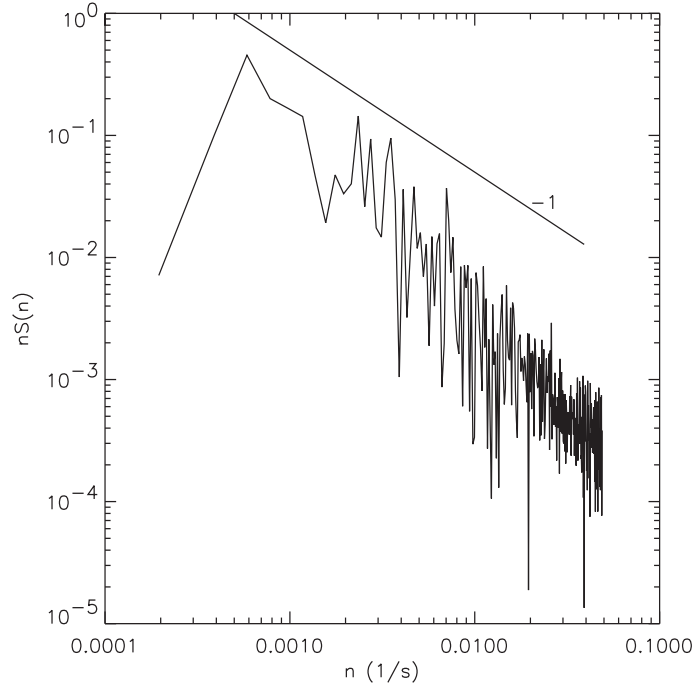


Figure 3.9: Lagrangian energy spectra of the vertical velocity for a particle released in the middle of the boundary layer.

whereas the presence of the CBL boundaries affects the particles' motion at longer time. As will be discussed later, these two effects have a direct influence on the shape of the autocorrelation and consequently on the values of the Lagrangian time scale.

Figure 3.9 shows the spectra of the vertical velocity for a particle released in the middle of the CBL. As explained by *Corssin* (1963), the Lagrangian spectra in the inertial subrange follows a n^{-2} slope. With respect to the Eulerian one, the peak shifts towards smaller frequencies, as shown by *Hanna* (1981). The value of the spectral peak frequency with respect to the one calculated in the Eulerian framework will be discussed later.

Lagrangian autocorrelations calculated using (3.30) are shown in Figure 3.10 as a function of the dimensionless time t_* . To have statistically sound results, they are presented as average over particles released at three different heights: particles released below $z/z_i = 0.25$ (10240 particles), particles released between $z/z_i = 0.25$ and $z/z_i = 0.75$ (30720 particles) and particles released above 0.75 (10240 particles).

There is a noticeable difference between the autocorrelation for the horizontal (v) and the vertical (w) wind component. The horizontal autocorrelation (Figure 3.10a) closely follows an exponential decay (i.e. at $z/z_i = 0.5$ $R(\tau) = \exp(-\tau/200)$), characteristic of a Markov process. The shape of the autocorrelation is independent of the height of the release, but it is clear that the integral of the autocorrelation for particle released above $z/z_i = 0.75$ is slightly larger than the one for particles released in the middle of the CBL.

The vertical autocorrelation departs from an exponential function. The shapes of the autocorrelation of particles released below $z/z_i = 0.25$ or between $z/z_i = 0.25$ and $z/z_i = 0.75$ are quite

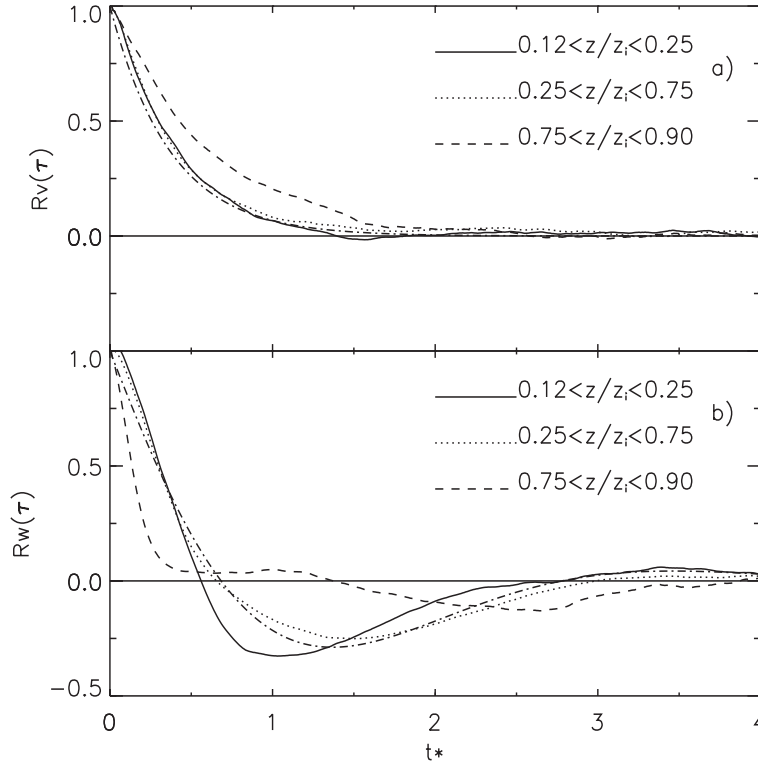


Figure 3.10: a) Lagrangian autocorrelation for the horizontal (v) motion for particles released at different heights. The function $R(\tau) = \exp(-\tau/200)$ is also shown (dashed-dotted line). b) Lagrangian autocorrelation for the vertical (w) motion for particles released at different heights. Equation (3.18) is also shown (dashed-dotted line).

similar and peculiar. Both have a strong minimum (at $t_* = 1$ and 1.4 , respectively), and they reach constant value close to zero at larger times. This particular shape of the autocorrelation is found for periodic (or wave-like) motions, as explained by *Csanady* (1973). In the CBL, the particles' vertical motion is limited by the bottom and the top boundaries, and the particles move periodically within the CBL, as shown in Figure 3.8. This autocorrelation is analytically reproduced by combining a stochastic motion (characterized by an exponential autocorrelation) and a wave-like motion (characterized by a sinusoidal autocorrelation). The resulting autocorrelation has a shape similar to the analytical function (*Csanady*, 1973),

$$R^L(\tau) = e^{-m\tau} \left[\cos(n\tau) - \frac{m}{n} \cos(n\tau) \right]. \quad (3.18)$$

As Figure 3.10b shows, the function (3.18) with $m = 0.9$ and $n = 1.5$ fits the LES results accurately for the release at $z/z_i = 0.5$.

As mentioned previously, experimental measurements of Lagrangian statistics in the CBL are extremely rare. In his study, *Hanna* (1981) calculates the integral time arbitrarily assuming that T_L corresponds to the time lag at which $R(\tau)$ first drops to 0.37 , therefore implicitly assuming an exponential shape for $R(\tau)$. However, he pointed out that the autocorrelation curves do not approach

3.5. Lagrangian statistics

zero at the largest time lags available. This may implicate that his dataset (30 minutes record) was too short to show the negative behavior of the autocorrelation function at large times.

In their study of synoptic scale Lagrangian autocorrelation function, *Daoud et al.* (2002) analyzed a large database of modelled 10-day atmospheric trajectories, and they showed indeed an autocorrelation function whose shape is similar to that in our study (although in their case, it is the horizontal velocity autocorrelation). They also relate this shape to wave-like motion of the particle in the atmosphere.

Numerical investigations of Lagrangian statistics in turbulent flow are reported by *Wang et al.* (1995) and *Yeung and Pope* (1989). The latter performed a DNS of isotropic turbulence at relatively low Reynolds number (< 100); therefore their study is not directly comparable with atmospheric turbulence. *Wang et al.* (1995) performed a LES of a turbulent channel flow at Reynolds number of 21900, which can be regarded as an idealization of a neutral atmospheric boundary layer. In our opinion, particles released in a neutral BL have a different behavior compared to a pure-convective CBL. As shown by *Dosio et al.* (2003), a tracer released in a near neutral BL is transported horizontally rather than vertically; the vertical dispersion is reduced whereas the horizontal dispersion is enhanced. Therefore, the vertical wave-like motion, which leads to the negative-shaped autocorrelation, is largely reduced in a neutral BL.

In fact, as Figure 3.10b shows, the shape of the autocorrelation for particles released above $z/z_i = 0.75$ (where the turbulence characteristics are different than in the bulk of the CBL) is much more close to an exponential shape, especially at short time. At longer time ($t_* > 2$) when the particles are in the middle of the CBL the autocorrelation shows the negative minimum (but smaller than the other cases), and finally it reaches zero.

From the autocorrelation function the following function is calculated:

$$T_j^L(t) = \int_0^t R_j^L(\tau) d\tau \quad (3.19)$$

By definition (3.6), the Lagrangian time T_j^L is therefore the limit for large times of $T_j^L(t)$.

Figure 3.11 shows the function $T_j^L(t)$ for the horizontal and vertical motion as a function of t_* . For the horizontal motion, $T_v^L(t)$ grows constantly until it reaches a (fairly) constant asymptotic value. This asymptote represents the Lagrangian time (3.6) and it has a value $T_v^L = 230s$ for particles released between $z/z_i = 0.25$ and $z/z_i = 0.75$. The time at which the autocorrelation drops to $1/e$ is $T_e = 200s$. Such small discrepancy is due to statistical errors related to the small fluctuations around zero for large time lags ($2 < t_* < 4$) (Figure 3.10a). In fact, as shown in Figure 3.10a, the analytical function $R(\tau) = \exp(-\tau/200)$ fits very well the autocorrelation calculated by the LES. The Lagrangian time for particles released above $z/z_i = 0.75$ has a larger value ($T_v^L = 310s$), as explained previously.

For the vertical motion, the curve $T_w^L(t)$ follows closely the one for the horizontal motion for short times ($t_* < 0.5$) before reaching a maximum and finally dropping to zero. The value and the position of the maximum depend on the release height, being $T_w^L = 175s$ for particles released below $z/z_i = 0.75$ and $T_w^L = 100s$ for particles released above $z/z_i = 0.75$.

It is therefore clear that in the atmospheric CBL the Lagrangian properties at short times depend on the release height, due to the turbulence vertical structure. Moreover, a peculiar difference exists at large times between vertical and horizontal direction, due to the limitation by the lower and upper

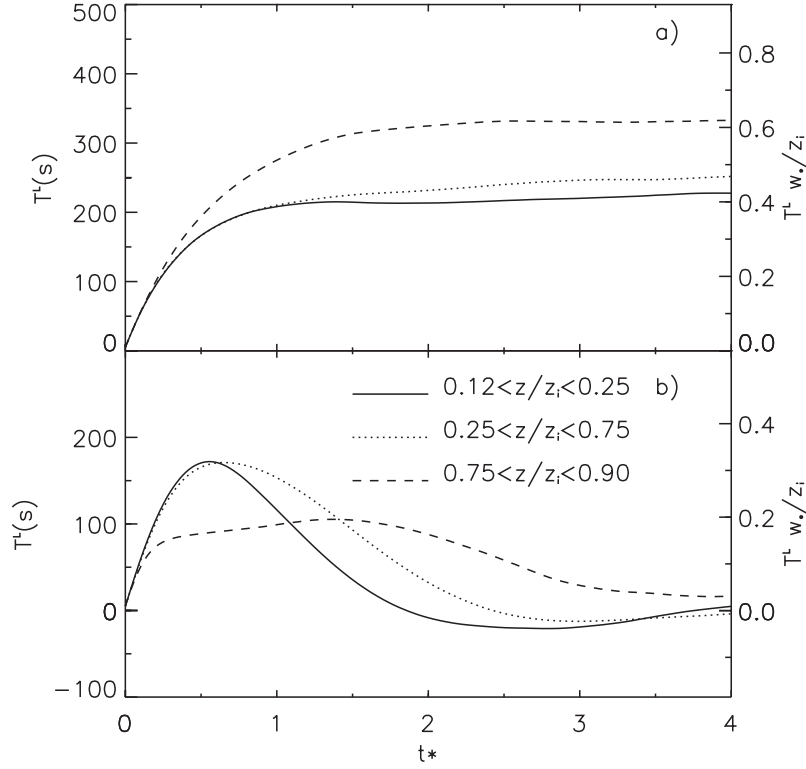


Figure 3.11: Integral of the autocorrelation (3.19) for the horizontal (a) and vertical (b) wind components for particles released at two different heights (Continuous line: $z/z_i = 0.5$, dashed line: $z/z_i = 0.85$).

boundaries to the vertical motion. These effects have a large influence on the autocorrelation shape and the value of the Lagrangian time, as shown. This difference between horizontal and vertical motion has also a great effect on the particle displacement (dispersion), as it will be discussed in the next Section.

3.6 Horizontal and vertical dispersion

In this Section, the relationship between the flow properties and the dispersion characteristics is analyzed. In particular, dispersion characteristics are calculated in both Eulerian and Lagrangian frameworks. Taylor's relation (equation 5.14) relates the autocorrelation $R(\tau)$ to the particles' displacement $\overline{x_j'^2(t)}$ (3.1); both these quantities are calculated in the Lagrangian framework. As pointed out by Blackadar (1998), for practical applications the Lagrangian quantity is often replaced with the Eulerian one $\sigma_{x_j}^2$. The latter refers to the standard deviation of the position of all the particles that lie at distance $X = Ut$ downwind the source, whereas $\overline{x_j'^2(t)}$ refers to all the particles that have travelled a time t since leaving the source. Some of them will be situated closer and some further from the source than the distance X . In practical application, the Eulerian quantity $\sigma_{x_j}^2$ is calculated (measured) instead of the Lagrangian $\overline{x_j'^2(t)}$, assuming that the difference is not

3.6. Horizontal and vertical dispersion

very great.

By using the LES results, we calculate both $\sigma_{x_j}^2$ and $\overline{x_j'^2}(t)$ and compare them with Taylor's relationship (5.14). To calculate the Eulerian dispersion, particles are tracked as function of space, instead of time, and $\sigma_{x_j}^2$ is calculated at intervals equal to the grid size from the initial position. The results are shown in Figures 3.12-3.13 and discussed below.

3.6.1 Horizontal dispersion

For the horizontal motion (Figure 3.12) Taylor's theory is satisfactorily fulfilled. The Lagrangian displacement $\overline{y'^2}(t)$ is similar to the Eulerian dispersion parameter σ_y^2 , and both agree with previous studies and laboratory measurements (*Lamb, 1978, Willis and Deardorff, 1981*). Equation (3.2) follows closely the displacement curves, and it shows the expected limits at short and long times, respectively $\sigma_v t$ and $2\sigma_v (T_v^L t)^{1/2}$. This satisfactory agreement is closely related to the exponential shape of the autocorrelation (Figure 3.10), leading to a constant limit at long times for the value of the Lagrangian integral time (Figure 3.11).

3.6.2 Vertical dispersion

The results for the vertical dispersion are shown in Figure 3.13. It is first important to notice that also in this case, the Lagrangian displacement $\overline{z'^2}(t)$ and the Eulerian dispersion parameter σ_z^2 are very similar, which implies that, for practical purposes using Eulerian dispersion parameters instead of the Lagrangian one does not lead to large errors. This is related to the fact that Taylor's hypothesis of frozen turbulence holds in the simulated CBL, as shown before. As a result, dispersion statistics calculated for particles that travelled a time t after the release are equivalent to those calculated for particles that lie at distance $X = U/t$ from the source.

However, for the vertical motion the comparison between the particle displacement and Taylor relationship (3.2) is less satisfactory and requires a more detailed analysis and discussion. Since the shape of the vertical autocorrelation function and the Lagrangian time depend on the particle release height, the results are presented separately for particles released below and above $z/z_i = 0.75$.

Particles released below $z/z_i = 0.75$

The vertical displacement (3.1) calculated from the particle trajectories agrees with previous experiments (*Lamb, 1978*) and reaches a constant limit of $\overline{z'^2}(t) \sim 0.3$, characteristic of an ensemble of particles uniformly mixed within the CBL. Equation (3.2), on the other hand, agrees with the displacement and previous experiments only at short times ($t_* < 0.7$). This time is of the same order of magnitude as the turnover time and corresponds to the period when the particles, just after being released, are still unaffected by the CBL boundaries. In other words, the particles are in a regime of "free motion".

As Figure 3.13b shows, at longer times equation (3.2) reaches a constant limit of about 0.5. This limit is due to the peculiar shape of the autocorrelation for vertical motion for $t_* > 2$, which leads

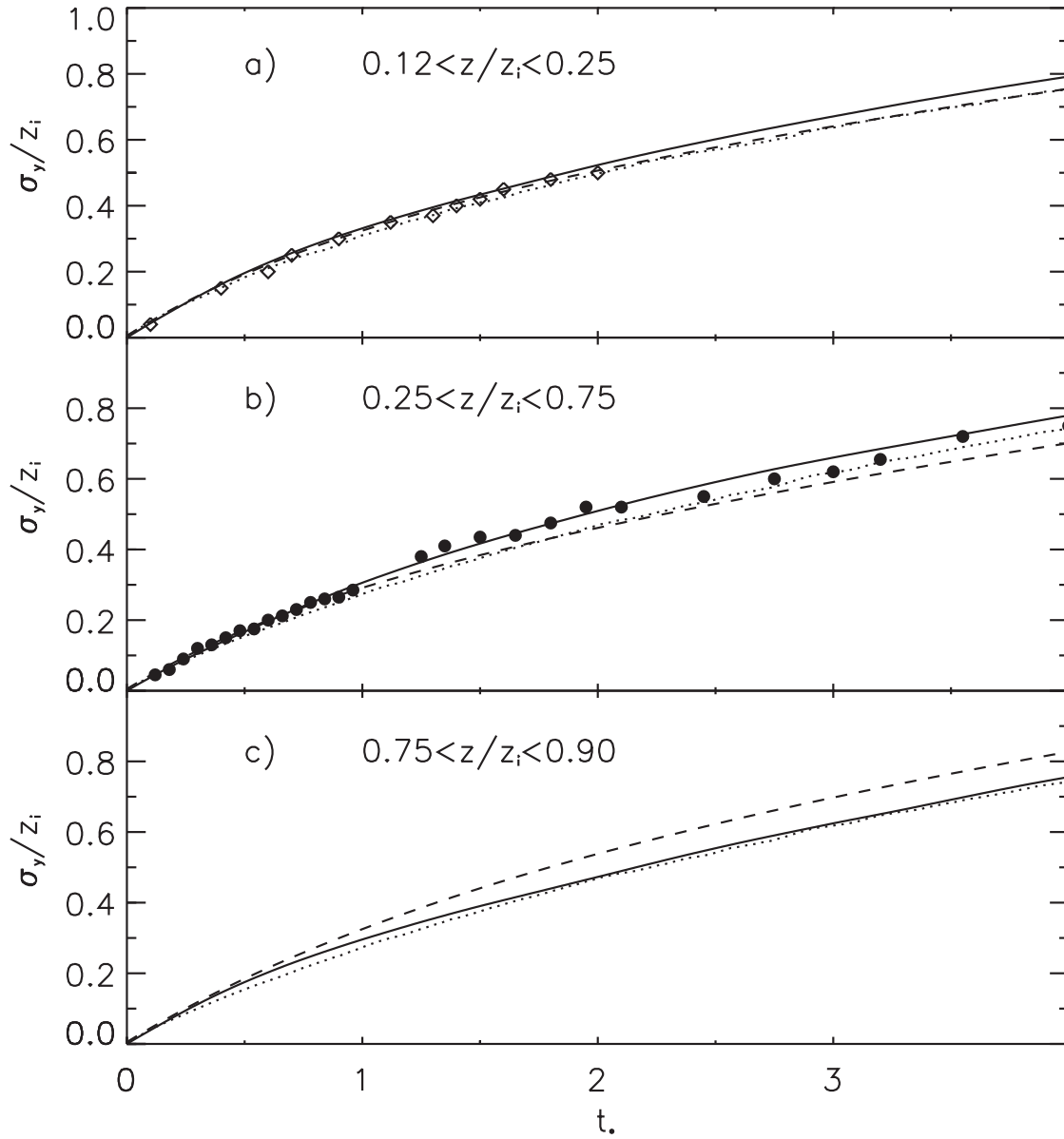


Figure 3.12: Normalized horizontal dispersion parameters as a function of the dimensionless time t_* . The continuous lines are the Eulerian displacements $\overline{y^2}(t)$ (3.1), the dotted lines are the Eulerian dispersion parameters σ_y , and the dashed line represent Taylor's theory (5.14). a) Horizontal dispersion for particles release below $z/z_i = 0.25$. Data (\diamond) from the numerical experiment by Lamb (1978) are also shown. b) Same as a), but for particles released between $z/z_i = 0.25$ and $z/z_i = 0.75$. The water-tank data (\bullet) from Willis and Deardorff (1981) are also shown. c) Same as a) for particles released above $z/z_i = 0.75$.

3.6. Horizontal and vertical dispersion

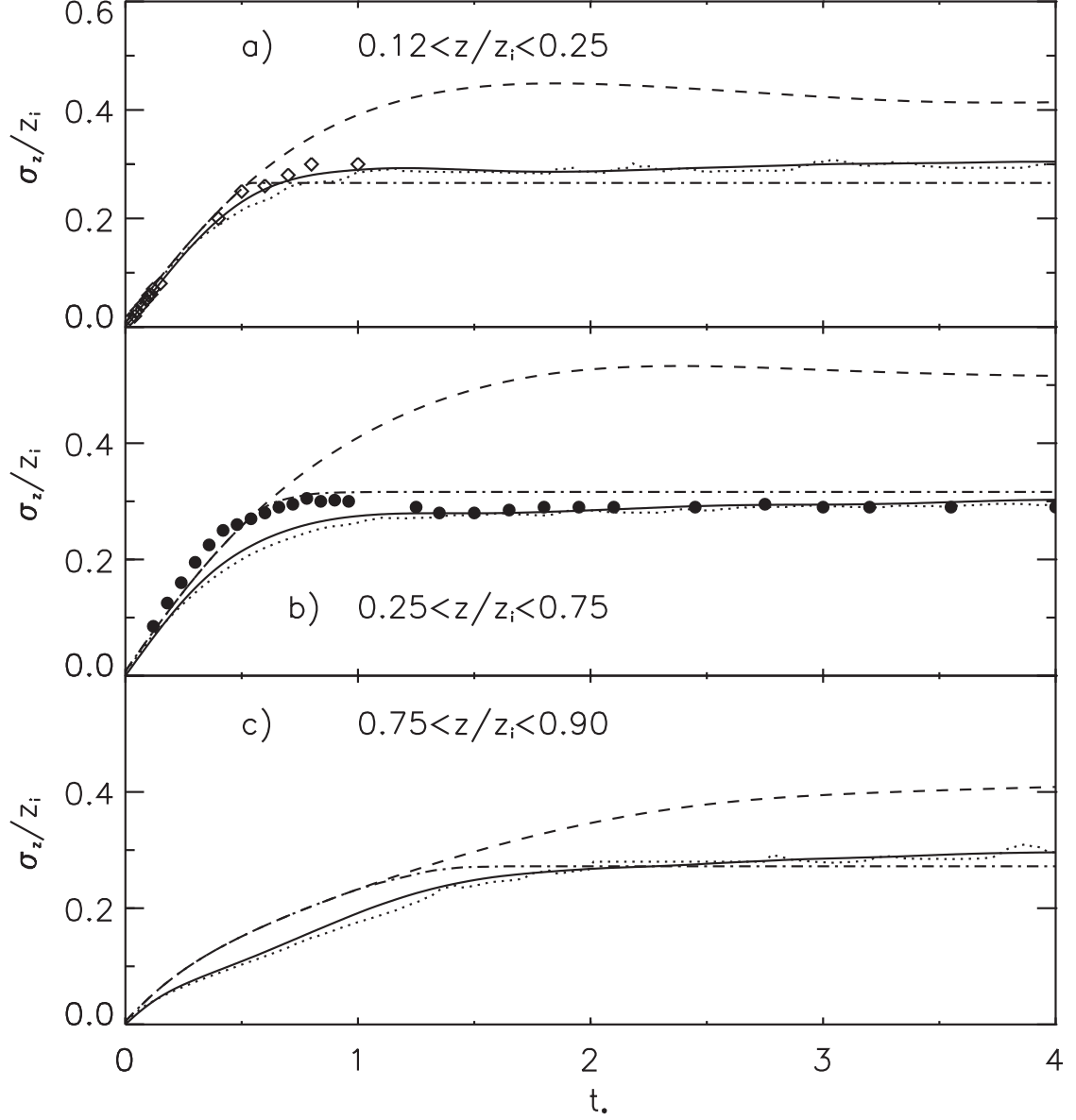


Figure 3.13: Normalized vertical dispersion parameters as function of the dimensionless time t_* . The continuous lines are the Eulerian displacements $\overline{z'^2}(t)$ (3.1), the dotted lines are the Eulerian dispersion parameters σ_z , and the dashed line represent Taylor's theory (3.2). a) Vertical dispersion parameters for particles release below $z/z_i = 0.25$. The dashed-dotted line represent expression (3.2) calculated using the function $T_L'(t)$. Data (\diamond) from the numerical experiment by Lamb (1978) are also shown. b) Same as a), but for particles released between $z/z_i = 0.25$ and $z/z_i = 0.75$. The water-tank data (\bullet) from Willis and Deardorff (1981) are also shown. c) Same as b), but for particles released above $z/z_i = 0.75$.

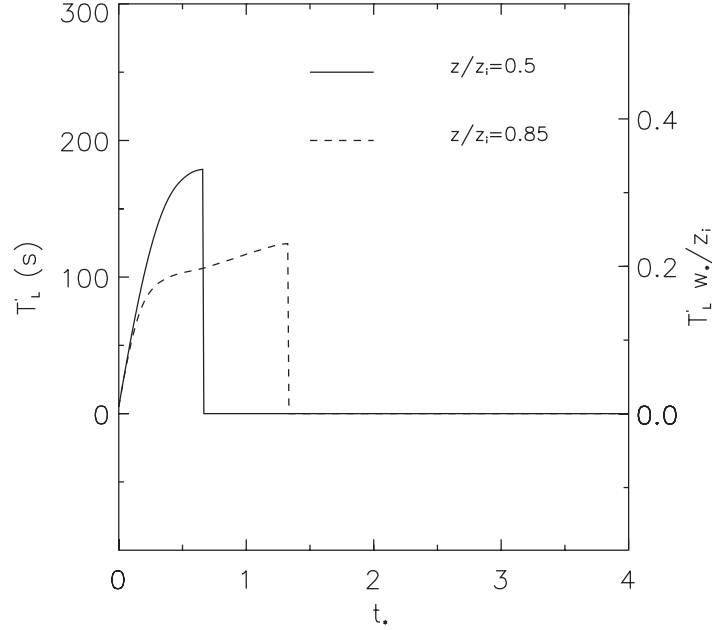


Figure 3.14: Time scale $T_L'(t)$ (equation 3.21) for particles released at $z/z_i = 0.5$ (continuous line) and $z/z_i = 0.85$ (dashed line).

to $T_w^L = \lim_{t \rightarrow \infty} T_w^L(t) \simeq 0$ (see Figure 3.11b). As a result, equation (3.2) becomes

$$\overline{x_j'^2(t)} \sim \int_0^t \int_0^{t'} R_w^L(\tau) d\tau dt' = \int_0^t T_w^L(t') dt' = \text{const} \quad (3.20)$$

As mentioned earlier, Taylor's diffusion theory was developed for homogeneous turbulence, whereas the CBL is characterized by vertically inhomogeneous turbulence. Moreover, the vertical motion is bounded by the CBL boundaries and in strongly convective conditions the particles are transported in a wave-like motion as shown in Figure 3.8. Therefore we consider it more appropriate to make a distinction between free and bounded motion, as discussed later.

Particles released above $z/z_i = 0.75$

The displacement of particles released above $z/z_i = 0.75$ is strongly affected by the turbulent structure in the upper part of the CBL. As discussed previously, the turbulence structure near the top of the CBL is different than in the lower layers, due to the strong capping inversion, and vertical motion is converted into horizontal. As a result, at short times, when the particles have not reached yet the middle of the CBL, the vertical displacement is diminished. At longer times ($t_* > 3$) the particles are well mixed within the entire CBL and the displacement (3.1) reaches the constant limit of about 0.3 as explained earlier. However, also in this case, equation (3.2) overestimates this limit at longer times (Figure 3.13c).

Distinction between free and bounded motion

A more adequate interpretation of the LES results with respect to expression (3.2) is obtained if the two regimes (free motion and bounded motion) are considered separately, in other words, when a distinction is made between shorter and longer times after the release.

As previously shown, the period of time in which the particles are in a regime of free motion (before being affected by the CBL boundaries) is of the same order of magnitude as the turnover time. If t_0 is the time at which the function $T_w^L(t)$ reaches its maximum value, then $T_w^L(t_0) = T_w^L$ according to (3.11). A new time scale is defined as:

$$\begin{cases} T_L'(t) = T_w^L(t) & t \leq t_0 \\ T_L'(t) = 0 & t > t_0 \end{cases} \quad (3.21)$$

The function $T_L'(t)$ is shown in Figure 3.14 for particles released at $z/z_i = 0.5$ and $z/z_i = 0.85$. This function is consistent with the two limits (for shorter and longer times) that the function $T_w^L(t)$ must fulfill.

If we now recalculate (3.2) using the new function $T_L'(t)$, the result agrees more satisfactorily with the experiments and the particle displacement $\overline{z'^2}$, as shown in Figure 3.13.

3.7 Relationship between Eulerian and Lagrangian frameworks

In this Section, we derive relationships between the Lagrangian and Eulerian frameworks from the LES results for the autocorrelation functions and spectra.

3.7.1 Integral Lagrangian time scale

Figures 3.15a and 3.15c show the vertical profiles of time scales T_j^L calculated from the autocorrelation functions according to (3.11). Both the horizontal and the vertical Lagrangian time scales are almost constant with height for $z/z_i < 0.7$. The vertically averaged values below $z/z_i < 0.7$ are $T_v^L = 220$ s and $T_w^L = 180$ s respectively. As explained earlier, the Lagrangian time scale can also be calculated directly from the spectra, using an expression similar to (??). By using this method, averaged values of $T_v^L = 235$ s and $T_w^L = 210$ s are found, which shows that the two ways of determining T_j^L are equivalent. However, the determination of the integral time by the spectral technique leads to greater uncertainties due to the difficulty to locate precisely the spectral peak.

Our results are in agreement with the measurements by *Phillips and Panofsky* (1982) ($T_v^L \sim 190$ s). Other previous experimental studies show a large uncertainty in the value of the Lagrangian time. For instance, atmospheric measurements range from 70 – 80s (*Hanna*, 1981) to 10^4 s (*Gifford*, 1982). The numerical studies by *Wang et al.* (1995) and by *Uliasz and Sorbjan* (1999) do not provide a direct value of the calculated integral time scale. As pointed out by *Hanna* (1981), atmospheric measurements are influenced by the complexity of the experimental setup and the short sampling time. Moreover, the results depend on different meteorological conditions during

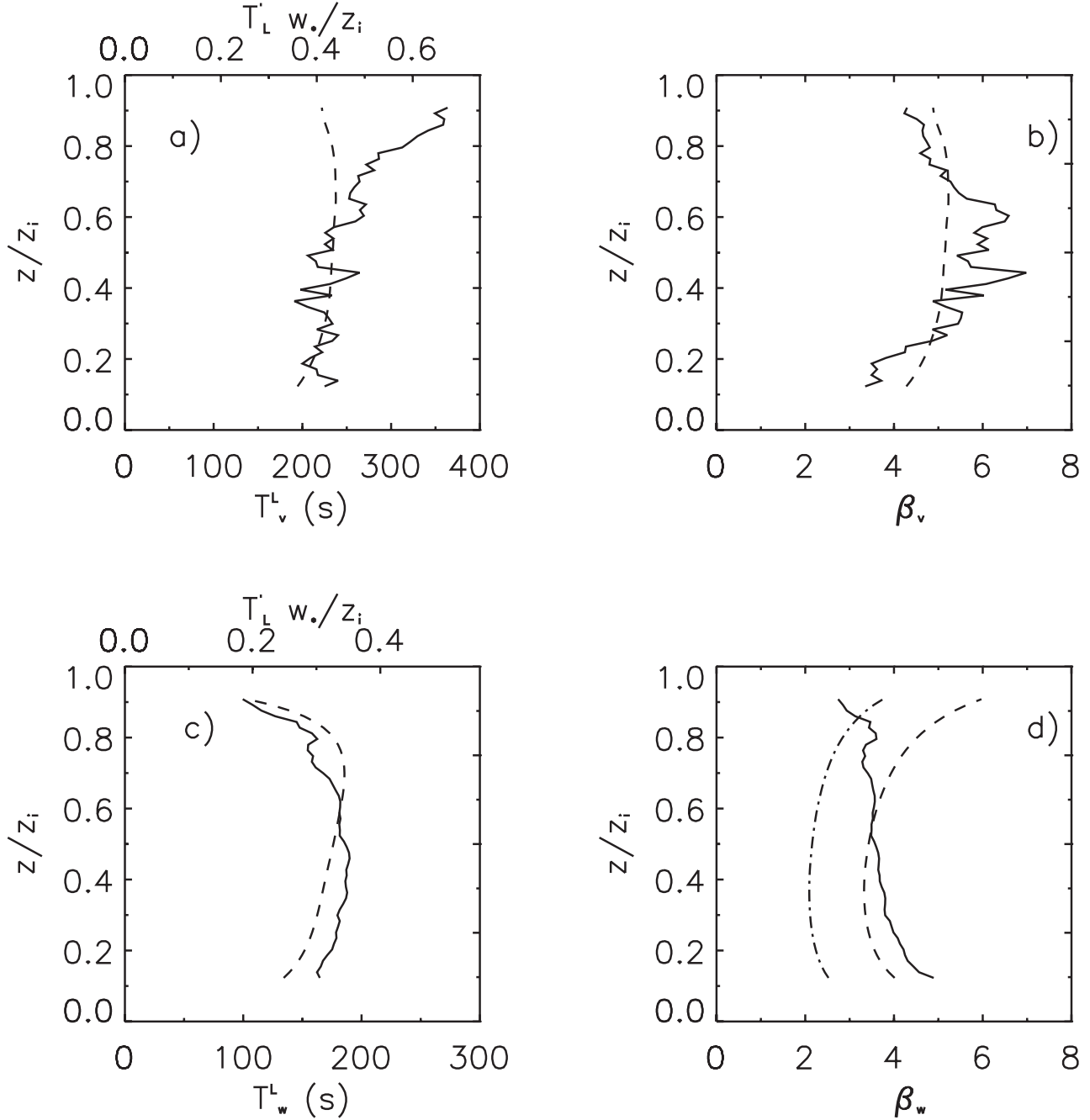


Figure 3.15: a) Vertical profiles of horizontal Lagrangian time scale as calculated by LES (continuous line) and parameterized according to (3.23) (dashed line). b) Ratio between the horizontal Lagrangian and Eulerian time scales as calculated by LES (continuous line) and parameterized according to (3.25) (dashed line). c) Same as a), but for the vertical wind component. d) Same as b), but for the vertical wind component.

3.7. Relationship between Eulerian and Lagrangian frameworks

the measurement campaign. The LES results, on the contrary, are obtained from a more controlled experiment and from a longer time series of data.

The value of the Lagrangian time scale is commonly parameterized as a function of CBL Eulerian characteristics (*Angell, 1964*). In particular, T_j^L is related to the wavelength of the spectral peak Λ_j according to (*Degrazia et al., 1998*)

$$T_j^L = \frac{\sqrt{\pi} \Lambda_j}{16 \sigma_j}. \quad (3.22)$$

By substituting in (3.22) the values of Λ_j calculated by the LES (expressions 3.12 and 3.13) the following relationships are found:

$$T_v^L = 0.17 \frac{z_i}{\sigma_v} \quad (3.23)$$

$$T_w^L = 0.2 \frac{z_i}{\sigma_w} [1 - \exp(-8z/z_i) - 0.0003 \exp(8.5z/z_i)]. \quad (3.24)$$

As shown by *Degrazia et al. (1998)*, equations (3.23) and (3.24) agree with the atmospheric measurements by *Hanna (1981)* in the middle of the CBL. In Figures 3.15a and 3.15c expressions (3.23) and (3.24) are compared with the LES results. Both parameterizations are able to reproduce the LES results correctly for heights below $z/z_i = 0.7$.

Above $z/z_i = 0.7$ the LES results show an increase of T_v^L with height (Figure 3.15a). This is consistent with the calculation of the integral time scale from the spectral peak, which shows an averaged (above $z/z_i = 0.7$) value of $T_v^L = 260$ s. As discussed in Section 4a, the value of the wavelength Λ_j calculated by the LES is $\Lambda_{u,v} = 1.8z_i$ at $z/z_i = 0.9$ and $\Lambda_{u,v} = 1.9z_i$ at $z/z_i = 1$. If these values are used in (3.22), a better agreement is found between the LES results and the parameterization.

3.7.2 Value of the ratio β_j

Figures 3.15b and 3.15d show the ratio β_j of the Lagrangian to Eulerian time scales for the horizontal and vertical wind components. For the horizontal wind component, β_v varies between 4 and 6, with a vertically averaged value of $\beta_v = 5$. The irregular vertical profile of β_v is due to fluctuations in the autocorrelation function (Figure 3.10a). For the vertical wind component, the values of β_w calculated by the LES has a vertically averaged value of 4. Values in literature range from 1.8 (*Hanna, 1981*) to 4 (*Angell, 1964*).

The value of β_j is usually related to the intensity of turbulence $i = \sigma_j/U$ by (3.9), as explained previously. In Figure 3.15b the following parameterization proposed by *Hanna (1981)* is also shown:

$$\beta_j = C \frac{U}{\sigma_j} = 0.7 \frac{U}{\sigma_j}. \quad (3.25)$$

As it can be seen, despite the fluctuations, the parameterization is in satisfactory agreement with the LES results.

As shown in Figure 3.15d, the parameterization (3.25) for the vertical component agrees with the LES results only for $z/z_i < 0.7$. Other values of the constant C range in the literature from 0.35 to 0.8 as reported by *Pasquill* (1974). Theoretical analysis by *Wandel and Kofoed-Hansen* (1962) leads to $C = 0.44$ whereas the numerical simulation by *Wang et al.* (1995) gives a value of $C = 0.6$. To illustrate the dependence of the parameterization on the value of the constant C , expression (3.25) is shown in Figure 3.15d for two values of the constant, respectively $C = 0.4$ and $C = 0.7$. As stated by *Hanna* (1981) the value $C = 0.7$ gives the best fit for the overall dataset, whereas the value $C = 0.4$ fits the experimental data for high wind speed better, and it is in better agreement with the LES results for $z/z_i > 0.7$.

3.8 Conclusions

Eulerian and Lagrangian statistics were calculated by means of a LES. A large numerical domain and a long integration time were used in order to obtain reliable statistics both in space and in time. The flow characteristics were studied by analyzing the energy spectra and velocity autocorrelations in both the Eulerian and Lagrangian frameworks.

Three main research issues were studied. First, Eulerian statistics were calculated by means of spatial and temporal analysis. The two frameworks are related by Taylor's hypothesis of frozen turbulence. Characteristic length and temporal scales were derived by means of two different methods, namely through the analysis of the autocorrelation function and the spectral peak, allowing a direct validation of Taylor's hypothesis, the results of which were satisfied in the simulated CBL.

Second, the relationship between flow properties (autocorrelations) and dispersion characteristics (particles' displacements) was discussed through Taylor's analysis of turbulent dispersion. Results showed that for the horizontal velocity, the autocorrelation had an exponential shape, characteristic of a stochastic motion. As a result, horizontal dispersion was satisfactorily described by Taylor's diffusion theory. On the contrary, the autocorrelation function for the vertical velocity had a more complicated shape, due to the vertical inhomogeneity of the turbulent flow. Moreover, the particle vertical motion is confined between the CBL boundaries. As a result, particles move following a wave-like motion and the value of the integral scale was zero. Taylor's analysis correctly predicted the particles' displacement at short times, but overestimated the asymptotic limit at longer times.

The use of a different method to calculate the Lagrangian integral time (3.11), allowed us to distinguish better between free and bounded motion, and a better agreement between Taylor's relationship and particle vertical displacement was found.

This study was completed by verifying the equivalence between Lagrangian particles' displacement $\overline{x_j'^2}$ and the Eulerian dispersion parameter $\sigma_{x_j}^2$. The comparison showed that, for practical purposes, using Eulerian dispersion parameters instead of the Lagrangian one does not lead to large errors. This is related to the fact that Taylor's hypothesis of frozen turbulence holds in the simulated CBL.

Finally, the relationship between Lagrangian and Eulerian framework was investigated through the calculation of the Lagrangian integral scales and the ratio β . Vertical profile of T_j^L showed that the integral scales remain constant at heights $z/z_i = 0.7$. The difference in the turbulence characteristics near to the inversion, influenced the particles' motion, which is transformed from vertical into

3.8. Conclusions

horizontal. This affected the values of the integral scales in the upper layers of the CBL, where the horizontal time scale increased, whereas the vertical time scale was reduced. Currently used parameterizations for the ratio β , derived either in previous field atmospheric experiments or through theoretical analysis, were compared with the LES results, showing a satisfactory agreement. The present study indicates the need of further investigation on the values of time and length scales near the inversion zone ($z/z_i > 0.7$) of the CBL, and their implication on atmospheric dispersion.

3.9 APPENDIX A: Definition of statistics

3.9.1 Eulerian statistics

Time series of Eulerian velocities u_t are measured at different fixed positions (1024 points uniformly horizontally distributed for each vertical layer). The Eulerian autocorrelation function is calculated according to (Daoud *et al.*, 2002)

$$R^E(\tau) = \frac{\sum_{t=1}^{N-j} [(u_t - \bar{u}_t)(u_{t+j} - \bar{u}_{t+j})]}{\left[\sum_{t=1}^{N-j} (u_t - \bar{u}_t)^2 \right]^{1/2} \left[\sum_{t=1}^{N-j} (u_{t+j} - \bar{u}_{t+j})^2 \right]^{1/2}}, \quad (3.26)$$

where $\tau = j\Delta t$ is the time lag, and N is the number of time steps Δt . The mean velocities are defined according to

$$\bar{u}_t = \frac{\sum_{t'=1}^{N-j} u_{t'}}{N-j} \quad (3.27)$$

$$\bar{u}_{t+j} = \frac{\sum_{t'=1}^{N-j} u_{t'+j}}{N-j} = \frac{\sum_{t'=j+1}^N u_{t'}}{N-j}. \quad (3.28)$$

The autocorrelation is then spatially averaged over all the fixed measurement positions. Spatial autocorrelation is calculated from the velocities u_i measured at different positions along the wind direction (recorded every 10 minutes) as follows:

$$R^E(r) = \frac{\sum_{i=1}^{N-j} [(u_i - \bar{u}_i)(u_{i+j} - \bar{u}_{i+j})]}{\left[\sum_{i=1}^{N-j} (u_i - \bar{u}_i)^2 \right]^{1/2} \left[\sum_{i=1}^{N-j} (u_{i+j} - \bar{u}_{i+j})^2 \right]^{1/2}}, \quad (3.29)$$

where $r = j\Delta x$ is the space lag and Δx is the grid size. Autocorrelations calculated according to (3.29) have been subsequently averaged over all the parallel lines and over time.

3.9.2 Lagrangian statistics

In the Lagrangian framework, the autocorrelation function is calculated using the particle velocities $u^i(t)$ derived according to (3.10). At each time $t_0 + \tau$ (where t_0 is the release time and τ is the time lag) the Lagrangian autocorrelation $R^L(\tau)$ is calculated following Wang *et al.* (1995) as

$$R^L(\tau) = \frac{\langle [u^i(t_0) - \langle u^i(t_0) \rangle] [u^i(t_0 + \tau) - \langle u^i(t_0 + \tau) \rangle] \rangle}{\langle [u^i(t_0) - \langle u^i(t_0) \rangle]^2 \rangle^{1/2} \langle [u^i(t_0 + \tau) - \langle u^i(t_0 + \tau) \rangle]^2 \rangle^{1/2}} \quad (3.30)$$

where the average (indicated by $\langle \rangle$) is made over all the particles released at the same height.

Chapter 4

Statistics of absolute and relative dispersion in the Atmospheric Convective Boundary Layer

4.1 Introduction

To understand and predict the dispersion of compounds in the Atmospheric Boundary Layer, it is very important to determine with great accuracy concentration statistics such as mean, variance and skewness.

In fact, the variance of the plume distribution is a direct measure of the plume spread (dispersion parameter), whereas concentration fluctuations quantify the variability of the compound distribution. Concentration fluctuations are a consequence of the turbulent mixing that generates complex and inhomogeneous distribution of the compound within the plume, and they can be of the same order of the mean concentration, even at large distances from the emission source (*Fackrell and Robins*, 1982; *Deardorff and Willis*, 1984; *Sykes and Henn*, 1992).

Third-order moments such as the skewness of the plume position, provide information on the structure and the shape of the plume, and quantify the asymmetry of the concentration distribution with respect to its mean position. In the Convective Boundary Layer (CBL), the main responsible of this asymmetric concentration distribution is the inhomogeneous and non-Gaussian large-scale turbulent motion. Moreover, a further contribution to the skewness of the plume shape is given by the reflection of the plume at the CBL boundaries, which tends to accumulate the scalar near the surface and in the entrainment zone at the top of the CBL.

Briefly, turbulence in the CBL is characterized by eddies with a large range of temporal and spatial scales, from the Kolmogorov scale (10^{-4} m) to the entire depth of the CBL (10^3 m). By relating the length scale l of the turbulent eddies to a characteristic length scale of the plume σ_r (the plume width in a coordinate system relative to the centerline instantaneous position), *Yee and Wilson* (2000) proposed three regimes that characterize the growth and structure of the plume. If $\sigma_r \ll l$, typically close to the source, the larger eddies cause the plume *meandering*, which is the large-

The content of this Chapter has been submitted for publication on *Journal of atmospheric Sciences* with J. Vilà-Guerau de Arellano as co-author

scale motion of the plume as a whole and the sweeping of the plume centerline. This large-scale motion is highly inhomogeneous and characterized by a vertical velocity that is positively skewed. In addition, the vertical motion is constrained by a rigid surface at the ground and a more permeable one (depending on the inversion strength) at the entrainment zone, at the top of the CBL.

When $\sigma_r \sim l$, the scalar concentration is affected by the increasing entrainment of air into the body of the plume. This process is known as *relative diffusion* and it is the main responsible for the growth of the instantaneous plume width.

Finally, when $\sigma_r \geq l$ the turbulent eddies are mainly responsible of the internal (in-plume) mixing of contaminant. This internal mixing is quantified by the relative concentration fluctuation intensity i_{cr} (defined as the ratio of the standard deviation to the mean concentration in relative coordinates), which is the main contribution to the production of concentration fluctuation at large distances from the source, where the meandering component becomes small.

To distinguish and quantify the different contributions of large-scale (meandering) and small-scale motion (relative diffusion) on the evolution of a dispersing plume, it is useful to calculate second- and third-order moments in two different coordinate systems. By analyzing dispersion in *absolute* framework, which is the coordinate system defined relative to a fixed point (e.g. the source location), the statistical properties of the scalar concentration are influenced by the full spectrum of turbulent eddies. As a result, the (square of the) plume spread σ is the sum of the meandering and the relative diffusion. In the *relative* framework, the coordinate system moves with the instantaneous plume centerline position. In this framework, therefore, the (vertically) inhomogeneous meandering motion is removed, and consequently the concentration statistics are only dependent on the small turbulent eddies ($l \ll \sigma_r$), which are homogeneous and isotropic.

Although there is not a clear physical separation between "large" and "small" scales, the meandering component and the relative diffusion were assumed to be statistically independent in the pioneer study by Gifford (1959), who developed an analytical model for the calculation of higher-order concentration statistics as a function of two independent terms: the Probability Distribution Function (PDF) of the plume centerline position and the PDF of the concentration in relative coordinates.

Gifford's analysis provided the basis for later studies (Yee *et al.*, 1994; Yee and Wilson, 2000; Luhar *et al.*, 2000; Reynolds, 2000; Franzese, 2003), which incorporated in-plume fluctuations (that were neglected in Gifford's model) by specifying the PDF of the relative concentration, and took into account the inhomogeneous and skewed turbulence structure of the CBL by calculating the position of the plume centerline from one-particle Lagrangian model trajectories. In all these studies, the intensity of relative concentration fluctuations is the key variable for the determination of the relative concentration PDF, but neither observational nor numerical data in the atmospheric CBL is currently available for an appropriate estimation of i_{cr} .

Measurements of dispersion statistics (PDFs) in absolute and relative frameworks have been recently discussed by Munro *et al.* (2003a) and Munro *et al.* (2003b) who analyzed seven different datasets of Lidar measurements. Unfortunately, measurements were only available in the horizontal (crosswind) direction at a fixed height. As a result, the vertical non-Gaussian inhomogeneous structure of the plume could not be analyzed. Moreover, the plume centerline could have been wrongly estimated, in particular under convective conditions, when the instantaneous plume centerline was above the line of sight of the Lidar.

4.2. Theoretical background

In the study by *Ott and Jørgensen* (2001) a Lidar was used to obtain vertical cross sections of a dispersing plume at 100 m from the source. Mean and variances of absolute and relative concentrations were calculated, but only vertically and horizontally averaged results were presented.

In our study, a Large-Eddy Simulation (hereafter LES) is used to analyze the dispersion of a passive scalar in absolute and relative coordinate systems. More explicitly, we first calculate the mean concentration, concentration fluctuations, dispersion parameters and skewness of the vertical position in both reference coordinate systems. To the best of our knowledge, this is the first time that a complete three dimensional field of concentration statistics of a dispersing plume is analyzed in both frameworks in the atmospheric CBL.

Second, we calculate the PDF of the plume centerline and the PDF of the relative concentration. These results are further analyzed and related in terms of the skewness of the centerline position and the intensity of relative concentration fluctuation, which are critical variables in the formulation of operational models. Third, following Gifford's analysis and by using the estimated PDFs, we derive concentration statistics that are finally compared with the ones directly calculated by the LES.

The Chapter is structured as follows: the theoretical background is exposed in Section 4.2. In Section 4.3 the numerical model and the experimental setup are described. The results are presented and discussed in Section 4.4. Finally, conclusions and remarks are discussed in Section 4.5.

4.2 Theoretical background

Let $c = c(x, y, z, t)$ be the instantaneous concentration of a scalar at the downwind position x from the source. By definition, the $n - th$ moment of concentration in a fixed (absolute) reference frame reads:

$$\overline{c^n}(x, y, z) \equiv \int_0^\infty c^n p_c(c|x, y, z) dc, \quad (4.1)$$

where p_c is the concentration PDF.

At each time t and any downwind distance x , let (y_m, z_m) be the position of the plume centerline. It is now possible to define the system of coordinates relative to the instantaneous plume centerline position as:

$$\begin{cases} y_r = y_r(y_m) = y - y_m \\ z_r = z_r(z_m) = z - z_m. \end{cases} \quad (4.2)$$

Consequently, for each downwind position x , the concentration field relative to the plume centerline coordinate system is defined as:

$$c_r(x, y_r, z_r, t) = c(x, y_m + y_r, z_m + z_r, t). \quad (4.3)$$

Similarly to Equation (4.1), the $n - th$ moment of the relative concentration can be calculated as:

$$\overline{c_r^n}(x, y_r, z_r) \equiv \int_0^\infty c_r^n p_{cr}(c|x, y_r, z_r) dc, \quad (4.4)$$

where p_{cr} is the PDF of the concentration in the reference frame of the plume centroid. Assuming that the meandering and relative diffusion contributions are statistically independent, Gifford (1959) related the absolute concentration PDF to the relative concentration PDF by:

$$p_c(c|x, y, z) \equiv \int \int p_{cr}(c|x, y_r, z_r) p_m(x, y_m, z_m) dy_m dz_m, \quad (4.5)$$

where p_m is the PDF of the instantaneous plume centroid position. By substituting Equations (4.5) and (4.4) into (4.1) we obtain:

$$\bar{c}^n(x, y, z) = \int \int \bar{c}_r^n(x, y_r, z_r) p_m(x, y_m, z_m) dy_m dz_m, \quad (4.6)$$

which relates the absolute and the relative concentration statistics.

By simulating the plume dispersion with a LES, in this paper we investigate the validity of Equation (4.6). In particular, we calculate and discuss the PDFs of both the plume centerline (p_m) and the relative concentration (p_{cr}). These results are first used to test the validity of current parameterizations for p_m and p_{cr} . These PDFs are subsequently used to derive higher-order moments by calculating the r.h.s of Equation (4.6). These results are finally compared with the statistics directly calculated by the concentration fields (l.h.s of Equation 4.6).

4.3 Numerical Setup

4.3.1 Model description

The LES code used here is the parallelized version of the one described by Cuijpers and Duynkerke (1993) and Siebesma and Cuijpers (1995), in which a set of filtered prognostic equations for the dynamic variables (wind velocity, potential temperature, turbulent kinetic energy) is solved on a staggered numerical grid. The space and time integrations are computed with a Kappa (Vreugdenhil and Koren, 1993) and leap-frog numerical schemes respectively.

The subgrid fluxes are closed by relating them to the gradient of the solved variable by means of an exchange coefficient, which depended on the subgrid turbulent kinetic energy, and a length scale, which is related to the grid size.

A conservation equation for the passive tracer is added to the governing set of equations. It reads

$$\frac{\partial \bar{c}}{\partial t} = -\bar{u}_i \frac{\partial \bar{c}}{\partial x_i} - \frac{\partial \overline{u'_i c'}}{\partial x_i}, \quad (4.7)$$

where \bar{c} is the mean (filtered) scalar concentration, \bar{u}_i is the mean wind and $\overline{u'_i c'}$ is the subgrid flux. The horizontal numerical domain covers an area of $5.120 \times 5.120 \text{ km}^2$. In order to be able to solve the small scales of motion a very fine grid is used, with a resolution of 10 m in all the directions (512 grid points in each horizontal direction and 128 in the vertical).

The aspect ratio, that is, the ratio between the horizontal domain dimension to the CBL height z_i , is around 6.6 (with $z_i \sim 780 \text{ m}$). Lateral periodic boundary conditions are imposed for all the variables. However, as soon as the scalar reaches the lateral boundaries the simulation is ended, as the plume statistics become meaningless. A time step of 0.25 s is used.

4.3. Numerical Setup

4.3.2 Flow characteristics

At the top of the CBL, an inversion strength of $\Delta\theta = 5$ K is imposed, A geostrophic wind of 2 m/s aligned in the x -direction and a heat flux of 0.1 K.m/s are prescribed as constant forcing (lateral and surface boundary conditions). The simulation is run for an initialization period of 2 hours (i.e. the period of CBL development needed to ensure that a (quasi)stationary state is reached). After this period, the gradients of the mean variables are independent on time and the turbulent kinetic energy has become constant. The average values of the convective velocity scale w_* is 1.38 m/s and the shear/buoyancy ratio u_*/w_* is equal to 0.14 (where u_* is the friction velocity). The value of the stability parameter $-z_i/L$ is ~ 136 . According to the classification used in *Holtslag and Nieuwstadt* (1986) this simulated flow is mainly driven by convective turbulence.

4.3.3 Plume concentration calculation

After the initialization period, an instantaneous line source (ILS) of scalar (non-buoyant tracer) is emitted along the x axis at $z_s/z_i = 0.28$. The line source measures one grid spacing both in the vertical and in the horizontal (y) direction. The line source can be equivalently interpreted in terms of a continuous point source (CPS), by using the relationship $t = x/\bar{u}$ as explained by *Willis and Deardorff* (1981) and *Nieuwstadt and de Valk* (1987). As the numerical grid moves with the mean wind along the x direction, this relationship transforms the numerical x coordinate in the physical elapsed time after the release of the scalar. The line source after a certain time t is therefore equivalent to the time evolution of the concentration pattern of a scalar released from a CPS at a certain distance $x = \bar{u}t$.

In order to obtain statistically sound results, nine different realizations are performed, in which the horizontal position of the instantaneous release is changed. The results are subsequently ensemble-averaged over the different realizations.

4.3.4 Definition of statistical parameters

Figure 4.1 shows a vertical cross section of an idealized instantaneous line source $c(x, z)$ at a certain time t after the release. As explained in the previous Section, the spatial coordinate x is equivalent to the physical time t due to the equivalence between ILS and CPS. As a result, all the statistics can be interpreted as a function of the downwind distance $x = \bar{u}t$.

Let z be the instantaneous (vertical) position of a particle in the plume. The instantaneous centerline position z_m and the mean plume height \bar{z} are defined as follows:

$$z_m = \frac{\int z c dy dz}{\int c dy dz} \quad \text{and} \quad (4.8)$$

$$\bar{z} = \frac{\int z c dV}{\int c dV}, \quad (4.9)$$

where $dV = dx dy dz$.

From these mean quantities, the fluctuation of the absolute (z'), relative (z'_r) and centerline (z'_m)

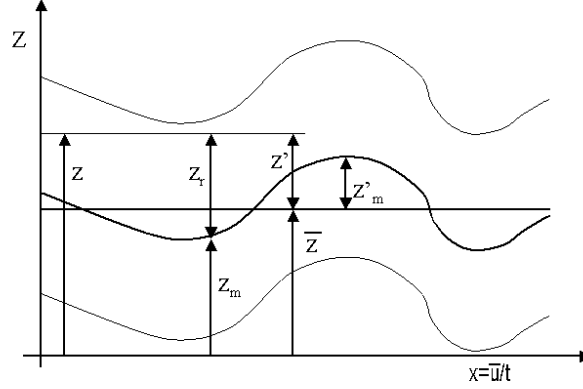


Figure 4.1: Idealized instantaneous line source dispersing in the simulated CBL. The spatial coordinate x is equivalent to the physical time $t = \bar{u}/x$ for the equivalence between ILS and CPS. In the figure, the vertical position z , the mean plume height \bar{z} and the instantaneous plume centerline position z_m are shown together with their respective instantaneous fluctuations (z' and z'_m). Note that $z'_r = z_r$. The relative coordinate system is defined with respect to the instantaneous plume centerline position z_m .

positions are calculated as follows:

$$z' = z - \bar{z} \quad (4.10)$$

$$z'_r = z - z_m = z_r \quad (4.11)$$

$$z'_m = z_m - \bar{z}. \quad (4.12)$$

The absolute vertical dispersion parameters σ_z is defined according to *Nieuwstadt* (1992) as follows:

$$\sigma_z^2 = \frac{\int c z'^2 dV}{\int c dV}. \quad (4.13)$$

The absolute dispersion σ_z is decomposed into meandering (σ_{zm}) and relative dispersion (σ_{zr}) according to:

$$\sigma_z^2 = \sigma_{zm}^2 + \sigma_{zr}^2, \quad (4.14)$$

where:

$$\sigma_{zm}^2 = \frac{\int z_m'^2 c dV}{\int c dV} \quad \text{and} \quad (4.15)$$

4.4. Results and discussion

$$\sigma_{zr}^2 = \frac{\int z_r^2 c dV}{\int c dV}. \quad (4.16)$$

Similarly, the third-order moments of the vertical position are defined as:

$$\overline{z'^3} = \frac{\int z'^3 c dV}{\int c dV} \quad (4.17)$$

$$\overline{z'_m{}^3} = \frac{\int z'_m{}^3 c dV}{\int c dV} \quad (4.18)$$

$$\overline{z'_r{}^3}(t) = \frac{\int z'_r{}^3 c dV}{\int c dV}. \quad (4.19)$$

Similar expressions to (4.8-4.19) hold for the horizontal position y .

The absolute and relative concentration fluctuations are derived using:

$$\sigma_c^2(t, y, z) = \frac{\int (c - \bar{c})^2 dx}{L_x} \quad \text{and} \quad (4.20)$$

$$\sigma_{c_r}^2(t, y_r, z_r) = \frac{\int (c_r - \bar{c}_r)^2 dx}{L_x}, \quad (4.21)$$

where $t = x/\bar{u}$, L_x is the domain size, and \bar{c} is

$$\bar{c}(y, z, t) = \frac{\int c dx}{L_x}. \quad (4.22)$$

A similar expression holds for \bar{c}_r .

From the instantaneous centerline position, the PDF p_{ym} and p_{zm} are derived as:

$$p_{ym}(t, y'_m) dy'_m = \text{prob}\{y'_m < y_m(x, t) < y'_m + dy'_m\} \quad (4.23)$$

$$p_{zm}(t, z'_m) dz'_m = \text{prob}\{z'_m < z_m(x, t) < z'_m + dz'_m\}, \quad (4.24)$$

where the horizontal and vertical increments (dy'_m and dz'_m) are defined by the numerical grid size (10 m).

4.4 Results and discussion

4.4.1 Dispersion in absolute coordinate system

The plume statistics (first-, second- and third-order moments) in the absolute coordinate system are now discussed. As explained earlier, the statistical properties of the scalar concentration in the absolute coordinates system are influenced by both meandering and relative diffusion.

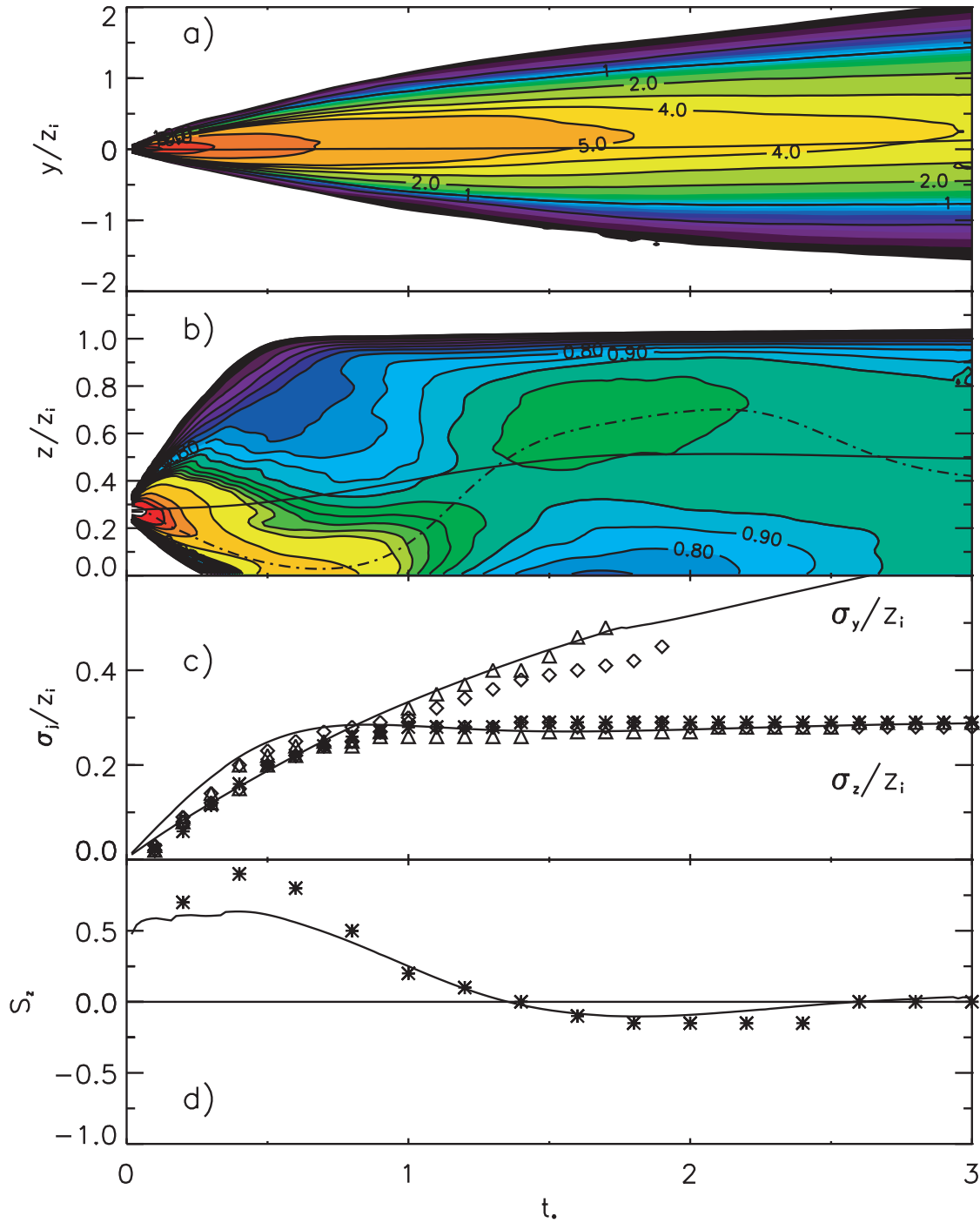


Figure 4.2: a) Normalized vertically-integrated mean concentration as a function of the dimensionless time t_* . b) Normalized cross-integrated mean concentration. In the picture, the normalized mean plume height \bar{z}/z_i (continuous line) and the position of the maximum concentration (dashed line) are also shown. c) Normalized horizontal (σ_y) and vertical (σ_z) dispersion parameters. The following experimental and numerical data are also shown: Willis and Deardorff (1978) (\triangle); Hibberd (2000) (*); Nieuwstadt (1992) (\diamond). d) Skewness of the vertical plume position $S_z = \bar{z}'^3 / \sigma_z^3$. In the picture, the data by Luhar et al. (2000) are also shown (*).

4.4. Results and discussion

Mean concentration, variance and skewness

Figures 4.2a and 4.2b show the vertically-integrated and crosswind-integrated concentrations as a function of the normalized distance t_* , defined as

$$t_* = \frac{w_*}{z_i} \frac{x}{\bar{u}} = \frac{w_*}{z_i} t. \quad (4.25)$$

Figure 4.2a shows that, in the horizontal plane, the mean concentration has a Gaussian shape. The centerline position, also shown in the picture, moves slightly with time due to the presence of a small wind in the crosswind (y) direction.

The crosswind-integrated concentration is shown in Figure 4.2b, where both the plume mean height position \bar{z} and the position of the maximum concentration are also shown. The value of \bar{z} calculated by the LES overestimates slightly the water-tank results by *Willis and Deardorff* (1978) (not shown), probably because of the small difference in the initial plume position ($z_s/z_i = 0.28$ in our study compared with $z_s/z_i = 0.25$ in *Willis and Deardorff*, 1978). The ground-level maximum occurs at $t_* = 0.65$, in close agreement with the water-tank experiment. The elevated maximum, due to the fast rise of the plume caught by the updrafts, occurs at $t_* = 1.7$, and the correspondent surface minimum is present around $t_* = 1.75$. At larger distances ($t_* \sim 2.6$), the position of the maximum concentration descends below the plume mean position \bar{z} , meaning that the plume is not perfectly well-mixed yet. This result is in agreement with the data by *Willis and Deardorff* (1978) and *Deardorff and Willis* (1982), who stated that the well-mixed condition is achieved only at very large distances from the source ($t_* = 6$).

The total horizontal and vertical dispersion parameters (σ_y and σ_z), are shown in Figure 4.2c, where they are compared with laboratory data (*Willis and Deardorff*, 1978; *Hibberd*, 2000) and other LES results (*Nieuwstadt*, 1992), showing a satisfactory agreement. The vertical dispersion σ_z reaches an asymptotic limit around 0.29 when the plume is vertically confined between the ground and the top of the CBL. The horizontal dispersion parameter, on the contrary, follows closely Taylor's relation of turbulent dispersion, that is, $\sigma_y \propto t$ at short times, and $\sigma_y \propto t^{1/2}$ at longer times.

The skewness of the vertical position is defined as

$$S_z = \frac{\overline{z'^3}}{\sigma_z^3}, \quad (4.26)$$

where $\overline{z'^3}$ is calculated according to equation (4.17). In a flow characterized by the inhomogeneity of the turbulence, the skewness quantifies the asymmetry of the plume with respect to its mean position (first-order moment).

The evolution of S_z is shown in Figure 4.2d. The skewness is positive between $0 < t_* < 1.4$. In fact, since the CBL is characterized by a positively skewed vertical velocity, the plume is more likely to be caught by a downdraft and, consequently, it is transported towards the surface. As a result, the plume is more likely to be below its mean position \bar{z} , as shown by the maximum plume concentration, which is closer to the ground than the plume mean height (Figure 4.2b). Because, by definition, the average of the instantaneous plume position must coincide with \bar{z} , this means that the tail of the PDF of the plume position has to be highly positive. As a consequence, the value of the skewness S_z is positive.

For $1.4 < t_* < 2.6$ the skewness has a negative value. As Figure 4.2b shows, the plume is caught by an updraft, and an elevated maximum is present at distances $1.2 < t_* < 2.2$. It is now more probable that the plume lies above its mean position. The skewness, therefore, must have a negative value. At $t_* = 2.6$ the skewness becomes slightly positive, correspondingly to the descent of the plume maximum concentration. As explained early, only at large distances the plume is well mixed and S_z approaches zero. The evolution of S_z is in very good agreement with the data by *Luhar et al.* (2000), calculated from his Lagrangian particle model.

Concentration fluctuations

Figure 4.3a shows the horizontal cross section of the concentration fluctuation intensity $i_c = \frac{\sigma_c}{\bar{c}}$ near the ground ($z/z_i = 0.007$). Figure 4.3b shows the contour of i_c in the plume mean horizontal position ($y/z_i = 0$). The LES results agree with previous experimental and numerical studies (*Deardorff and Willis*, 1984; *Luhar et al.*, 2000; *Weil et al.*, 2002). As expected, the concentration fluctuation is larger at the edges of the plume, and it has the smallest values near the plume centroid. It is noteworthy that even at relatively large distances ($t_* = 2$) the fluctuation concentration is of the same order as the mean concentration.

The concentration fluctuation intensity along the plume mean horizontal position (\bar{y}) at ground is shown in Figure 4.3c. Our results agree generally with all the previous studies and are in very good agreement with the water-tank experiment by *Weil et al.* (2002). The results show that i_c decreases rapidly with distance from the source, and it reaches an asymptotic limit of about 0.35. However, there is still a large uncertainty on the value of i_c at short distances. The numerical results by *Franzese* (2003) (not reported here) show a minimum at $t_* = 0.4$ and a maximum at $t_* = 1.2$, which are not present in our results. *Franzese* (2003) explained the presence of the maximum as a combination of two different effects: the decay of i_c (in the plume's centerline) with distance from the source, and the growth of i_c with distance from the centerline at any fixed position from the source. At any distance t_* from the source, the value of the ground concentration (and consequently the value of i_c) depends strongly on the plume spread σ_z and the position of the plume mean height \bar{z} . Since in the work by *Franzese* (2003) the value of \bar{z} overestimates the experimental results, especially between $0.5 < t_* < 2$, the edge of the plume is located close to the ground. Since σ_c reaches its maximum value at the plume's edges, as a result the value of i_c may be overestimated. Also the water-tank experiments by *Deardorff and Willis* (1984) show a relative maximum of i_c around $t_* = 1.4$, but they doubted about the validity of their data. If the "anomalous" maximum in the data by *Deardorff and Willis* (1984) is excluded (as suggested by the same authors) a good agreement is found among all the experimental data and the LES results. The LES results by *Henn and Sykes* (1992) are in contrast with the other results at short distance ($t_* < 2$) probably due to the low vertical resolution (40 m) and the relative high ratio between the source size and the eddy dimension.

4.4.2 Meandering component

In this Section the plume meandering is discussed by analyzing the second- and third-order moments, and the PDF of the plume instantaneous centerline position. An example of trajectories of the plume centerline position z_m is shown in Figure 4.4a. Close to the source ($t_* < 0.8$), the shape

4.4. Results and discussion

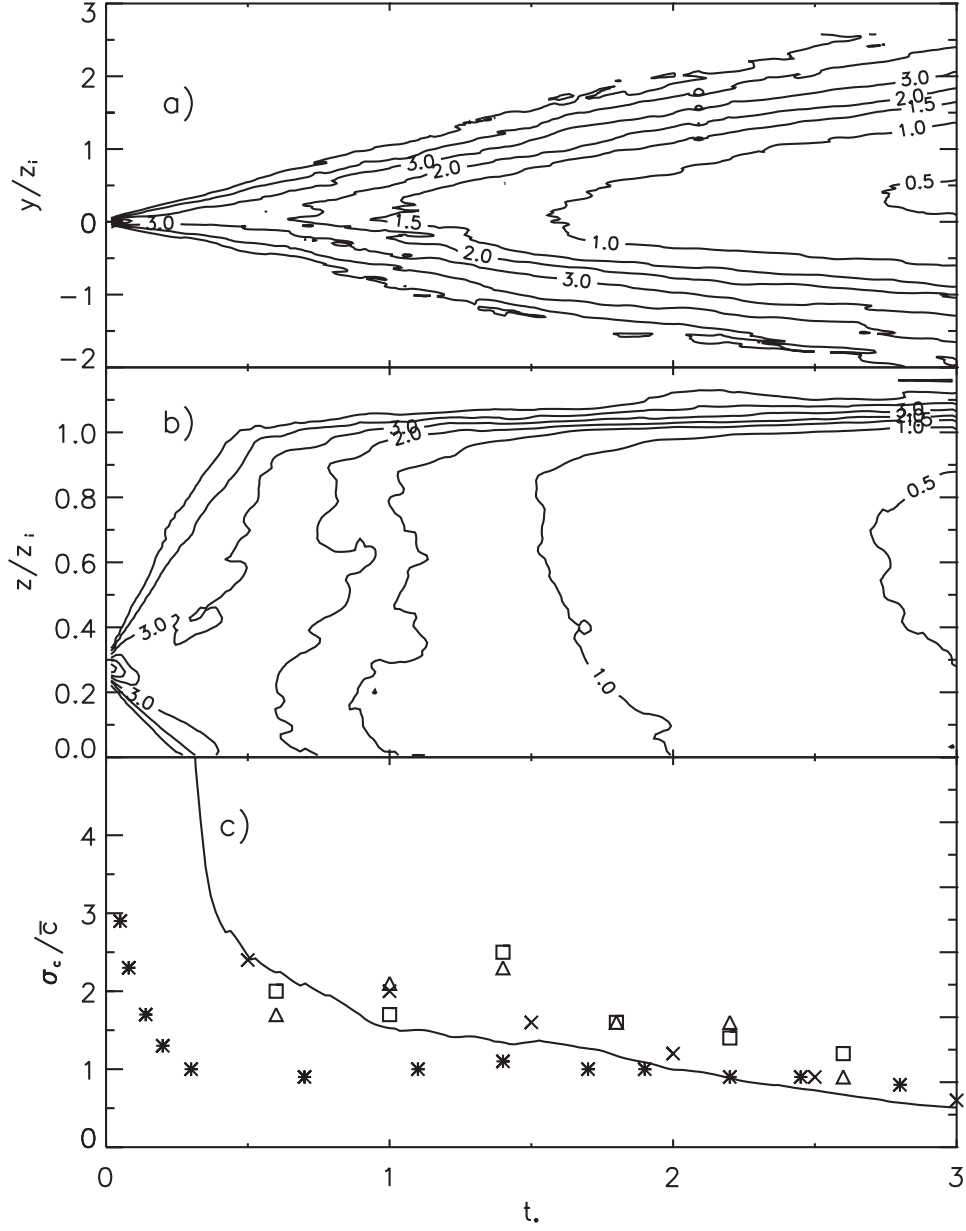


Figure 4.3: a) Horizontal cross section of the concentration fluctuation intensity i_c at ground ($z/z_i = 0.007$). b) Vertical cross section of i_c in the plume mean horizontal position \bar{y} . c) Concentration fluctuation intensity along the plume mean horizontal position (\bar{y}) at ground. The following experimental and numerical data are also shown: *Weil et al.* (2002) (\times); *Deardorff and Willis* (1984) (\square and \triangle); *Henn and Sykes* (1992) (*).

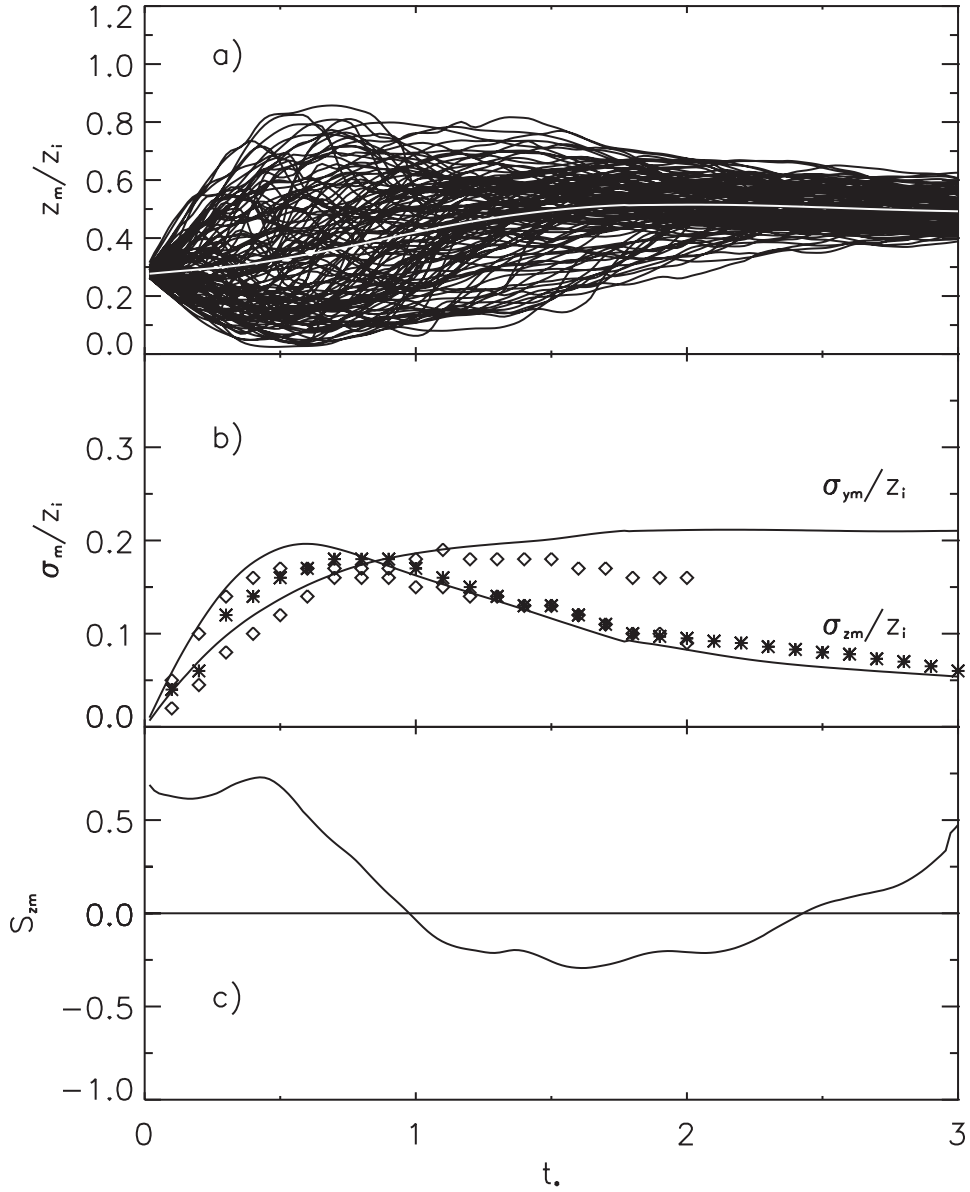


Figure 4.4: a) Example of trajectories of the plume instantaneous centerline position z_m . The plume mean height position \bar{z} is also shown. b) Normalized horizontal (σ_{ym}) and vertical (σ_{zm}) variances of the plume centerline position (meandering). The laboratory data by Hibberd (2000) (*) and the LES data by Nieuwstadt (1992) (\diamond) are also shown. c) Skewness of the vertical meandering $S_m = \overline{z_m'^3} / \sigma_{zm}^3$.

4.4. Results and discussion

of the ensemble of trajectories is similar to the mean cross-integrated concentration (Figure 4.2b), because meandering is the main contribution to the plume motion when the plume size is smaller than the characteristic turbulent length-scale. The spread of the instantaneous plume centerline position reaches its maximum around $t_* = 0.5$, and then it slowly diminishes. Far from the source, when the plume is vertically confined between the CBL boundaries, the instantaneous plume position becomes similar to the mean plume height \bar{z} , which has reached the asymptotic value of 0.5. The second-order moment of the horizontal and vertical centerline position (σ_{ym} and σ_{zm}) calculated by the LES (equation 4.15) agrees satisfactorily with previous laboratory experiments and numerical simulation (Figure 4.4b). As explained, σ_{zm} reaches a maximum value around $t_* = 0.5$, and then it decays quickly to a very small value when the plume vertical motion is limited by the boundaries and $z_m \sim \bar{z}$. In the horizontal direction, the plume motion is not limited and the meandering component σ_{ym} is in agreement with the theoretical analysis by Csanady as reported by Weil *et al.* (2002)

$$\begin{cases} \sigma_{ym} = \sigma_v t & \text{at short distances} \\ \frac{d\sigma_{ym}^2}{dt} = 0 & \text{at long distances,} \end{cases} \quad (4.27)$$

which implies that σ_{ym} approaches a constant value at large distances.

The evolution of the skewness of the instantaneous centerline (vertical) position

$$S_{zm} = \frac{\overline{z_m'^3}}{\sigma_{zm}^3}, \quad (4.28)$$

is shown in Figure 4.4c. The skewness of the meandering position provides information on the distribution of the plume as transported by the large-scale turbulent motions. As pointed out by Luhar *et al.* (2000), there are no currently available data to validate the evolution of S_{zm} . The LES results provide an estimation of the downwind variation of the meandering skewness and they can be useful to derive a suitable parameterization.

Close to the source, meandering is the main contribution to plume dispersion, because the plume size σ_r is smaller than the turbulent length scale l . Therefore the concentration distribution is mainly affected by the large-scale motions. As a result, at $t_* < 0.5$ the meandering skewness is very similar to the total skewness S_z (Figure 4.2d).

The meandering skewness follows closely the motion of the plume carried by the large-scale eddies, because, by definition, the meandering represents the contribution of the large scale motion to the plume total dispersion. In particular, S_{zm} is positive when the plume is transported downward by the subsidence motion ($t_* < 1$ and $t_* > 2.4$), and it becomes negative when the plume is transported upward by the thermals, as shown by the position of the maximum concentration in Figure 4.2b. The meandering skewness has a different behavior than the total skewness at distances $t_* > 0.5$. For example, at $t_* = 1.1$, S_{zm} is negative, whereas S_z is still positive. This difference will be further discussed below, when the third-order moment of the relative diffusion is discussed.

In the numerical model by Luhar *et al.* (2000), the meandering skewness S_{zm} was assumed equal to the total one S_z . As explained, this assumption is valid only at very short distances from the sources ($t_* < 0.5$) when dispersion is dominated by meandering.

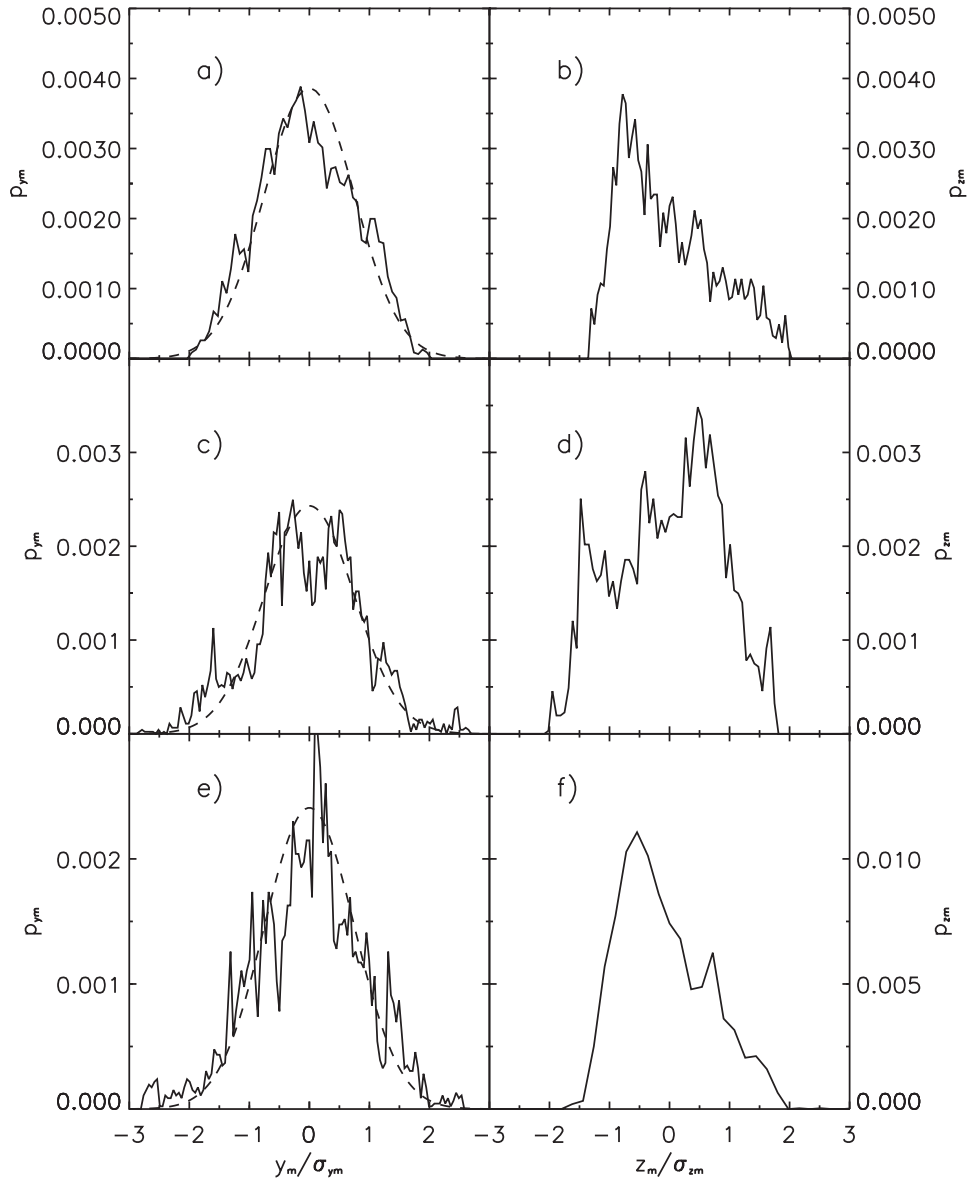


Figure 4.5: PDF of the plume centerline instantaneous position (p_{ym} and p_{zm} calculated by the LES according to equation 4.24 at different distances from the source ($t_* = 0.5, 1.2, 3$). The Gaussian parameterization (4.29) is also shown (dashed line).

4.4. Results and discussion

The evolution of the meandering skewness is closely related to the value of the PDF of the plume's centerline position. From the instantaneous centerline position $(y_m(x, t), z_m(x, t))$ (equation 4.8), the PDFs of the plume centerline p_{zm} and p_{ym} are calculated at any downstream distance. The results are shown in Figure 4.5 at selected distances from the source ($t_* = 0.5, 1.2, 3$), where the PDF are shown as a function of the normalized relative position $(z_m - \bar{z})/\sigma_{zm}$ (and equivalently for the horizontal PDF).

The horizontal PDF p_{ym} is well reproduced by the Gaussian function

$$p_{ym} = \frac{1}{\sqrt{2\pi}\sigma_{ym}} \exp \left[-\frac{y_m^2}{2\sigma_{ym}^2} \right], \quad (4.29)$$

which is commonly used as parameterization for the plume horizontal mean position PDF (Yee and Wilson, 2000; Luhar *et al.*, 2000; Franzese, 2003) based on the water-tank experiment by Willis and Deardorff (1978). This result is explained by the homogeneity of the horizontal motion in the atmospheric CBL.

The LES results for the p_{zm} are shown in Figures 4.5b, 4.5d, and 4.5f respectively. As previously discussed, when the meandering skewness was analyzed, three different shapes of the PDF can be distinguished: at short distances from the source, when the plume is transported by the downdraft, the PDF is positively skewed (Figure 4.5b). At larger distances ($t_* = 1.2$, Figure 4.5d), the plume is transported upwards by the thermal motions. Therefore it is now more likely that the plume instantaneous centerline lies above its mean value. As a result, p_{zm} becomes negatively skewed. Finally, the PDF becomes once again positively skewed ($t_* = 3$ Figure 4.2f). It must be noticed that for a uniformly well-mixed plume, the PDF would have a Gaussian shape, centered on the plume mean position. Our LES results are consistent with the water-tank data by Willis and Deardorff (1978), who showed that the well-mixed condition is reached only at very large distances from the source ($t_* > 6$).

Although out of the scope of this work, finding a suitable parameterization for the PDF of the vertical plume position would be of great practical interest, because it would allow the estimation of concentration statistics through Gifford's formula (4.6) without the need of calculating the position of the plume centerline by means of a LES or Lagrangian stochastic models. As the LES results show, the shape of p_{zm} is highly complex, and it may depend on different factors such as the turbulent characteristics of the CBL, plume characteristics (such as σ_{zm} and S_{zm}), distance from the source, and height of the release.

4.4.3 Dispersion in relative coordinate system

Mean concentration, variance and skewness

Figures 4.6a and 4.6b show the normalized vertically- and cross-integrated mean concentration in the relative coordinate system. The vertically integrated concentration (Figure 4.6a) has a Gaussian shape similar to the one in absolute coordinates (Figure 4.2a), as expected. In the relative coordinates system, the concentration pattern is always aligned along the line $y_r = 0$, which is the position of the centerline. The crosswind-integrated concentration is shown in Figure 4.6b. Moreover, to allow a direct comparison, vertical cross sections of averaged absolute and relative concentrations

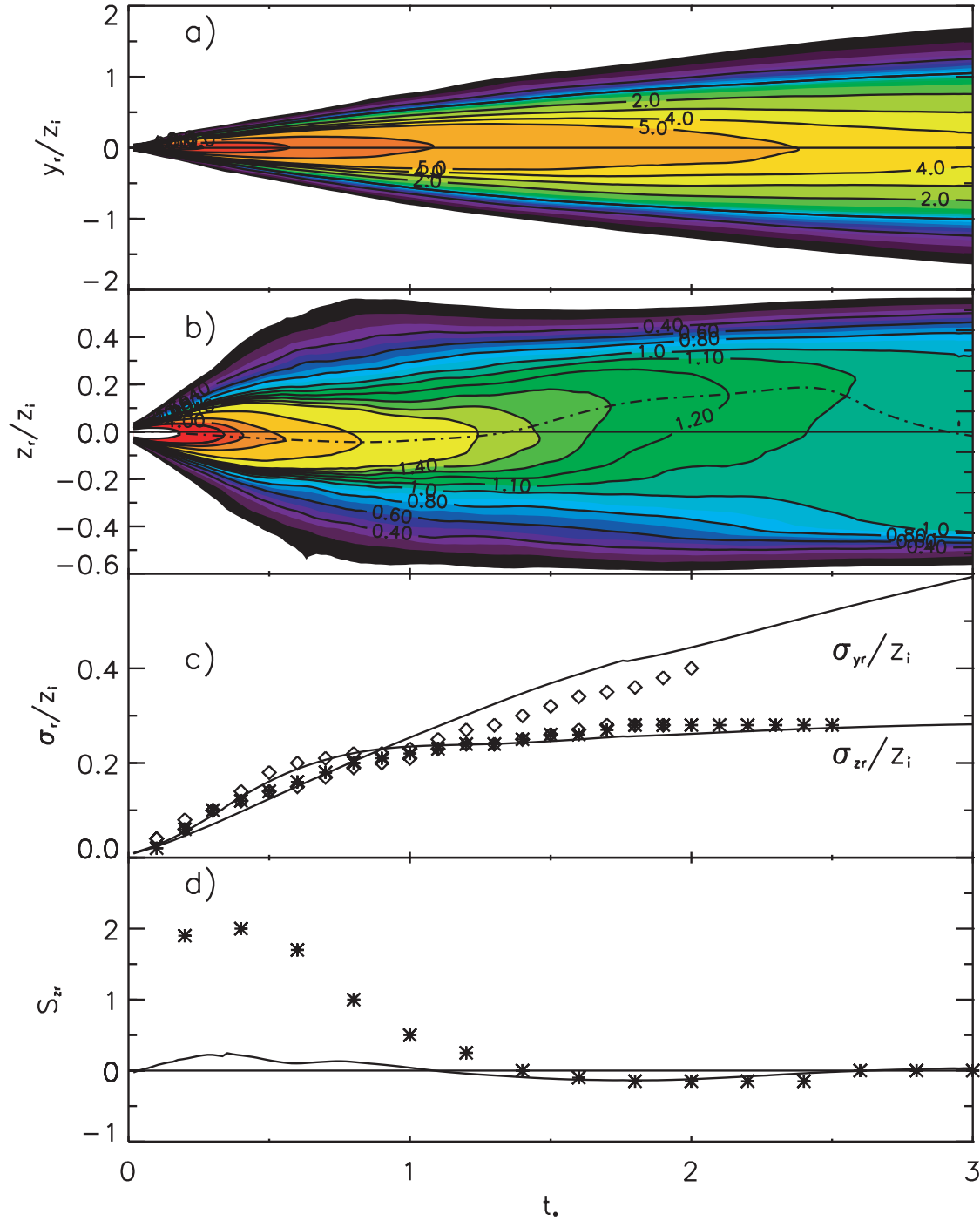


Figure 4.6: a) Normalized vertically-integrated relative concentration as a function of the dimensionless time t_* . b) Normalized cross-integrated relative concentration. In the picture, the position of the maximum concentration (dashed line) are also shown. c) Normalized horizontal (σ_{yr}) and vertical (σ_{zr}) relative diffusion parameters. The following experimental and numerical data are also shown: *Hibberd* (2000) (*); *Nieuwstadt* (1992) (\diamond). d) Skewness of the vertical relative plume position $S_{zr} = \overline{z_r'^3}/\sigma_{zr}^3$. In the picture, the data by *Luhar et al.* (2000) are also shown (*).

4.4. Results and discussion

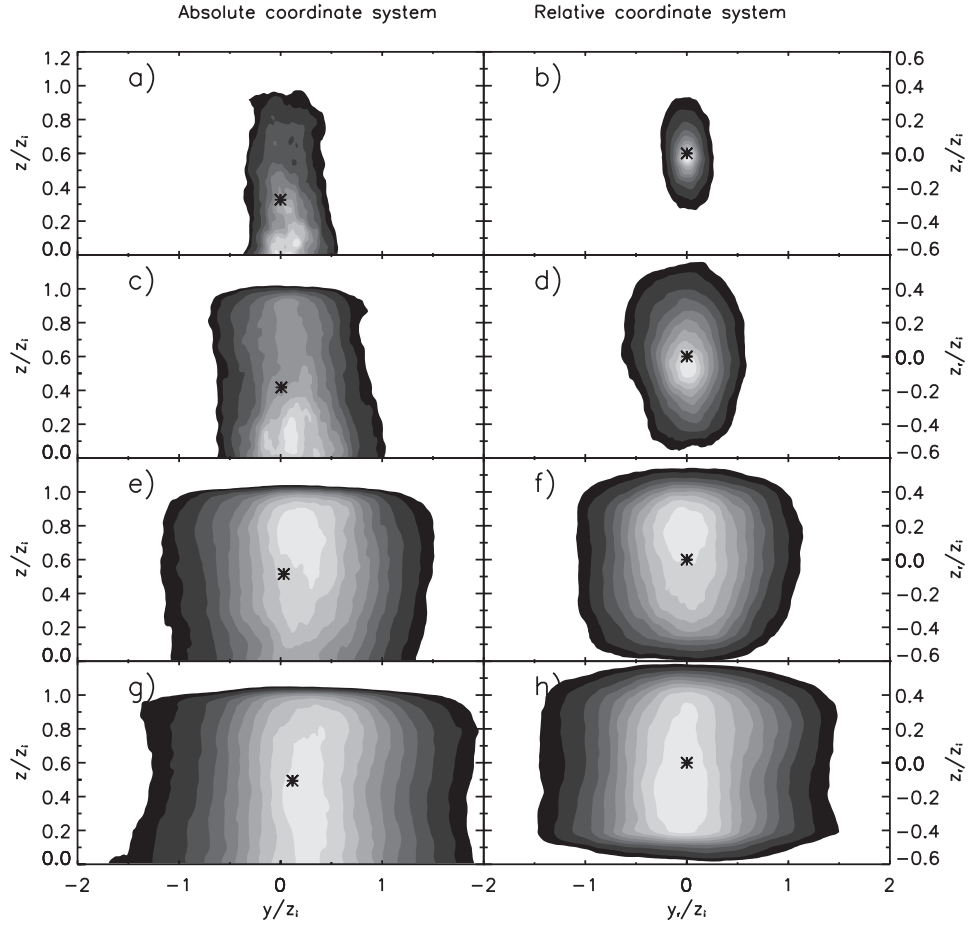


Figure 4.7: Vertical cross-sections of averaged concentration in absolute (a, c, e, and g) and relative coordinates system (b, d, f, and h) at different distances from the source ($t_* = 0.5, 1, 2, 3$ respectively).

at different distances from the sources ($t_* = 0.5, 1, 2, 3$ respectively) are shown in Figure 4.7.

Since in the relative coordinate system the meandering, which characterized the large-scale inhomogeneous and skewed motion, has been removed, one expects that the relative concentration has a more homogeneous and Gaussian distribution. This is evident especially close to the source ($t_* < 1$), where the plume is still very narrow ($\sigma_r \ll l$) and it has not reached the boundaries yet. For instance, at $t_* = 0.5$, the scalar distribution in absolute coordinate is vertically highly inhomogeneous. The distribution is skewed, and the maximum concentration is located close to the ground (Figure 4.7a). In relative coordinates, on the contrary, the plume is very narrow and it shows a Gaussian distribution both in the horizontal and vertical direction (Figure 4.7b). At $t_* = 1$ the plume in relative coordinates has reached the CBL boundaries and it still shows a quasi-Gaussian distribution (Figure 4.7d), but the maximum concentration is somehow below the plume centerline (Figure 4.6b). This deviation from the Gaussian distribution is an effect of the reflection of the plume by the ground, which occurs at $t_* = 0.5$ (Figure 4.2b), and causes the relative concentration to be positively skewed (see below).

At larger distances ($t_* > 1.2$), the maximum lies above the relative mean height. Both the absolute and relative concentration present an elevated maximum around $t_* = 2$ caused by the reflection with the CBL top after the plume was transported upward by the thermals (Figures 4.7e and 4.7f). It is noteworthy that the relative concentration shows a distribution very similar to the absolute concentration (figs. 4.7g and 4.7h). Since at large distances from the source the meandering component becomes small, the relative diffusion is the main contribution to the plume dispersion as shown by Figure 4.6c, where the vertical and horizontal relative dispersion parameters are shown. As a result, the concentration distribution in absolute coordinates is influenced mainly by the in-plume, small-scale motions, and the absolute concentration is very similar to the relative concentration for $t_* > 1.5$.

This result is corroborated by the analysis of the skewness of the vertical relative plume position $S_{zr} = \overline{z_r'^3} / \sigma_{zr}^3$, shown in Figure 4.6d. Generally the relative skewness has a little value, because the relative concentration distribution is affected mainly by the small-scale motion, which is homogeneous and Gaussian. These small asymmetries in the relative concentration distribution are due solely to the reflections by the CBL boundaries. The reflection by the ground is the cause of the small positive value of S_{zr} at distances between $0.5 < t_* < 1.5$. At larger distances ($t_* > 1.5$), the relative skewness becomes negative due to the reflection by the CBL top, and S_{zr} becomes very similar to total skewness S_z . This result is explained by the fact that the meandering contribution becomes very small at $t_* > 1.5$ and consequently $\overline{z'^3} \sim \overline{z_r'^3}$. The numerical data by *Luhar et al.* (2000) overestimate significantly the LES results, especially close to the source. In their work, *Luhar et al.* (2000) assumed the following balancing relationship between the meandering and relative third-order moment:

$$\overline{z_L'^3} = \overline{z_m'^3} + \overline{z_r'^3}. \quad (4.30)$$

From the definition of the third moments (equations 4.17, 4.18 and 4.19), it can be shown that

$$\overline{z_L'^3} = \overline{z_m'^3} + \overline{z_r'^3} - 3\overline{z_m z_r'^2} + 3\overline{z_m z_r'^2} = \overline{z_m'^3} + \overline{z_r'^3} - 3\overline{z_m z_r'^2} + 3\overline{z_m z_r'^2}. \quad (4.31)$$

The different terms in equation (4.31) are shown in Figure 4.8 as a function of t_* . As explained, close to the source ($t_* < 0.5$), the total dispersion is dominated by the meandering, because the plume is very narrow. As a result, $\overline{z_r'} \sim 0$ and $\overline{z'^3} \sim \overline{z_m'^3}$. Far from the source ($t_* > 1.5$), the meandering contribution becomes small because the instantaneous plume centerline position z_m approaches its mean value \bar{z} (Figure 4.4a). As a result, $\overline{z_m'} \sim 0$ and $\overline{z'^3} \sim \overline{z_r'^3}$. Figure 4.8 shows that the non-linear cross-terms $-3\overline{z_m z_r'^2}$ and $3\overline{z_m z_r'^2}$ do not balance themselves, and their contribution is very important especially at distances between $0.4 < t_* < 1.5$. These cross-terms are significant as a result of the reflection of the plume by the ground and the top of the CBL. A physical interpretation of the cross-terms and their influence on the relative concentration is discussed thoroughly in the next Section.

Concentration fluctuations

Figures 4.9a and 4.9b show the contour of the relative concentration fluctuation intensity $i_{cr} = \frac{\sigma_{cr}}{\bar{c}_r}$ in the plume mean height (\bar{z}) and in the plume mean horizontal position (\bar{y}) respectively. To our knowledge, this is the first time that complete horizontal and vertical two-dimensional fields of

4.4. Results and discussion

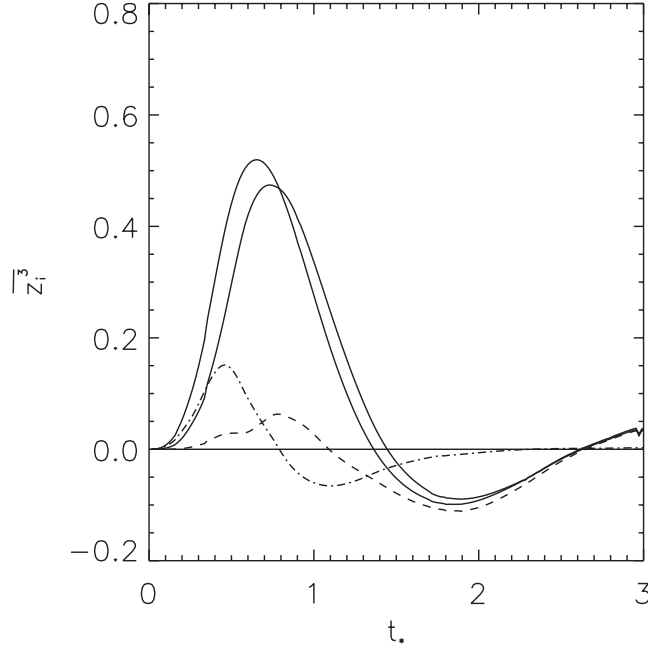


Figure 4.8: Evolution of the third-order moments of the total (continuous line), meandering (dashed line) and relative (dashed dotted line) vertical plume position. In the Figure, the sum of the the non-linear cross-terms $-3\bar{z}\sigma_{zr}^2$ and $3z_m z_r'^2$ is also shown as dashed dotted dotted line. Note that, for clarity, all the terms have been divided by the factor 10^6 .

relative concentration fluctuations are shown. In their study, *Fackrell and Robins* (1982) showed relative intensity of fluctuation concentration calculated as the maximum r.m.s. of concentration ($\hat{\sigma}$) divided by the maximum mean concentration (\hat{c}) at any downstream position. This approach is valid in neutral conditions, when the plume centerline coincides with the position of the maximum concentration. As shown earlier, in the CBL these two heights are different, and i_{cr} may be different than $\frac{\hat{\sigma}}{\hat{c}}$.

The horizontal cross section of relative concentration fluctuation (Figure 4.9a) has a shape similar to the one in absolute coordinates (Figure 4.3a), because the horizontal motion is homogeneous and Gaussian in both the reference coordinate systems. The vertical cross section (Figure 4.9b) shows a pattern similar to the relative mean concentration (Figure 4.6b): at short distances i_{cr} spreads uniformly until it is influenced by the boundaries, around $t_* = 1$.

The value of i_{cr} in the plume centerline (\bar{y}, \bar{z}) is shown in Figure 4.9c. Very close to the source, σ_{cr} is zero because the plume is so narrow that the only the very small eddies can generate in-plume fluctuation. As a result, $c_r(t) \sim \bar{c}_r$. As the plume grows, the mixing process is driven by an increasing number of eddies, and σ_{cr} grows consequently. The intensity of relative concentration fluctuations reaches a maximum of $i_{cr} = 1.4$ around $0.5 < t_* < 1$ when the plume size is of the same order of the turbulent length scale and all the turbulent eddies participate to the internal mixing. At larger distances, i_{cr} slowly decreases with the distances from the source. At very large distance, for an ideally well-mixed condition, the scalar concentration must be close to its mean value, so that σ_{cr} is relatively small.

In the previous studies by *Yee et al.* (1994) and *Yee and Wilson* (2000), the value of i_{cr} was as-

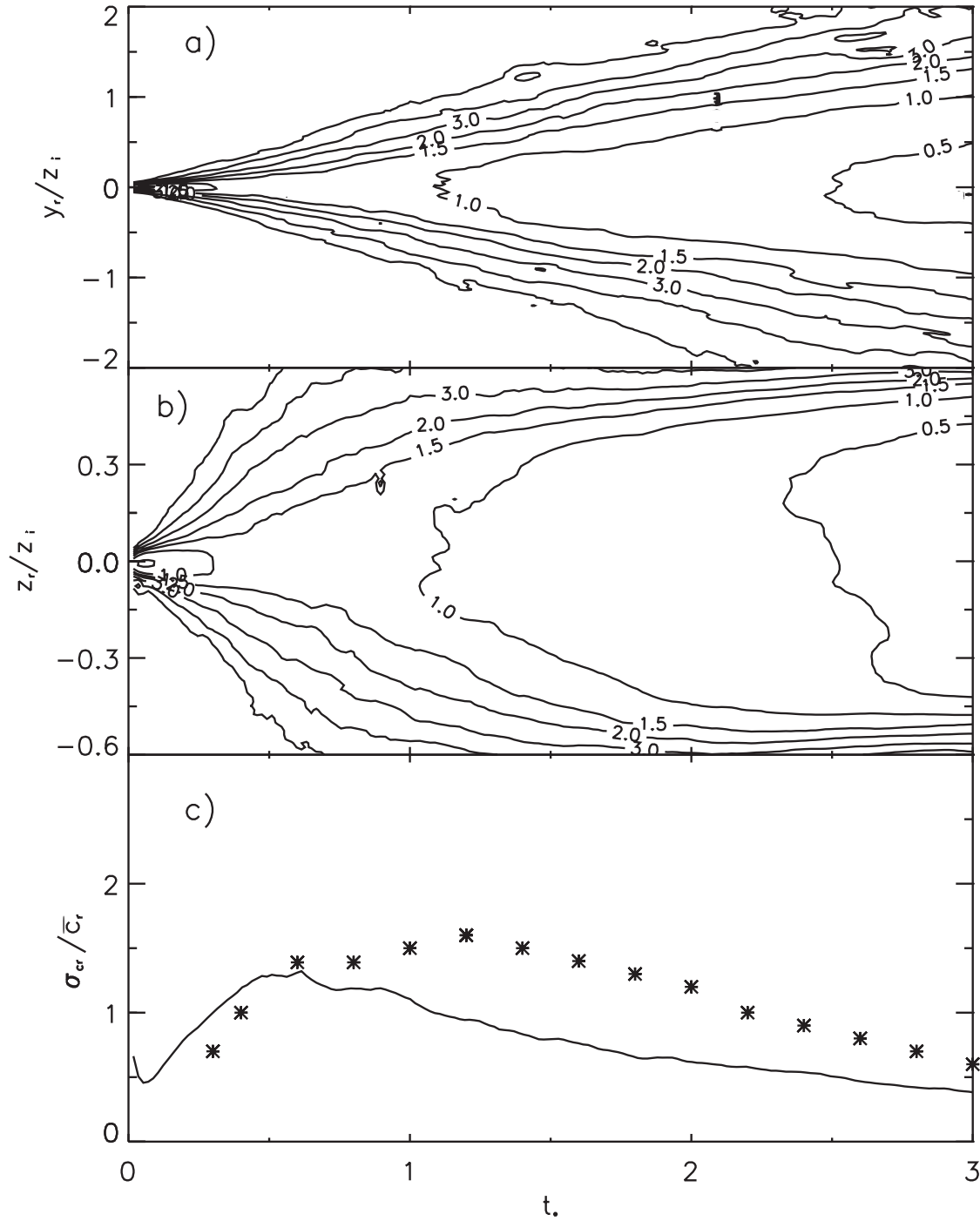


Figure 4.9: a) Horizontal cross section of the relative concentration fluctuation intensity i_{cr} in the plume mean position \bar{z} . b) Vertical cross section of i_{cr} in the plume mean horizontal position \bar{y} . c) Relative concentration fluctuation intensity along the plume mean position (\bar{y}, \bar{z}) . The numerical data by Luhar *et al.* (2000) are also shown (*).

4.4. Results and discussion

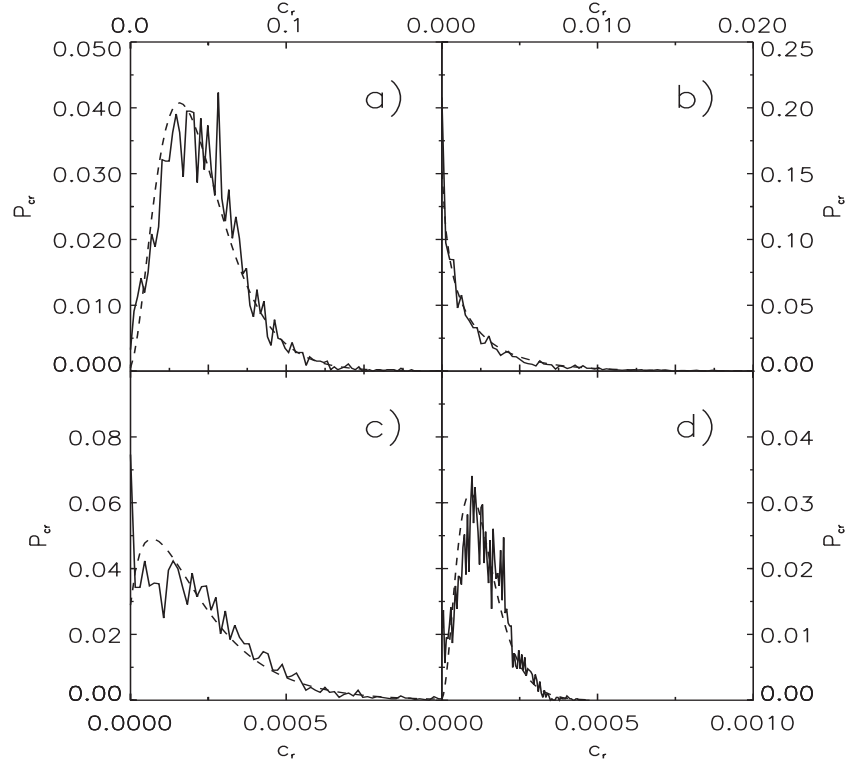


Figure 4.10: PDF of relative concentration in the mean plume position (\bar{y}, \bar{z}) at different distance from the source ($t_*=0.1, 0.5, 1.5, 2.5$ respectively). In the Figure the parameterization (4.33) is also shown as a dashed line.

sumed to be constant in a crosswind cross-section of the instantaneous plume at any distance, because their model was develop to be used in homogeneous and isotropic turbulence.

In the study by *Luhar et al.* (2000), the value of i_{cr} was parameterized in order to obtain the best fit of the total calculated concentration fluctuation i_c . The values of i_{cr} calculated by *Luhar et al.* (2000) are also shown in Figure 4.9c. Although the general shape is similar, the parameterizations predict the maximum at larger distances from the source than the LES results. It must be noticed that whereas the LES results are obtained by direct calculation of i_{cr} , the parameterization is explicitly calculated in order to obtain the best fit of the results for the total intensity i_c .

PDF of relative concentration

The PDF of the relative concentration is calculated from the evolution of c_r as:

$$p_{cr}(c|t_*, y_r, z_r)dc = \text{prob}\{c < c_r < c + dc\}, \quad (4.32)$$

where the concentration increment dc is taken equal to one hundredth of the maximum concentration. Figure 4.10 shows the PDF calculated in the plume mean position (\bar{y}, \bar{z}) at different distance from the source ($t_*=0.1, 0.5, 1.5, 2.5$ respectively). The LES results show that p_{cr} has mainly two

characteristics shapes: an unimodal type with the mode at non-zero value of c_r , and an exponential type (or unimodal with the mode at $c_r = 0$ (fig. 4.10b). As expected, the former type is the most probable in the plume centerline, as shown by *Munro et al.* (2003a), because the relative concentration in the mean plume position is very often different than zero. On the contrary, far from the centerline, small concentrations are more probable, and consequently the PDF shows an exponential shape. However, the LES results shows that at distances between $0.5 < t_* < 1$ p_{cr} has an exponential shape also in the plume centerline (Figure 4.10b). This may be explained by the fact that the at distances between $0.5 < t_* < 1.5$, when dispersion is dominated by meandering, the plume instantaneous vertical position z_m is very unlikely to coincide with its mean position \bar{z} (Figure 4.4a). As a result the time evolution of the relative concentration c_r is highly intermittent. When the instantaneous plume position z_m is closer to its mean value ($t_* > 1.5$, Figure 4.4a) the PDF of relative concentration is once again unimodal with the mode at non-zero (Figures 4.10c and 4.10d).

The LES results are compared with the following Gamma parameterization (*Yee and Wilson*, 2000; *Luhar et al.*, 2000):

$$p_{cr}(c|t_*, y, z, y_m, z_m) = \frac{\lambda^\lambda}{\bar{c}_r \Gamma(\lambda)} \left(\frac{c}{\bar{c}_r} \right)^{\lambda-1} \exp \left(-\frac{\lambda c}{\bar{c}_r} \right), \quad (4.33)$$

where $\lambda = 1/i_{cr}^2$. As shown in Figure 4.10, parameterization (4.33) is able to reproduce correctly the shape of p_{cr} at any distances from the source. Since the parameterization depends heavily on the value of the intensity of relative concentration fluctuation i_{cr} , the agreement between the LES results and relationship (4.33) demonstrates the accuracy of the calculation of i_{cr} .

4.4.4 Validation of Gifford formula

As explained in Section 4.2, the absolute and relative mean concentrations (and higher-order moments) are related by Gifford's formula (4.6). In his study, *Gifford* (1959) pointed out that possible statistical variations in the shape of c_r^n are not taken into account, since c_r should approach its average value if the sampling time is long enough. However, equation (4.6) is strictly true only if the plume is not affected by the boundary conditions. When the plume is reflected by the boundaries, in fact, the shape of the relative concentration is changed and, as a consequence, equation (4.6) has to be modified, as will be shown.

In order to visualize the physical process, one can consider the time evolution of the plume at a fixed distance from the source, as illustrated schematically in Figure 4.11a. The centerline position $z_m(t)$ shows the instantaneous vertical motion of the plume in the absolute coordinate system. If the plume is transported by a downdraft and reaches the ground (for instance between $t_1 < t < t_2$ and $t_3 < t < t_4$ in the Figure), it is reflected by the surface and the concentration is enhanced as illustrated by the shaded area in the Figure. In the relative coordinate system (Figure 4.11b) the relative concentration has a Gaussian distribution centered on the plume centerline only when the plume is not affected by the boundaries (for instance between $t_0 < t < t_1$ and $t_2 < t < t_3$ in the Figure). If the plume reaches the ground and it is reflected, the relative concentration is modified and its distribution is skewed as illustrated by the shaded areas in Figure 4.11b. Since the concentration is higher, the plume spread must be smaller, as illustrated by the fact the relative concentration between $t_1 < t < t_2$ is narrower than between $t_0 < t < t_1$. Therefore, the instantaneous relative plume

4.4. Results and discussion

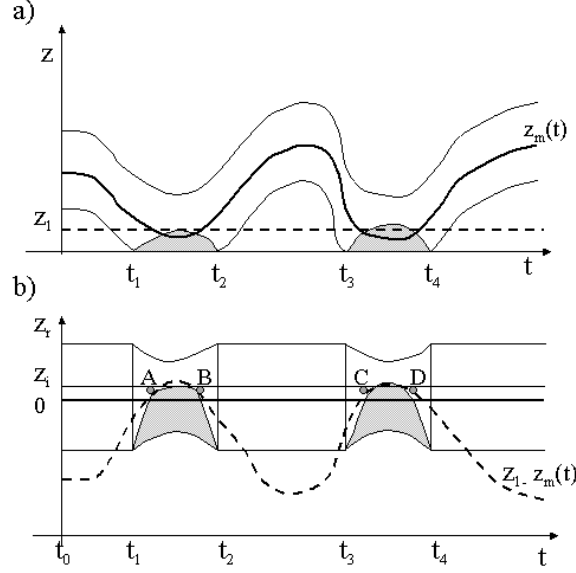


Figure 4.11: a) Time evolution of an idealized plume at a certain fixed position downwind the source in the absolute coordinate system. the continuous line $z_m(t)$ represents the instantaneous plume centerline position. the shaded areas between $t_1 < t < t_2$ and $t_3 < t < t_4$ represent the concentration reflected by the surface. b) Same as a) but in the coordinate system relative to the plume position $z_m(t)$ (relative coordinate system). The continuous solid line at $z_r = 0$ is the plume centerline (corresponding to $z_m(t)$ in absolute coordinates). The shaded areas represent the concentration reflected by the surface. The dashed line represent the path of integration $z_1 - z_m(t)$.

width $z_r'^2(t)$ between $t_1 < t < t_2$ does not coincide with its mean value $\sigma_{z_r}^2$. This is the reason why the cross terms $-3\bar{z}\sigma_{z_r}^2$ and $3\overline{z_m z_r'^2}$ in equation (4.31) do not balance themselves.

The absolute mean concentration at the height $z = z_1$ is related to the relative mean concentration by the equation:

$$\overline{c(z_1)} = \overline{c_r(z_1 - z_m(t))} \quad (4.34)$$

by the definition of the relative coordinate system. The r.h.s of equation (4.34) implies that one has to integrate the relative concentration along the path $z_1 - z_m(t)$, which is illustrated by the dashed line in Figure 4.11b. By considering a finite sampling time, one can write:

$$\overline{c(z_1)} = \overline{c_r(z_1 - z_m(t))} = \sum_{j=1}^N \frac{c_r(t_j)}{N} = \sum_i \sum_1^{N_{z_i}} \frac{c_r(z_i)}{N_{z_i}} \frac{N_{z_i}}{N} = \sum_i \overline{c_r(z_i)}^l p(z_i), \quad (4.35)$$

where N is the number of the samplings t_j , N_{z_i} is the number of times that the integration path $z_1 - z_m(t)$ encounters the height z_i (illustrated by the points A,B,C, and D in Figure 4.11b), $\overline{c_r(z_i)}^l$ is the relative concentration locally averaged over the points A,B,C, and D, and finally $p(z_i) = N_{z_i}/N$ is the PDF of the plume centerline in the position z_i .

It is evident that equation (4.35) is equivalent to Gifford's formula (4.6) only if the local average $\overline{c_r(z_i)}^l$ coincides with the mean relative concentration $\overline{c_r(z_i)}$. This is true only if the relative concentration c_r varies little with time, i.e. the plume is not perturbed by the CBL boundaries.

The importance of the effect of the boundaries on the calculation of the absolute mean concentration is illustrated in Figure 4.12 where Gifford's formula (4.6) is directly applied to the LES results. Figure 4.12a shows the cross-wind integrated absolute mean concentration calculated directly from the LES results as a function of the dimensionless time t_* (note that this figure is the same than Figure 4.2b). Figure 4.12b shows the cross-wind integrated absolute mean concentration calculated through Gifford's formula (4.6) from the relative mean concentration $\overline{c_r}$ and the PDF of the plume centerline p_m . It is evident that Gifford's formula gives a satisfactory result for distances $t_* < 0.4$, before the impact of the plume on the surface. For $t_* > 0.4$, Gifford's formula reproduces correctly the general plume behavior but it underestimates sensibly the mean concentration, especially close to the ground ($z/z_i < 0.2$). As explained previously, this result is due to the use in equation (4.6) of the mean relative concentration $\overline{c_r}$ instead of the more correct local average $\overline{c_r}^l$. Since the calculation of the local average requires the knowledge of the time evolution of the relative concentration, it is evident that its direct calculation for use in equation (4.6) is unsuitable for practical use. However, a more practical way to compute the absolute mean concentration can be found, in which instead of $\overline{c_r}^l$ a parameterization of $\overline{c_r}$ is used that takes into account the skewness of the relative plume position. This methodology is explained in the next Section.

Parameterization of the relative mean concentration

In their model for isotropic dispersion *Yee et al.* (1994) assumed for $\overline{c_r}$ a simple circular symmetric Gaussian, both in y and z . Both *Luhar et al.* (2000) and *Franzese* (2003), on the contrary, distinguished between horizontal and vertical motion, by assuming:

$$\overline{c_r} = \frac{Q}{u} p_{yr} p_{zr}, \quad (4.36)$$

where Q is the amount of contaminant emitted per unit time, and p_{yr} and p_{zr} are the PDF of mean particle positions relative to the plume centerline. In the horizontal direction a simple Gaussian relationship is assumed:

$$p_{yr} = \frac{1}{\sqrt{2\pi}s_y} \exp \left[-\frac{(y - y_m)^2}{2s_y^2} \right]. \quad (4.37)$$

The Gaussian parameterizations (4.37) fits closely the values of $\overline{c_r}$ calculated by the LES normalized by its value in the plume centerline ($z = z_m$) (not shown).

For the vertical PDF, both *Luhar et al.* (2000) and *Franzese* (2003) assumed a Gaussian form with multiple reflections due to the CBL boundaries. Moreover, *Luhar et al.* (2000) incorporated the skewness of the relative position by assuming the same closure procedure used in *Luhar*

4.4. Results and discussion

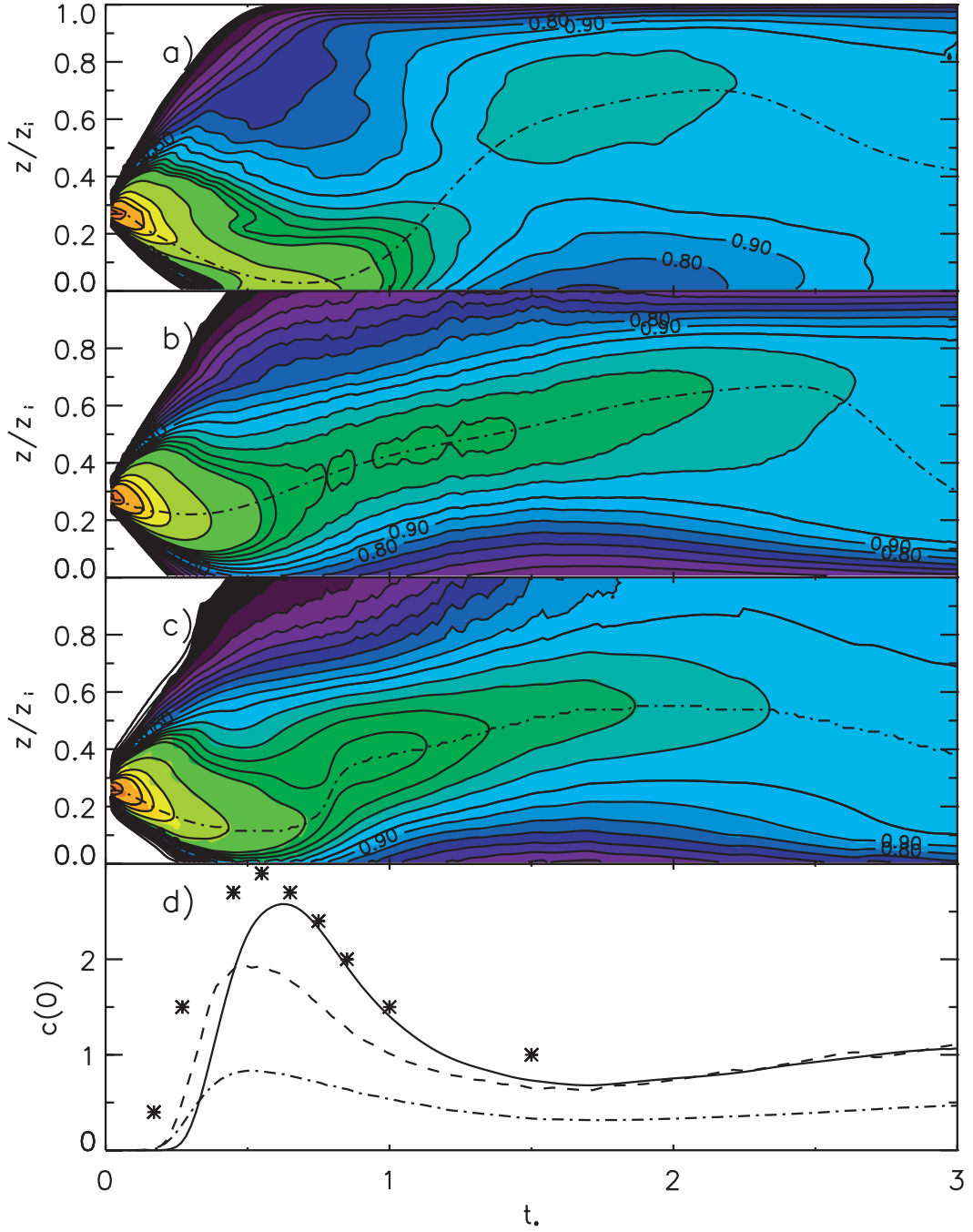


Figure 4.12: a) Normalized cross-integrated mean concentration as a function of the dimensionless time t_* as calculated by the LES. The position of the maximum concentration is also shown (dashed line). b) Normalized cross-integrated mean concentration as calculated by Gifford's formula (4.6) using the relative mean concentration \bar{c}_r . c) Normalized cross-integrated mean concentration as calculated by Gifford's formula (4.6) using the parameterization (4.39) for the relative mean concentration. d) Absolute mean concentration at ground in the plume horizontal mean position (\bar{y}) as calculated by the LES (continuous line); as calculated by using Gifford's formula with the relative mean concentration \bar{c}_r (dashed-dotted-line); as calculated by using Gifford's formula with the parameterization (4.39) (dashed line). The water-tank data by Willis and Deardorff (1978) are also shown (*).

et al. (1996) for the vertical velocity PDF. As a result, the parameterization for the vertical relative position PDF reads:

$$p_{zr} = \sum_{j=1}^2 \sum_{n=-N}^N \frac{a_j}{\sqrt{2\pi}\sigma_j} \left\{ \exp \left[-\frac{(z - z_m + 2nz_i - \bar{z}_j)^2}{2\sigma_j^2} \right] + \exp \left[-\frac{(-z - z_m + 2nz_i - \bar{z}_j)^2}{2\sigma_j^2} \right] \right\}, \quad (4.38)$$

where N is the number of reflections (3 in this work), and the other parameters are defined as *Luhar et al.* (2000):

$$\begin{aligned} \bar{z}_1 &= \tilde{S}_{zr} f \sigma_1 / |\tilde{S}_{zr}| \\ \bar{z}_2 &= -\tilde{S}_{zr} f \sigma_2 / |\tilde{S}_{zr}| \\ \sigma_1 &= \tilde{\sigma}_z r a_2 / [a_1 (1 + f^2)]^{1/2} \\ \sigma_2 &= \tilde{\sigma}_z r a_1 / [a_2 (1 + f^2)]^{1/2} \\ a_1 &= 1 - [r / (4 + r)]^{1/2} / 2 \\ a_2 &= 1 - a_1 \\ r &= [(1 + f^2)^3 \tilde{S}_{zr}^2] / [(3 + f^2)^2 f^2] \\ f &= 2/3 |\tilde{S}_{zr}|^{1/3} \end{aligned}$$

In our work, the same parameterization is used, in which the relative skewness S_{zr} is replaced by:

$$\tilde{S}_{zr} = \frac{1}{\sigma_{zr}^3} \left(\overline{z_r'^3} - 3\bar{z} \sigma_{zr}^2 + 3\bar{z}_m \overline{z_r'^2} \right) = \frac{S_z}{\sigma_{zr}^3} \left[\sigma_z^3 - \frac{S_{zm}}{S_z} \sigma_{zm}^3 \right]. \quad (4.39)$$

By so doing, the instantaneous variability of the relative concentration is taken into account by means of the cross terms. Expression (4.39) is similar to the parameterization for the relative skewness used by *Luhar et al.* (2000), but in their formulation the value of the skewness S_z was assumed equal to the meandering one S_{zm} , which is valid only close to the source, as discussed previously.

It must be noticed that since the parameterization (4.38) already includes reflections, the relative dispersion parameter $\tilde{\sigma}_z$ is parameterized similarly to *Franzese* (2003):

$$\tilde{\sigma}_z = \frac{at_*^3}{[1 + (at_*^2/b)^{2/3}]^{3/2}}, \quad (4.40)$$

where the parameters $\tilde{a} = 1/2(0.4w_*^3/z_i)$ and $b = 100$ are chosen in a way that $\tilde{\sigma}_z \sim \sigma_{zr}$ close to the source and $\tilde{\sigma}_z \propto t$ at large distances.

If parameterization (4.39) is used in Gifford's formula (4.6), the resulting absolute mean concentration is more similar to the value of \bar{c} directly calculated by the LES, as shown in Figure 4.12c. In particular, it is evident that the position of the maximum concentration (indicated in the figure by the dashed line) is better reproduced, especially at short distances ($t_* < 1$) where the reflection by the ground occurs. The importance of calculating correctly the position of the maximum concentration is corroborated by analyzing the evolution of the ground concentration shown in Figure 4.12d. The value of \bar{c} at ground calculated directly by the LES (continuous line) agrees satisfactorily with the water-tank data by *Willis and Deardorff* (1978). If the relative concentration \bar{c}_r is used directly in Gifford's formula (4.6), the resulting absolute ground concentration (dashed-dotted line)

4.5. Conclusions

underestimates sensibly the LES results. If parameterization (4.39) is used instead, the resulting absolute ground concentration (dashed line) is closer to the LES results. Discrepancies still exist especially at distances $0.5 < t_* < 1$, which may indicate the need for a better parameterization of the relative concentration. Discrepancies between the calculated mean concentration and the LES results are also noticeable near the top of the CBL. This result is explained by the fact that a simple parameterization like equation (4.38) does not consider the difference between the reflection at ground and in the inversion zone. When the plume reaches the ground it is simply reflected by the surface, because no deposition is taken into account in the model. The entrainment zone, on the contrary, does not act like a simple reflecting barrier, because the structure of the turbulence in that area is very complex and the plume can be transported even beyond z_i . This effect is evident at distances $t_* > 1.5$, when the position of the maximum concentration calculated by using parameterization (4.39) (Figure 4.12c) is underestimated when compared to the one directed calculated by the LES (Figure 4.12a). In this case, the direct use of the relative concentration \bar{c}_r gives a better results (Figure 4.12b).

4.5 Conclusions

By means of Large Eddy Simulation (LES), plume dispersion in the atmospheric Convective Boundary Layer (CBL) was studied in two reference systems: the absolute coordinate system, and the coordinate systems relative to the plume's instantaneous center of mass. By so doing, it was possible to separate the different contributions of small- and large-scale motions on the plume's evolution. In the relative coordinate system, in fact, the (vertically) inhomogeneous meandering motion was removed, and only the small homogeneous turbulent eddies contributed to the dispersion process.

The evolution, shape, and symmetry of the scalar distribution was first analyzed by calculating the mean plume position, the dispersion parameters (variance), and the skewness of the plume position in both the coordinate systems. In particular, the analysis of the third-order moments showed that the structure and the symmetry of the scalar distribution was affected by both the turbulent characteristics of the CBL (inhomogeneity of the vertical large-scale motion), and the presence of the boundary conditions (surface and top of the CBL). In fact, the skewness of the plume's center-line position was mainly influenced by the meandering of the plume as it was transported by the updrafts and dowdrafts. On the contrary, the skewness of the relative position was mainly affected only by the reflection of the plume by the CBL boundaries, because in the relative coordinate system the large-scale motion was removed. However, it is noteworthy that the third-order moment of the absolute position is not balanced by the sum of the meandering and relative diffusion contributions, but non-linear cross terms generated by the reflection of the plume by the boundaries have to be taken into account.

Mean concentrations and concentration fluctuations were also studied in absolute and relative coordinate systems. In particular, the internal (in-plume) mixing of the scalar within the plume was analyzed by calculating the intensity of relative concentration fluctuation i_{cr} . The evolution of i_{cr} was used in the parameterization of the probability distribution function (PDF) of the relative concentration, showing a very good agreement with the LES results.

Finally, the validity of Gifford's formula, which relates the absolute concentration's high-order

moments to the relative concentration and the PDF of the plume's centerline, was studied. It was found that, due to the presence of the CBL boundaries, Gifford's formula is not able to correctly reproduce the value of the absolute mean concentration, especially near to the ground. This result was explained in terms of the effect of the reflection of the plume by the boundaries, which causes the relative concentration to depart from a Gaussian distribution and to become skewed. As a result, the need of using a local average for the calculation of the relative mean concentration in Gifford's formula was shown. Alternatively, the results were improved by using a parameterization for the relative mean concentration that takes into account the skewness of the relative plume position.

However, the present study indicates the need of further investigation for the effect of the CBL boundaries on dispersion. In particular, the evolution, the structure, and the shape of the relative concentration need to be further analyzed in order to find a suitable parameterization for the locally-averaged relative concentration, to be used in Gifford's formula when the plume is affected by the CBL boundaries.

Chapter 5

Dispersion of a passive tracer in buoyancy- and shear-driven boundary layers

5.1 Introduction

Atmospheric dispersion is a process governed by the turbulent characteristics of the Atmospheric Boundary Layer (ABL). The structure of the ABL during convective conditions (Convective Boundary Layer, hereafter CBL) is strongly influenced by the combination of the thermal (buoyancy) and the mechanical forcing (wind shear). In very unstable conditions ($-z_i/L > 10$ where z_i is the height of the CBL and L the Monin-Obukhov length) buoyancy is the main driving mechanism for the turbulence production through the whole layer, and the flow field is characterized by large subsidence motions of cold air (downdrafts) surrounded by narrow strong updrafts of warm air. The effect of this asymmetric turbulent structure on dispersion was widely investigated by means of laboratory experiments (*Willis and Deardorff*, 1976; *Willis and Deardorff*, 1981; *Deardorff and Willis*, 1985 and *Weil et al.*, 2002), field campaigns (*Briggs*, 1993) and numerical simulations using fine-scale models which resolved explicitly the most relevant scales of the CBL (*Lamb*, 1982; *Henn and Sykes*, 1992; *Nieuwstadt and de Valk*, 1987; *Nieuwstadt*, 1992; *Liu and Leung*, 2001).

In contrast with this flow, the structure of the CBL in conditions of weaker stability ($-z_i/L < 10$), when the flow is forced by the combined effect of buoyancy and shear, was studied recently and the formation of two-dimensional roll structures aligned with the wind was observed. The turbulent field was classified according to scaling parameters such as the shear-buoyancy ratio u_*/w_* (where u_* is the friction velocity and $w_* = (\frac{g}{\theta} z_i \overline{w'\theta'})^{1/3}$ is the convective velocity scale) and it was found to be different from either the pure convective or pure shear flow, as shown for example by *Moeng and Sullivan* (1994) and *Sykes and Henn* (1989). Here, g is the acceleration of gravity, θ is the potential temperature, w is the vertical velocity, primes indicate perturbations, and an overbar indicates averaging.

However, less is known about the dispersion in this situation of weak and moderate convection ($-z_i/L < 10$) as pointed out by *Weil* (1988). Only a few studies (*Mason*, 1992; *Gopalakrishnan and Avissar*, 2000; *Luhar*, 2002; *Fedorovich and Thäter*, 2002) have investigated dispersion

The content of this Chapter has been published in *Journal of Applied Meteorology* (**42**, 8, 1116-1130, 2003) with J. Vilà-Guerau de Arellano, A.A.M. Holtslag and P.J.H. Bultjes as co-authors.

in a convective boundary layer driven by both shear and buoyancy. In those works, results from (mainly) stochastic models and wind tunnel experiments were presented, and only *Mason* (1992) used a Large-Eddy Simulation model to investigate the evolution of the dispersion parameters. In his study, however, a clear systematic relationship between the properties of the turbulent flow and the dispersion characteristics under various stability regimes was missing.

Here we use a Large-Eddy Simulation (LES) to generate CBLs with different combinations of surface heat flux and geostrophic wind. The simulated CBLs range from pure convective to near-neutral conditions, and they are classified according to scaling parameters such as u_*/w_* and $-z_i/L$. The dispersion characteristics of a plume of passive scalar released at different heights are studied as a function of these dimensionless parameters. In addition, the effect of the increasing wind shear on the plume meandering and the concentration fluctuations is discussed in relation to the different stability regimes.

Once the dispersion process is described in terms of the scaling parameters, we propose parameterizations for the dispersion parameters σ_z and σ_y for flows driven by the combined effect of buoyancy and shear. In conditions of weak convection, in fact, the understanding of the dispersion process still presents large uncertainties (*Weil*, 1988) and suitable parameterizations of the dispersion parameters are therefore needed.

In Section 5.2 we describe the numerical code used and the classification of the various simulated CBLs. The LES results for the flow structure and dispersion characteristics are thoroughly discussed in Section 5.3, where they are validated for the pure convective cases, for which extensive datasets are available. The effect of increasing wind shear on the flow dynamics (velocity variances) and dispersion statistics is then studied in Section 5.4. The parameterizations for the dispersion parameters in buoyancy- and shear-driven boundary layers (BLs) are proposed in Section 5.5 and validated against the LES results. Symbols are listed and defined in the Appendix.

5.2 Description of the numerical experiment

The LES code used in this work is described by *Cuijpers and Duynkerke* (1993) and *Siebesma and Cuijpers* (1995), in which a set of filtered prognostic equations for the dynamic variables (wind velocity, potential temperature, turbulent kinetic energy) is solved on a staggered numerical grid. The subgrid fluxes are closed by relating them to the gradient of the solved variable by means of an exchange coefficient. A conservation equation for the passive tracer is added to the governing set of equations. It reads

$$\frac{\partial \bar{\psi}}{\partial t} = -\bar{u}_i \frac{\partial \bar{\psi}}{\partial x_i} - \frac{\partial \overline{u'_i \psi'}}{\partial x_i}, \quad (5.1)$$

where $\bar{\psi}$ is the mean (filtered) scalar concentration, \bar{u}_i is the mean wind and $\overline{u'_i \psi'}$ is the subgrid flux. The space and time integrations are computed with a Kappa (*Vreugdenhil and Koren*, 1993) and a Runge-Kutta numerical schemes respectively. Lateral periodic boundary conditions are imposed for all the variables. However, as soon as the scalar reaches the lateral boundaries the simulation is ended, as the plume statistics becomes meaningless. A time step of 1 s. is used.

Four different values of the geostrophic wind (0.5, 5, 10, 15 m/s) and three different surface heat

5.2. Description of the numerical experiment

Cases	$U_g (ms^{-1})$	$-z_i/L$	u_*/w_*	S_*
B1	0.5	7.5×10^4	0.02	0
B2	0.5	1.8×10^4	0.03	0
B3	0.5	5.8×10^3	0.04	0
B4	5	100	0.15	0.17
B5	5	41	0.21	0.27
SB1	5	18	0.27	0.74
SB2	10	7.8	0.34	0.88
S1	10	4.0	0.46	2.1
S2	15	3.4	0.47	1.6
NN	15	1.9	0.59	3.1

Table 5.1: Classification of the different simulated cases. For the definition of the dimensionless shear S_* see equation (5.31).

fluxes (0.052, 0.1, 0.156 mK/s) are prescribed in order to generate CBLs with different combinations of thermal and mechanical forcing.

The numerical domain covers an area of 10 Km x 10 km solved with a horizontal grid length of 62.5 m. A grid of 40 points is used in the vertical direction; the vertical grid spacing (25 m, 30 m and 50 m) is modified, depending on the case being investigated, on the basis of the different initial conditions (surface heat flux). The CBL height is computed analyzing the vertical profile of a inert tracer continuously released by means of a constant surface flux. The value of the roughness length z_0 is set to 0.15 m for all the cases. The aspect ratio, that is, the ratio between the horizontal domain dimension to the CBL height, varies from 6.6 for the most convective case ($z_i \sim 1500$ m) to 12 for the near-neutral one ($z_i \sim 800$ m).

An initialization period (i.e., the period of CBL development) of 4 hours is needed to insure that a (quasi)stationary state is reached for all the simulated flows. The simulated wind profiles are characterized by shear at the bottom and at the top of the BL. Moreover, for high values of the geostrophic wind, a change of the wind direction with height is observed.

The simulated CBLs are classified according to the values of the shear-buoyancy ratio u_*/w_* . When $u_*/w_* > 0.35$, two-dimensional roll structures appear in the velocity fields aligned with the mean wind direction, as shown by the numerical simulation of *Sykes and Henn* (1989). This change in the turbulent pattern can influence the diffusion process because of the disruption of the horizontal turbulence's isotropy and the increase of the horizontal velocity variances.

To complete this classification, the stability parameter $-z_i/L$ is used, following *Holtslag and Nieuwstadt* (1986), to define the four simulated BL archetypes used in this study: pure-convective BL (cases B1 trough B5: $-z_i/L \geq 40$, $u_*/w_* \leq 0.2$), shear-buoyancy-driven BL (cases SB1 and SB2: $u_*/w_* = 0.25$ and $u_*/w_* = 0.35$, respectively), shear-driven BL (cases S1 and S2, $-z_i/L \sim 4$, $u_*/w_* \sim 0.46$) and near-neutral BL (case NN, $-z_i/L \sim 2$, $u_*/w_* = 0.58$). The initial conditions and the dimensionless parameters for the simulated cases are summarized in Table 5.1.

An instantaneous line source (ILS) of scalar (non-buoyant tracer) is emitted along the x axis at

two different heights ($z_s/z_i = 0.078$ and $z_s/z_i = 0.48$, where z_s is the release height) after a well mixed boundary layer has been established (i.e. at the beginning of the fifth hour of simulation). These two emission heights are selected to study the diffusion process from both a "near-ground" (i.e. in the surface layer, $z_s < 0.1z_i$) and an "elevated" release.

The line source measured two grid spacings in the vertical direction and one grid spacing in the horizontal (y) direction. The line source can be equivalently interpreted in terms of a continuous point source (CPS) by using the relationship $t = x/\bar{u}$ as explained by *Willis and Deardorff* (1981) and *Nieuwstadt and de Valk* (1987). As the numerical grid moves with the mean wind along the x direction, this relationship transforms the numerical x coordinate in the physical elapsed time after the release of the scalar. The line source after a certain time t is equivalent to the time evolution of the concentration pattern of a scalar released from a CPS at a certain distance $x = \bar{u}t$.

For each simulated case, three different realizations are performed, in which the horizontal position of the instantaneous release was changed. The results are subsequently ensemble-averaged over the different realizations and the above-mentioned CBL classification.

In order to analyze the dispersion characteristics of the plumes in the various flows, it is convenient to introduce the statistical parameters used in our study.

The vertical and horizontal dispersion parameters σ_z and σ_y are defined according to *Nieuwstadt* (1992) as follows:

$$\sigma_z^2 = \frac{\int c(z - \bar{z})^2 dV}{\int c dV} \quad \text{and} \quad (5.2)$$

$$\sigma_y^2 = \frac{\int c(y - \bar{y})^2 dV}{\int c dV}, \quad (5.3)$$

where c is the space-dependent concentration, $dV = dx dy dz$, and \bar{z} and \bar{y} are the mean plume height and the mean plume horizontal position, respectively, defined according to

$$\bar{z} = \frac{\int cz dV}{\int c dV} \quad \text{and} \quad (5.4)$$

$$\bar{y} = \frac{\int cy dV}{\int c dV}. \quad (5.5)$$

The spatial integration along the x coordinate is equivalent to the physical time integration, due to the equivalence between ILS and CPS discussed earlier.

Because in many experimental studies (e.g., the water-tank experiments of *Willis and Deardorff*, 1976; *Willis and Deardorff*, 1981) the vertical dispersion parameter is calculated as the displacement from the source height, rather than from the mean plume height, we computed also this vertical dispersion parameter σ'_z defined as

$$\sigma'^2_z = \frac{\int c(z - z_s)^2 dV}{\int c dV}. \quad (5.6)$$

5.3. Dispersion in a pure-convective boundary layer

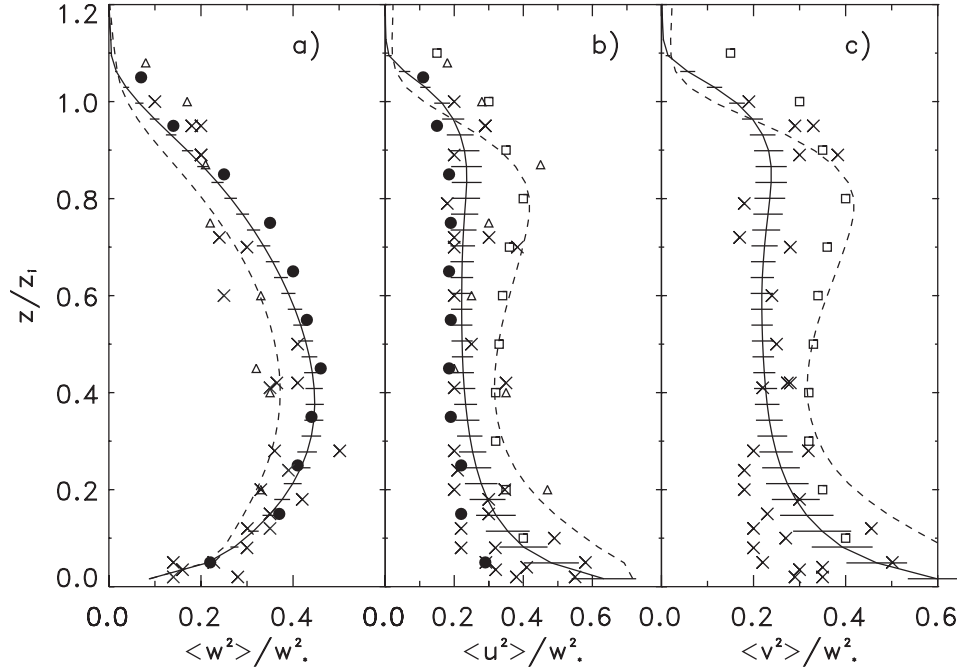


Figure 5.1: Dimensionless vertical profiles of the velocity variances for the pure-convective cases B1-B5. The LES results and standard deviation are represented by continuous line and horizontal bars respectively. The following data from laboratory experiments and field campaigns are shown: \bullet Willis and Deardorff (1974); \times Lenschow *et al.* (1980); \triangle Deardorff and Willis (1985); \square average of field measurements of Caughey and Palmer (1979) as reported by Schmidt and Schumann (1989). The LES results for the SB1-SB2 cases ($u_*/w_* \sim 0.3$) are also shown as dashed line.

The dimensionless crosswind-integrated concentration C_y , is calculated (Nieuwstadt and de Valk, 1987) by

$$C_y = \frac{z_i \int c dx dy}{\int c dV}. \quad (5.7)$$

Last, from the concentration's time series, the concentration fluctuation is derived using

$$\sigma_c^2 = \frac{\int (c - \bar{c})^2 dt}{\Delta t}, \quad (5.8)$$

where $t = x/\bar{u}$, $\Delta t = 1$ hour, and the time-averaged concentration

$$\bar{c} = \frac{\int c dt}{\Delta t} \quad (5.9)$$

5.3 Dispersion in a pure-convective boundary layer

In this Section, we discuss the dynamics and the dispersion characteristics simulated by means of LES under pure convective conditions (averaged over the cases B1-B5, $u_* < 0.3$). They are

presented not only in order to confirm the correct behavior of the model by comparing them with available laboratory and atmospheric experiments, but also as a reference point for the simulations when shear is introduced.

We first analyze the vertical profiles of the velocity variances as they provide direct information on the flow structure and are directly related to the dispersion parameters. The diffusion characteristics (plume spread and ground concentrations) are next discussed and are compared with the experimental data. Various commonly used parameterizations (interpolations of laboratory or numerical results) designed for buoyancy-driven boundary layers are further compared with the LES results.

5.3.1 Velocity variances

Figure 5.1 shows the profiles of vertical and horizontal velocity variances scaled with the convective velocity scale w_*^2 . The velocity variances are calculated as space (cross horizontal) and time (one hour) average of the velocity fluctuations. Various experimental data (laboratory and field campaign) are also shown for comparison (*Willis and Deardorff*, 1974; *Lenschow et al.*, 1980; *Deardorff and Willis*, 1985; *Caughey and Palmer*, 1979). Although the scatter in the measurements is large, the LES results are in reasonable agreement. A maximum value of $\langle w^2 \rangle / w_*^2$ of around 0.42 is found at $z/z_i = 0.4$, in agreement with previous numerical simulations (*Schmidt and Schumann*, 1989; *Moeng and Sullivan*, 1994; *Henn and Sykes*, 1992; *Nieuwstadt et al.*, 1991, not shown in the Figures). On the other hand, although both the calculated profiles of horizontal variances, $\langle u^2 \rangle / w_*^2$ and $\langle v^2 \rangle / w_*^2$, are in close accord with the data of *Willis and Deardorff* (1974) and *Lenschow et al.* (1980), they significantly underestimate the Minnesota and Ashchurch data by *Caughey and Palmer* (1979) and the water-tank data by *Deardorff and Willis* (1985) (Figures 5.1b and 5.1c). Our LES data however are in agreement with other numerical simulations (*Schmidt and Schumann*, 1989; *Moeng and Sullivan*, 1994; *Henn and Sykes*, 1992; *Nieuwstadt et al.*, 1991). Moreover, in the very recent water-tank experiment by *Weil et al.* (2002), from the least-square fit of the horizontal dispersion data (for a plume released at $z_s/z_i = 0.15$) they extrapolated a value of $\sigma_v/w_* = (\langle v^2 \rangle / w_*^2)^{1/2} = 0.51$ in agreement with our numerical simulation results.

As suggested by *Schmidt and Schumann* (1989), in a pure CBL, buoyancy is the main production term of vertical variance, whereas the horizontal variance, driven by pressure fluctuations, is really only important near the surface. In their opinion the data by *Deardorff and Willis* (1985) were influenced by shear caused by the horizontal inhomogeneities in the surface heat flux. Also, the data by *Caughey and Palmer* (1979) may have been influenced by surface shear. In fact, we note that the variances calculated by the LES for the SB cases ($u_*/w_* = 0.3$, also shown in Figure 5.1) are in better agreement with their results.

5.3.2 Mean plume height and dispersion parameters

Near-ground release

Figures 5.2 shows the dispersion characteristics (mean plume height, vertical and horizontal dispersion parameter) for a near-ground release ($z_s/z_i = 0.078$). The dimensionless space (time) is

5.3. Dispersion in a pure-convective boundary layer

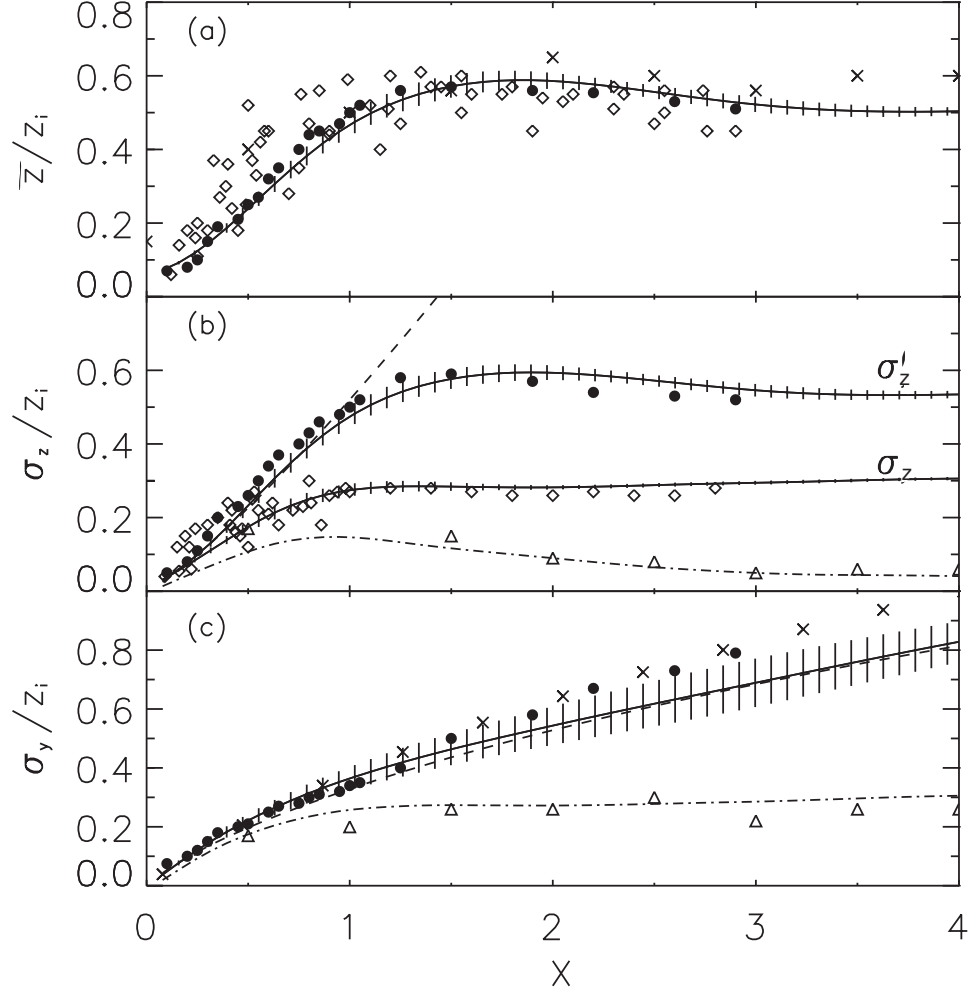


Figure 5.2: a) Mean plume height in a pure convective boundary layer (cases B1-B5) for a near-ground release as function of the dimensionless distance (time) X defined by equation (5.10). The LES results and standard deviations are represented with solid line and vertical bars, respectively. The following laboratory experiments and field data are shown: \bullet Willis and Deardorff (1976); \times Weil et al. (2002); \diamond Briggs (1993). b) Vertical dispersion parameter as calculated from the LES results by equation (5.2) (σ_z) and (5.6) (σ'_z). The laboratory experiments by Willis and Deardorff (1976) (\bullet) and Briggs (1993) (\diamond) are also shown. The dashed line represents equation (5.11). The dashed-dotted line represents the meandering component calculated by the LES compared with the water-tank data by Weil et al. (2002) (\triangle). c) Horizontal dispersion parameter as calculated by the LES (solid line) and parameterized according to equation (5.14) (dashed line). The following laboratory experiments and field data are shown: \bullet Willis and Deardorff (1976); \times Weil et al. (2002). The dashed-dotted line represents the meandering component calculated by LES compared with the water-tank data by Weil et al. (2002) (\triangle).

defined as:

$$X = \frac{w_*}{z_i} \frac{x}{\bar{u}} = \frac{w_*}{z_i} t. \quad (5.10)$$

Although the scatter in the CONDORS data (*Briggs*, 1993) is large, the mean plume height calculated by the LES (Figure 5.2a) is in satisfactory agreement with the experiments (in particular with the water-tank results).

In Figure 5.2b, the LES results for the vertical dispersion parameter, as calculated by both equations (5.2) and (5.6) are shown. As mentioned earlier, the two differ in that one uses the release height whereas the other uses the mean plume height in the definition of the vertical dispersion parameter. The LES results are compared with the laboratory data by *Willis and Deardorff* (1976) and the CONDORS data by *Briggs* (1993), and they are found to be in good agreement with the experimental data in both cases.

For short times ($X < 1$) the model results fit well with the expression

$$\frac{\sigma'_z}{z_i} = 0.52X^{6/5}, \quad (5.11)$$

which is very similar to that proposed by *Lamb* (1982), who suggested $\frac{\sigma'_z}{z_i} = 0.5X^{6/5}$, for $X < 6/5$ in case of near-ground release ($z_s/z_i < 0.1$).

The LES results for the horizontal dispersion parameter (Figures 5.2c) are in very good agreement with the laboratory data for $X < 2$. Several parameterizations (extrapolation of numerical results or experimental campaign) were proposed in the literature. The numerical results by *Lamb* (1982) suggested

$$\begin{cases} \frac{\sigma_y}{z_i} = \frac{3}{5}X & X < \frac{1}{6} \\ \frac{\sigma_y}{z_i} = \frac{1}{3}X^{2/3} & \frac{1}{6} < X < 3, \end{cases} \quad (5.12)$$

whereas *Briggs* (1985) suggested

$$\frac{\sigma_y}{z_i} = \frac{0.6X}{(1 + 2X)^{1/2}} \quad (5.13)$$

as best fit to many different experimental data (both surface and elevated release). As suggested by *Briggs* (1985), equation (5.13) might be regarded as the limiting minimum value for the horizontal dispersion parameter for the CBL, with higher values expected in presence of wind shear. In the same Figure, we depict the following relationship derived from experimental data (*Gryning et al.*, 1987):

$$\frac{\sigma_y}{z_i} = \frac{\sigma_v/z_i t}{(1 + t/2T_v)^{1/2}} = \frac{\sigma_v/w_* X}{(1 + \frac{X}{2T_v} \frac{z_i}{w_*})^{1/2}}, \quad (5.14)$$

which is in excellent agreement with the LES results. The Lagrangian time T_v is parameterized following *Luhar* (2002) as:

$$T_v = 1.7 \left(\frac{\sigma_v}{w_*} \right)^2 \frac{z_i}{w_*} \sim 300s, \quad (5.15)$$

5.3. Dispersion in a pure-convective boundary layer

and it is in agreement with the experimental values of *Weil et al.* (2002).

Although all the equations (5.12), (5.13), and (5.14) fit the LES results within the standard deviation, we consider that equation (5.14) is the one that includes explicitly the dependence of the dispersion parameters on the turbulence, rather than empirical constants either derived by statistical theory or extrapolated by experimental data.

Last, we discuss the decomposition of the (vertical) dispersion parameters into two components, the meandering (m_z) and the relative dispersions (s_z) as proposed by *Nieuwstadt* (1992):

$$\sigma_z^2 = m_z^2 + s_z^2 \quad (5.16)$$

The meandering part describes the contribution of the large-scale turbulent eddy motion, and the relative dispersions quantifies the increasing size of the plume due to small-scale mixing. They are defined as follows:

$$m_z^2 = \frac{\int (z_l - \bar{z})^2 c dV}{\int c dV} \quad (5.17)$$

$$s_z^2 = \frac{\int (z - z_l)^2 c dV}{\int c dV}, \quad (5.18)$$

where the local plume height z_l is defined as

$$z_l = \frac{\int z c dy dz}{\int c dy dz}, \quad (5.19)$$

Similar expressions hold for the horizontal components.

Although *Nieuwstadt* (1992) already studied the differentiation between meandering and relative diffusion, his results were influenced by the small domain used that limited the horizontal scale of motion. Moreover no data (either field campaign nor laboratory studies) were available at that time for the comparison. The meandering components calculated by the LES agrees well with the numerical simulation by *Nieuwstadt* (1992), the laboratory data, and the theoretical analysis by *Csanady* as reported by *Weil et al.* (2002)

$$\begin{cases} m_y = \sigma_y t & X \ll T_v \\ \frac{dm_y^2}{dt} = 0 & X \gg T_v \end{cases} \quad (5.20)$$

which implies that m_y approaches a constant value at large distances.

Elevated release

In Figure 5.3, the dispersion statistics for the plume emitted from an elevated release ($z_s/z_i = 0.48$) are shown. The LES results show a satisfactory agreement with laboratory and experimental data. In Figure 5.3b only σ_z [equation (5.2)] is shown as the mean plume height does not differ too much

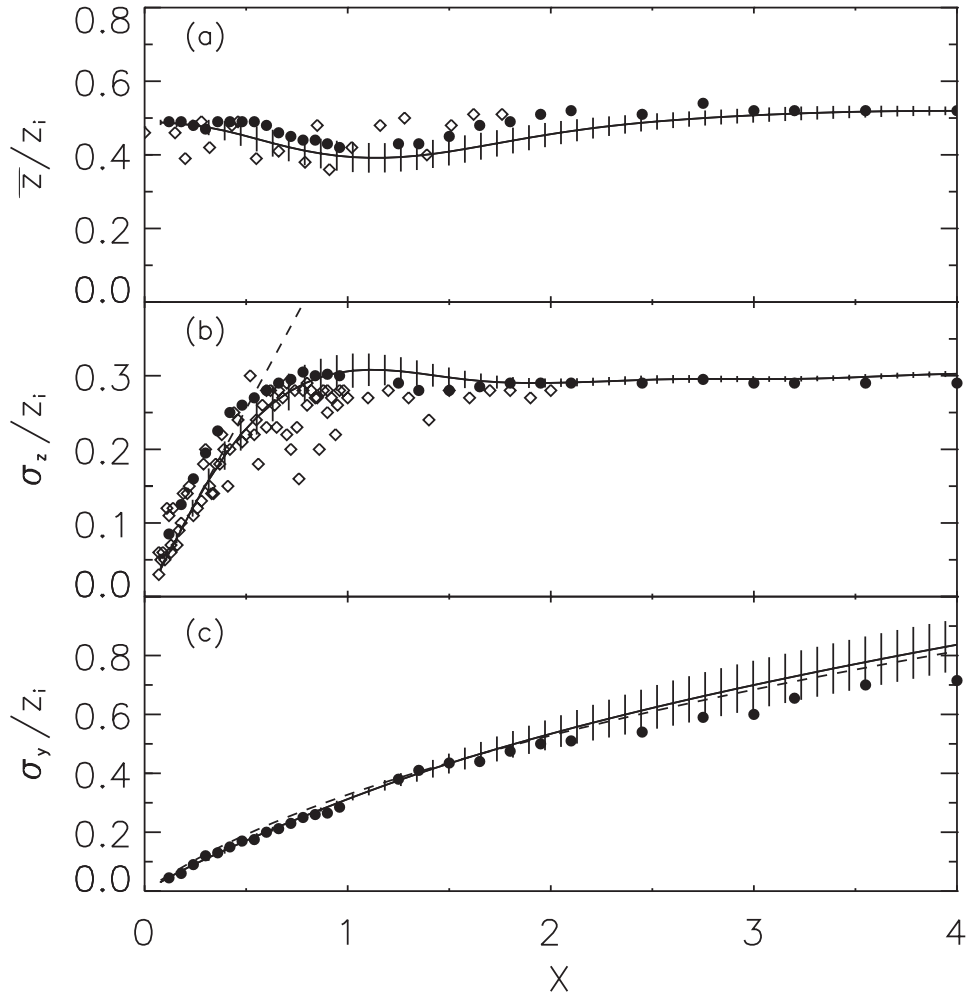


Figure 5.3: As Figure 5.2 but for the elevated emission. The laboratory data by *Willis and Deardorff* (1981) are shown as \bullet ; For the mean plume height (a) the CONDORS data (\diamond) are used as they appeared in *van Haren and Nieuwstadt* (1989). The parameterizations are represented with dashed lines [in (b) equation (5.21); in (c) equation (5.14)].

5.3. Dispersion in a pure-convective boundary layer

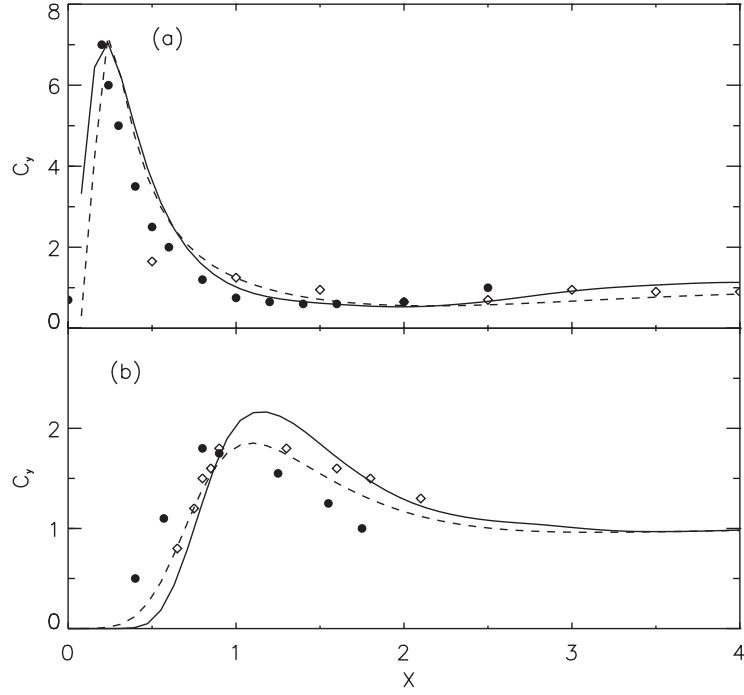


Figure 5.4: Crosswind-integrated ground concentrations for a near-ground release (a) and an elevated release (b) in the pure-convective cases B1-B5. The LES results are represented with the continuous line. The following laboratory data are shown: in (a) ● *Willis and Deardorff* (1976); ◇ *Weil et al.* (2002). In (b) ● *Willis and Deardorff* (1981). The numerical results by *Lamb* (1982) are also shown (◇). For both the release height the empirical formula by *Briggs* (1985) is shown as dashed line [equation (5.24)].

($\sim 15\%$) from the initial release height (Figure 5.3a), and in consequence $\sigma_z \sim \sigma'_z$. The best fit for the LES results at short times is the following relationship:

$$\frac{\sigma_z}{z_i} = 0.52X \quad (5.21)$$

which is in good agreement with the parameterization suggested by *Lamb* (1982) for $X < 2/3$ for elevated releases: $\frac{\sigma_z}{z_i} = 0.5X$.

The results for the horizontal dispersion parameter are shown in Figure 5.3c. They are very similar to the experimental data obtained by *Willis and Deardorff* (1981) up to $X = 2$.

Some further considerations can be addressed by comparing the horizontal dispersion results for the near-ground release (Figure 5.2c) with the elevated release (Figure 5.3c). As pointed out by *Briggs* (1985) and confirmed by our LES results, the horizontal spread at short distances ($X < 1$) for a near-ground release grows faster than that of the elevated release. This is due to the conversion of vertical motion into horizontal at the base of the updrafts and the downdrafts near the surface. In spite of these differences, equation (5.14) reproduces correctly (within the standard deviation) the horizontal spread for both the releases (near-ground and elevated).

On the contrary, at large distances the LES results have the same values independent of the release height. This result is explained by the fact that the plume released near the ground is rapidly raised

up by the updrafts and is above the surface layer at distances $X > 0.3$. Because the vertical profile of $\langle v^2 \rangle / w_*^2$ remains constant above the surface layer (Figure 5.1c), one expects similar values of the horizontal parameter for both the near-ground and the elevated release. This is consistent with the analysis of *Briggs* (1993), who shows that the empirical fit of CONDORS data for the near-ground release approaches that for the elevated release as time increases. *Lamb* (1982) suggested the same empirical formulation for σ_y/z_i both for near-ground and elevated releases, for $X > 1$:

$$\frac{\sigma_y}{z_i} = \frac{1}{3}X^{2/3} \quad (5.22)$$

which agrees well with our LES results.

5.3.3 Non dimensional crosswind-integrated ground concentrations

Figure 5.4 shows the normalized crosswind-integrated ground concentrations [C_y calculated by means of equation (5.7) at $z=0$] for the near-ground and the elevated release. The cross section of the normalized crosswind-integrated concentrations (contours of C_y as function of height) will be shown in the following Section (Figures 5.8a and 5.9a). For the near-ground release, the pattern generally agrees with the laboratory results of *Willis and Deardorff* (1976) and other numerical simulations (*Nieuwstadt and de Valk*, 1987; *Lamb*, 1978). The maximum occurs at $X = 0.25$ in close agreement with the water-tank experiment, and although the LES results slightly overestimate the data by *Willis and Deardorff* (1976) and *Weil et al.* (2002) for $0.25 < X < 1$, they reproduce correctly the slope which follows the expression

$$C_y = 0.9X^{-3/2}, \quad (5.23)$$

suggested by *Nieuwstadt* (1990) and by *Briggs* (1993) as the best fit for the Prairie Grass and CONDORS experimental data, respectively.

The surface minimum due to the fast rise of the plume caught by the updrafts occurs at $X = 1.8$, close to that observed by *Willis and Deardorff* (1976) and the value $C_y = 0.8$ at $X = 1.5$ suggested by *Briggs* (1993).

Several parameterizations exist that are used to predict the ground concentrations. From the laboratory results of *Willis and Deardorff* (1976) and *Willis and Deardorff* (1981), *Briggs* (1985) extrapolated the empirical curve

$$C_y = \frac{0.9X'^{9/2}Z_s^{-11/2}}{[Z_s^{-3/4} + 0.4X'^{9/2}Z_s^{-9/2}]^{4/3}} + \frac{1}{1 + 3X'^{-3/2}Z_s^{1/2} + 50X'^{-9/2}}, \quad (5.24)$$

where $Z_s = z_s/z_i$. This formula reproduces correctly the $X^{-3/2}$ tendency for $0.2 < X < 1$. In addition, it predicts a surface minimum corresponding to the lifting of the tracer in the upper half of the CBL and finally it approaches the uniform vertical mixing asymptote $C_y = 1$ at large distances. Following *Gryning et al.* (1987), in order to fit our LES results the curve is shifted towards higher values of X substituting $X' = 0.8X$.

For the elevated release (Figure 5.4b), we note that the surface maximum occurs at $X = 1.1$, whereas both *Willis and Deardorff* (1981) and *Nieuwstadt and de Valk* (1987) give $C_y = 1.7$ at

5.4. Dispersion in a buoyancy- and shear-driven boundary layer

$X = 0.8$. This suggests that the plume calculated by our LES reaches the ground later than the laboratory experiment. Our results agree with previous numerical simulations by *Lamb* (1982), *Henn and Sykes* (1992), and *Liu and Leung* (2001), whereas in the CONDORS data discussed by *Briggs* (1993) the location of the maximum is unclear (before or after $X = 1$). *Willis and Deardorff* (1981) and *Nieuwstadt and de Valk* (1987) show that the plume lifts off rapidly and the ground concentration reaches a surface minimum around $X = 2.5$. The LES predicts that the tracer remains near the surface at longer distances from the source, with the minimum occurring at $X = 3.5$ (as it can be seen in Figure 5.9a in which the crosswind-integrated concentrations are shown), in agreement with *Lamb* (1982) and *Henn and Sykes* (1992). The faster lifting off in the water-tank may be explained by a small positive buoyancy acquired by the droplets used in their experiment, as suggested by *Willis and Deardorff* (1981).

Although we are aware that a complete validation of a numerical model would require a much wider and deeper comparison with experimental data, in this Section we showed that the LES results are in good agreement with available experimental data, previous numerical studies, and the fitting expressions derived from field campaigns. Therefore we are confident that the LES is able to simulate dispersion under conditions of pure convection.

5.4 Dispersion in a buoyancy- and shear-driven boundary layer

We now discuss the results for the CBL driven by both buoyancy and shear. From here on, all the results are scaled by the velocity scale:

$$w_m^3 = w_*^3 + 5u_*^3. \quad (5.25)$$

This expression was proposed firstly by ? (?) on the scaling of the turbulent kinetic energy equation, and it was modified by *Moeng and Sullivan* (1994) on the basis of their numerical simulation results. The velocity scale w_m takes into account both the characteristic velocity scales for convective and shear driven flows as well as providing a suitable scaling for the second-order moments of turbulence (*Moeng and Sullivan*, 1994).

we similarly define the new dimensionless distance (time) as follows:

$$X_m = \frac{w_m}{z_i} \frac{x}{\bar{u}} = \frac{w_m}{z_i} t. \quad (5.26)$$

5.4.1 Velocity variances

As in the previous Section, we first discuss the LES results for the dynamic variables and then analyze the plume dispersion characteristics. The increasing wind shear modifies the turbulent flow structure, and this modification is reflected by the profiles of velocity variances. As pointed out previously, the dispersion parameters are directly proportional to the velocity variances. As a consequence, a correct calculation of these variables is essential to understand and parameterize the behavior of the dispersion characteristics under different flow regimes.

As pointed out by previous studies (*Sykes and Henn*, 1989; *Moeng and Sullivan*, 1994), buoyancy and shear act differently on the turbulence's structure. The interaction between these two mechanisms results in the disruption of the horizontal isotropy of the flow. According to *Moeng and*

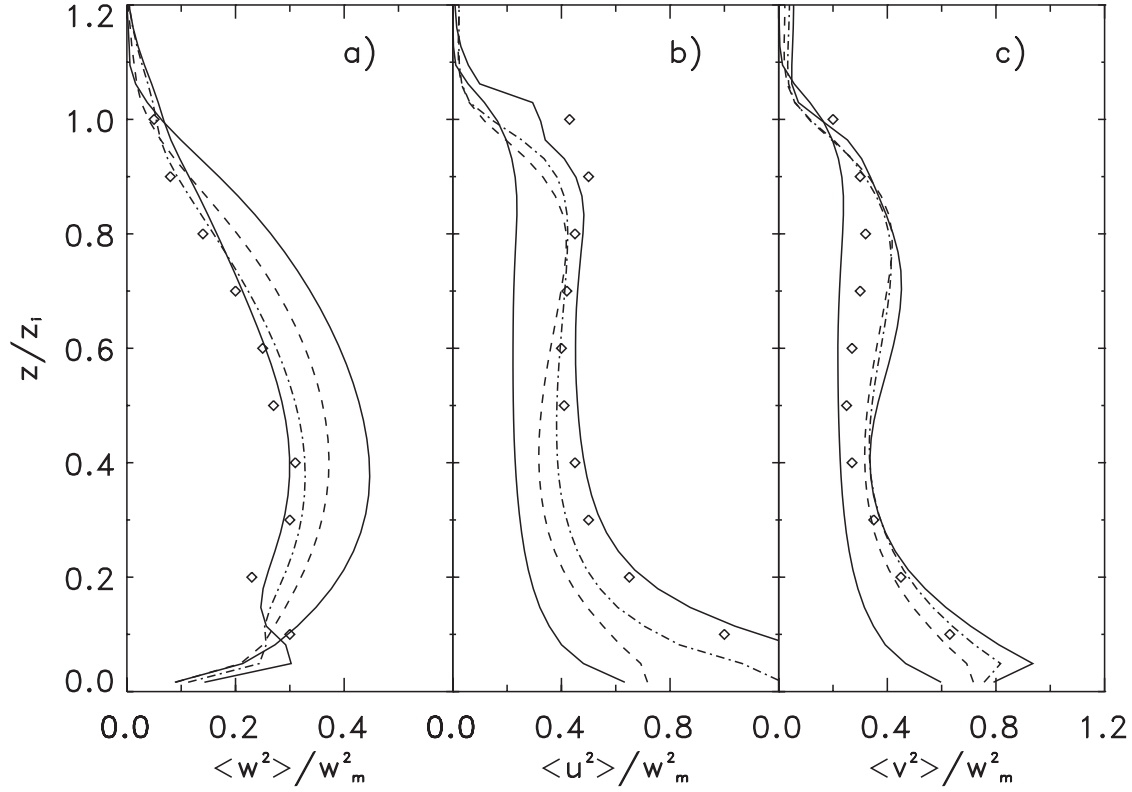


Figure 5.5: Dimensionless vertical profiles of the velocity variances calculated by the LES are shown for all the cases: continuous line (pure buoyancy cases: B1-B5); dashed line (shear-buoyancy cases: SB1-SB2); dotted-dashed line (shear cases: S1-S2); dashed-dotted-dotted-dotted line (near neutral case: NN). For comparison, the numerical results of *Moeng and Sullivan* (1994) for their SB1 case ($u_*/w_* \sim 0.6$) are also shown (\diamond).

Sullivan (1994), in a CBL driven by both shear and buoyancy the turbulent pattern is peculiarly different from either a pure-convective or a neutral situation. In fact, the shear near the ground creates small streaky structures which are lifted up by buoyancy and merged to form two dimensional rolls in the middle of the CBL.

The effect of shear in the u and v wind components is clearly noticeable in Figure 5.5, in which the profiles of the velocity (fluctuations) variances are shown for the run classified according to increasing wind shear (see Section 5.2). Numerical simulations (*Sykes and Henn*, 1989; *Moeng and Sullivan*, 1994) and wind-tunnel measurements (*Fedorovich et al.*, 2001, not shown) show similar profiles of $\langle u^2 \rangle$ and $\langle v^2 \rangle$ characterized by the presence of maxima at the bottom and at top of the CBL. In these regions, in fact, the energy is transferred from the vertical to the horizontal scale, because the thermals are influenced by the shear and the presence of the boundaries. As shown in Figure 5.5a, another important feature is the reduction of the vertical velocity variance by the increasing of wind.

5.4.2 Mean plume height and dispersion parameters

Near-ground release

Figure 5.6 shows the statistics of the dispersion process (mean plume height, vertical and horizontal dispersion parameter) for the near-ground source for all the simulated CBLs, averaged according to the classification discussed above. As pointed out by *Mason* (1992) and *Gopalakrishnan and Avissar* (2000), the mean effect of the increasing wind speed is the reduction of the vertical mixing. This reduction is related to the decrease in the value of the vertical velocity variances profiles, discussed previously.

The mean plume height and the vertical spread (Figures 5.6a and 5.6b) show similar characteristics. As the wind speed increases, the tracer is lifted up more slowly as it is advected horizontally by the wind. As explained previously, the presence of the ground reduces the vertical motion so that the vertical spread grows slowly for the near-ground releases. For the near-neutral case (NN; $-z_i/L = 1.8$) the buoyancy is too weak to lift up the tracer and, in consequence, it remains close to the surface. The vertical spread grows almost linearly up to a distance of $X_m = 1$, and only at very large distances does it slowly reaches an asymptotic limit as the tracer is spread all over the layer. For short distances ($X_m < 1$), the growth of σ'_z/z_i is consistent with the neutral limit proposed by *Briggs* (1985)

$$\frac{\sigma'_z}{z_i} = 0.64 \frac{u_* t}{z_i} = 0.64 \frac{u_*}{w_m} X_m \sim 0.28 X_m, \quad (5.27)$$

which is also shown in the Figure. The growth of σ'_z/z_i for the intermediate cases (SB and S1-S2) lies between the two extreme situations, pure buoyancy and near-neutral, in agreement with other numerical results by *Mason* (1992) and *Gopalakrishnan and Avissar* (2000). A parameterization which encompasses all the cases, from pure buoyancy to neutral situation will be presented and discussed in the next Section.

In Figure 5.6c the results for the horizontal spread (σ_y/z_i) are shown. As the wind shear increases, the horizontal spread is enhanced and, in the near-neutral cases, its value can double that for the pure-convective cases, in agreement with the research conducted by *Mason* (1992) and *Luhar* (2002).

To determine the importance of the shear contribution, we can study the effect of wind shear on the horizontal dispersion by decomposing (*Venkatram*, 1988)

$$\sigma_y^2 = \sigma_{yb}^2 + \sigma_{ys}^2, \quad (5.28)$$

where σ_{yb} refers to the buoyancy-generated dispersion and σ_{ys} is the contribution due to the change in the wind direction with height (shear-generated dispersion). A parameterization for the shear contribution was proposed by *Luhar* (2002) for coastal fumigation models. In the next Section we will use that approach to develop a parameterization for the horizontal dispersion in a buoyancy- and shear-driven boundary layer and it will be compared with the LES results.

Elevated release

Figure 5.7a shows the mean plume height for all the simulated cases for an elevated release. The pure-buoyancy (B1-B5) and the shear-buoyancy cases (SB1-SB2) show a very similar pattern,

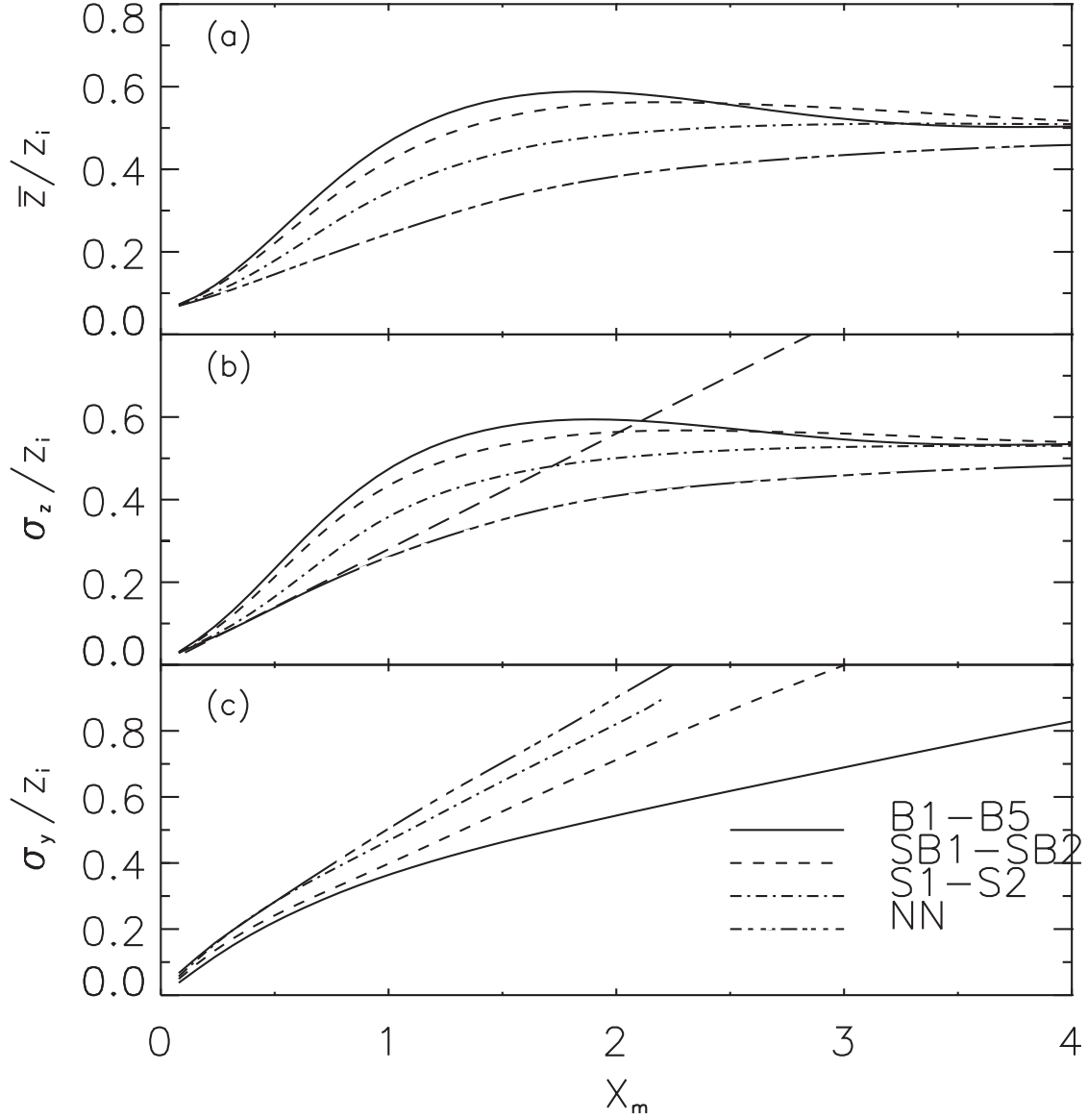


Figure 5.6: (a) Mean plume height, vertical dispersion parameter (b) and horizontal dispersion parameter (c) for a near-ground release for all the cases as calculated by the LES as function of the dimensionless distance (time) X_m defined by equation (5.26). In b) the long-dashed line represents the neutral limit [equation (5.27)].

5.4. Dispersion in a buoyancy- and shear-driven boundary layer

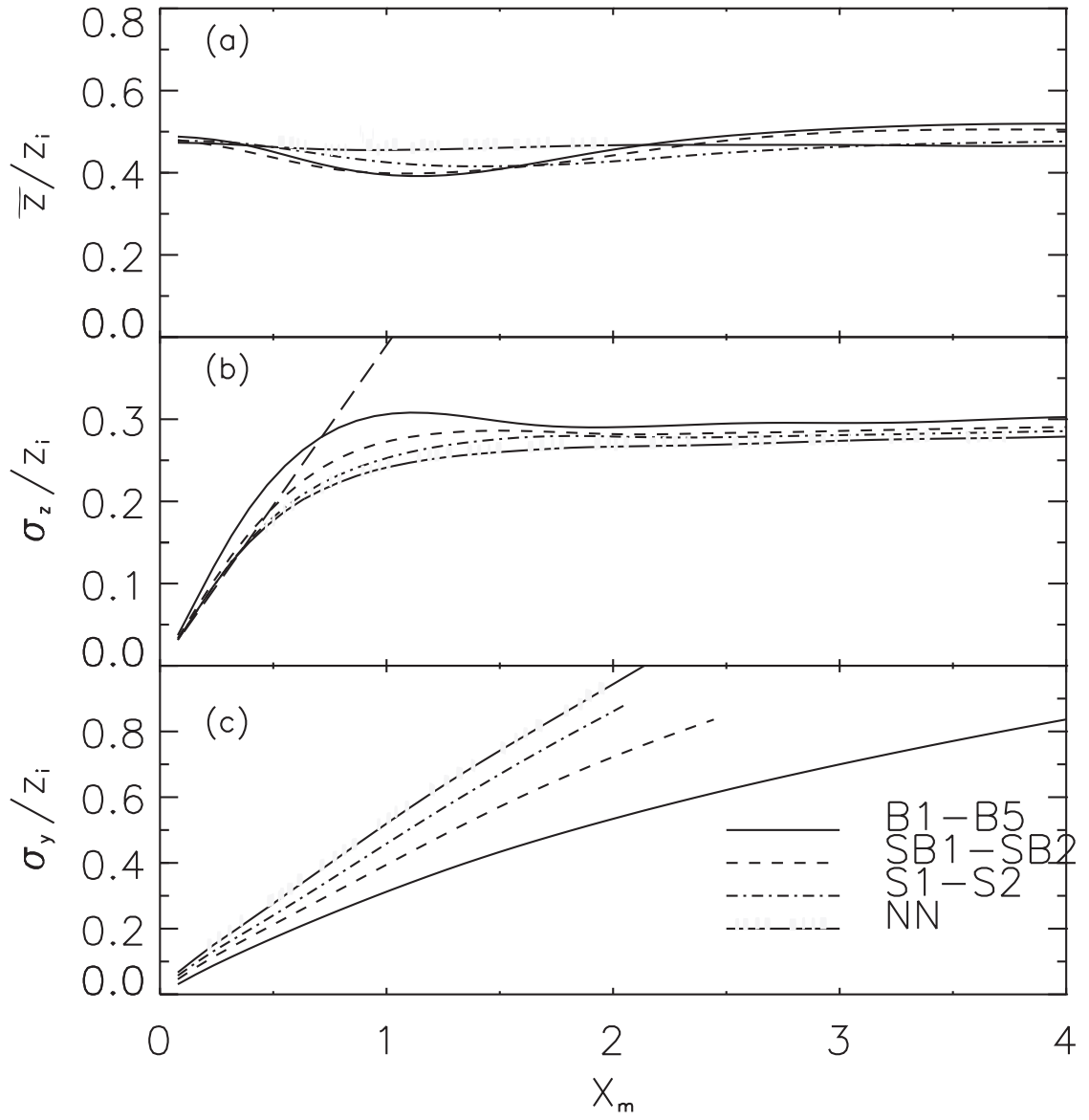


Figure 5.7: As Figure 5.6 but for an elevated release. In (b) the long-dashed line represents the neutral limit [equation (5.29)].

whereas in the shear cases (S1-S2) the minimum in the mean plume height is reached at further distances away from the sources ($X_m = 1.7$), because the tracer is advected horizontally by the wind and simultaneously transported downward. Moreover, in the near-neutral case the mean plume height does not show a sensible displacement from its initial value, as the tracer is scarcely influenced by the thermal forcing.

The vertical and horizontal dispersion parameters are shown in Figure 5.7b and 5.7c respectively. They have the same general behaviors as previously discussed for the near-ground release for all the cases. The vertical spread for short times ($X_m < 0.5$) is generally consistent with the Taylor's law

$$\frac{\sigma_z}{z_i} = \sigma_w \frac{t}{z_i} = 0.51 \frac{w_*}{w_m} X_m, \quad (5.29)$$

as shown for the near-neutral case.

The horizontal spread is enhanced, and far enough away from the source ($X_m > 1$), its value is similar to that for the near-ground release, as discussed previously for the pure-convective cases.

5.4.3 Crosswind-integrated and ground concentrations

Near-ground release

Figures 5.8a-d show the crosswind-integrated concentrations (C_y) for the near-ground release. The relative ground concentrations are shown in Figure 5.8e. C_y is strongly affected by the relative importance of buoyancy and shear. In fact, as the shear-buoyancy ratio increases the tracer is advected horizontally for a longer time before being lifted up by the thermals. In the shear-buoyancy case (SB), the pattern is somewhat similar to the pure convective BL; an elevated maximum is present at $X_m = 2$ but the surface minimum is now extended to $X_m = 3.5$. In the shear cases (S1 and S2, Figure 5.8c) the tracer is transported by the wind for a long time before being lifted up by the weak buoyancy. A surface minimum is present at $X_m = 3$, but the relative elevated maximum is not evident. In the near-neutral case (NN), the wind is so dominant that it keeps the tracer close to the ground even at large distance from the source.

This behavior has an important effect on the ground concentrations, as shown by Figure 5.8e. All the simulated cases show a similar concentration maximum at $X_m = 0.25$. In fact, at very short distances ($X_m < 0.2$), the plume is still in the surface layer, as shown by Figure 5.6a. In this region the vertical structure of turbulence is similar in all the cases, as shown by the value of the vertical velocity variance close to the surface (Figure 5.5a). The vertical dispersion parameter (Figure 5.6b) also shows similar value in all the stability regimes for $X_m < 2$.

At greater distances from the source ($X_m > 0.2$), the different contribution of thermal and mechanical turbulence strongly modifies the vertical dispersion (as shown in Figure 5.6b) and, as a consequence, the ground concentration, which increases markedly with the wind speed. Finally, a common asymptotic value is reached around $X_m = 4$ when the tracer is uniformly spread within the mixed layer.

5.4. Dispersion in a buoyancy- and shear-driven boundary layer

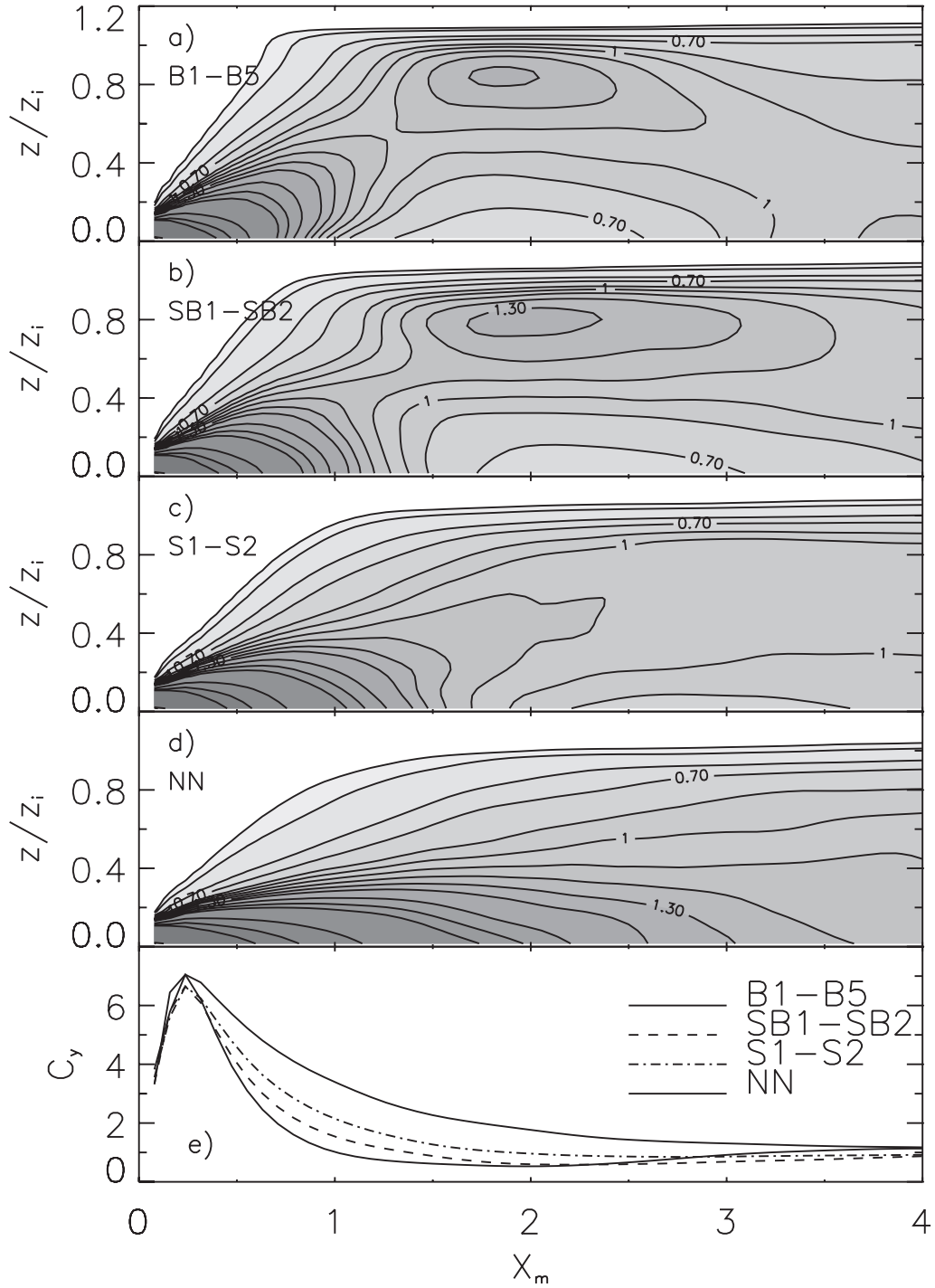


Figure 5.8: a-d): Normalized crosswind-integrated concentrations (C_y) for a near-ground release. Contour lines are shown every 0.1 for $C_y > 1$ and every 0.15 for $C_y < 1$. (e) Ground concentrations (C_y at $z=0$) for all the simulated cases.

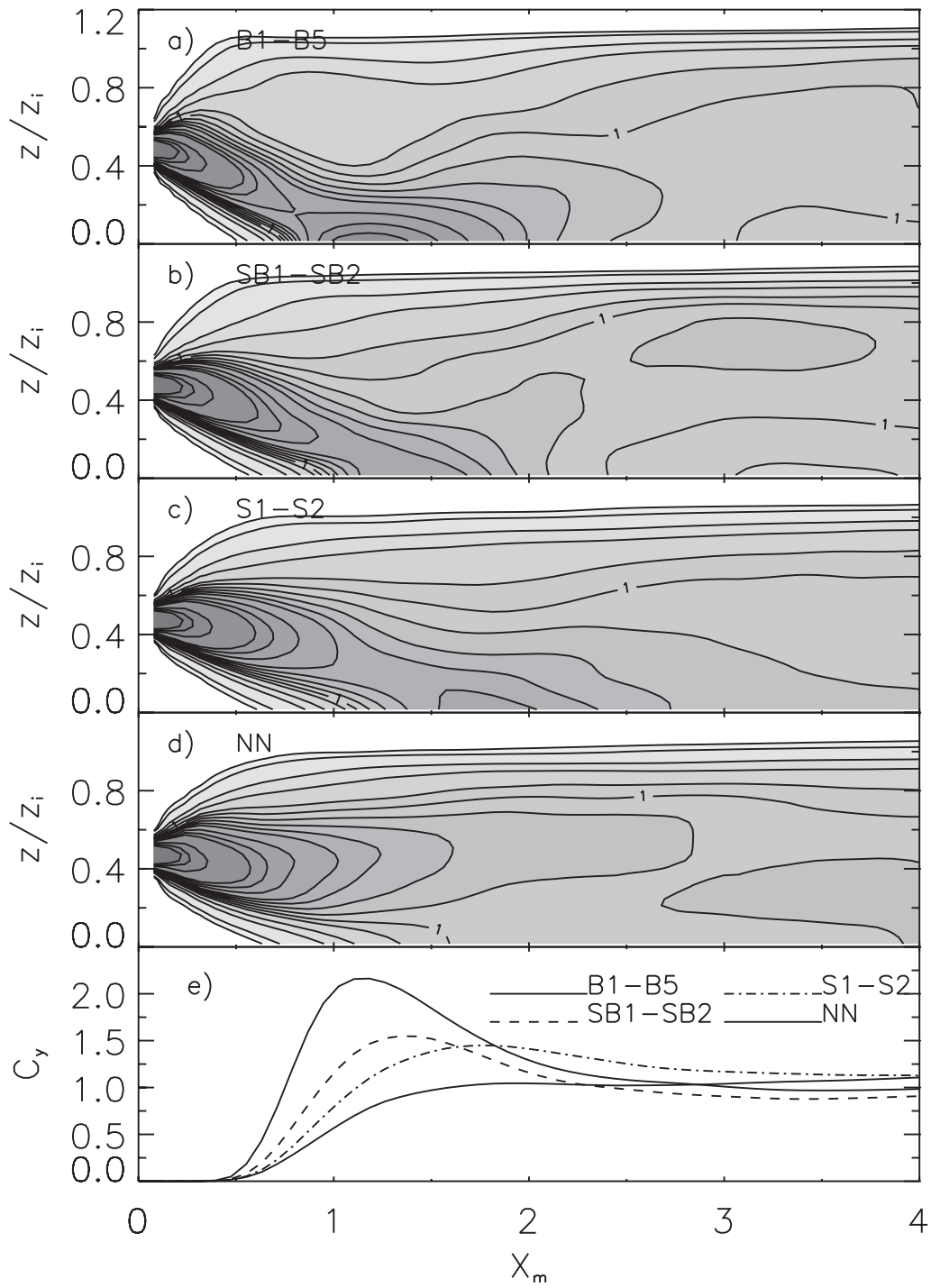


Figure 5.9: Same as Figure 5.8, but for the elevated release.

5.4. Dispersion in a buoyancy- and shear-driven boundary layer

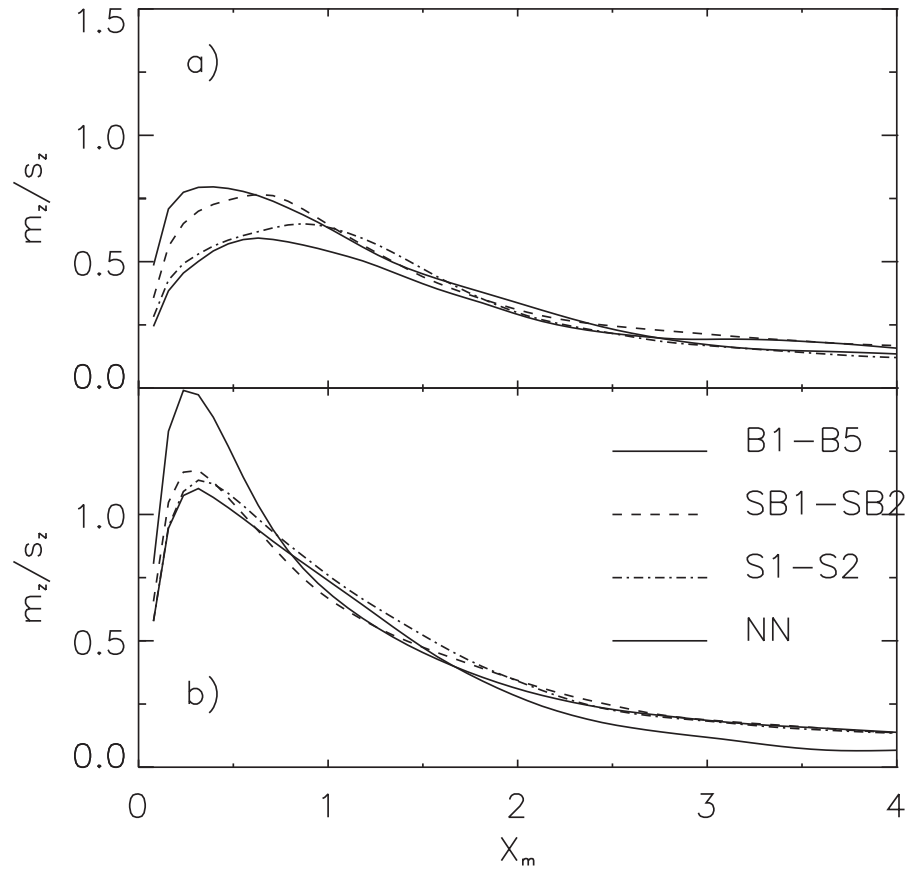


Figure 5.10: The ratio of meandering to relative-dispersion (m_z/s_z) calculated by the LES for all the simulated cases for the near-ground (a) and the elevated release (b).

Elevated release

Figure 5.9 shows the crosswind-integrated and ground concentrations for the elevated release. As for the near-ground release, the increasing wind and the simultaneous reducing of the buoyancy affect the plume dispersion, which show different behaviors according to the increasing shear/buoyancy ratio.

The shear-buoyancy cases (SB1-SB2) show the same general pattern as the pure buoyancy condition, but the elevated minimum that was visible for the pure-convective cases ($X_m = 1$, $z/z_i = 0.75$, Figure 5.9a) is now no longer present (Figure 5.9b) and the maximum ground concentration is shifted to a greater distance from the source ($X_m \sim 1.3$, see Figure 5.9e). The buoyant force starts raising the plume at $X_m = 2.5$, and a ground minimum is visible around $X_m = 3.4$. In the shear situation (cases S1-S2) the ground maximum is shifted further towards large distances ($X_m = 1.8$) and no surface minimum is found, proving that the buoyancy is unable to raise the tracer after it has reached the ground. In the near-neutral regime, the plume show a typical Gaussian behavior, the tracer remains elevated even at large distances and no surface maxima is present.

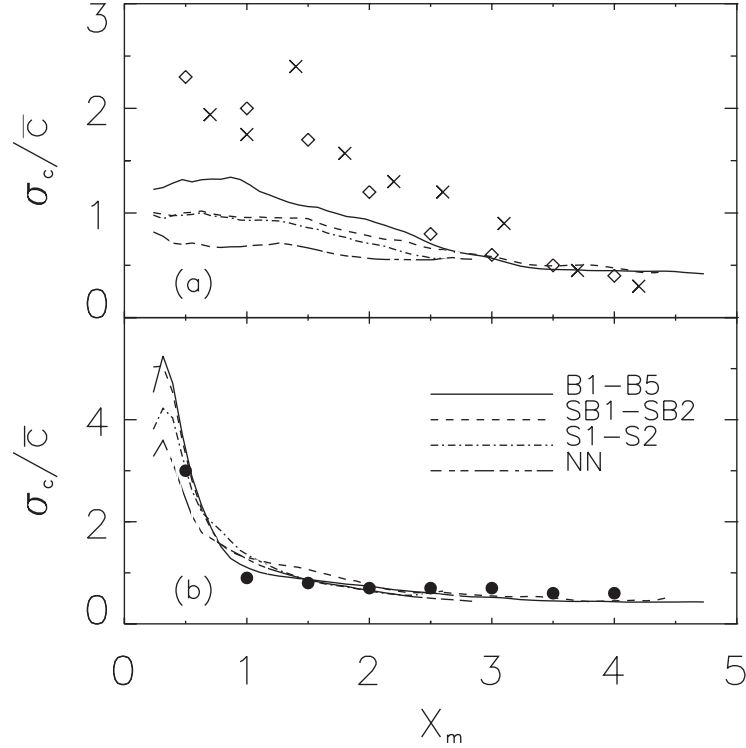


Figure 5.11: Relative concentration fluctuation intensity on the plume centerline at ground level is shown for the near-ground (a) and the elevated release (b) for all the simulated cases. The following experimental data are also shown: \diamond : *Weil et al.* (2002); \times : *Deardorff and Willis* (1984); \bullet : *Henn and Sykes* (1992).

5.4.4 Meandering and relative dispersion in a buoyancy- and shear-driven boundary layers

As shown previously, the vertical dispersion parameter can be represented as the sum of the meandering and relative diffusion components, according to equation (5.16). The results in a pure CBL have already been discussed by *Nieuwstadt* (1992) but the investigation of the relative importance of meandering and relative dispersion in case of weak convection is still missing.

In Figure 5.10 the ratio between the meandering component and the relative diffusion (m_z/s_z) is shown as function of the distance from the source X_m for all the simulated cases. As shown by *Nieuwstadt* (1992) the meandering is important especially at short distances, where the plume motion is governed by the thermals. After reaching a maximum, the meandering component rapidly decreases, because the plume motion starts being affected by the surface and the inversion zone (CBL top). It finally reaches a constant value when the tracer is uniformly mixed. This general pattern is confirmed by our results as shown in the Figure.

For a near-ground release (Figure 5.10a), we note that the contribution of the meandering to the vertical spread is always less important than the relative diffusion. The meandering is reduced by the increasing wind shear especially at short distances ($X_m < 1$). This is explained by the presence of the ground which limits the vertical motion; as the wind increases and the buoyancy diminishes,

5.4. Dispersion in a buoyancy- and shear-driven boundary layer

the tracer remains close to the surface for a longer time before being lifted up, and so the vertical motion (meandering) remains limited.

For the elevated release (Figure 5.10b), the plume motion in the pure-convective flow is dominated by the meandering at short distances ($m_z/s_z > 1$), in agreement with the results of *Nieuwstadt* (1992). As the wind increases, it reduces the vertical motion but for $X_m < 0.75$ the meandering still remains the principal contribution to the vertical spread; in fact, as discussed previously, the wind profile shows a strong shear only near the ground, that means that in the middle of the BL the buoyancy force is still the main driving process in the plume dispersion.

5.4.5 Concentration fluctuations

The study of the concentration fluctuations has a great importance in the atmospheric dispersion problems as they can be of the same order of magnitude as the mean concentrations. The valuation of the concentration uncertainty was investigated in the past either in convective conditions or in neutral flows by laboratory experiments (*Fackrell and Robins*, 1982; *Deardorff and Willis*, 1984 and *Weil et al.*, 2002) and numerical simulations (*Henn and Sykes*, 1992 and *Sykes and Henn*, 1992). From the concentration fields calculated by the LES, the value of the concentration fluctuations intensity are explicitly calculated [equation (5.8)] and is compared with the experimental results. It is unfortunate that, because the fluctuations intensity depends strongly on the source size (*Fackrell and Robins*, 1982) and, moreover, the results in the literature for the neutral scale were scaled with different length and velocity scales, only a qualitative comparison is carried out.

The relative concentration fluctuation intensities σ_c/\bar{c} on the plume centerline at ground level are shown in Figure 5.11a and in Figure 5.11b for the near-ground and the elevated release, respectively.

The LES results for the near-ground release (Figure 5.11a) in the pure convective cases (B1-B5) show that the concentration fluctuation intensity decreases with the distance from the source, similar to the results for the experimental data. However, they underestimate the water tank data by *Deardorff and Willis* (1984) and *Weil et al.* (2002) due to the differences in the values of the source size and release height ($z_s/z_i = 0.134$, $z_s/z_i = 0.15$ and $z_s/z_i = 0.078$ for *Deardorff and Willis*, 1984; *Weil et al.*, 2002 and our study, respectively). The source size and the ratio between it and the eddy size, in particular, are the main factors that determine the value of the maximum, as explained by *Henn and Sykes* (1992). Our initial plume size (instantaneous line source) is determined by the vertical grid length (varying from 25 to 50 meters) and it may be larger than the eddy size at this source height resulting in a underestimation of the fluctuation maximum.

The major source of concentration fluctuation is the meandering of the plume, as explained by *Fackrell and Robins* (1982). As the wind shear increases, the meandering and, as a consequence, the concentration fluctuations are reduced. In the near-neutral situation (NN), a nearly constant value is found at each distance from the source consistently with the wind tunnel data by *Fackrell and Robins* (1982) (around 0.5).

The results for the elevated release (Figure 5.11b) are in a very good agreement with the numerical experiment by *Henn and Sykes* (1992), and a marked maximum is found at $X_m = 0.3$. This is consistent with the maximum in the meandering component shown in Figure 5.10b. In fact, for the elevate release, the vertical motion of the plume is dominated at short distances by the large

eddies. Similar to the previous discussion, the reduction of the meandering is responsible for the diminution of the fluctuation intensity maximum as the wind shear increases.

5.5 Parameterization for the dispersion in a buoyancy- and shear-driven boundary layers

In this Section, parameterizations for the dispersion parameters σ_y and σ_z are proposed. These expressions are evaluated for all the simulated flows. Although many studies are available either in the pure convective or neutral limit, attempts to parameterize the behavior of the plume in a buoyancy and shear-driven BL are scarcer (*Briggs*, 1985). The dispersion parameters are directly related to the velocity variances whose vertical profiles change with the increasing wind shear because of the change in the turbulent structure (Figure 5.5).

Below, we propose parameterizations that include the combined effect of buoyancy and shear on dispersion. The parameterizations can be used to calculate the plume dispersion in condition of relatively flat terrain and homogeneous land surfaces.

5.5.1 Horizontal dispersion parameter

As stated previously, the veering of wind direction with height increases the horizontal dispersion according to equation (5.28) in which the shear contribution (σ_{ys}) is added to the buoyancy-generated dispersion (σ_{yb}) calculated by equation (5.14). Different expressions have been proposed for the shear-generated horizontal spread which are written below in a general form as

$$\sigma_{ys}^2 = aS_*^2 f(\sigma_w^b t^c T_w^d), \quad (5.30)$$

where t is time, T_w is the Lagrangian time for the vertical turbulent velocity, and a a constant. The coefficients b , c and d determine the curve's slope ranging from a cubic tendency at small values of t ($b = 2$, $c = 3$, $d = 1$) to a linear tendency at large times ($b = -2$, $c = 1$, $d = -1$). In our study the non dimensional wind direction shear S_* is defined, following *Luhar* (2002), as

$$S_* = \frac{V}{w_m} \theta_m, \quad (5.31)$$

where θ_m is the difference between the geostrophic wind direction and the wind direction at the mean plume height, and V is the total wind intensity ($V^2 = u^2 + v^2$) at the same height.

Explicit testing of expressions (5.30) are rare by either field campaign or numerical models and therefore our LES results could be useful in deriving and evaluating a suitable parameterization for horizontal dispersion under shear conditions.

As discussed previously, the buoyancy-generated dispersion can be satisfactorily parameterized with equation (5.14) whereas the shear contribution is calculated rearranging the formula proposed by *Luhar* (2002) as follows:

$$\sigma_{ys}^2 = \frac{a_0 S_*^2 \sigma_w^2 T_w X_m^3 z_i / w_m}{\left[1 + \left(\frac{X_m}{X_0}\right)^3\right]^{2/3}}. \quad (5.32)$$

5.5. Parameterization for the dispersion in a buoyancy- and shear-driven boundary layers

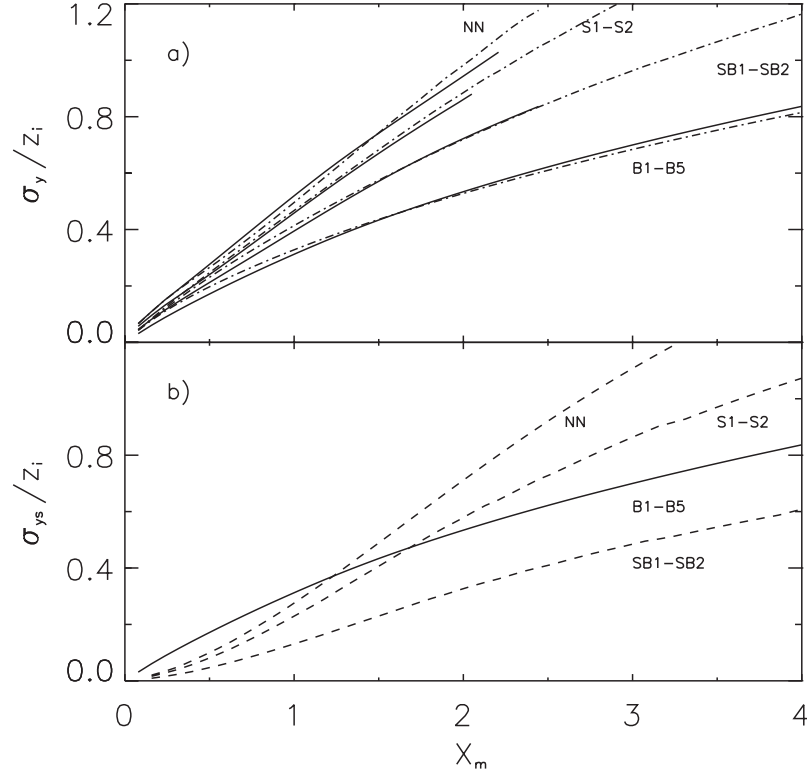


Figure 5.12: a) Horizontal dispersion parameter as calculated by the LES for the various cases (continuous lines) and parameterized according equation (5.28) (dotted-dashed lines). (b) Shear-generated horizontal dispersion as parameterized according to equation (5.32) for the various cases (dashed lines). The dispersion parameter σ_y/z_i for the pure buoyancy cases (continuous line) is shown to illustrate the contribution of shear to the horizontal dispersion.

Equation (5.32) is an interpolation between the cubic (X_m^3) and linear (X_m) dependence on X_m that were discussed previously. The distance X_0 marks the transition between the two tendencies, from cubic to linear, and it is defined as

$$X_0 = \left(\frac{z_i^4}{a_0 b_0 \sigma_w^4 T_w \tau_c} \right)^{1/2} \frac{w_m}{z_i}. \quad (5.33)$$

From the LES results, X_0 ranges from 2.7 in the SB1-SB2 cases to 3.3 in the near-neutral situation. The value of the constants a_0 and b_0 are fixed to 0.09 and 60, respectively, and $\tau_c = 0.7 z_i / w_m$, following *Luhar* (2002).

Figure 5.12a shows the value of σ_y calculated by equation (5.28) compared with the LES results. We found a good agreement for all the cases studied. Figure 5.12b shows the shear contribution only, compared with the total dispersion for the pure buoyancy cases (in this case $\sigma_y = \sigma_{yb}$ because the shear is absent). Our results show that for large values of the wind, the shear contribution is of the same order of magnitude or larger than the buoyancy-generated dispersion, in agreement with the analysis of *Luhar* (2002).

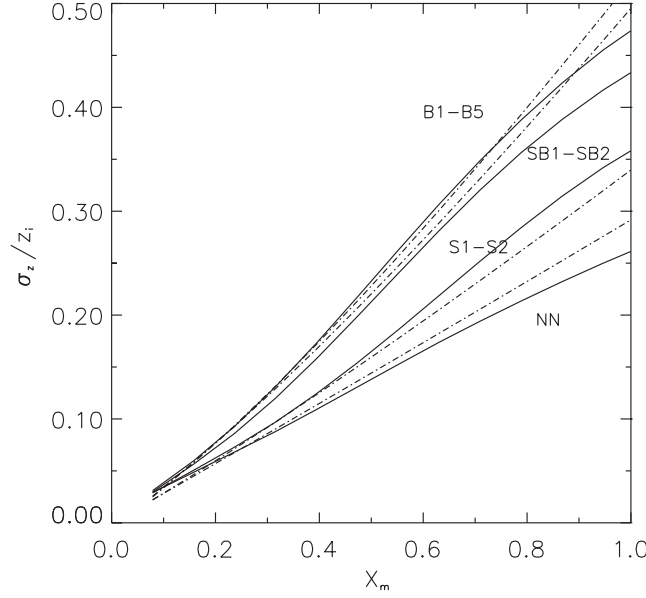


Figure 5.13: Vertical dispersion parameter for a near-ground release as calculated by the LES for the various cases (continuous lines) and parameterized according equation (5.38) (dotted-dashed lines).

5.5.2 Vertical dispersion parameter

The vertical spread is strongly dependent on the source height (*Weil*, 1988). For a elevated release, the dispersion parameter at short times must follow Taylor's law

$$\frac{\sigma_z}{z_i} = \frac{\sigma_w}{w_*} X. \quad (5.34)$$

For a near-ground release, on the contrary, the presence of the ground converts the vertical motion into horizontal motion. Therefore, the vertical spread is reduced, and the growth departs from linearity. Moreover, as discussed previously the increasing of the shear/buoyancy ratio produces a wind profile characterized by strong shear near the BL boundaries (surface and entrainment zone), whereas in the middle of the layer the u component of the wind remains constant with height.

For this reason, we propose two different parameterizations for σ_z , depending on the release height. The vertical dispersion parameter for a source above the surface layer (elevated release) can be successfully represented by the formula

$$\frac{\sigma_z}{z_i} = \frac{\sigma_w}{w_*} X = 0.51 \frac{w_*}{w_m} X_m, \quad (5.35)$$

which fits our LES results accurately.

For a near-ground release, at short distance from the source ($X_m < 0.5$), two opposite effects have to be taken into account: the reduction of the vertical spread due to the surface and the increasing contribution produced by the shear. Notice that, in order to facilitate the use of the parameterization, the vertical dispersion parameter is calculated as the displacement from the source height

5.6. Conclusions

[equation (5.6)], rather than from the mean plume height. As shown previously [equation (5.11)], in the pure-convective BL ($u_* \sim 0$) the growth of σ'_z/z_i follows

$$\frac{\sigma'_z}{z_i} = 0.52X^{6/5} \quad (5.36)$$

in the pure-convective limit, whereas in the near-neutral case the vertical spread grows linearly according to

$$\frac{\sigma'_z}{z_i} = 0.6 \frac{u_*}{w_m} X_m. \quad (5.37)$$

The constant 0.6 is the best fit for our results, and it is consistent with the field campaign neutral limit $\sigma_z = 0.64u_*t$ that was indicated by *Briggs* (1985).

In the intermediate cases, in which buoyancy and shear are acting simultaneously, the LES results show that the vertical spread growth falls in between the two limits (Figure 5.6b). In consequence, we suggest a parameterization which combines equations (5.36) and (5.37):

$$\frac{\sigma'_z}{z_i} = \left[\left(0.52 \frac{w_*}{w_m} \right)^{12/5} X_m^{2/5} f + \left(0.6 \frac{u_*}{w_m} \right)^2 \right]^{1/2} X_m, \quad (5.38)$$

where the function f depends on the atmospheric surface layer stability according to

$$f = \frac{(-0.2 \frac{z_i}{L})^3}{1 + (-0.2 \frac{z_i}{L})^3}. \quad (5.39)$$

Equation (5.38) has the correct limits for the pure buoyancy ($-z_i/L \rightarrow \infty$, $f = 1$) and neutral limits ($-z_i/L = 0$, $f = 0$) discussed above. The weighting function f [equation (5.39)] accounts for the reduction of vertical spread with shear already noticed by previous works (*Mason*, 1992 and *Gopalakrishnan and Avissar*, 2000). However, to our knowledge, this is the first time a parameterization which explicitly accounts for this effect is presented and evaluated.

In Figure 5.13 the parameterization [equation (5.38)] is compared to the LES results for all the simulated cases at short distances ($X_m < 1$). According to *Briggs* (1985) parameterizations for the vertical dispersion parameter are valid only when $X_m < 0.7$ because at greater distances, when the tracer is lifted off by the thermals, the vertical distribution becomes non-Gaussian. At greater distances ($X_m > 2$), when the tracer is uniformly mixed, the vertical spread reaches a constant values (about 0.55) as shown in Figure 5.6. As shown in Figure 5.13, equation (5.38) reproduces correctly the LES results at short distances ($X_m < 0.6$) for all the cases.

5.6 Conclusions

The dispersion of a passive scalar in boundary layers driven by different combinations of buoyancy and shear was investigated by means of large-eddy simulation and evaluated with laboratory

and field observations. Four boundary layer archetypes varying from the pure-convection to near-neutral situation were simulated and classified according to the shear-buoyancy ratio u_*/w_* and the scaling parameter $-z_i/L$. Particular attention was focused on the values of the dispersion parameters, the ground concentrations and the concentration fluctuations.

A good agreement between the LES results and the laboratory and field experiments was found in the pure-convective situation.

The influence of the increasing wind shear was first studied on the flow statistics (profiles of velocity variances) because the dispersion characteristics are directly dependent on the turbulence's properties. The results show an increase in the horizontal velocity variance and a reduction in the vertical velocity variance.

The main effect of the wind shear on dispersion statistics results in a reduction of the vertical spread, whereas the horizontal spread is enhanced. As a consequence, the ground concentrations are strongly influenced and the LES results show that the increasing wind tends to advect the plume horizontally for a longer time. The tracer therefore reaches the ground at greater distances from the source. For the near-ground releases, at very short distances the ground concentrations show a similar behavior in all the simulated flows. This is explained by the fact that for $X_m < 0.3$ the tracer is still in the surface layer where the turbulent and dispersion statistics (σ_w/w_m and σ_z/z_i) have similar values for all the stability regimes. At greater distances ($0.3 < X_m < 3$), the plume is strongly affected by the different ratio between the thermal and mechanical forcing, and the ground concentrations increase markedly with the increasing wind shear. Finally at $X_m > 3$ the tracer is uniformly spread within the mixed layer and a common asymptotic value for the ground concentration is found.

The meandering component of the vertical dispersion is also modified by the wind shear, in particular, near the ground where the presence of the surface tends to enhance the shear, which reduces the looping of the plume. This reduction is especially visible at short distances from the source ($X_m < 1$) where the plume motion is influenced by the large turbulent eddies and the meandering is the main contribution to the vertical dispersion.

Because meandering is the main source of concentration variance, the maximum of the concentration fluctuations is shown to diminish as the flow becomes less convective. Although the differences in source size and release height do not allow a direct comparison, the LES results agree qualitatively with the experimental results both in convective and in neutral conditions.

Parameterizations for the dispersion parameters that account for the combined effect of buoyancy and shear were proposed. The parameterization for σ_y is partially based on a previous study by *Luhar* (2002) in which the wind rotation was explicitly considered in the shear-generated dispersion. The parameterization of σ_z accounts for the two opposite effects: the reduction of the vertical motion near the ground and the shear generated turbulence. Both the parameterizations give satisfactory results when compared with the LES data in all the simulated cases and they will be further tested in operational models for dispersion.

5.7 APPENDIX A: List of symbols

C_y	Crosswind-integrated concentration
\bar{c}	Time averaged concentration
g	Acceleration of gravity
L	Monin-Obukhov length
m_y	Meandering component of the dispersion in the horizontal direction
m_z	Meandering component of the dispersion in the vertical direction
S_*	Dimensionless shear
s_z	Relative dispersion in the vertical direction
T_v	Lagrangian time for the horizontal turbulent velocity
T_w	Lagrangian time for the vertical turbulent velocity
u, v, w	Wind components
$\langle u'^2 \rangle = \sigma_u^2$	Horizontal (u) velocity variance
u_*	Friction velocity
U_g	Geostrophic wind
V	Total mean wind
$\langle v'^2 \rangle = \sigma_v^2$	Horizontal (v) velocity variance
$\langle w'^2 \rangle = \sigma_w^2$	Vertical velocity variance
w_m	Convective velocity scale for BLs driven by buoyancy and shear
w_*	Convective velocity scale
X	Dimensionless distance (time)
X_m	Dimensionless distance (time) for BLs driven by buoyancy and shear
\bar{y}	Mean plume horizontal position
z_0	Roughness length
\bar{z}	Mean plume height
z_i	CBL height
z_l	Local plume height
z_s	Source height
σ_c^2	Concentration fluctuation
σ_y	Horizontal dispersion parameter
σ_{yb}	Horizontal dispersion parameter: buoyancy contribution
σ_{ys}	Horizontal dispersion parameter: shear contribution
σ_z	Vertical dispersion parameter
σ_z'	Vertical displacement from the source height
θ	Potential temperature
θ_m	Difference between the direction of the geostrophic wind and the wind at the mean plume height

Chapter 5. Dispersion of a passive tracer in buoyancy- and shear-driven boundary layers

Chapter 6

The dispersion of chemically reactive species in the atmospheric boundary layer

6.1 Introduction

Turbulence is the most important characteristic of the Atmospheric Boundary Layer (ABL), which extends from the Earth's surface to the free troposphere. In this region, turbulence is fully three-dimensional (*Tennekes and Lumley, 1972; Holtslag and Nieuwstadt, 1986; Wyngaard, 1992*), and is the driving process that disperses and mixes chemical species. Consequently, the reactivity of chemical reactions can depend on the ability of turbulence to mix the reactants. In the ABL, mixing conditions are very different from those in a laboratory chemical chamber, where species are homogeneously mixed and there is a large concentration of reactants (*Finlayson-Pitts and Pitts, 1986*). For instance, it is known that the coherent structures present in the convective boundary layer or the stratified flow in the stable boundary layer create conditions where the reactants are not well mixed. As a result, under certain atmospheric and chemical conditions, turbulence can limit the reactivity of the species. In this paper, we review how turbulence influences the chemical transformations and how we can represent this process in large scale atmospheric chemistry models.

Since the seminal papers by *Donaldson and Hilst (1972)*, *Bilger (1978)*, *Fitzjarrald and Lenschow (1983)* and *Thompson and Lenschow (1984)*, the role that physical processes, and in particular turbulence, play in the transformation of reactants has become clearer. Following these pioneering studies, other authors (*Brost et al., 1988; Kramm et al., 1991; Hamba, 1993; Gao and Wesely, 1994; Vilà-Guerau de Arellano et al., 1995; Galmarini et al., 1997a; Verver et al., 1997; Galmarini et al., 1997b; Petersen et al., 1999*) have investigated various ABL reacting flows in order to find out under which conditions and for which scaling parameters chemistry is limited by turbulence. The majority of these studies account for the influence of turbulence on the chemistry by including a chemical term in the governing equations. Under specific conditions of turbulence and chemical reactivity, a scale analysis of these governing equations reveals that the chemical terms can be of the same order of magnitude as the dynamic terms. In particular, this occurs when the

The content of this Chapter has been published on *Meteorology and Atmospheric Physics* (**87**, 23-38, 2004) with J. Vilà-Guerau de Arellano, A. Dosio, J.-F. Vinuesa, A.A.M. Holtslag and S. Galmarini as authors.

time scale of the chemical reactions is of similar order to the time scale of the turbulent mixing. In such situation, atmospheric turbulence controls the chemical reactivity. As a consequence, the behavior of chemically active species can differ from the behavior observed and modelled of inert scalars. A well-studied example of the slow down of chemical reaction because of the inefficient turbulent mixing in the ABL is the transformation between NO and O_3 .

Almost all the studies mentioned above are based on attempts to model the discretized governing equations and to analyze how the presence of the chemical terms causes deviations from inert scalar behavior. A shortcoming of these studies is that they require a parameterization of the vertical turbulent mixing. This parameterization is normally based on weak physical assumptions concerning the mixing-length scales. The research carried out by means of large-eddy simulation (LES) has helped to overcome this problem. *Stevens and Lenschow* (2001) stated that LES allows us to control flow simulations, and thereby to confine the relevant aspects of a given flow found previously in theoretical studies. It is in this context that LES has enabled us to investigate further the governing parameters and the main characteristics of turbulent reacting flows. The Damköhler number, identified and used previously in the cited modelling studies, was used successfully to classify the archetypal flows simulated by LES. The majority of LES studies have simulated ABL under convective conditions by using different, but rather simple, chemical schemes. A brief summary of the most important LES studies of atmospheric reactive flows is given below.

Schumann (1989) carried out the first LES of an atmospheric boundary layer with reactive species. He focused mainly on the segregation of species caused by the coherent structures generated in a convective boundary layer (CBL) and showed that chemical transformation proceeds at a slower rate in the CBL because of insufficient mixing. In a simulated CBL flow with similar characteristics, *Krol et al.* (2000) studied the effect of heterogeneous mixing on a more complex chemical mechanism. They found that, although the species are largely segregated, the effect of turbulence on the chemical reactions is almost negligible because species are close to a chemical equilibrium, *i.e.* there is a balance between production and destruction. However, the perturbation of this equilibrium, triggered by non-uniform emissions, leads to a decrease in the reaction rate. As *Patton et al.* (2001) showed in their LES study of a turbulent reacting flow in and above a plant canopy, these disturbances can have a larger effect close to the sources and sinks of the reactants. Recent spectral analysis of reactants, based on LES results (*Jonker et al.*, 2004), confirms that the variance power spectra of the reactive compounds also depends on the Damköhler number and on the state of chemical equilibrium between the reactants.

The role of turbulence in the reactivity of species is particularly important close to the point sources or urban areas where large amounts of pollutants are released. Since the growth of the plume and the transformation of species are strongly dependent on the interaction of different scales, the reaction rate of certain chemical reactions in and around the plume can be slowed down (in the case of non-premixed species) or enhanced (in the case of premixed species). Here, we will first show how a simple chemical decay modifies the relative variability of the plume dispersion downstream from the reactant release and across the plume. Secondly, with regard to non-linear reactions, we discuss how the segregation of species can considerably reduce the chemical reactivity. We also examine several modelling techniques that have been used to explain the main processes of chemically reactive plumes.

It is important to notice that majority of the processes mentioned, and in particular turbulent mix-

6.2. Governing equations and dimensionless numbers

ing and the emissions at a point or from a surface area, occur on spatial and time scales that are too small to be explicitly resolved by the grid prescribed in large scale atmospheric models. These sub-grid processes therefore require an adequate parameterization that includes the relevant parameters of the transformation of species in the atmospheric boundary layer. Some examples of sub-grid parameterizations are described.

The fundamental concepts, which include the governing equations and the main dimensionless numbers, are discussed in Section 6.2. In Section 6.3, we show the contribution that the chemical term makes to the flux of reactive species and we introduce a key variable in atmospheric turbulent reacting flows: the intensity of segregation. This variable quantifies the heterogeneity of the mixing between the reactants. In Section 6.4, we describe and analyze the main characteristics of the dispersion of chemically active plumes and we include a summary of the most relevant studies. In the concluding Section, we provide suggestions for future research studies on turbulent reacting flows in the atmospheric boundary layer.

6.2 Governing equations and dimensionless numbers

To determine the evolution of chemical species in the ABL, one needs to solve not only the flow-governing equations, but also the conservation equation of chemical species. The concentration (mass per volume) of each constituent must satisfy the following equation (*Lamb and Seinfeld, 1973*):

$$\frac{\partial c_i}{\partial t} + \frac{\partial(u_\alpha c_i)}{\partial x_\alpha} = D_i \left(\frac{\partial^2 c_i}{\partial x_\alpha \partial x_\alpha} \right) + R_i(c_1, \dots, c_N, T, F) + S_i(x, t), \quad (6.1)$$

where c_i is the concentration of species i , t is time, u_α is the α -component of the wind velocity, x_α is the α -component of the space variable, D_i is the molecular diffusivity, R_i is the rate of chemical production or loss, N is the total number of chemical species, T is the temperature, F is the actinic flux (of photochemically active species), and S_i accounts for the sources and sinks. The repeated subscript α indicates a summation over the three components. The chemical term in (6.1) can be written explicitly as:

$$R_i = \sum_{j=1}^M \eta_{ij} k_j \prod_{l=1}^N c_l^{\beta_{lj}}, \quad (6.2)$$

where η_{ij} is the stoichiometric coefficient for species i in reaction j , k_j is the reaction rate constant for reaction j and β_{lj} is the reaction order of species l in reaction j . The number M represents the total number of reactions that species i undergoes. The dependence of the reaction term on the temperature and actinic flux is included in the reaction rate k_j .

By defining the following scales of the turbulent reacting flow: length (L), velocity (U), temperature (Θ) and concentration (C_{0i} , $i=1, \dots, N$), one can formulate equation (6.1) in a dimensionless form:

$$\frac{\partial \tilde{c}_i}{\partial \tilde{t}} + \frac{\partial(\tilde{u}_\alpha \tilde{c}_i)}{\partial \tilde{x}_\alpha} = (ReSc_i)^{-1} \left(\frac{\partial^2 \tilde{c}_i}{\partial \tilde{x}_\alpha \partial \tilde{x}_\alpha} \right) + \tilde{R}_i(\tilde{c}_1, \dots, \tilde{c}_N, \tilde{\theta}, \tilde{f}) + \tilde{S}_i(\tilde{x}, \tilde{t}), \quad (6.3)$$

where the symbol \sim refers to a dimensionless variable, Re is the Reynolds number and Sc_i is the Schmidt number (the ratio of the kinematic viscosity to the molecular diffusivity of species i).

Turbulent flows in the ABL typically have a Reynolds number of 10^7 and a Schmidt number around 1. Hence, $(ReSc_i)^{-1}$ is generally a small number. Consequently, the molecular diffusivity term can be omitted in equation (6.3).

The dimensionless reaction term \tilde{R}_i reads:

$$\tilde{R}_i = \sum_{j=1}^M \eta_{ij} Da_j \prod_{l=1}^N \tilde{c}_l^{\beta_{lj}}. \quad (6.4)$$

The term (6.4) is therefore a function of the Da_j and the ratio of the concentration scales ($r = \frac{\langle B \rangle}{\langle A \rangle}$), where $\langle B \rangle$ and $\langle A \rangle$ are the concentrations. This chemical term can be written in a generic form as:

$$\tilde{R}_i = Da_j r = \left(\frac{\tau}{\tau_c} \right) r. \quad (6.5)$$

The dimensionless number Da_j depends on the ratio of the flow time scale ($\tau=L/U$) to the chemical time scale (τ_c), which varies according to the reaction order. If $Da < 1$, we know that the chemical reaction proceeds at a slower rate compared to the turbulence, and one can assume that turbulence can mix the species homogeneously before the reaction takes place. With $Da \approx O(1)$, turbulence and chemistry interact with each other, such as in combustion processes. In combustion, turbulence can limit the chemistry if the turbulent mixing between species is inefficient. On the other hand, the heat release caused by a chemical reaction can modify the velocity fields of the turbulent reacting flows. Because of the low concentrations of reacting species in the ABL, the heat release due to chemical reactions has a negligible effect on the temperature field. As a consequence, it is only turbulence that exerts an effect on the chemical reactions.

Because atmospheric flows are characterized by a large number of spatial and temporal scales, and we want to achieve a proper classification of the turbulent reacting flows, it is convenient to define two Damköhler numbers to determine the effect of large and small dynamic scales on the reaction. The corresponding numbers are defined as (Bilger, 1980; Komori *et al.*, 1991; Molemaker and Vilà-Guerau de Arellano, 1998):

$$Da_t = \frac{\tau_t}{\tau_c} \quad \text{and} \quad Da_k = \frac{\tau_k}{\tau_c} = \left(\frac{\nu}{\epsilon} \right)^{(1/2)} (\tau_c)^{-1}. \quad (6.6)$$

The first number, Da_t , accounts for the mixing driven by the large scales. For instance, in the convective boundary layer, τ_t is the turnover time of the large-eddies generated by convection, and is defined as the ratio of the boundary layer depth to the convective velocity scale (Deardorff, 1970a). The second number, Da_k , relates the mixing activity of the smallest atmospheric turbulent scales, defined by the Kolmogorov time scale, to the chemical reaction rate. The time scale τ_k is a function of the kinematic viscosity of the air (ν) and the turbulent kinetic energy dissipation rate (ϵ). For a second-order chemical reaction, the characteristic time scale of the chemical reaction is defined as $\tau_c = (kC)^{-1}$ where k is the reaction rate and C is the concentration of species.

Another relevant scaling parameter in (6.5) is the ratio of the species concentration. Species that

6.2. Governing equations and dimensionless numbers

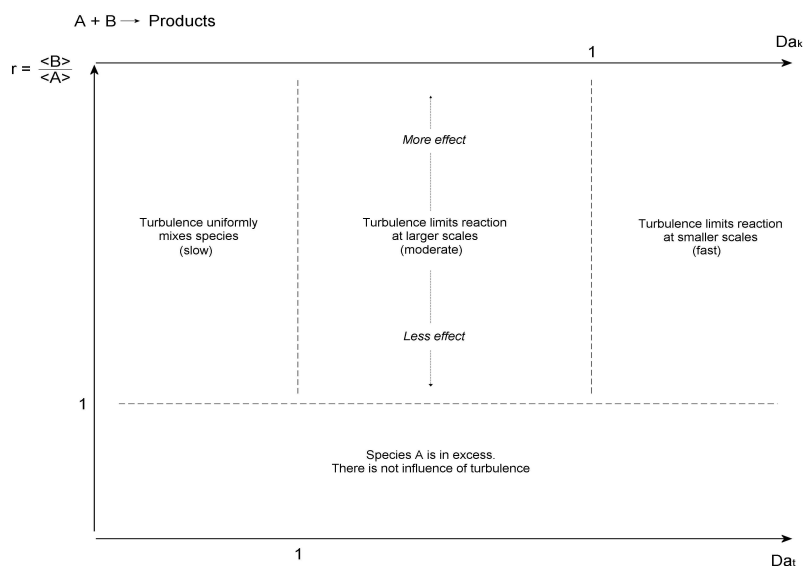


Figure 6.1: A description of the relation between the Damköhler numbers (Da_t , lower x axis, and, Da_k , upper x axis) and the concentration ratio (r). The Figure depicts the specific effects of turbulence on species A that in a non-premixed situation reacts with B , according to the non-linear reaction $A + B \rightarrow P$. Notice that $Da_t > Da_k$ always.

are relatively less abundant than other reactants are influenced more by the effects of turbulence on the reactivity. The relation between the Damköhler numbers and the concentration ratio r is represented in Figure 6.1 for a non-linear reaction $A + B \rightarrow P$ where A and B are non-premixed. The Figure shows the effects of turbulence specifically for the reactant A . For the slow chemistry regime, $Da_t < 1$, turbulence is able to mix the reactants uniformly. For $Da_k < 1 < Da_t$, a moderate chemistry regime, the larger turbulent scales are unable to mix the reactants uniformly, and the segregation between them causes either a reduction or enhancement of the reaction rate. In this regime, one can expect that once the species are mixed by the large scales, the mixing at smaller scales will proceed faster than the chemical reaction, since τ_t is always larger than τ_k . As a consequence, the reactivity is not limited by the small-scale turbulence. For $Da_k \gg 1$ (fast chemistry regime), turbulence controls the chemical reactions at all the turbulent scales. If $r < 1$, similar limitations due to turbulence can be expected for species B .

Table 6.1 shows the large span of time scales associated with atmospheric phenomena, and the chemical transformation time scales of some important atmospheric compounds. It is evident that a realistic chemical mechanism can contain species that react in all three of the above-mentioned regimes. *Stockwell* (1995) calculated the Damköhler number Da_t for a complete gas-phase atmospheric chemistry. Although he used a different definition of Da_t , he found that $Da_t > 1$ for a large number of species. In particular, reactions involving hydroxyl radicals and reactions of peroxy radicals with nitric oxide fall into the categories of moderate and fast chemistry.

However, the conditions $Da_t > 1$ and $r > 1$ are necessary, but not sufficient to determine the extent to which turbulence limits the chemical transformations. In the moderate and fast chemical

Approximate time scale (s)	Chemical species	Atmospheric phenomena
$10^{-1} - 1$	$OH, HO_2(HO_x)$	Turbulence
$10^2 - 10^3$	$NO, NO_2(NO_x)$	Thermal updrafts
$10^3 - 10^4$	$CH_2O, Isoprene$	Convection, thunderstorms
$10^5 - 10^6$	H_2O, SO_2^b	Synoptic weather fronts
10^7	O_3^t, CO	General circulation
$10^8 - 10^9$	CH_4	Climate changes

Table 6.1: Typical time scales of transformation of chemical species and of some atmospheric phenomena (superscript *b* refers to the atmospheric boundary layer and superscript *t* refers to the free troposphere).

regimes, the complementary condition which defines the state of the turbulent reacting flow, is whether the reactants are in or out of chemical equilibrium. In fact, in a situation where chemistry is in balance, species are produced and depleted at comparable rates and consequently reactants will act as inert scalars (*Krol et al.*, 2000; *Vilà-Guerau de Arellano and Cuijpers*, 2000). Chemical mechanisms have a tendency to adjust towards equilibrium. Nevertheless, these equilibria can be prevented or disturbed by driving atmospheric processes like the separation of species by updrafts and downdrafts in the convective boundary layer, by insufficient mixing in a stably stratified boundary layer (*Galmarini et al.*, 1997a), by the presence of clouds (*Vilà-Guerau de Arellano and Cuijpers*, 2000), or by the emission of species in the ABL (*Krol et al.*, 2000).

6.3 The presence of the chemical terms in the averaged equations

It is not feasible to resolve all the relevant spatial and time scales of the atmospheric flow numerically. As a consequence, equations (6.1) and (6.3) must be solved in terms of the statistical moments of the concentration distribution. The wind and the concentration variables are decomposed into an average component ($\langle u_\alpha \rangle$ and $\langle c_i \rangle$, i.e., first moments or the mean) and a fluctuation or stochastic component (u'_α and c'_i), that is, the Reynolds decomposition is applied. Several definitions of averages, which are indicated here by the general symbol $\langle \rangle$, can be used to average the governing equations of the chemical species: the ensemble average, the time average, the one-dimensional average or the volume average (*Garratt*, 1992). By applying the Reynolds decomposition to the variables u_α and c_i , the Reynolds averaging properties ($\langle \langle u_\alpha \rangle \rangle = \langle u_\alpha \rangle$ and $\langle u'_\alpha \rangle = 0$) and making use of the incompressible form of the continuity equation, one arrives at the following form for equation (6.3):

$$\frac{\partial \langle \tilde{c}_i \rangle}{\partial \tilde{t}} + \langle \tilde{u}_\alpha \rangle \frac{\partial \langle \tilde{c}_i \rangle}{\partial \tilde{x}_\alpha} + \frac{\partial \langle \tilde{u}'_\alpha \tilde{c}'_i \rangle}{\partial \tilde{x}_\alpha} = \langle \tilde{R}_i \rangle + \langle \tilde{S}_i \rangle \quad (6.7)$$

6.3. The presence of the chemical terms in the averaged equations

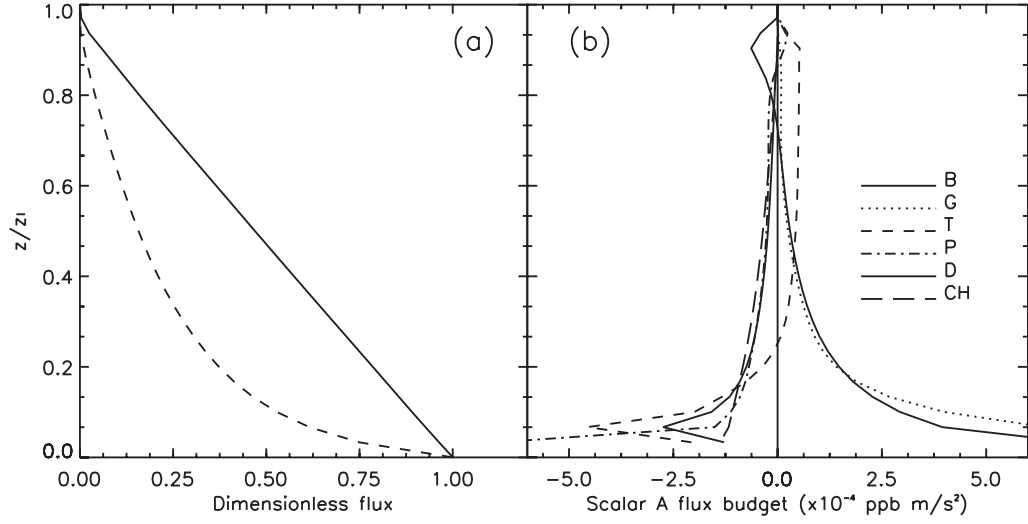


Figure 6.2: a) Vertical profile of the dimensionless fluxes for a species emitted at the surface. The inert species is represented by a continuous line and the species characterized by a $Da_t = 4.1$ and $Da_k = 0.27$ is represented by a dashed line. The values are made dimensionless using mixed layer scaling: the boundary layer height (z_i) and the convective velocity scale (w_*) (Deardorff, 1970a). b) Vertical profiles of the flux budget for the reactant characterized by $Da_t = 4.1$ and by $Da_k = 0.27$. The following contributions are presented: B: buoyancy; G: concentration gradient; T: turbulent transport; P: pressure correlation; D: dissipation and CH: chemistry

where $\langle \tilde{R}_i \rangle$ reads:

$$\langle \tilde{R}_i \rangle = \left\langle \sum_{j=1}^M \eta_{ij} Da_j \prod_{l=1}^N (\langle \tilde{c}_l \rangle + \tilde{c}_l')^{\beta_{lj}} \right\rangle. \quad (6.8)$$

In the ABL, the main reactions of chemical species are of first or second-order. Important third-order reactions can generally be reduced to quasi second-order chemical reactions. Therefore, one can assume that the order of reactions is equal to or smaller than 2, i.e. $(\sum_{j=1}^M \beta_{lj} \leq 2)$; and in that case, the non-dimensional chemical term in the average concentration equation reads:

$$\langle \tilde{R}_i \rangle = \sum_{j=1}^M \eta_{ij} Da_j \left[\prod_{l=1}^N \langle \tilde{c}_l \rangle^{\beta_{lj}} + \left\langle \prod_{l=1}^N \tilde{c}_l'^{\beta_{lj}} \right\rangle \right]. \quad (6.9)$$

Equation (6.7) governs the average concentration evolution, and contains the new terms $\langle \tilde{u}'_\alpha \tilde{c}_i' \rangle$ and $\langle \prod_{l=1}^N \tilde{c}_l'^{\beta_{lj}} \rangle$, i.e. second-order moments. The presence of these terms leads to the usual closure problem: there are more unknown variables than there are equations to solve. In equation (6.7), the term $\langle \tilde{u}'_\alpha \tilde{c}_i' \rangle$ is the turbulent flux of species i . This term describes important processes in the ABL, such as exchange between the free troposphere and the ABL, turbulent transport, mixing in the ABL, and deposition at the surface. The term $\langle \prod_{l=1}^N \tilde{c}_l'^{\beta_{lj}} \rangle$ in (6.9) accounts for the variances and covariances of reactive species. It describes the variability of the average concentration distribution and quantifies the capacity of turbulent reacting flows to mix chemical species. The Reynolds

averaged governing equations for the second-order moment with suitable parameterizations of the pressure gradient term, the dissipation term, and the third-order terms, make it possible to close the average concentration equation. The derivation of these second-order equations can be found elsewhere (Stull, 1988; Garratt, 1992).

Here, we concentrate only in the chemical terms in the second-moment equations for chemically reactive species. Note that the terms are written in a general and compact form. In this way, and after algebraic manipulations, one can derive the chemical term for the first-, second- or higher-order reactions explicitly.

The chemical term in the flux equation $\langle \tilde{u}'_\alpha \tilde{c}'_i \rangle$ reads:

$$\langle R \rangle_{\langle u'_\alpha c'_i \rangle} = \sum_{j=1}^M \eta_{ij} k_j \prod_{l=1}^N \langle u'_\alpha (\langle c_l \rangle + c'_l)^{\beta_{lj}} \rangle. \quad (6.10)$$

The chemical term in the variance equation ($\langle c_i'^2 \rangle$) can be written as:

$$\langle R \rangle_{\langle c_i'^2 \rangle} = 2 \sum_{j=1}^M \eta_{ij} k_j \prod_{l=1}^N \langle c'_i (\langle c_l \rangle + c'_l)^{\beta_{lj}} \rangle, \quad (6.11)$$

and, finally, the chemical term in the governing equation for the covariance between two different species ($\langle c'_i c'_k \rangle, i \neq k$) is:

$$\langle R \rangle_{\langle c'_i c'_k \rangle} = \sum_{k=1}^N \sum_{j=1}^M \eta_{ij} k_j \prod_{l=1}^N \langle c'_k (\langle c_l \rangle + c'_l)^{\beta_{lj}} \rangle. \quad (6.12)$$

It is important to mention that the chemical terms (6.10), (6.11), and (6.12) introduce a new Damköhler number for the flux and (co-)variances what is now a function of the concentration flux/(co-)variances scales instead of the averaged concentration (Vinuesa and Vilà-Guerau de Arellano, 2003).

6.3.1 Non-linear flux of the reactive species

To demonstrate the importance of the chemical terms in the governing equations, we study the role of the chemical term in the flux budget equation. On the assumption that there is horizontal homogeneity, the flux equation reads:

$$\begin{aligned} \frac{\partial \langle w' c'_i \rangle}{\partial t} = & - \underbrace{\langle w'^2 \rangle \frac{\partial \langle c_i \rangle}{\partial z}}_G + \underbrace{\frac{g}{\Theta_o} \langle w' c'_i \rangle}_{B} - \underbrace{\frac{\partial \langle w'^2 c'_i \rangle}{\partial z}}_T - \underbrace{\frac{1}{\rho} \langle c'_i \frac{\partial p'}{\partial z} \rangle}_P \\ & + \underbrace{v \langle c'_i \frac{\partial^2 w'}{\partial z^2} \rangle + v_{c_i} \langle w' \frac{\partial^2 c'_i}{\partial z^2} \rangle}_D + \underbrace{\langle R \rangle_{\langle w' c'_i \rangle}}_{CH}, \end{aligned} \quad (6.13)$$

where the letters on the right-hand side are: (G) the concentration gradient term, (B) the buoyancy term, (T) a turbulent transport term, (P) a pressure-concentration interaction term, (D) the molecular dissipation term, and (CH) the chemical term.

6.3. The presence of the chemical terms in the averaged equations

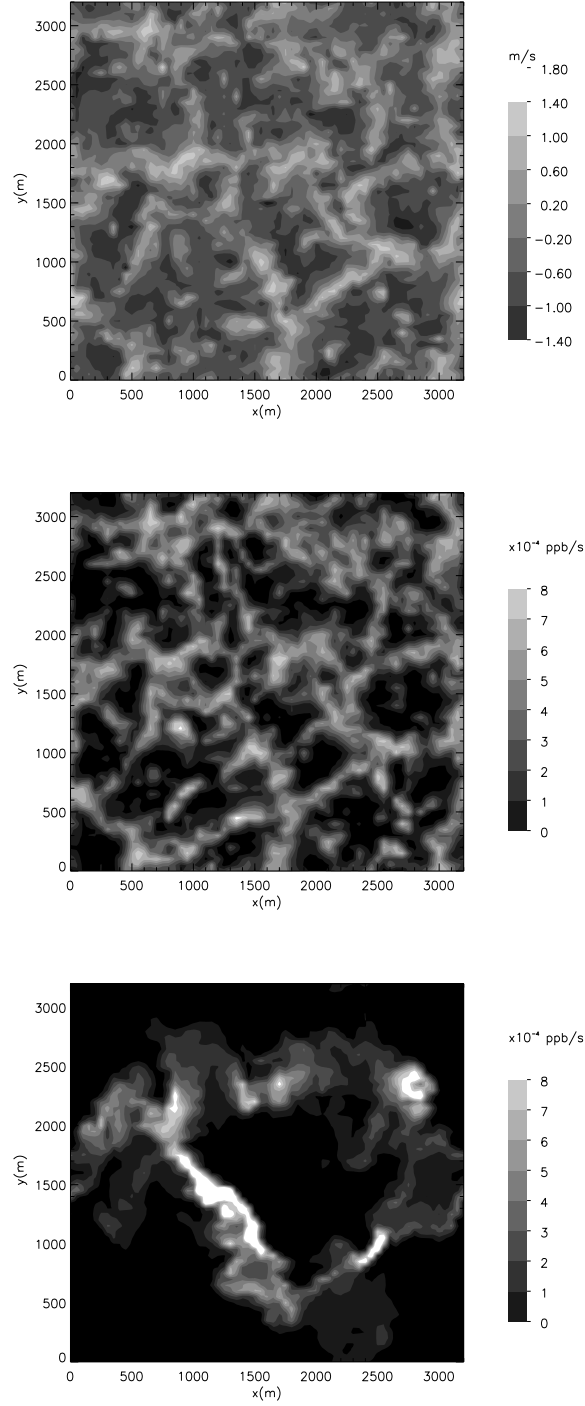


Figure 6.3: Instantaneous horizontal distributions at $z/z_i = 0.1$ of the (a) vertical velocity, (b) reaction zone for a uniform emission and (c) reaction zone for a non-uniform emission.

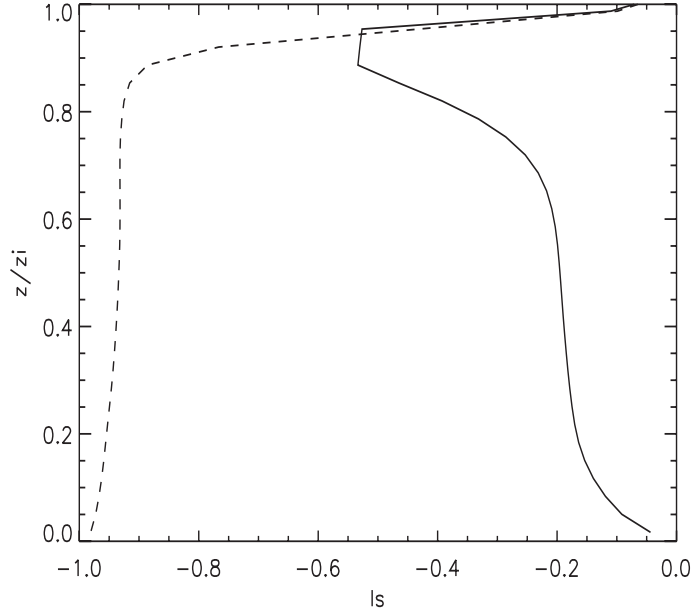


Figure 6.4: Vertical profiles of the intensity of segregation for the turbulent reacting flow characterized by $Da_t = 4.1$ for the uniform emission (continuous line) and for the non-uniform emission (dashed line).

For a second-order reaction of species A and B with a reaction rate k the chemical term $\langle R \rangle_{\langle w'a' \rangle}$ (term 6.10) of species A reads:

$$\langle R \rangle_{\langle w'a' \rangle} = -k (\langle w'a' \rangle \langle b \rangle + \langle w'b' \rangle \langle a \rangle + \langle w'a'b' \rangle). \quad (6.14)$$

Vinuesa and Vilà-Guerau de Arellano (2003) used a LES technique to study the importance of the chemical terms for the fluxes and (co)-variances of reactants in a CBL. They explicitly calculate the chemical term (6.14) in the flux budget equation. As an example, the vertical profiles of the fluxes of a passive scalar and of a reactant emitted uniformly (species A) at the surface are shown in Figure 6.2a. The fluxes are calculated from the fluctuating quantity estimated from a horizontal slab average. They were averaged over a period of one hour. The other reactant (species B) is entrained at the top of the convective boundary layer. The reaction between A and B is an irreversible second-order reaction. In this turbulent reaction flow, the turbulent Damköhler number of species A is 4.1 and the Kolmogorov Damköhler number is 0.27. These numbers indicate that turbulence is limiting the chemical transformation (moderate chemistry regime). As the Figure shows, the flux of the reactant species departs from the linear profile; which is characteristic for the flux of inert species emitted at the surface (Wyngaard, 1992).

Figure 6.2b shows the vertical profiles of the thermodynamic terms and the chemical term (6.14) of the flux budget equation of the reactant species previously shown in Figure 6.2a. The order of magnitude of the chemical term is comparable to that of the thermodynamic terms, and, consequently, it has an effect on the flux profile, causing it to depart from linearity. In this particular case, the chemical term is a negative term throughout the boundary layer and tends to destroy the flux of reactive species.

6.3.2 Segregation of species

The compounds in the ABL are generally not well mixed. To illustrate the heterogeneity of the mixing, we use the results of turbulent reacting flows calculated by means of LES. The numerical experiment simulates a CBL with two reactive species. The first one is released at the surface and the second one is entrained at the top of the boundary layer. Figure 6.3 shows an instantaneous horizontal distribution of the vertical velocity at $z/z_i = 0.1$ (Figure 6.3a) and the reaction zones (Figure 6.3b and Figure 6.3c) for the reactant ($Da_t = 4.1$) shown in Figure 6.2. For a second-order transformation with a reaction rate k , the reaction zone is defined by the product $\langle kAB \rangle$.

To study the effect of discontinuous emissions, two different LES numerical experiments were carried out. In the first one, we prescribed a uniform source emission at the surface. In the second numerical experiment, the emission released followed a Gaussian distribution centered at the middle of the simulation domain. A large amount of the emission (95 %) took place within an area of 700 m radius. This distribution is similar to the emission pattern in an urban area, with large releases of pollutants in the city center and fewer emissions towards the outskirts.

As the Figure shows, in the lower part of the CBL, the reaction zones are located at the core of the thermal updraft motions, which are characterized by positive vertical velocities. Figures 6.3b and 6.3c show the differences between a uniform release and a non-uniform release. In addition to the segregation due to the transport asymmetry of the CBL, the discontinuity of surface emission enhances the segregation between the reactants. In Figure 6.3c, all the reactions zones are found close to the edge of the Gaussian distribution emission, where the majority of the reaction is concentrated.

It is therefore important to quantify how efficiently the species are mixed by turbulence. The intensity or coefficient of segregation (Is) is the variable that characterizes the mixing of the reactants. It is derived from the chemical term of the average concentration equation (6.9) (Danckwerts, 1953). Once again, using the assumption $\sum_{j=1}^M \beta_{lj} \leq 2$ and factorizing equation (6.9), one obtains:

$$\langle \tilde{R}_i \rangle = \sum_{j=1}^M \eta_{ij} Da_j \left[\prod_{l=1}^N \langle \tilde{c}_l \rangle^{\beta_{lj}} (1 + Is_j) \right] \quad (6.15)$$

where Is_j is the intensity of segregation for reaction j defined as follows:

$$Is_j \equiv \frac{\langle \prod_{l=1}^N \tilde{c}_l^{\beta_{lj}} \rangle}{\prod_{l=1}^N \langle \tilde{c}_l \rangle^{\beta_{lj}}}. \quad (6.16)$$

For a second-order reaction with species A and B this term reads:

$$Is = \frac{\langle A'B' \rangle}{\langle A \rangle \langle B \rangle}. \quad (6.17)$$

The above quantity describes the extent to which the reactants are mixed (or segregated). The limiting values of Is depend on the Damköhler number, the transport direction of the species, and the ratio of the concentrations of species. The minimum value, $Is = -1$, corresponds to the situation in which species are transported in opposite directions (case of non-premixed reactants), and the chemical reaction rate is infinitely fast, i.e., $Da_j \rightarrow \infty$. In that circumstances, the reaction takes

place in an infinitely thin zone. The maximum limiting value, $Is = \infty$, is also given by a reaction characterized by $Da_j \rightarrow \infty$. In this case, species are transported in the same direction and have been previously mixed homogeneously.

Figure 6.4 shows Is for the turbulent reacting flow of the uniform emission (Figure 6.3b) and non-uniform release (Figure 6.3c). In the bulk of the CBL, the asymmetry created by the different dynamic characteristics of the thermals and subsidence motions, leads to a segregation of the reactants. This inefficient mixing causes a reaction to undergo 20 % slower than a reaction that takes place when species are homogeneously mixed. Moreover, the discontinuity of the Gaussian emission field causes an additional segregation of the species. For this particular case, the Is value is close to the minimum value of -1 , which implies that there is hardly any chemical reaction because of the almost total segregation of species.

6.4 Chemically reactive plumes

Plumes of reactive species constitute a particular, but important, case of turbulent reacting flows in the ABL. Large quantities of compounds are normally discharged into the ABL by point sources. The released pollutants are dispersed by atmospheric turbulence, and undergo chemical transformations by reacting with ambient species. These plumes are characterized by emissions with high concentrations. The atmospheric turbulence not only drives the plume dispersion and mixing, but it can also limit the transformation of species. Therefore, to study the distribution and evolution of chemically active plumes one can make use of the dimensionless numbers presented in the previous Section.

We first discuss the dispersion of a plume that decays with a first-order reaction and, secondly, we analyze the effect of turbulence on the mixing on the transformation of species that react with second-order reactions. In the first numerical experiment (Section 6.4.1), turbulence is driving the dispersion, but the chemical transformation of species does not depend on the capacity of turbulence to mix the compounds. In the second situation (Section 6.4.2), we discuss the emission of species from a point source (for instance NO) which reacts non-linearly with an ambient species (for instance O_3). In this case, the reactivity depends on how efficient the turbulent mixing is in bringing species together.

6.4.1 The effect of chemistry: simple decay

The dispersion of a passive tracer in a CBL has been studied by means of LES (Dosio *et al.*, 2003). On the basis of the same numerical experimental setup, we analyzed the dispersion characteristics of a plume formed by a reactant that decays at a reaction rate $j \text{ s}^{-1}$ in a boundary layer driven mainly by convection, with a constant geostrophic wind equal to 5 ms^{-1} . For this simple decay, the turbulence Damköhler number Da_t is defined by the turbulent time $\tau_t = (z_i/w_*)$, where w_* is the convective velocity scale (see Deardorff, 1970a) and z_i is the depth of the boundary layer. The chemical time scale is simply $\tau_c = j^{-1} \text{ s}$. Different simulations in which Da_t is varied, were carried out to determine the effect of a chemical decay on the averaged concentration and the concentration fluctuations. Figure 6.5 shows the time evolution of the instantaneous concentration in the plume centreline, at 750 m downstream from the point release. The point source is located in the

6.4. Chemically reactive plumes

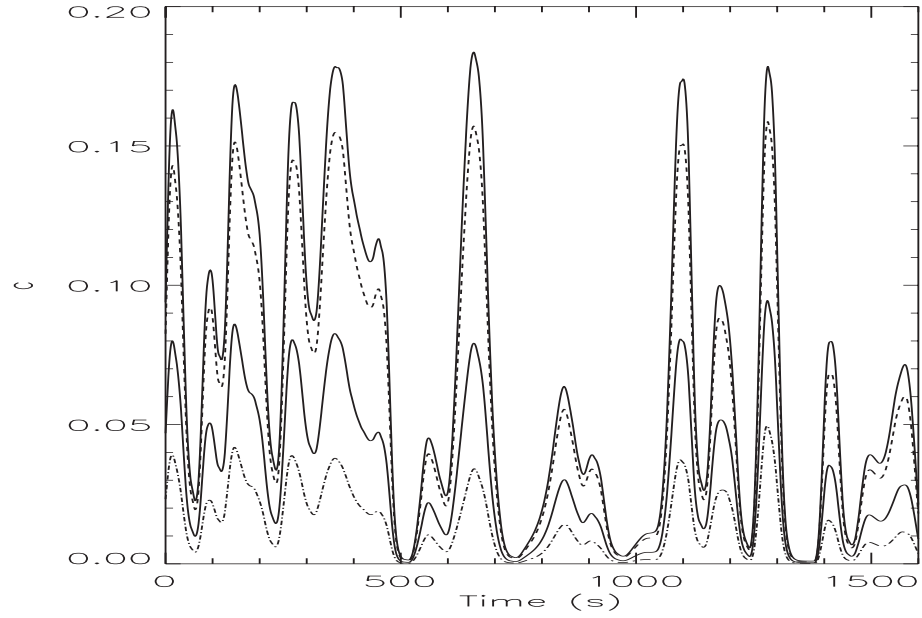


Figure 6.5: Time evolution of species undergoing a decay in a first-order reaction with different Damköhler numbers: 0.06 (continuous line), 0.6 (dashed), 3 (dashed-three dots) and 6 (dashed-dotted).

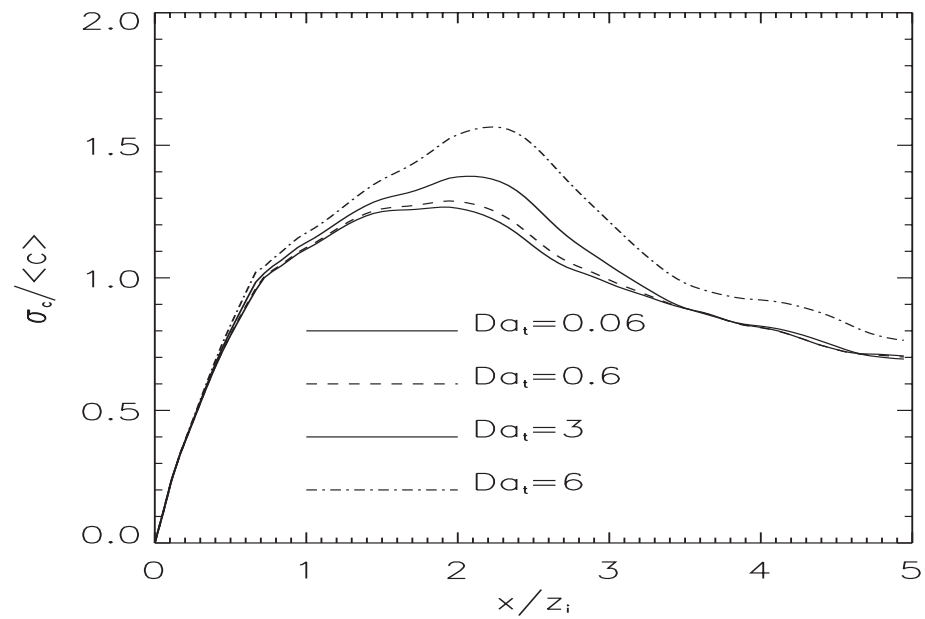


Figure 6.6: Hourly averages of relative concentration fluctuations in the plume centreline, as a function of the downstream position for different values of the turbulent Damköhler number.

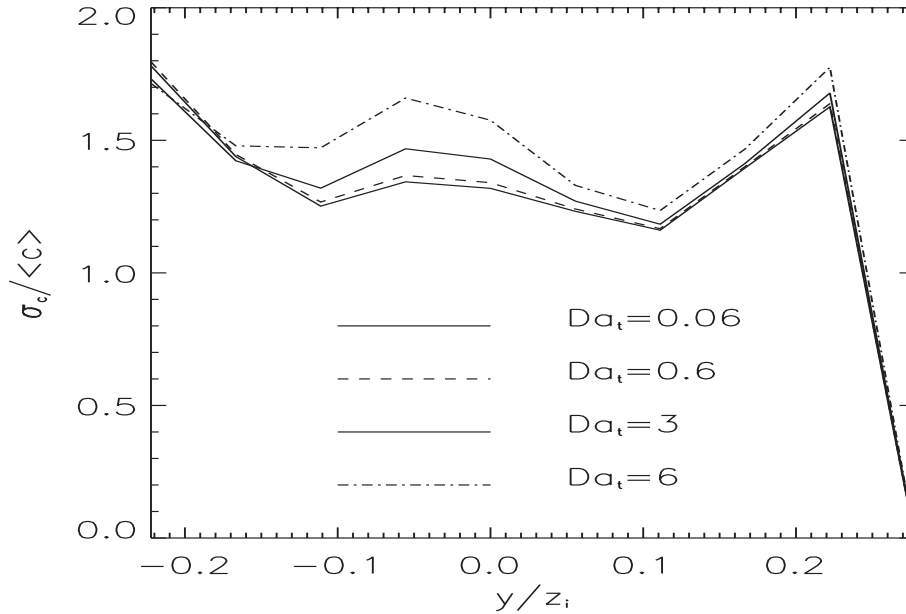


Figure 6.7: Horizontal profile of the relative concentration fluctuations across the plume centreline at $x=750$ m, for different values of the turbulent Damköhler number. The plume edge is located at the value $y/z_i=0.2$.

middle of the ABL. It can be seen that the intermittent nature of the concentration is maintained for all cases shown ($Da_t=0.06$ (almost inert), $Da_t=0.6$ (slow chemistry), $Da_t=3$ (moderate chemistry), $Da_t=6$ (fast chemistry)). For all the Da_t numbers, the instantaneous concentrations show an identical pattern for the fluctuations generated by the atmospheric turbulence. The variation in the absolute value of the concentration is due only to the chemical decay.

Because of the chemical transformation, the variability, quantified by the concentration variance, is also modified. The presence of the chemical term in the concentration fluctuation equation (term 6.11) modifies the concentration variance, which now will depend on the turbulent Damköhler number. Notice that this term for a first-order decay is $-j\langle c'^2 \rangle$. Figure 6.6 shows the relative concentration fluctuations for the same simulation as in Figure 6.5. All the simulations are conducted with the same initial and boundary conditions (source size, emission release, boundary layer characteristics). The four cases show the characteristic pattern found in experimental and numerical studies, with a maximum of $\sigma_c/\langle C \rangle$ downstream from the release (*Fackrell and Robins, 1982; Sykes et al., 1992*). However, for the chemically active plume, we found that the decay enhances the relative value of the concentration fluctuations with respect the absolute value, and shifts the position of the maximum further downstream. Consequently, the value of the maximum and its downstream location depend not only on the plume position, the source size and the dispersion characteristics, but also on the reactivity of the species. Figure 6.7 shows the horizontal profiles of the relative concentration fluctuation across the plume at 750 meters from the point release. The $\sigma_c/\langle C \rangle$ values increase with the Damköhler number at the plume edge ($y/z_i = 0.2$) and close to the centreline ($y/z_i = 0.0$). Plume variability depends on the interaction of the plume with the boundary layer characteristics and the reactivity of the emitted species.

6.4.2 The effect of turbulence on chemistry: non-linear reaction

As mentioned in the previous Sections, turbulence limits the reactivity of the non-linear reactions because it is unable to mix the species uniformly. For elevated plumes, this effect is even larger than for surface releases, because plumes are normally characterized by high concentration gradients. As a consequence, species are highly segregated in the vicinity of the plume.

Before continuing with the discussion, it is important to describe how the spatial scales of turbulence affect the dispersion of plumes. Large spatial scales govern the dispersion of the plume in a process called meandering, or macro-mixing. The smallest scales of the turbulence are the most active in mixing the plume reactant with the ambient species. These fluctuations are called “in-plume” fluctuations. The process is also known as micro-mixing. In the discussion below, we focus on the effect of “in-plume” fluctuations on the chemical reactivity. *Joergensen and Mikkelsen* (1993) described a method for removing the effect of meandering in the plume dispersion to study solely the “in-plume” fluctuations. Although there is still a lack of complete observational evidence, experiments and field campaigns showed the effect of turbulent fluctuations on chemical reactions (*Builtjes and Talmon*, 1987; *Ibrahim et al.*, 1987; *Komori et al.*, 1991; *Brown and Bilger*, 1998). The intensity of segregation was measured in the majority of these experiments. Figure 6.8 shows the value of Is as a function of the ratio r , for an NO -plume (NO is nitric oxide) released in the atmospheric surface layer and then reacting with ambient ozone (O_3), according to the reaction $NO + O_3 \rightarrow P$ (*Komori et al.*, 1991). This reaction is normally characterized by $Da \approx O(1)$, that is, turbulence controls the chemistry. In spite of the scatter in the observational data, it is clear that Is values are not negligible and they increase with the concentration ratio (as previously shown in Figure 6.1). Similar results were found in laboratory experiments performed by *Brown and Bilger* (1998) (Figure 9 in their paper) for the same species and chemical reaction. Their observations show the increase of Is for a large Damköhler number and the decrease of Is downwind of the point release. To complete the discussion of the observational studies, we show in Figure 6.9 the variation of the intensity of segregation across the horizontal direction of the plume, at various distances from the release point. For a chemically reactive plume, Is was calculated using a full second-order turbulent closure model implemented in a discretized Gaussian plume model (*Galmarini et al.*, 1995). As in Figure 6.7, the large concentration fluctuations are located in the plume centreline ($r/\sigma=0$; note that in the Figure r is now the distance from the plume centerline). The values range from -1 at $x=1200$ m to -0.05 at $x=2600$ m. The absolute value of Is increases with downwind distance (minimum values at 1200 m) and finally the Is values diminish until they are negligible, i.e., until the species are uniformly mixed with ambient air. The distance where the segregation effects are relevant depends on the strength of the source emission and the boundary layer characteristics.

LES studies of chemically active plumes corroborate the discussed earlier results. *Sykes et al.* (1992) found that, for the same reaction, the control of turbulence can reduce the rate by a factor of six. *Meeder and Nieuwstadt* (2000) agreed with the previous results by *Sykes et al.* (1992), and stressed the importance of the smallest turbulent scales for fast chemical reactions ($Da_k \gg 1$). In their LES, they introduced a sub-grid parameterization that accounts for the incomplete mixing inside the grid cell. Recently, other LES studies have dealt with more complex chemical mechanisms. *Herwehe et al.* (2002) showed that the intensity of segregation can be positive if species are premixed before they are emitted and introduced into the ABL. As a consequence the reactivity of

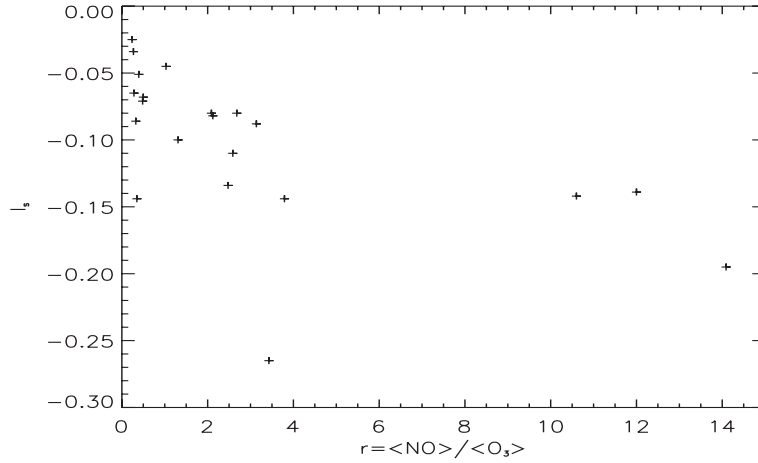


Figure 6.8: Observations of the intensity of segregation ($I_s = \langle NO'O'_3 \rangle / \langle NO \rangle \langle O_3 \rangle$) as a function of the ratio $r = \langle NO \rangle / \langle O_3 \rangle$ for an NO-plume released in the atmospheric surface layer and reacting with ambient O_3 (Komori *et al.*, 1991).

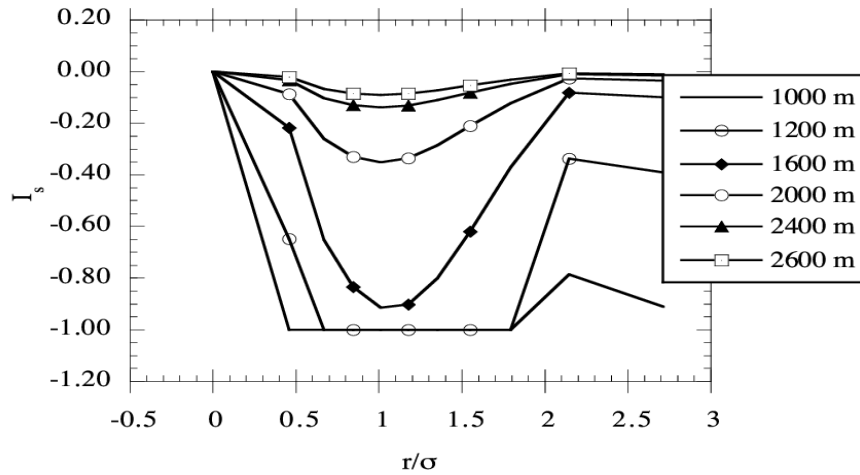


Figure 6.9: The intensity of segregation as a function of the distance from the plume centreline (r) made dimensionless by the dispersion parameter (σ) at various distances from the release point. The intensity of segregation was calculated using a chemically reactive plume model (Galmarini *et al.*, 1995).

6.5. Conclusions and future perspectives

the species can be enhanced. *Lewellen and Lewellen* (2001) found that the reaction rates within a wake plume generated by the emission of species from an aircraft, were largely reduced. The latter LES results and aircraft observations by *Tan et al.* (1998) demonstrated that the chemistry related to the HO_x species is limited by the turbulent fluctuations in and around the plume. Several other modelling techniques have been used to explain the role of turbulence on chemical reactions of species emitted at point sources. *Bilger et al.* (1991) and *Brown and Bilger* (1998) overcame the problem of the chemical term in the governing equations by solving them for a conserved scalar. This conserved scalar is a combination of several reactants, and it acts as a passive species. Another possible approach is based on calculating the statistics of reactive plumes using methods that are based on the probability distribution functions (PDF) of the species (*Pope*, 1985; *Fraigneau et al.*, 1996; *Gonzalez*, 1997). Other modelling studies have attempted to close the covariance term $\langle c'_i c'_k \rangle$ by relating it to the variance (*Karamchandani and Peters*, 1987) or by explicitly solving the covariance equations (*Galmarini et al.*, 1995). *Lamb* (1978) and *Georgopoulous and Seinfeld* (1986) proposed parameterizations to calculate the covariance $\langle c'_i c'_k \rangle$ as a function of the instantaneous concentrations. A more applied type of methodology proposed by *Bange et al.* (1991) is based on the estimation of new dispersion parameters calculated from instantaneous concentration measurements. By characterizing a plume by more adequate dispersion parameters, these authors attempt to reduce the effect of concentration fluctuations on the model calculations. These studies agree about the importance of turbulent mixing for controlling the plume reactivity, and about the necessity of using the Damköhler number and the concentration ratio to describe the turbulent reacting flows.

6.5 Conclusions and future perspectives

Atmospheric turbulence is the main mechanism that drives the dispersion, the mixing, and the transformation of chemically active species. In the case of emitted compounds that react with ambient species according to a second-order reaction, the reaction rate can decrease because the reactants are segregated. This reduction is more significant when the time scales of turbulence and chemistry are comparable. The key scaling numbers, which determine the effect of turbulence on the chemical transformations, are the Damköhler numbers and the ratios of the concentrations in the species. On the basis of these numbers, one can identify three regimes for turbulent reacting flows: slow, moderate and fast. For moderate and fast chemistry regimes, turbulence strongly controls the reactivity of the transformation. In the ABL, the chemical reactions associated with the compounds NO_x and HO_x are normally in the moderate and fast regimes. In order to account for the effect of turbulence on chemistry, one should include the chemical term in the average concentration equation (term 6.8) and in the flux and (co-)variance equations (terms 6.10 to 6.12). When these terms are included the distribution and evolution of the mean concentration and the second-order moments can deviate largely from the moments of the inert species. Another relevant factor is the state of equilibrium between species. If the species are in chemical equilibrium, they act as passive species. Physical processes such as turbulent mixing, injection of species at the surface or at the inversion zone, and the presence of clouds can disturb this equilibrium. The LES technique has let us study all these processes numerically and has given us a fundamental understanding and a detailed description of the atmospheric turbulent reacting flows. However, close to the emission

sources, the LES results can be affected by errors due to the assumption of uniform mixing within the grid cell. In the future, more research should be directed towards the development of a parameterization to account for this effect. The effect can be particularly important for species that react at a fast reaction rate (for instance radicals) or in conditions where the ABL is stably stratified.

Regional and large-scale atmospheric chemistry models have to treat the aforementioned processes in the form of sub-grid parameterizations since they occur at scales smaller than the grid size. It is therefore necessary in modelling studies to incorporate the modification of the reaction rate caused by heterogeneous mixing. Several studies have already proposed sub-grid parameterizations to account for these effects. In their study of the convective boundary layer, *Chatfield and Brost* (1987) and *Petersen et al.* (1999) proposed using the mass-flux approximation to represent the segregation of species due to the asymmetry of the rising and subsiding motions within the boundary layer using the mass-flux approximation. Because of the complexity of the atmospheric chemistry, a more simpler approach may be useful to start with. Let us introduce an effective chemical reaction rate k_{eff} which accounts for the non-uniform mixing in atmospheric flows and is defined as $k_{eff} = k(1 + I_s)$, where k is the reaction rate measured under homogeneous conditions. The intensity of segregation should be estimated from observations (*Builtjes and Talmon*, 1987; *Brown and Bilger*, 1998; *Kramm and Meixner*, 2000) or using a parameterization that relates I_s to known quantities (*Petersen and Holtslag*, 1999; *Vinuesa and Vilà-Guerau de Arellano*, 2003). This parameterization can be applied to surface and point source releases. For the latter, k_{eff} might depend on the downstream position and the distance from the plume centreline. In the turbulent reacting flows with large emission release associated to power plants or urban areas the influence of turbulence on chemistry can lead to large errors and discrepancies in the measurements. Close to the sources, species are highly segregated and far from chemical equilibrium. *Hilst* (1998) and *Russell and Dennis* (2000) stressed that plumes can only be crudely approximated in large-scale models. A well-known example is the emission of nitrogen compounds in rural areas characterized by large emissions of biogenic compounds (*Verver et al.*, 2000). Generally, models assume that the nitrogen compounds are mixed instantaneously which can lead to model errors. Consequently, plumes embedded in large-scale models should take into account for the effects of turbulent mixing on chemical reactions. Following this line, *Karamchandani et al.* (2000) developed a model that includes the effects of turbulent fluctuations on non-linear reactions in the dispersion of a reacting plume with a complex chemical mechanism. They found that the inclusion of turbulent fluctuations in the reaction between nitric oxide and ozone gives a more accurate representation of the dispersion of chemically reactive species (see Figure 3 in their paper).

In spite of the large numbers of process modelling studies performed in the last decade, more experimental evidence is needed to investigate the role of physical processes in chemical reactions and to provide a data base that can validate model results (*Kramm and Meixner*, 2000; *Vilà-Guerau de Arellano*, 2003). Specific questions that still need to be studied on the basis of observations are: (1) the divergence with height of the reactive species in the atmospheric surface layer and (2) the measurement of the intensity of segregation for different chemical species and under various conditions of atmospheric stability and dispersion. Further research activities should combine laboratory experiments, observations and modelling studies in order to derive a similarity theory for turbulent reacting flows. On the basis of this theory, it should be possible to incorporate into regional and global models scaling laws that will account for the influence of turbulence on chemical reactions.

Chapter 7

Summary and Perspectives

7.1 General conclusions

The dispersion of a plume in the Atmospheric Boundary Layer is a very complex phenomenon that includes the transport, the mixing and the chemical transformations of the plume material. When a plume is dispersed in the ABL, its shape, evolution, and internal structure are determined by the interaction between the plume and the turbulent eddies that characterize the atmospheric motion. To understand and predict atmospheric dispersion, it is therefore essential to study and analyze the characteristics and the properties of the atmospheric turbulent motion.

Nowadays, a broad range of tools and methodologies are available for investigating turbulent dispersion. In particular, the fast growth in computer' performance has allowed one to simulate the atmospheric flow by numerically solving a system of mathematical equations that describe the evolution of the main atmospheric variables, such as wind speed, temperature, and humidity. This technique is known as numerical simulation. One of the most powerful numerical techniques available for the study of the ABL, is the Large-Eddy Simulation (LES), which explicitly solves the most relevant scales of turbulent motion. The LES technique is particularly suited to study the Convective Boundary Layer (CBL), which is characterized by large-scale, organized motion of warm air (updrafts) and cold air (downdrafts) known as thermal convection. In this doctoral research, a LES has been used to simulate with great detail the evolution in space and in time of a plume dispersing in the CBL.

The main novelty of the research is the simultaneous investigation of turbulent dispersion in different frameworks. By studying dispersion in two coordinate systems, namely the absolute (or fixed) coordinate system, and the relative coordinate system (that is the coordinate system of the plume's center of mass), it was possible to separate the different contributions of small- and large-scale motion on the plume evolution. In the relative coordinate system, in fact, the (vertically) inhomogeneous meandering motion was removed, and only the small homogeneous turbulent eddies contributed to the dispersion process.

Turbulent dispersion was also studied in both the Eulerian and the Lagrangian frameworks. In the Eulerian framework, dispersion properties, such as the concentration of the pollutant, are calculated or measured at fixed points in space. In the Lagrangian framework, each particle in the plume is followed singularly, and dispersion properties are calculated in a reference frame that moves

with the particles themselves.

The use of different reference systems allowed many research questions to be addressed, as discussed in Chapter 1. The main results of this research are summarized below.

In **Chapter 3**, atmospheric dispersion was studied by calculating energy spectra and velocity autocorrelations in both the Eulerian and the Lagrangian frameworks (*Research Question 1*).

In particular, Eulerian statistics were calculated by means of both spatial and temporal analysis. Spatial analysis is mostly used in numerical or laboratory experiments, where data is collected at different locations at a fixed time (or averaged over a certain time). Temporal analysis is mainly used in field experiments, where statistics are calculated by the analysis of time series collected at fixed positions. These two analysis are usually related by Taylor's hypothesis of frozen turbulence, which is always assumed but seldom validated. By deriving characteristic length and temporal scales through the analysis of the autocorrelation function and the spectral peak, Taylor's hypothesis was successfully validated in the simulated CBL.

The relationship between flow properties (autocorrelations) and dispersion characteristics (particles' displacements) was also discussed through Taylor's analysis of turbulent dispersion. A distinction was made between horizontal and vertical motion, in order to study the effect of the inhomogeneity of the vertical structure of the turbulence and the presence of the CBL boundaries (surface and top of the CBL) on the particle's motion. The results showed that the horizontal dispersion was satisfactorily described by Taylor's diffusion theory, because the homogeneous horizontal motion was characterized by an exponential autocorrelation function. On the contrary, the autocorrelation function for the vertical velocity had a more complicated shape, due to the vertical inhomogeneity of the turbulent flow and the presence of the CBL boundaries, which limited the vertical particles' motion. As a result, particles moved following a wave-like motion. Taylor's analysis correctly predicted the particles' displacement at short times, when the particles' motion was not affected by the boundaries, but overestimated the asymptotic limit at longer times. The use of a different method to calculate the Lagrangian integral time, allowed us to distinguish better between free and bounded motion, and a better agreement was found between Taylor's relationship and particles' vertical displacement.

This study was completed by verifying the equivalence between Lagrangian particle displacement (that is, the particles' displacement measured at fixed travel times) and the Eulerian dispersion parameter (that is, the particle displacement as a function of the distance from the source). The comparison showed that, for practical purposes, using Eulerian dispersion parameters instead of Lagrangian ones does not lead to larger errors. This is related to the fact that Taylor's hypothesis of frozen turbulence holds in the simulated CBL.

Finally, the relationship between the Lagrangian and the Eulerian frameworks was investigated by calculating the ratio β between Lagrangian and Eulerian time scales. These time scales can equally be derived either by calculating the integral of the autocorrelation function, or by determining the frequency of the spectral peak. Since there is usually a large scatter in the spectra, the use of the autocorrelation function gives the most accurate results.

Currently used parameterizations for the Lagrangian time scale and the ratio β , derived either in previous field atmospheric experiments or through theoretical analysis, were calculated as a function of the flow characteristics (CBL height and velocity variances). These parameterizations were

7.1. General conclusions

compared with the LES results, and showed a satisfactory agreement.

In **Chapter 4**, plume dispersion in the CBL was studied in two coordinate systems: the absolute coordinate system and the coordinate systems relative to the plume's instantaneous center of mass. By so doing, it was possible to separate the different contributions of small- and large-scale motions on the plume's evolution (*Research Question2*). The shape and the symmetry of the plume distribution was also analyzed by calculating the mean plume position, the dispersion parameters (variance), and the skewness of the plume position in both the coordinate systems (*Research Question3*).

The analysis of the third-order moments showed that the symmetry of the scalar distribution was affected by both the turbulent characteristics of the CBL (inhomogeneity of the vertical large-scale motion), and the presence of the CBL boundaries. In fact, the skewness of the plume's centerline position was mainly influenced by the meandering of the plume as it was transported by the up-drafts and dowdrafts. On the contrary, the skewness of the relative position was mainly affected only by the reflection of the plume by the CBL boundaries, because in the relative coordinate system the large-scale motion was removed.

Mean concentrations and concentration fluctuations (that quantify the concentration variability) were also studied in absolute and relative coordinate systems. In particular, the intensity of relative concentration fluctuation i_{cr} was calculated, because it quantifies the internal (in-plume) mixing of the scalar within the plume. The evolution of i_{cr} is a critical parameter in operational models for turbulent dispersion, because it is used in the parameterization of the probability distribution function (PDF) of the relative concentration. A currently used parameterization for the PDF of the relative concentration was calculated as a function of i_{cr} , and showed very good agreement with the LES results.

Finally, the validity of Gifford's formula, which relates the absolute concentration to the relative concentration and the position (PDF) of the plume's centerline, was studied. It was found that, due to the presence of the CBL boundaries, Gifford's formula was not able to correctly reproduce the value of the absolute mean concentration, especially near to the ground. This result was explained in terms of the effect of the reflection of the plume by the boundaries, which caused the relative concentration to depart from a Gaussian distribution and to become skewed. The results were improved by using a parameterization for the relative mean concentration that took into account the skewness of the relative plume position.

This study showed the importance of analyzing higher-order statistics in order to understand the evolution of a plume dispersing in the atmospheric CBL, and to derive an operational model for turbulent dispersion. Moreover, the LES technique was shown to be an ideal tool for the detailed study of the plume's internal structure and variability. Therefore, the LES results can be used to better interpret the measurements of remote-sensing instruments (such as lidars), which are able to directly measure the in-plume structures of a dispersing plume.

In **Chapter 5**, the dispersion of a plume in boundary layers driven by different combinations of buoyancy and shear was investigated (*Research Question4*).

Different boundary layer archetypes varying from the pure-convection to near-neutral situation were simulated and systematically classified according to the shear-buoyancy ratio u_*/w_* and the scaling parameter $-z_i/L$.

Good agreement was found between the LES results and the laboratory and field experiments in the pure-convective situation.

The influence of the increasing wind shear was first studied on the flow statistics (profiles of velocity variances) as the dispersion characteristics are directly dependent on the turbulence's properties. The results showed an increase in the horizontal velocity variance and a reduction in the vertical velocity variance.

The main effect of the wind shear on the dispersion statistics resulted in a reduction of the vertical spread whereas the horizontal spread was enhanced. Consequently, the ground concentrations were strongly modified, because the increasing wind tended to advect the plume horizontally for a longer time, and the tracer therefore reached the ground at greater distances from the source. The meandering component of the vertical dispersion was also studied as a function of the increasing wind shear. Meandering is the main contribution to dispersion especially near to the emitting source, where the plume is transported by the large-scale eddies. The meandering component was modified by the wind shear, in particular for plumes emitted near to the ground, where the presence of the surface enhanced the shear, which in turn, reduced the looping of the plume. As meandering is the main source of concentration variance, the maximum of the concentration fluctuations was shown to diminish as the flow becomes less convective.

Finally, parameterizations for the dispersion parameters that account for the combined effect of buoyancy and shear were derived. In the parameterization for σ_y , the wind rotation was explicitly considered in the shear-generated dispersion. The parameterization of σ_z accounted for the two opposite effects: the reduction of the vertical motion near the ground and the shear generated turbulence. Both the parameterizations gave satisfactory results when compared with the LES data in all the simulated cases.

Chapter 6 consisted in a complete review of the studies of dispersion of chemically reactive species in the ABL (*Research Question 5*). In particular, the effect of turbulent mixing on chemical transformations within a plume was analyzed. In fact, the reaction rate of compounds that react with ambient species can decrease if the reactants are segregated because of a non-uniform mixing. In a plume, characterized by emissions with high concentrations, this segregation between the species within the plume and the ambient air is relevant especially near the edge of the plume, where the concentration gradients are high.

It was also shown in this Chapter that one of the key scaling numbers that determine the effect of turbulence on the chemical transformations, is the ratio of the time scale of turbulence to the time scale of the chemical reaction (the Damköhler number). On the basis of the Damköhler number, three regimes for turbulent reacting flows were identified: slow, moderate and fast. For moderate and fast chemistry regimes, characteristic of compounds like NO_x and HO_x , turbulence strongly controls the reactivity of the transformation, and the mean concentration and the second-order moments can deviate largely from the moments of the inert species. In particular, it was shown that, for a plume formed by species that decay with a first-order reaction (such as, for instance, a radioactive decay), both the absolute concentration and the concentration variability (concentration fluctuations) strongly depend on the Damköhler number.

The effect of turbulent mixing on a second-order chemical transformation in a plume has been studied by many authors by means of different modelling techniques and measurements. All of

7.2. Future perspective

these studies agreed on the importance of turbulent mixing for controlling the plume, and the need to use the Damköhler number to characterize the turbulent reacting flows.

The effect of turbulent mixing on chemical reaction is critically important especially for regional and large-scale atmospheric chemistry numerical models, because they generally assume that the chemical species are instantaneously and uniformly mixed within the grid cells. It is therefore necessary to incorporate, in the form of a parameterization, the modification of the reaction rate caused by heterogeneous turbulent mixing. An intuitive and simple approach is to define an effective chemical reaction rate k_{eff} , which accounts for the non-uniform mixing in atmospheric flows as a function of the reaction rate measured under homogeneous conditions, and the intensity of segregation (that is the ratio between the covariance of the reactive species and the product of their mean concentration). The intensity of segregation should be estimated from observations, or using a parameterization that relates it to known quantities.

7.2 Future perspective

Although atmospheric dispersion has been widely investigated since the beginning of the last century, it was only in the last two decades that the development of increasingly complex numerical models (such as LES) allowed one to simulate in detail the structure and the evolution of the atmospheric turbulent motion. The results of these models have greatly improved the knowledge and the understanding of the processes that influence the transport, the mixing, and the chemical reactions of species in a dispersing plume.

However, there are still open questions that need further investigation and can be addressed in future researches.

First, in our study, only idealized domains, characterized by flat terrain and homogeneous heat flux, were studied. Dispersion in the atmosphere is influenced by local features such as topography, inhomogeneity of the terrain and the land use (such as canopy and forests), and presence of obstacles and buildings (such as urban areas). In addition, the variability of the meteorological conditions, such as mesoscale and synoptic circulation, entrainment processes, and cloud formation and evolution, can alter significantly the flow circulation and the turbulent motions. The investigation of these issues requires further developments in the LES codes (in order to account for a larger number of physical processes), and a growth in the numerical capabilities of the computers (in order to run such a code).

Additionally, the improvement in the computational performances would allow one to describe in greater detail the smallest scales of motion, which were shown to be mainly responsible for the internal mixing of contaminants within the plume, and, as a consequence, of great importance in the study of the effect of turbulent mixing on chemical reactions.

Finally, the numerical simulation of ABL in stable conditions is still very uncertain, although significant progresses have been made in the recent years. Atmospheric dispersion in conditions of stable stratification may lead to very high ground concentrations. Therefore, a systematic investigation of turbulent dispersion in the stable boundary layer is a great, but very important, challenge. Numerical simulations are not the only tool available to study atmospheric dispersion, and observational evidence (through laboratory experiments and field campaigns) is essential to validate and complement the numerical experiments. This is true especially for the study of the interaction be-

tween atmospheric turbulence and chemical reactions, because of the difficulty to detect accurately very small and very fast variations of chemical concentrations in the ABL. In particular, specific questions that still need to be addressed by means of experimental observations are: (1) the divergence with height of the reactive species in the atmospheric surface layer, and (2) the measurement of the intensity of segregation for different chemical species and under various conditions of atmospheric stability and dispersion.

Further research activities should combine laboratory experiments, observations and modelling studies in order to increase our understanding of the above mentioned processes. On the basis of this knowledge, it should be possible to incorporate into operational local, regional, and global models, scaling laws and parameterizations that will account for the majority of the processes responsible for atmospheric dispersion.

Bibliography

- Angell, J. K., Measurements of Lagrangian and Eulerian properties of turbulence at a height of 2500 ft, *Quart. J. Roy. Meteor. Soc.*, **90**, 57–71, 1964.
- Bange, P., L. H. J. M. Janssen, F. T. M. Nieuwstadt, H. Visser, and J. J. Erbrink, Improvements of the modelling of daytime nitrogen oxide oxidation in plumes by using instantaneous plume dispersion parameters, *Atmos. Environ.*, **25A**, 2321–2328, 1991.
- Barad, M. L., *Project Prairie Grass, A Field Program In Diffusion*, Geophysical Research Paper, No. 59, 439 p., Air Force Cambridge Research Center, U.S. Air force, Bedford, MA, 1958.
- Batchelor, G. K., Diffusion in a field of homogeneous turbulence, *Aus. J. Sci. Res.*, **2**, 437–450, 1949.
- Beare, R. J., and 16 co-authors, An intercomparison of large-eddy simulations of the stable boundary layer, *Bound.-Layer Meteor.*, *in press*, 2005.
- Bilger, R. W., The effect of admixing fresh emissions on the photostationary state relationship in photochemical smog, *Atmos. Environ.*, **12**, 1109–1118, 1978.
- Bilger, R. W., *Turbulent reacting flows*, chap. 3: Turbulent flows with non-premixed reactants, pp. 243, Springer, 1980.
- Bilger, R. W., L. R. Saeiran, and L. V. Krishnamoorthy, Reaction in a scalar mixing layer, *J. Fluid Mech.*, **233**, 211–242, 1991.
- Blackadar, A. K., *Turbulence and diffusion in the atmosphere*. Springer, 1998.
- Bretherton, C. S., and 15 co-authors, An intercomparison of radiatively-driven entrainment and turbulence in a smoke cloud, as simulated by different numerical models, *Quart. J. Roy. Meteor. Soc.*, **125**, 400–425, 1999.
- Briggs, G. A., Analytical parameterizations of diffusion: the convective boundary layer, *Journal of climate and applied meteorology*, **24**, 1167–1186, 1985.
- Briggs, G. A., Plume dispersion in the convective boundary layer. Part II: Analysis of CONDORS field experiment data, *J. Appl. Meteorol.*, **32**, 1388–1425, 1993.
- Brost, R. A., A. C. Delany, and B. Huebert, Numerical modelling of concentrations and fluxes of HNO₃, NH₃ and NH₄NO₃ near the surface, *J. Geophys. Res.*, **93**, 7137–7152, 1988.
- Brown, A. R., and 12 co-authors, Large-eddy simulation of the diurnal cycle of shallow cumulus convection over land, *Quart. J. Roy. Meteor. Soc.*, **128**, 1075–1093, 2002.

- Brown, R. J., and R. W. Bilger, Experiments on a reacting plume. 1. conventional concentration statistics, *Atmos. Environ.*, **32**, 611–628, 1998.
- Builtjes, P. J. H., and A. M. Talmon, Macro- and micro-scale mixing in chemical reactive plumes, *Bound.-Layer Meteo.*, **41**, 417–426, 1987.
- Businger, J., J. Wyngaard, Y. Izumi, and E. Bradley, Flux profile relationships in the atmospheric surface layer, *J. Atmos. Sci.*, **28**, 181–189, 1971.
- Carruthers, D. J., and J. C. Hunt, Velocity fluctuations near an interface between a turbulent region and a stably stratified layer, *J. Fluid Mech.*, **165**, 475–501, 1986.
- Caughey, S. J., Observed characteristics of the atmospheric boundary layer, in *Atmospheric Turbulence and Air Pollution Modelling*, pp. 107–158, Reidel Publishing Company, Dordrecht, 1982.
- Caughey, S. J., and S. G. Palmer, Some aspects of turbulence structure through the depth of the convective boundary layer, *Quart. J. Roy. Meteor. Soc.*, **105**, 811–827, 1979.
- Chatfield, R., and R. Brost, A two-stream model for the vertical transport of trace species in the convective boundary layer, *J. Geophys. Res.*, **92**, 13263–13276, 1987.
- Corssin, S., Estimate the relation between Eulerian and Lagrangian scales in large Reynolds number turbulence, *J. Atmos. Sci.*, **20**, 115–119, 1963.
- Courtney, M., and I. Troen, Wind speed spectrum from one year of continuous 8Hz measurements, *J. Atmos. Sci.*, **20**, 115–119, 1990.
- Csanady, G. T., *Turbulent diffusion in the environment*, pp. 248, D. Reidel Publishing company, 1973.
- Cuijpers, J. W. M., Subgrid parameterization in a large-eddy simulation model, in *9th Symposium on Turbulence and diffusion*, pp. 176–179, American Meteorological Society, Risø, Roskilde, Denmark, 1990.
- Cuijpers, J. W. M., *Large eddy simulation of cumulus convection*. PhD thesis, Technische Universiteit Delft, 1994.
- Cuijpers, J. W. M., and P. G. Duynkerke, Large eddy simulation of trade wind cumulus clouds, *J. Atmos. Sci.*, **50**, 3894–3908, 1993.
- Danckwerts, P. V., The definition and measurement of some characteristics of mixtures, *Appl. Sci. Res.*, **3**, 276–296, 1953.
- Daoud, W. Z., J. W. D. Kahl, and J. K. Ghorai, On the synoptic-scale Lagrangian autocorrelation function, *J. Appl. Meteorol.*, **42**, 318–324, 2002.
- de Baas, A. F., H. van Dop, and F. T. M. Nieuwstadt, An application of the Langevin equation for inhomogeneous conditions to dispersion in a convective boundary layer, *Quart. J. Roy. Meteor. Soc.*, **112**, 165–180, 1986.
- de Roode, S. R., P. G. Duynkerke, and H. J. J. Jonker, Large-eddy simulation: How large is large enough?, *J. Atmos. Sci.*, **61**, 403–421, 2004.
- Deardorff, J., Convective velocity and temperature scales for the unstable planetary boundary layer and rayleigh convection, *J. Atmos. Sci.*, **27**, 1211–1213, 1970a.

Bibliography

- Deardorff, J. W., A numerical study of three-dimensional turbulent channel flow at large Reynolds numbers, *J. Fluid Mech.*, **41**, 453–480, 1970b.
- Deardorff, J. W., Three-dimensional numerical study of the height and mean structure of a heated planetary boundary layer, *Bound.-Layer Meteo.*, **7**, 81–106, 1974.
- Deardorff, J. W., and G. E. Willis, Ground-level concentration due to fumigation into an entraining mixed layer, *Atmos. Environ.*, **16**, 1159–1170, 1982.
- Deardorff, J. W., and G. E. Willis, Ground-level concentration fluctuations from a buoyant and non-buoyant source within a laboratory convectively mixed layer, *Atmos. Environ.*, **18**, 1297–1309, 1984.
- Deardorff, J. W., and G. E. Willis, Further results from a a laboratory model of the convective planetary boundary layer, *Bound.-Layer Meteo.*, **32**, 205–236, 1985.
- Degrazia, G., D. Anfossi, H. F. D. C. Velho, and E. Ferrero, A Lagrangian decorrelation time scale in the convective boundary layer, *Bound.-Layer Meteo.*, **86**, 525–534, 1998.
- Donaldson, C. P., and G. Hilst, Effect of inhomogeneous mixing on atmospheric photochemical reactions, *Environ. Sci. and Technol.*, **6**, 813–816, 1972.
- Dosio, A., J. Vilà-Guerau de Arellano, A. A. M. Holtslag, and P. J. H. Builtjes, Dispersion of a passive tracer in buoyancy- and shear-driven boundary layers, *J. Appl. Meteorol.*, **42**, 1116–1130, 2003.
- Duynkerke, P. G., and 9 co-authors, Intercomparison of three- and one-dimensional model simulations and aircraft observations of stratocumulus, *Bound.-Layer Meteo.*, **92**, 453–487, 1999.
- Dyer, A. J., A review of flux-profile relationships, *Bound.-Layer Meteo.*, **7**, 363–372, 1974.
- Eberhard, W. L., W. R. Moninger, and G. A. Briggs, Plume dispersion in the Convective Boundary Layer. Part i: CONDORS field experiment and example measurements., *J. Appl. Meteorol.*, **27**, 599–616, 1988.
- Fackrell, J. E., and A. G. Robins, Concentration fluctuations and fluxes in plumes from point sources in a turbulent boundary layer, *J. Fluid Mech.*, **117**, 1–26, 1982.
- Fedorovich, E., dispersion of passive tracer in the atmospheric boundary layer with wind shears: a review of laboratory and numerical model studies, *Meteorol. Atmos. Phys.*, **87**, 3–21, 2004.
- Fedorovich, E., and J. Thäter, A wind tunnel study of gaseous tracer dispersion in the convective boundary layer capped by a temperature inversion, *Atmos. Environ.*, **36**, 2245–2255, 2002.
- Fedorovich, E., F. T. M. Nieuwstadt, and R. Kaiser, Numerical and laboratory study of horizontally evolving convective boundary layer. part ii: Effects of elevated wind shear and surface roughness, *J. Atmos. Sci.*, **58**, 546–560, 2001.
- Finlayson-Pitts, B. J., and J. N. Pitts, *Atmospheric chemistry: fundamentals and experimental techniques*. John Wiley and sons, 1986.
- Fitzjarrald, D. R., and D. H. Lenschow, Mean concentration and flux profiles for chemically reactive species in the atmospheric surface layer, *Atmos. Environ.*, **17**, 2505–2512, 1983.

- Fraigneau, Y., M. Gonzalez, and A. Coppale, The influence of turbulence upon the chemical reaction of nitric oxide released from a ground source into ambient ozone, *Atmos. Environ.*, **30**, 1467–1480, 1996.
- Franzese, P., Lagrangian stochastic modelling of a fluctuating plume in the convective boundary layer, *Atmos. Environ.*, **37**, 1691–1701, 2003.
- Galmarini, S., and P. Thunis, On the validity of Reynolds assumptions for running-mean filters in the absence of a spectral gap, *J. Atmos. Sci.*, **56**, 1785–1796, 1999.
- Galmarini, S., J. Vilà-Guerau de Arellano, and P. G. Duynkerke, The effect of micro-scale turbulence on the reaction rate in a chemically reactive plume, *Atmos. Environ.*, **29**, 87–95, 1995.
- Galmarini, S., P. G. Duynkerke, and J. Vilà-Guerau de Arellano, Evolution of nitrogen oxide chemistry in the nocturnal boundary layer, *J. Appl. Meteorol.*, **36**, 943–957, 1997a.
- Galmarini, S., J. Vilà-Guerau de Arellano, and P. G. Duynkerke, Scaling the turbulent transport of chemical compounds in the surface layer under neutral and stratified conditions, *Quart. J. Roy. Meteor. Soc.*, **123**, 223–242, 1997b.
- Galmarini, S., C. Beets, P. G. Duynkerke, and J. Vilà-Guerau de Arellano, Stable nocturnal boundary layers: a comparison of one-dimensional and large eddy simulation models, *Bound.-Layer Meteo.*, **88**, 181–210, 1998.
- Gao, W., and M. L. Wesely, Numerical modelling of the turbulent fluxes of chemically reactive trace gases in the atmospheric boundary layer, *J. Appl. Meteorol.*, **33**, 835–847, 1994.
- Garratt, J. R., *The Atmospheric Boundary Layer*, p. 316. Cambridge University Press, 1992.
- Georgopoulos, P. G., and J. H. Seinfeld, Estimate of relative dispersion parameters from atmospheric turbulence spectra, *Atmos. Environ.*, **22**, 31–41, 1988.
- Georgopoulos, P. G., and J. H. Seinfeld, Mathematical modelling of turbulent reacting plumes. I. general theory and model formulation, *Atmos. Environ.*, **20**, 1791–1807, 1986.
- Ghosal, S., and P. Moin, The basic equations for the large-eddy simulation of turbulent flows in complex geometry, *J. Comput. Phys.*, **118**, 24–37, 1995.
- Gifford, F. A., A simultaneous Lagrangian-Eulerian turbulence experiment, *Mon. Wea. Rev.*, **83**, 293–301, 1955.
- Gifford, F. A., Statistical properties of a fluctuating plume dispersion model, *Adv. Geophys.*, **6**, 117–137, 1959.
- Gifford, F. A., Atmospheric dispersion calculations using the generalized gaussian plume model, *Nuclear safety*, **2**, 56–59, 1960.
- Gifford, F. A., Horizontal diffusion in the atmosphere: a Lagrangian-dynamical theory, *Atmos. Environ.*, **16**, 505–512, 1982.
- Gifford, F. A., The time-scale of atmospheric diffusion considered in relation to the universal diffusion function f_1 , *Atmos. Environ.*, **21**, 1315–1320, 1987.
- Gonzalez, M., Analysis of the effect of microscale turbulence on atmospheric chemical reactions by means of the p.d.f approach, *Atmos. Environ.*, **31**, 575–586, 1997.

Bibliography

- Gopalakrishnan, S. G., and R. Avissar, An LES study of the impacts of land surface heterogeneity on dispersion in the convective boundary layer, *J. Atmos. Sci.*, **57**, 352–371, 2000.
- Graf, J., and U. Schumann, Simulation of the convective boundary layer in comparison to aircraft measurements, in *Air pollution modelling and its application IX*, pp. 587–593, Plenum Press, 1992.
- Gryning, S. E., A. A. M. Holtslag, J. S. Irwin, and B. Siversten, Applied dispersion modelling based on meteorological scaling parameter, *Atmos. Environ.*, **21**, 79–89, 1987.
- Hamba, F., A modified K model for chemically reactive species in the planetary boundary layer, *J. Geophys. Res.*, **98**, 5173–5182, 1993.
- Hanna, S. R., Lagrangian and Eulerian time-scale relations in the daytime boundary layer, *J. Appl. Meteorol.*, **20**, 242–249, 1981.
- Henn, D. S., and R. I. Sykes, Large eddy simulation of dispersion in the convective boundary layer, *Atmos. Environ.*, **26A**, 3145–3159, 1992.
- Herwehe, J. A., R. T. McNider, and R. K. Decker, Initial application of a couple LES-photochemical model to examine near-source ozone production from industrial emissions, in *15th Symposium on boundary layers and turbulence*, pp. 233–236, American Meteorological Society, 2002.
- Hibberd, M. F., Vertical dispersion of a passive scalar in the convective boundary layer; new laboratory results, in *11th AMS Conference on the Applications of Air Pollution Meteorology*, pp. 18–23, American Meteorological Society, Boston, MA, 2000.
- Hilst, G. R., Segregation and chemical reaction rates in air quality models, *Atmos. Environ.*, **32**, 3891–3895, 1998.
- Hinze, O., *Turbulence*, p. 790. Mc-Graw-Hill, 1975.
- Hirsch, C., *Numerical computation of internal and external flows, Volume 2*, 691 pp. J. Wiley and Sons, 1990.
- Hogstrom, U., Non-dimensional wind and temperature profiles in the atmospheric surface layer: A re-evaluation, *Bound.-Layer Meteo.*, **42**, 55–78, 1988.
- Holtslag, A. A. M., and F. T. M. Nieuwstadt, Scaling the atmospheric boundary layer, *Bound.-Layer Meteo.*, **36**, 201–209, 1986.
- Hundsdoerfer, W., B. Koren, M. van Loon, and J. Verwer, A positive finite-difference advection scheme, *J. Comput. Phys.*, **117**, 35–46, 1996.
- Ibrahim, S. S., R. W. Bilger, and N. R. Mudford, Turbulence effects on chemical reactions in smog chamber flows, *Atmos. Environ.*, **21**, 2609–2621, 1987.
- Joergensen, H. E., and T. Mikkelsen, Lidar measurements of plume statistics, *Bound.-Layer Meteo.*, **62**, 361–378, 1993.
- Jones, A., Atmospheric dispersion modelling at the Met Office, *Weather*, **59**, 311–316, 2004.
- Jonker, H. J. J., P. Duynkerke, and J. W. M. Cuijpers, Mesoscale fluctuations in scalars generated by boundary layer convection, *J. Atmos. Sci.*, **56**, 801811, 1999.

- Jonker, H. J. J., J. Vilà-Guerau de Arellano, and P. G. Duynkerke, Characteristic length scales of reactive species in a convective boundary layer, *J. Atmos. Sci.*, **61**, 41–56, 2004.
- Kaiser, R., and E. Fedorovich, Turbulence spectra and dissipation rates in a wind tunnel model of the atmospheric convective boundary layer, *J. Atmos. Sci.*, **55**, 580–594, 1999.
- Karamchandani, P., and L. K. Peters, Three-dimensional behavior of mixing-limited chemistry in the atmosphere, *Atmos. Environ.*, **21**, 511–522, 1987.
- Karamchandani, P., L. Santos, I. Sylkes, Y. Zhang, C. Tonne, and C. Seigneur, Development and evaluation of a state-of-the-science reactive plume model, *Environ. Sci. and Technol.*, **34**, 870–880, 2000.
- Khanna, S., and J. B. Brasseur, Three-dimensional buoyancy- and shear-induced local structure of the atmospheric boundary layer, *J. Atmos. Sci.*, **55**, 710–743, 1998.
- Komori, S., J. C. R. Hunt, T. Kanzaki, and Y. Y. Murakami, The effect of turbulent mixing on the correlation between two species and on concentration fluctuations in non-premixed reacting flows, *J. Fluid Mech.*, **228**, 629–659, 1991.
- Koren, B., A robust upwind discretization method for advection, diffusion and source terms, in *Numerical methods for advection-diffusion problems*, pp. 117–137, Vieweg, 1993.
- Kramm, G., and F. X. Meixner, On the dispersion of trace species in the atmospheric boundary layer: a re-formulation of the governing equations for the turbulent flow of the compressible atmosphere, *Tellus A*, **52A**, 500–522, 2000.
- Kramm, G., G. Müller, D. Fowler, K. H. Höfken, F. X. Meixner, and E. Scaller, A modified profile method for determining the vertical profiles of NO, NO₂, ozone and HNO₃ in the atmospheric surface layer, *J. Atmos. Chem.*, **13**, 265–288, 1991.
- Krol, M. C., M. J. Molemaker, and J. Vilà-Guerau de Arellano, Effects of turbulence and heterogeneous emissions on photochemically active species in the convective boundary layer, *J. Geophys. Res.*, **105**, 6871–6884, 2000.
- Lamb, R. G., A numerical simulation of dispersion from an elevated point source in the convective planetary boundary layer, *Atmos. Environ.*, **12**, 1297–1304, 1978.
- Lamb, R. G., Diffusion in the convective boundary layer, in *Atmospheric Turbulence and Air Pollution Modelling*, pp. 159–229, Reidel Publishing Company, Dordrecht, 1982.
- Lamb, R. G., and J. H. Seinfeld, Mathematical modelling of urban air pollution, *Environ. Sci. and Technol.*, **7**, 253–261, 1973.
- Lenschow, D. H., and B. B. Stankov, Length scales in the boundary layer, *J. Atmos. Sci.*, **43**, 1198–1209, 1986.
- Lenschow, D. H., J. C. Wyngaard, and W. T. Pennell, Mean-field and second-moment budgets in a baroclinic, convective boundary layer, *J. Atmos. Sci.*, **37**, 1313–1326, 1980.
- Leonard, A., Energy cascade in large-eddy simulation of turbulent fluid flows, *Adv. Geophys.*, **18A**, 237–248, 1974.

Bibliography

- Lewellen, D. C., and W. S. Lewellen, Effects of aircraft wake dynamics on measured and simulated NO_x and HO_x wake chemistry, *J. Geophys. Res.*, **106**, 27611–27672, 2001.
- Liu, C. H., and D. Y. C. Leung, Turbulence and dispersion studies using a three-dimensional second-order closure Eulerian model, *J. Appl. Meteorol.*, **40**, 92–113, 2001.
- Lovejoy, S., Area-perimeter relation for rain and cloud areas, *Science*, **216**, 185–187, 1982.
- Luhar, A. K., The influence of vertical wind direction shear on dispersion in the convective boundary layer and its incorporation in coastal fumigation models, *Bound.-Layer Meteo.*, **102**, 1–38, 2002.
- Luhar, A. K., M. F. Hibberd, and P. J. Hurley, Comparison of closure schemes used to specify the velocity PDF in Lagrangian stochastic dispersion models for convective conditions, *Atmos. Environ.*, **30**, 1407–1418, 1996.
- Luhar, A. K., M. F. Hibberd, and M. S. Borgas, A skewed meandering plume model for concentration statistics in the convective boundary layer, *Atmos. Environ.*, **34**, 3599–3616, 2000.
- Lumley, J. L., and H. A. Panofsky, *The structure of atmospheric turbulence*, 239 pp. Interscience Publishers, 1964.
- Mason, P. J., Large-eddy simulation of the convective boundary layer, *J. Atmos. Sci.*, **46**, 1492–1516, 1989.
- Mason, P. J., Large-eddy simulation of dispersion in convective boundary layer with wind shear, *Atmos. Environ.*, **26A**, 1561–1571, 1992.
- Meeder, J. P., *Numerical simulation of chemical reactions in point-source plumes*. PhD thesis, Utrecht University, 1998.
- Meeder, J. P., and F. T. M. Nieuwstadt, Large-eddy simulation of a turbulent dispersion of a reactive plume from a point source into a neutral atmospheric boundary layer, *Atmos. Environ.*, **34**, 3563–3573, 2000.
- Ministry for the Environment New Zealand, *Good Practice Guide for Atmospheric Dispersion Modelling*, p. 142. ME number: 522, available online at <http://www.mfe.govt.nz/publications/>, 2004.
- Moeng, C.-H., Large Eddy Simulation of Atmospheric Boundary Layer, in *Clear and cloudy boundary layers*, pp. 67–82, Royal Netherlands Academy of Arts and Sciences, Amsterdam, 1998.
- Moeng, C. H., and R. Rotunno, Vertical velocity skewness in the buoyancy driven boundary layer, *J. Atmos. Sci.*, **47**, 1149–1162, 1990.
- Moeng, C.-H., and P. P. Sullivan, A comparison of shear- and buoyancy-driven planetary boundary layer flows, *J. Atmos. Sci.*, **7**, 999–1022, 1994.
- Moeng, C.-H., and J. C. Wyngaard, statistics of conservative scalars in the convective boundary layer, *J. Atmos. Sci.*, **41**, 3161–3169, 1984.
- Moeng, C. H., and 12 co-authors, Simulation of a stratocumulus-topped planetary boundary layer: intercomparison among different numerical codes, *Bull. Amer. Met. Soc.*, **77**, 261–277, 1996.

- Molemaker, M. J., and J. Vilà-Guerau de Arellano, Turbulent control of chemical reactions in the convective boundary layer, *J. Atmos. Sci.*, **55**, 568–579, 1998.
- Munro, R. J., P. C. Chatwin, and N. Mole, A concentration pdf for the relative dispersion of a contaminant plume in the atmosphere, *Bound.-Layer Meteo.*, **106**, 411–436, 2003a.
- Munro, R. J., P. C. Chatwin, and N. Mole, Some simple statistical models for relative and absolute dispersion, *Bound.-Layer Meteo.*, **107**, 253–271, 2003b.
- Neggers, R., *Shallow cumulus convection*. PhD thesis, Wageningen University, 2002.
- Neggers, R., H. J. J. Jonker, and A. P. Siebesma, Size statistics of cumulus cloud populations in large-eddy simulations, *J. Atmos. Sci.*, **60**, 1060–1074, 2003.
- Nieuwstadt, F. T. M., Application of mixed-layer similarity to the observed dispersion from a ground-level source, *J. Appl. Meteorol.*, **19**, 157–162, 1990.
- Nieuwstadt, F. T. M., A Large-Eddy simulation of a line source in a convective atmospheric boundary layer-I. dispersion characteristics, *Atmos. Environ.*, **26A**, 485–495, 1992.
- Nieuwstadt, F. T. M., and R. A. Brost, the decay of convective turbulence, *J. Atmos. Sci.*, **43**, 532–546, 1986.
- Nieuwstadt, F. T. M., and J. P. J. M. M. de Valk, A large eddy simulation of buoyant and non-buoyant plume dispersion in the atmospheric boundary layer, *Atmos. Environ.*, **21**, 2573–2587, 1987.
- Nieuwstadt, F. T. M., P. J. Mason, C. H. Moeng, and U. Schumann, Large-eddy simulation of the convective boundary layer: a comparison of four computer codes, in *8th Symp. on Turbulent Shear Flows*, pp. 343–367, 1991.
- Ott, S., and H. E. Jørgensen, Meteorology and lidar data from the URAHFREP field trials, *Risø Report R-1212(EN)*, 119 pp., 2001.
- Ott, S., and J. Mann, An experimental investigation of the relative diffusion of particle pairs in three-dimensional turbulent flow, *J. Fluid Mech.*, **422**, 207–223, 2000.
- Pasquill, F., The estimation of the dispersion of windborne material, *Meteorolog. Mag.*, **90**, 33–49, 1961.
- Pasquill, F., *Atmospheric diffusion*, 429 pp., Ellis Horwood Limited, 1974.
- Patton, E. G., K. J. Davis, M. C. Barth, and P. P. Sullivan, Decaying scalars by a forest canopy: a numerical study, *Bound.-Layer Meteo.*, **100**, 91–129, 2001.
- Petersen, A. C., and A. A. M. Holtslag, A first-order closure for covariance and fluxes of reactive species in the convective boundary layer, *J. Appl. Meteorol.*, **38**, 1758–1776, 1999.
- Petersen, A. C., C. Beets, H. van Dop, P. G. Duynkerke, and A. P. Siebesma, Mass-flux characteristics of reactive scalars in the convective boundary layer, *J. Atmos. Sci.*, **56**, 37–56, 1999.
- Phillips, P., and H. A. Panofsky, A re-examination of lateral dispersion from continuous sources, *Atmos. Environ.*, **16**, 1851–1859, 1982.
- Pino, D., J. Vilà-Guerau de Arellano, and P. G. Duynkerke, Role of the shear in the convective boundary layer, *J. Atmos. Sci.*, **60**, 1913–1926, 2003.

Bibliography

- Pope, S. B., P.d.f methods for turbulent reactive flows, *Prog. Energy. Combust. Sci.*, **11**, 119–192, 1985.
- Reynolds, A. M., Representation of internal plume structure in Gifford's meandering plume model, *Atmos. Environ.*, **34**, 2539–2545, 2000.
- Russell, A., and R. Dennis, NARSTO critical review of photochemical models and modelling, *Atmos. Environ.*, **34**, 2283–2324, 2000.
- Sato, Y., and K. Yamamoto, Lagrangian measurements of fluid-particle motion in an isotropic turbulent field, *J. Fluid Mech.*, **175**, 183–199, 1987.
- Schmidt, H., and U. Schumann, Coherent structure of the convective boundary layer derived from large-eddy simulations, *J. Fluid Mech.*, **200**, 511–562, 1989.
- Schumann, U., Large-eddy simulation of turbulent diffusion with chemical reactions in the convective boundary layer, *Atmos. Environ.*, **23**, 1713–1729, 1989.
- Siebesma, A., and A. Holtslag, Model impacts of entrainment and detrainment rates in shallow cumulus convection, *J. Atmos. Sci.*, **53**, 2354–2364, 1996.
- Siebesma, A. P., and J. W. M. Cuijpers, Evaluation of parametric assumptions for shallow cumulus convection, *J. Atmos. Sci.*, **52**, 650–666, 1995.
- Siebesma, A. P., and H. J. J. Jonker, Anomalous scaling of cumulus cloud boundaries, *Phys. Rev. Lett.*, **85**, 214–217, 2000.
- Siebesma, A. P., et al., A large eddy simulation intercomparison study of shallow cumulus convection, *J. Atmos. Sci.*, **60**, 1201–1219, 2003.
- Squires, K. D., and J. K. Eaton, Lagrangian and Eulerian statistics obtained from direct numerical simulation of homogeneous turbulence, *Phys. Fluids A*, **3**, 130–143, 1991.
- Stevens, B., and 16 co-authors, Evaluation of Large-Eddy Simulations via observations of nocturnal marine stratocumulus, *Mon. Wea. Rev.*, *in press*, 2004.
- Stevens, B., and D. H. Lenschow, Observations, experiments, and Large Eddy Simulation, *Bull. Amer. Met. Soc.*, **82**, 283–294, 2001.
- Stevens, B., et al., Simulations of trade wind cumuli under a strong inversion, *J. Atmos. Sci.*, **58**, 1870–1891, 2001.
- Stockwell, W. R., Effects of turbulence on gas-phase atmospheric chemistry: calculation of the relationship between time scales for diffusion and chemical reaction, *Meteorol. Atmos. Phys.*, **57**, 159–171, 1995.
- Stull, R. B., *An introduction to Boundary Layer Meteorology*. Kluwer Academic Publisher, 1988.
- Suratanakavikul, V., and A. J. Marquis, A comparative study of flux-limiters in unsteady and steady flows, in *13th National mechanical engineering conference*, Cholburi, 1999.
- Sykes, R. I., and D. S. Henn, Large-eddy simulation of turbulent sheared convection, *J. Atmos. Sci.*, **46**, 1106–1119, 1989.
- Sykes, R. I., and D. S. Henn, Large eddy simulation of concentration fluctuations in a dispersing plume, *Atmos. Environ.*, **26A**, 3127–3144, 1992.

- Sykes, R. I., S. F. Parker, and W. S. Lewellen, Large-eddy simulation of a turbulent reacting plume, *Atmos. Environ.*, **26**, 2565–2574, 1992.
- Tan, D., I. Faloona, W. H. Brune, A. Weinheimer, T. Campos, B. Ridley, S. Vay, J. Collins, and G. Sachse, In situ measurements of HO_x in aircraft exhaust plumes and contrails during SUCCESS, *Geoph. Res. Let.*, **25**, 1721–1724, 1998.
- Taylor, G. I., Diffusion by continuous movements, *Proc. Roy. Soc. Ser.*, **A20**, 196–211, 1921.
- Tennekes, H., and J. L. Lumley, *A first course in turbulence*, 300 pp., MIT Press, Cambridge, MA, 1972.
- Thompson, A. M., and D. H. Lenschow, Mean profiles of trace reactive species in the unpolluted marine surface layer, *J. Geophys. Res.*, **89**, 4788–4796, 1984.
- Turner, D. B., *Workbook of atmospheric dispersion estimates*. Lewis publishers-CRC press, Boca Ration, Florida, 1994.
- Uliasz, M., and Z. Sorbjan, Lagrangian statistics in atmospheric boundary layer derived from LES, in *13th Symposium on Boundary Layers and Turbulence*, P2A.6, American Meteorological Society, 1999.
- van Haren, L., and F. T. M. Nieuwstadt, The behavior of passive and buoyant plumes in a convective boundary layer, as simulated with a large-eddy model, *J. Appl. Meteorol.*, **28**, 818–832, 1989.
- van Ulden, A., and A. A. M. Holtslag, Estimation of abl parameters for diffusion applications, *J. of Climate and Applied Met.*, **24**, 1196–1207, 1985.
- van Zanten, M., *Entrainment processes in stratocumulus*. PhD thesis, Utrecht University, 2000.
- Venkatram, A., Dispersion in the stable boundary layer, in *Lectures on Air Pollution Modelling*, pp. 228–265, American Meteorological Society, Boston, MA, 1988.
- Verver, G., H. van Dop, and A. A. M. Holtslag, Turbulent mixing of reactive gases in the convective boundary layer, *Bound.-Layer Meteo.*, **85**, 197–222, 1997.
- Verver, G. H. L., H. V. Dop, and A. Holtslag, Turbulent mixing and the chemical breakdown of isoprene in the atmospheric surface layer, *J. Geophys. Res.*, **93**, 3983–4002, 2000.
- Vilà-Guerau de Arellano, J., Bridging the gap between atmospheric physics and chemistry in studies of small-scale turbulence, *Bull. Amer. Met. Soc.*, **84**, 51–56, 2003.
- Vilà-Guerau de Arellano, J., and J. W. M. Cuijpers, The chemistry of a dry cloud: the effects of radiation and turbulence, *J. Atmos. Sci.*, **57**, 1573–1584, 2000.
- Vilà-Guerau de Arellano, J., P. G. Duynkerke, and K. F. Zeller, Atmospheric surface layer similarity theory applied to chemically reactive species, *J. Geophys. Res.*, **100**, 1397–1408, 1995.
- Vinuesa, J. F., and J. Vilà-Guerau de Arellano, Fluxes and (co-)variances of reacting scalars in the convective boundary layer, *Tellus B*, **55B**, 935–949, 2003.
- Vinuesa, J. F., and J. Vilà-Guerau de Arellano, Introducing effective reaction rates to account for the inefficient mixing of the convective boundary layer, *Atmos. Environ.*, p. In press, 2004.
- Voth, G. A., K. Satyanarayan, and E. Bodenschatz, Lagrangian acceleration measurements at large Reynolds numbers, *Phys. Fluids A*, **10**, 2268–2280, 1998.

Bibliography

- Vreugdenhil, C. B., and B. Koren (eds.), Numerical methods for advection-diffusion problems, in *Numerical fluid mechanics*, 373 p., Vieweg, 1993.
- Wandel, C. F., and O. Kofoed-Hansen, On the Eulerian-Lagrangian transform in the statistical theory of turbulence, *J. Geophys. Res.*, **76**, 3089–3093, 1962.
- Wang, Q., K. D. Squires, and X. Wu, Lagrangian statistics in turbulent channel flow, *Atmos. Environ.*, **29**, 2417–2427, 1995.
- Weil, J. C., Dispersion in the convective boundary layer, in *Lectures on Air Pollution Modelling*, pp. 167–227, American Meteorological Society, Boston, MA, 1988.
- Weil, J. C., W. Synder, R. E. L. Jr., and M. S. Shipman, Experiments on buoyant plume dispersion in a laboratory convection tank, *Bound.-Layer Meteo.*, **102**, 367–414, 2002.
- Weil, J. C., P. Sullivan, and C. H. Moeng, On the use of large-eddy simulations in lagrangian particle dispersion models, *J. Atmos. Sci.*, p. In press, 2004.
- Willis, G. E., and J. W. Deardorff, A laboratory model for the unstable boundary layer, *J. Atmos. Sci.*, **31**, 1297–1307, 1974.
- Willis, G. E., and J. W. Deardorff, A laboratory model of diffusion into the convective planetary boundary layer, *Quart. J. Roy. Meteor. Soc.*, **102**, 427–445, 1976.
- Willis, G. E., and J. W. Deardorff, A laboratory study of dispersion from an elevated source within a modelled convective planetary boundary layer, *Atmos. Environ.*, **12**, 1305–1311, 1978.
- Willis, G. E., and J. W. Deardorff, A laboratory study of dispersion from a source in the middle of the convectively mixed layer, *Atmos. Environ.*, **15**, 109–117, 1981.
- Wyngaard, J. C., Atmospheric turbulence, *Annu. Rev. Fluid Mech.*, **24**, 205–233, 1992.
- Wyngaard, J. C., and J. C. Weil, Transport asymmetry in skewed turbulence, *Phys. Fluids A*, **3**, 155–162, 1991.
- Yee, E., and D. J. Wilson, A comparison of the detailed structure in dispersing tracer plumes measured in grid-generated turbulence with a meandering plume model incorporating internal fluctuations, *Bound.-Layer Meteo.*, **94**, 253–296, 2000.
- Yee, E., R. Chan, P. R. Kosteniuk, G. M. Chandler, C. A. Biltoft, and J. F. Bowers, Incorporation of internal fluctuations in a meandering plume model of concentration fluctuations, *Bound.-Layer Meteo.*, **67**, 11–39, 1994.
- Yeung, P. K., Lagrangian investigation of turbulence, *Annu. Rev. Fluid Mech.*, **34**, 115–142, 2002.
- Yeung, P. K., and S. B. Pope, Lagrangian statistics from direct numerical simulations of isotropic turbulence, *J. Fluid Mech.*, **207**, 531–586, 1989.

Bibliography

Samenvatting

De verspreiding van pluimen in de atmosferische grenslaag is een zeer complex fenomeen, waar zowel transport en de menging van het pluimmateriaal als de chemische omzettingen een rol spelen. Als een pluim zich verspreidt in de AGL, dan wordt haar interne structuur, vorm en evolutie bepaald door de interactie tussen de pluim en de turbulente wervels in de atmosfeer. Indien we atmosferische verspreiding willen begrijpen en voorspellen, dan is het essentieel om de karakteristieke eigenschappen van atmosferische turbulentie te bestuderen en te analyseren. We beschikken tegenwoordig over een breed scala aan methodieken en hulpmiddelen om turbulente verspreiding te onderzoeken. In specifieke zin is het zo dat het, door de sterke groei in de capaciteit van computers, mogelijk is geworden om atmosferische stromingen numeriek te simuleren. De numerieke simulatie bestaat uit het oplossen van een stelsel van gekoppelde vergelijkingen, welke de evolutie van de belangrijkste atmosferische variabelen zoals wind, temperatuur en vocht beschrijft. Deze techniek wordt ook wel kortweg "numerieke simulatie" genoemd. En van de meest krachtige technieken om numerieke simulatie van de AGL mee uit te voeren is de zogenaamde "Large-Eddy Simulatie" (LES), waarmee men in staat is om de meest relevante schalen van turbulente bewegingen op te lossen. De LES techniek is in het bijzonder geschikt om de zogenaamde convectieve grenslaag (CGL) te bestuderen, aangezien deze een zekere graad van grootschalige organisatie bezit met structuren van warme opstijgende lucht en structuren met koude dalende lucht (zogenaamd thermieksysteem). In dit promotieonderzoek is een LES gebruikt om pluimevolutie in de CGL in detail te simuleren, zowel in de ruimte als in de tijd. Het meest vernieuwende van het onderzoek is het feit dat turbulente dispersie simultaan in twee verschillende "frameworks" wordt bestudeerd. Door dispersie in twee verschillende coördinaatsystemen te bestuderen, namelijk in het absolute (of vaste) systeem en in het relatieve systeem (d.w.z. in het coördinatiesysteem t.o.v. het massacentrum van de pluim), was het mogelijk om een onderscheid te maken tussen de invloed van kleinschalige en van grootschalige beweging op de evolutie van de pluim. Zo werd bijvoorbeeld de bijdrage van verticale inhomogene meanderende bewegingen verwijderd in het relatieve coördinatensysteem, zodat alleen kleine homogene turbulente wervels nog een bijdrage leveren in het verspreidingsproces in dit framework. In de huidige studie is turbulente dispersie bestudeerd in zowel het Euleriaanse als in het Lagrangiaanse framework. In het Euleriaanse framework worden dispersie-eigenschappen zoals bijvoorbeeld de concentratie van een verontreiniging berekend en/of gemeten op een vast punt in de ruimte. In het Lagrangiaanse framework daarentegen, wordt elk afzonderlijk deeltje in de pluim gevolgd en worden de dispersie-eigenschappen berekend in het referentie-frame dat zich met de deeltjes meebeweegt.

Hieronder volgt een korte beschrijving van de inhoud van de afzonderlijke hoofdstukken.

Een algemene introductie over het belang om atmosferische dispersie te bestuderen wordt gegeven in hoofdstuk 1. Daarnaast komen verschillende hulpmiddelen bij de bestudering van turbulente dispersie in de AGL aan de orde en worden de belangrijkste onderzoeksvragen van deze studie geponeerd.

Hoofdstuk 2 geeft een overzicht van de verschillende numerieke technieken welke zoal gebruikt worden om de AGL te simuleren. Het model dat in deze studie gebruikt is, wordt uitvoerig beschreven. Daarbij ligt de focus op de basisvergelijkingen, de subgridparameterisatie en op het

oppervlaktelaagmodel. Tenslotte, worden de belangrijkste modificaties van het model en toevoegingen aan het model beschreven.

In hoofdstuk 3 wordt atmosferische dispersie bestudeerd door energiespectra en autocorrelaties van de snelheidscomponenten te berekenen en dat zowel in het Euleriaanse als in het Langrangiaanse framework. Zo wordt voor de "Euleriaanse statistiek" zowel ruimtelijke als temporele analyse toegepast. Ruimtelijke analyse wordt met name veel gebruikt in numerieke en laboratoriumexperimenten, waarbij gegevens worden verzameld op verschillende locaties voor een gegeven tijdstip (of eventueel gemiddeld over een zeker tijdsinterval). Temporele analyse daarentegen wordt vaak toegepast bij veldexperimenten, waarbij de statistiek wordt berekend uit analyse van tijdreeksen verzameld op specifieke (vaste) plaatsen. Deze twee analysetypen worden dikwijls aan elkaar gerelateerd via de zogenaamde "Frozen Turbulence" hypothese van Taylor. Deze hypothese wordt feitelijk altijd aangenomen maar zelden gevalideerd. In de huidige studie is Taylor's hypothese met succes gevalideerd voor de gesimuleerde CGL, namelijk door afleiding van de karakteristieke tijd- en lengteschalen uit de analyse van het spectrum (spectrale piek) en uit de analyse van de autocorrelatiefunctie. De relatie tussen stromingseigenschappen (autocorrelaties) en dispersiekenmerken (deeltjesverplaatsingen) is onderzocht door middel van Taylor's analyse van turbulente dispersie. Er is daarbij een onderscheid gemaakt tussen horizontale en verticale bewegingen, om zo het effect van inhomogeniteit van de verticale structuur van turbulentie op de deeltjesverspreiding te onderzoeken, alsmede om het effect van de aanwezigheid van 'randen' in de CGL (d.w.z. oppervlak en top) op deeltjesverspreiding te onderzoeken. De resultaten laten zien dat horizontale dispersie afdoende kan worden beschreven met behulp van Taylor's diffusie theorie, omdat de homogene horizontale bewegingen gekarakteriseerd kunnen worden met een exponentiele autocorrelatiefunctie. De autocorrelatiefunctie voor de verticale bewegingen heeft echter een meer gecompliceerde vorm, ten gevolge van de verticale inhomogeniteit in de turbulentie en t.g.v. de aanwezigheid van randen, welke een beperking opleggen aan de verticale bewegingsvrijheid van deeltjes. Dit resulteert in een golf-achtig bewegingspatroon van de deeltjes. Daarbij voorspelt Taylor's analyse de verplaatsing van de deeltjes op korte tijdschaal correct, d.w.z. wanneer de beweging nog niet beïnvloed is door randen, maar overschat zij de asymptotische limiet op langere tijdschaal. Door gebruik van een andere methode om de Langrangiaanse integraal-tijdschaal te berekenen, kunnen we een beter onderscheid te maken tussen vrije en 'begrensde' beweging en daarmee wordt een betere overeenstemming bereikt tussen Taylor's relatie en de werkelijke verticale verplaatsing van de deeltjes. Dit gedeelte van het onderzoek is voltooid door een verificatiestudie naar de equivalentie tussen de Langrangiaanse deeltjesverplaatsing (d.w.z. de verplaatsing van deeltjes gemeten op gezette reistijden) en de Euleriaanse dispersie parameter (d.w.z. de verplaatsing van de deeltjes als functie van de afstand tot de bron). De vergelijking liet zien dat het gebruik van Euleriaanse dispersieparameters in plaats van Langrangiaanse dispersieparameters, voor praktische doeleinden, niet leidt tot grote fouten. Dit heeft te maken met het feit dat Taylor's hypothese van "frozen turbulence" geldig is in de door ons gesimuleerde CGL. De relatie tussen de Langrangiaanse en de Euleriaanse schrijfwijze is onderzocht door de ratio tussen de Langrangiaanse tijdschaal en de Euleriaanse tijdschaal β te berekenen. Deze tijdschalen kunnen worden bepaald uit hetzij de integraalschaal van de autocorrelatiefunctie, hetzij uit de bepaling van waarde van de frequentie bij piek in het spectrum. Omdat er vaak veel spreiding zit in de spectra, geeft het gebruik

van bovengenoemde autocorrelatiemethode in de regel het meest nauwkeurige resultaat. De gangbare formuleringen uit de literatuur voor de Langrangiaanse tijdschaal en voor de ratio β , d.w.z. de parameterisaties die eerder zijn afgeleid uit veldexperimenten of uit theoretische overwegingen, zijn berekend uit de stromingskarakteristieken (CGL hoogte, varianties van wind snelheid). Deze parameterisaties zijn vergeleken met de LES resultaten, wat resulteerde in een voldoende goede overeenstemming.

In hoofdstuk 4 wordt pluimverspreiding in de CGL bestudeerd in vanuit twee verschillende coördinaatsystemen: het absolute coördinatiesysteem en het coördinatiesysteem relatief ten opzicht van de massazwaartelijns. Als zodanig is het mogelijk om de verschillende bijdrage van kleinschalige en grootschalige luchtbewegingen aan de pluimspreiding te scheiden en te kwantificeren. De vorm en symmetrie-eigenschappen van de pluimspreiding zijn geanalyseerd door de gemiddelde positie van de pluim te berekenen, alsmede de dispersie parameters (variantie) en de scheefheid van de pluimpositie te berekenen in beide coördinaatsystemen. De analyse van de derde-orde momenten laat zien dat de symmetrie van de verdeling van de scalar beïnvloed wordt door zowel de turbulentiekarakteristieken van de CGL (inhomogeniteit van de grootschalige verticale bewegingen) als door de aanwezigheid van de randen. Zo wordt de scheefheid van de massazwaartelijns van de pluim vooral bepaald door het meanderen van de pluim als gevolg van het transport door opwaartse en neerwaartse thermiekbellen. De scheefheid van de relatieve positie daarentegen wordt vooral bepaald door reflectie van de pluim aan randen van de CGL, aangezien de grootschalige beweging in het relatieve systeem uitgefilterd is. Er is ook een studie gemaakt naar de concentraties en de fluctuaties van concentraties (d.w.z. variabiliteit van concentraties) in zowel het absolute als in het relatieve coördinatensysteem. Zo is de intensiteit van de relatieve concentratiefluctuaties $i_c r$ berekend, aangezien deze een maat is voor de interne menging binnen de pluim. De tijdsontwikkeling van $i_c r$ is een kritische parameter in operationele dispersiemodellen, aangezien zij gebruikt wordt bij de parameterisatie van de kansdichtheidsfunctie (PDF) van de relatieve concentratie. In de huidige studie is een gangbare parameterisatie voor de PDF van de relatieve concentratie berekend als functie van $i_c r$, hetgeen resulteerde in een zeer goed overeenkomst met de LES resultaten. Tenslotte is de geldigheid van Gifford's formule onderzocht die de absolute concentratie relateert aan de relatieve concentratie en de positie (PDF) van de massazwaartelijns. Daar kwam uit dat Gifford's formule niet in staat is om de waarde van de absolute gemiddelde concentratie te reproduceren en dan voornamelijk vlak bij de grond, als gevolg van het feit dat de CGL begrensd is aan de randen. Dit kan worden verklaard als zijnde het gevolg van pluimreflectie aan de randen, waardoor de relatieve concentratie een scheve verdeling krijgt en daarmee afwijkt van een Gaussverdeling. De resultaten zijn verbeterd door voor de relatieve gemiddelde concentratie een parameterisatie te gebruiken die rekening houdt met de scheefheid van de relatieve pluimpositie. Deze studie laat zien dat analyse van hogere-orde statistiek van belang is om de ontwikkeling van pluimdispersie in de CGL te kunnen begrijpen en om te komen tot een operationeel dispersiemodel. Bovendien, heeft de LES techniek bewezen dat zij een ideaal hulpmiddel is om de interne structuur en variabiliteit in detail te kunnen bestuderen. Daarom kunnen LES resultaten worden ingezet om de metingen die verkregen zijn m.b.v. remote-sensing instrumenten (zoals bv. lidars) en die daarmee in staat zijn om direct de interne structuren in de pluim te bemeten, beter te interpreteren.

In hoofdstuk 5 is de dispersie van pluimen onderzocht in grenslagen die aangedreven worden door een combinatie van "shear" en "bouyancy". Verschillende archetypen van grenslagen zijn gesimuleerd, variërend van puur convectieve tot bijna neutrale grenslagen en zijn tevens systematisch geclassificeerd volgens de shear-bouyancy ratio u_*/w_* en de schaalparameter $-z_i/L$.

Voor de puur convectieve situaties werd een goede overeenkomst gevonden tussen de LES resultaten en de laboratorium- en veldexperimenten. De invloed van windschering is in eerste instantie bestudeerd vanuit de stromingsstatistiek (profielen van windsnelheidsvarianties), omdat de dispersiekaracteristieken direct afhangen van de turbulentie-eigenschappen. De resultaten laten een toename van de horizontale snelheidsvariantie zien en een afname in de verticale snelheidsvariantie. Het hoofdeffect van windschering op de statistiek van de dispersie is het feit dat zij de verticale spreiding reduceert, terwijl de horizontale spreiding juist toeneemt. Als gevolg hiervan treden er sterke veranderingen op in de concentraties nabij de grond, aangezien de toenemende wind de neiging heeft om de pluim gedurende langere tijd te advecteren, zodat de tracer op grotere afstand van de bron de grond pas bereikt. Ook de meanderende component van de verticale dispersie is onderzocht als functie van de toenemende windschering. Het meanderingsproces levert de hoofdbijdrage aan de dispersie, met name dicht bij de emissiebron, alwaar de pluim door grote wervels getransporteerd wordt. De meanderende component verandert door toedoen van de windschering en dan met name voor pluimen die dicht bij het aardoppervlak gemitteerd worden, waar de aanwezigheid van het oppervlak leidt tot een toename van de schering die op haar beurt het 'loop-en' van de pluim onderdrukt. Doordat meanderen de hoofdoorzaak is achter de variantie van concentraties, vermindert het maximum van de concentratiefluctuaties op het moment dat de stroming een minder convectief karakter krijgt. Tenslotte zijn er parameterisaties afgeleid voor dispersieparameters die rekening houden met het gecombineerde effect van bouyancy en windschering. Bij de parameterisatie voor σ_y is er expliciet rekening gehouden met rotatie in de bijdrage van windschering aan de dispersie. Bij de parameterisatie van σ_z wordt rekening gehouden met twee tegengestelde effecten: het feit dat turbulentie nabij de grond gegenereerd wordt door windschering en het feit dat grote verticale bewegingen nabij de grond worden onderdrukt. Voor al de gesimuleerde gevallen kwamen beide parameterisaties behoorlijk goed overeen in vergelijking met de LES resultaten.

In hoofdstuk 6 wordt een compleet overzicht gegeven van studies naar de verspreiding van chemisch reactieve stoffen in de AGL. In het bijzonder is er aandacht gegeven aan het effect van turbulente menging op chemische omzettingen. Het blijkt dat de reactiesnelheid van bepaalde chemische componenten die met stoffen in de omgeving reageren, omlaag kan gaan, wanneer de betreffende reactanten ruimtelijk van elkaar gescheiden zijn als gevolg van niet-uniforme menging. In het geval van een pluim, een emissievorm waarbij hoge concentraties kunnen optreden, is deze ruimtelijke scheiding tussen de pluim en de omgevingslucht vooral relevant aan de randen, daar waar de concentratiegradinten groot zijn. Er is in dit hoofdstuk tevens aangetoond dat de verhouding tussen de turbulentietijdschaal en de tijdschaal van de chemische omzettingen (het zogenaamde Damkhlergetal) een sleutelparameter is, die bepaalt hoeveel impact turbulentie heeft op chemische omzettingen. Op basis van het Damkhlergetal kunnen er drie regimes voor turbulente reactieve stromingen worden onderscheiden: regimes met langzame, matig snelle en snelle chemie. Voor de regimes met matig snelle en snelle chemie, karakteristiek voor componenten zoals NO_x en HO_x , wordt de uiteindelijke reactiviteit van de componenten sterk bepaald door de turbulentie. In een

dergelijke situatie kunnen de gemiddelde concentratie en de tweede-orde momenten sterk afwijken van dezelfde statistische momenten van inerte stoffen. In het bijzonder toont onderzoek naar een pluim bestaande uit een stof met een 'eerste-orde reactie verval' aan (zoals bv. bij radioactief verval), dat zowel de absolute concentratie als de variabiliteit van de concentratie (fluctuaties) sterk afhangt van het Damkhlergetal. Vele auteurs hebben, door gebruik van verschillende meet- en modelleringstechnieken, het effect van turbulente menging op tweede-orde chemische omzettingen in een pluim onderzocht. Uit alle studies kwam naar voren dat turbulente menging bepalend is voor pluim en dat het Damkhlergetal gebruikt moet worden om de turbulente reactieven stromingen te kunnen karakteriseren. Het effect van turbulente menging op chemische reacties is juist van kritisch belang voor regionale en grootschalige numerieke modellen, omdat deze in het algemeen de aanname doen dat chemische componenten instantaan en uniform gemengd zijn binnen een gridcel. Daarom is het noodzakelijk om de verandering van de reactiesnelheid ten gevolge van heterogene turbulente menging te verdisconteren in de vorm van een parameterisatie. Een eenvoudige en intuïtief aantrekkelijke aanpak is het definiëren van een zogenaamde effectieve reactiesnelheid K_{eff} , die de non-uniforme menging in de atmosfeer in rekening brengt, als functie van de reactiesnelheid zoals gemeten onder homogene condities en als functie van de segregatie-intensiteit. Met segregatie-intensiteit wordt daarbij bedoeld: de ratio tussen de covariantie tussen de reactieve componenten en het product van hun gemiddelde concentraties. De segregatie-intensiteit moet daarbij worden afgeleid uit observaties, of worden geparameteriseerd in termen van bekende grootheden.

Curriculum Vitae

Alessandro Dosio was born in Verbania (Italy) on August 6th 1974. After attending the Liceo Scientifico "E.Galois" in Verbania, he completed his undergraduate studies at the Università degli Studi di Milano (Italy), where he obtained the degree in physics in 1999. The work of his thesis entitled "Numerical simulation of flow circulation and ozone formation in the Po Plain" was prepared at the Joint Research Centre (JRC) of the European Commission in Ispra (Italy), under the supervision of Dr. G. Graziani and Dr. S. Galmarini. After obtaining the degree, he worked at the JRC for one year on numerical simulation of flow circulation in complex terrain.

In May 2000 he left for The Netherlands, where he joined the Netherlands Organization for Applied Research (TNO-MEP) as scientific researcher in the frame of the TRAPOS network (Optimization of Modelling Methods for Traffic Pollution in Streets), which operated in the framework of the European Commission Training and Mobility Researchers Programme (TMR).

In June 2001 he began a 4 year PhD project in atmospheric physics at the Meteorology and Air Quality Section of Wageningen University, where he worked on numerical simulation of atmospheric dispersion in the atmospheric Convective Boundary Layer.

Currently, he is working in the Atmospheric Sciences Section of the Centre for Ecology and Hydrology (CEH) in Edinburgh (UK).

Front cover:

A plume dispersing in the atmospheric Convective Boundary Layer as simulated by Large Eddy Simulation technique. During their travel from the source to the receptor point, the plume's constituents undergo several physical and chemical processes such as transport by the mean wind, turbulent mixing, and chemical/radioactive transformations.

Thesis printing: Print Partners Ipskamp B.V.